

GOODYEAR AEROSPACE CORPORATION

AKRON 15, OHIO

Copy No. 27

APPLICATION OF RICE/WILBERFORCE

GRAVITY-GRADIENT DAMPER TO NASA

LENTICULAR COMMUNICATION SATELLITE

Contract NAS-1-3114

Amendment No. 4

GER-11790

3 November 1964

TABLE OF CONTENTS

<u>Section</u>	<u>Title</u>	<u>Page</u>
LIST OF ILLUSTRATIONS		vii
LIST OF TABLES		xi
I INTRODUCTION		1
II DESCRIPTION OF SYSTEM		3
1. General		3
2. Physical Description		3
3. Mathematical Description		5
III DAMPER ANALYSIS AND TUNING THEORY		9
1. General		9
2. Analysis of Damper		9
a. General		9
b. Analysis of Damping Spectrum		17
c. Characteristic-Equation Root-Extraction Analysis		19
3. Tuning Theory		21
IV PERFORMANCE OF DAMPER ON SATELLITE		25
1. General		25
2. Lenticular Satellite and R/W Damper		25
3. Studies of Transient and Steady-State Response .		26
a. General		26
b. Analog-Computer Simulation of Transient and Steady-State Response		27
c. Results of Transient-Response Study		28
4. Studies of Steady-State Response		33
a. General		33
b. Moments Due to Solar Radiation Pressure .		34
c. Solar-Torque Forcing Functions		45

<u>Section</u>	<u>Title</u>	<u>Page</u>
	d. Effects of Orbital Eccentricity	46
	e. Results of Study	48
V	CONCLUSIONS AND RECOMMENDATIONS	55
LIST OF REFERENCES		57
<u>Appendix</u>		
A	NOMENCLATURE, ENERGY, AND DISSIPATION FUNCTIONS AND EIGHT-DEGREES-OF-FREE- DOM EQUATIONS	A-1
1.	Nomenclature	A-1
2.	Energy Equations	A-2
a.	Kinetic Energy	A-2
b.	Potential Energy	A-3
c.	Dissipation Function	A-3
3.	System Differential Equations (8 Deg of Free- dom)	A-3
B	RICE/WILBERFORCE SPRING EQUATIONS	B-1
1.	General	B-1
2.	Helical-Spring Shape Relationships	B-4
3.	Elastic Characteristics of a Helical Spring . .	B-7
4.	Evaluation of Helical-Spring-Stiffness Charac- teristics for Unstressed Condition; $L_o = 0$, $\theta_o = 0$	B-13
5.	Helical-Spring Parameters for Unstressed Helix Angle $\theta_o = 0$ Deg	B-14
6.	Stress-Parameter Relationships for Helical Springs Made from Round Wire with Un- stressed Helix Angle $\theta_o = 0$	B-16
C	LINEARIZED EIGHT-DEGREES-OF-FREEDOM EQUATIONS	C-1
D	TRANSIENT-RESPONSE AND STEADY-STATE- RESPONSE HISTORIES FROM ANALOG-COM- PUTER STUDY	D-1

TABLE OF CONTENTS

GER-11790

<u>Appendix</u>	<u>Title</u>	<u>Page</u>
E	TRANSIENT-RESPONSE AND STEADY-STATE- RESPONSE HISTORIES FROM DIGITAL-COM- PUTER STUDY	E-1

LIST OF ILLUSTRATIONS

<u>Figure</u>	<u>Title</u>	<u>Page</u>
1	Rice/Wilberforce Damper on Lenticular Communication Satellite	4
2	Configuration of System and Attitude Parameters	6
3	Schematic Diagram and Definition of Symbols for R/W Damper	10
4	Mechanical Impedance Diagram of Rice/Wilberforce Damper	12
5	Three-Degrees-of-Freedom Coupled versus Uncoupled Spring Natural Frequencies of R/W Damper for 30-Deg Helix Angle	14
6	Damping Spectrums for Preferred Configurations	20
7	Roots of Characteristic Equation for Preferred Configurations	23
8	Lens Subsystem	38
9	Torus Subsystem	39
10	Boom Subsystem	41
11	Canister Subsystem	43
12	Solar Torques About Body Axes (Sun Line in Plane of Orbit)	46
13	Solar-Torque Forcing Functions (Sun Line 45 Deg from Plane of Orbit)	47
B-1	Comparison of Spring Parameters	B-3
B-2	Geometric Parameters of Helical Spring	B-4
B-3	Helical Spring - Elastic Characteristics	B-9

<u>Figure</u>	<u>Title</u>	<u>Page</u>
B-4	Helical-Spring Stiffness Coefficients.	B-15
B-5	Helical-Spring Parameters for Unstressed Helical Angle $\theta_0 = 0$ Deg	B-17
D-1	Optimum Configuration, Pitch Transient Response	D-3
D-2	Optimum Configuration, Roll Transient Response.	D-4
D-3	Optimum Configuration, Pitch, Roll, and Yaw Transient Response	D-5
D-4	Optimum Configuration, Pitch and Roll Transient Response.	D-7
D-5	Analog-Digital Pitch Transient Response Comparison with Digital Run 103	D-25
D-6	Digital-Analog Pitch Transient Response Comparison with Digital Run 103	D-27
D-7	Analog-Digital Roll Transient Response Comparison with Digital Runs 115 and 118	D-31
D-8	Digital-Analog Roll Transient Response Comparison with Digital Runs 115 and 118	D-33
D-9	Analog-Digital Roll Transient Response Comparison with Digital Runs 115 and 118 (No Initial Yaw)	D-41
D-10	Preferred Configuration, Pitch Transient Response with Hysteresis Damping Only	D-43
D-11	Preferred Configuration, Roll Transient Response with Hysteresis Damping Only	D-45
D-12	Preferred Configuration, Pitch and Roll Transient Response with Hysteresis Damping Only	D-47
D-13	Preferred Configuration, Pitch Transient Response with Light Damping Fluid	D-49
D-14	Preferred Configuration, Roll Transient Response with Light Damping Fluid	D-51

<u>Figure</u>	<u>Title</u>	<u>Page</u>
D-15	Preferred Configuration, Pitch and Roll Transient Response with Light Damping Fluid	D-53
D-16	Preferred Configuration, Pitch Transient Response for Unphotolyzed Satellite	D-55
D-17	Preferred Configuration, Roll Transient Response for Unphotolyzed Satellite	D-57
D-18	Preferred Configuration, Pitch Transient Response for Symmetrical Satellite	D-59
D-19	Preferred Configuration, Roll Transient Response for Symmetrical Satellite	D-61
D-20	Preferred Configuration, Roll Transient Response for Symmetrical Satellite with Small Initial Roll . .	D-63
D-21	Optimum Configuration, Roll Transient Response with Small Initial Roll	D-64
D-22	Optimum Configuration with Plunging-Spring Constant Increased Four Percent with Small Roll. . . .	D-65
D-23	Optimum Configuration with Plunging-Spring Constant Increased Four Percent with Large Roll . . .	D-67
D-24	Optimum Configuration with Plunging-Spring Constant Decreased Four Percent with Small Roll . . .	D-69
D-25	Optimum Configuration with Plunging-Spring Constant Decreased Four Percent with Large Roll . . .	D-71
D-26	Optimum Configuration with Torsional-Spring Constant Increased 23 Percent with Large Pitch	D-73
D-27	Optimum Configuration with Torsional-Spring Constant Increased 23 Percent with Large Roll	D-74
D-28	Optimum Configuration with Torsional-Spring Constant Decreased 42 Percent with Large Pitch. . . .	D-75
D-29	Optimum Configuration with Torsional-Spring Constant Decreased 42 Percent with Large Roll	D-76

<u>Figure</u>	<u>Title</u>	<u>Page</u>
D-30	Optimum Configuration, Steady-State Response to 0.01 Eccentricity	D-77
D-31	Optimum Configuration, Steady-State Response to Sun in Orbital Plane	D-79
D-32	Optimum Configuration, Steady-State Response to Sun 45 Degrees to Orbital Plane	D-81
D-33	Preferred Unphotolyzed Configuration, Steady- State Response to 0.01 Eccentricity	D-83
D-34	Preferred Unphotolyzed Configuration, Steady- State Response to Sun in Orbital Plane	D-85
D-35	Preferred Unphotolyzed Configuration, Steady- State Response to Sun 45 Degrees to Orbital Plane	D-87

LIST OF TABLES

<u>Table</u>	<u>Title</u>	<u>Page</u>
I	Mass and Inertia for Degrees of Photolyzation . . .	26
II	Analog-Computer Study of Transient Response . . .	29
III	Digital-Computer Study of Transient Response . . .	35
IV	Analog-Computer Study of Steady-State Response . .	51
V	Digital-Computer Study of Steady-State Response . .	53

SECTION I - INTRODUCTION

Under Contract NAS-1-3114, Amendment 4, from National Aeronautics and Space Administration, Langley Research Center, Goodyear Aerospace Corporation (GAC) analyzed a proposed gravity-gradient stabilization system for the Langley passive lenticular communications satellite. The stabilization system used a Rice/Wilberforce gravity-gradient damper, a rotary dashpot attached to the satellite by a lossy helical spring.

The purpose of the study was to determine the transient-response and steady-state-response characteristics of the stabilization system, including the effects of gyroscopic cross-coupling between the librations of the satellite. The dynamics of the system were therefore studied through comprehensive eight-degrees-of-freedom equations of motion (solved by simulation on analog and digital computers).

Results show that transient librations about all three body axes of the satellite are damped out. The settling-time constant of transient libration in the pitch axis is roughly three orbital periods and for the roll axis, six orbital periods. Steady-state forced librations caused by solar-pressure torques and orbital eccentricity are less than 2 deg in amplitude. The study also shows that the use of photolyzable film in the lens of the satellite is not a requirement of the stabilization system. The use of unphotolyzed film in the satellite merely results in somewhat degraded but still acceptable transient and steady-state performance caused by the increased moment of inertia about the yaw axis of the satellite and the increased solar-pressure torque.

SECTION II - DESCRIPTION OF SYSTEM

1. GENERAL

The Rice/Wilberforce damper is somewhat like the lossy hysteresis spring damper developed by the Applied Physics Laboratory, John Hopkins University, for the TRAAC satellite. However, the R/W damper is a viscous-fluid damper that exploits resonant rises and the cross-coupling in a helical spring between the plunging and torsional modes, producing a high-articulation gain that converts the slow angular gravity-gradient librations into relatively fast rotation in the viscous damper. Thus, the usual limitation of performance of rate-sensitive damping devices in gravity-gradient systems is removed. Because yaw damping is developed through cross-coupling phenomena, damping is provided about all three axes of the satellite.

On the lenticular satellite, the damper is to maintain the attitude of the satellite within a nominal deviation of 3 deg from vertical. To do this, the damper system must damp out initial attitude errors within a reasonable time and prevent steady-state perturbing torques on the satellite, such as solar-pressure torques and orbital eccentricity, from building up errors larger than this nominal deviation.

2. PHYSICAL DESCRIPTION

Figure 1 shows the R/W damper on the satellite. The complete stabilization system consists of gravity-gradient booms with attached canister loads and the R/W damper. For stabilization, the important considerations are the moments of inertia of the principal axes of the satellite, the contribution of the gravity-gradient booms, and the energy-dissipation capability of the damper.

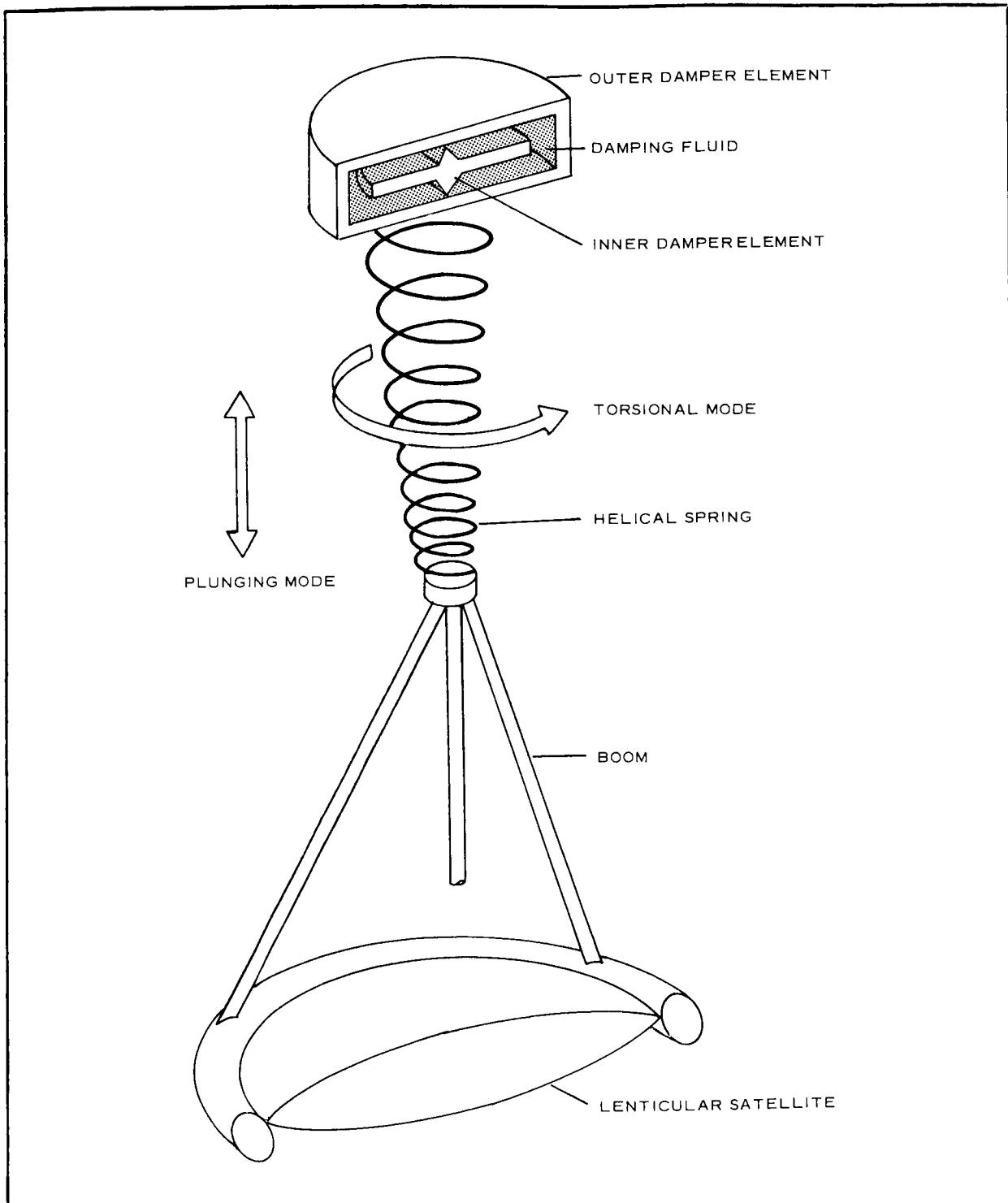


Figure 1 - Rice/Wilberforce Damper on Lenticular Communication Satellite

The R/W damper on the lenticular satellite will damp initial pitch and roll displacements of 25 deg down to the nominal deviation of 3 deg in 6 and 10 orbits, respectively. Depending upon the degree of photolyzation of the satellite structure and the orbital eccentricity, the steady-state attitude deviation from vertical will become even smaller with time in orbit.

The large size and moments of inertia of the satellite should be emphasized. The weight of the satellite in orbit is nominally 1000 lb for the study. The yaw-axis moment of inertia is 120,000 slug ft², and the pitch and roll moments of inertia are approximately 1,000,000 slug ft². The satellite is 720 ft high and 500 ft between the lower canister and the upper canister. The tip mass of the R/W damper weighs 100 lb. The cadmium-plated copper helical spring is 220 ft long and 8 in. in diameter.

3. MATHEMATICAL DESCRIPTION

The equations of motion presented here were used in the eight-degrees-of-freedom analog computer simulation. Simplified versions have been used for digital-computer simulation, damping spectrum, and characteristic-equation root-extraction analyses.

The coordinate systems, Euler-angle set, and nomenclature are identical to those used in TG-502, Dynamic Analysis of Gravity-Gradient Satellite with Passive Damping,¹, a with the addition of terms necessary to describe the additional degree of freedom of the R/W damper. The term $M/(M + m)$ has been retained as a multiplying factor in the energy expressions. The configuration of the system and the YXZ Euler-angle orientation are shown in Figure 2.

The assumptions pertinent to these complete eight-degrees-of-freedom equations are:

^aSuperior numbers in the text refer to items in the List of References.

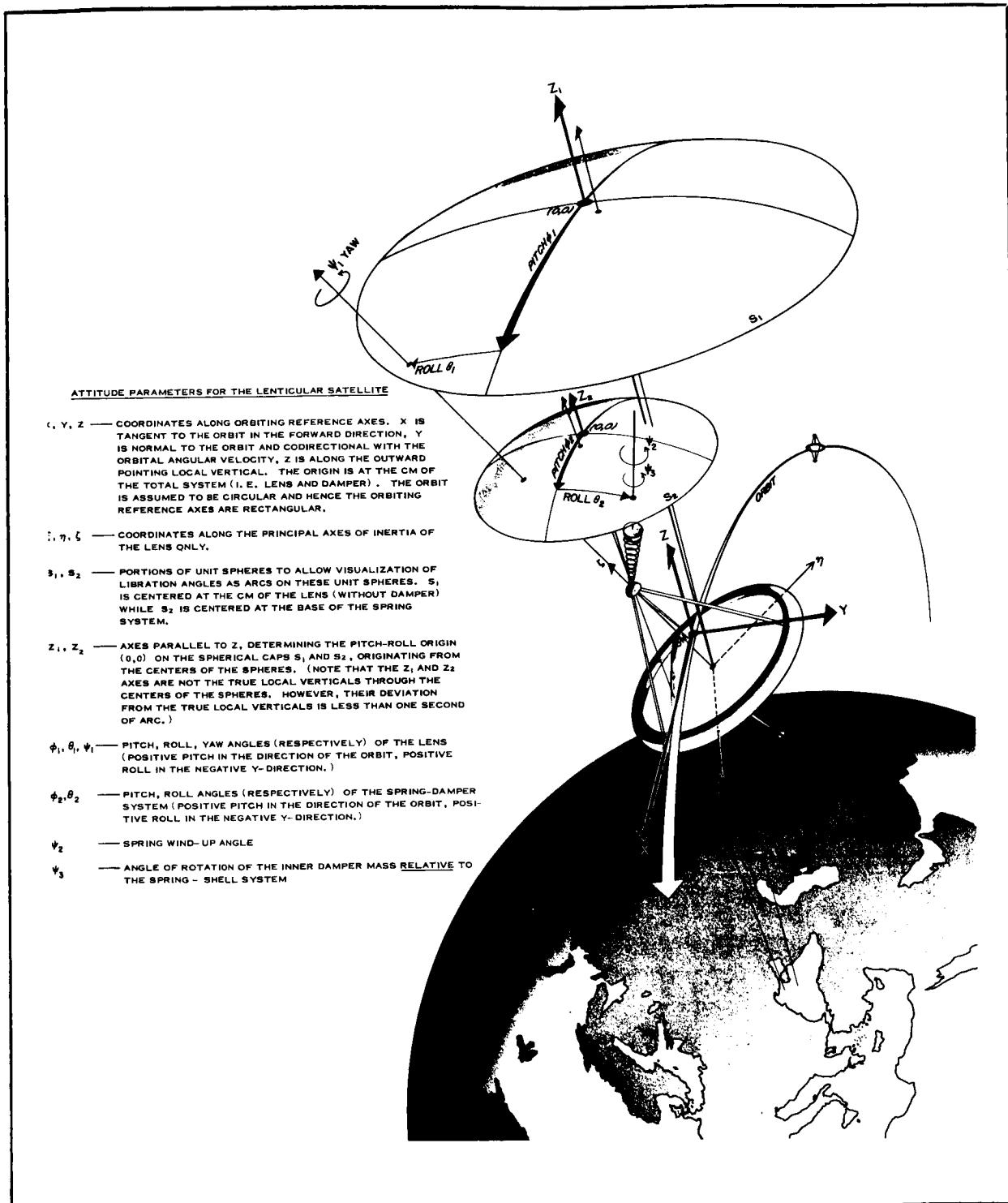


Figure 2 - Configuration of System and Attitude Parameters

1. Orbit of the center of mass (c. m.) of the satellite-damper system is inexorably circular.
2. Inner and outer masses at the end of the spring are considered point masses. However, the spin moments of inertia are considered. The weight of the spring is neglected.
3. The spring is essentially a flexible shaft transmitting yaw rotation; bending of its axis does not alter the apparent yaw rotation (of the damper or satellite) transmitted through the spring. Also, satellite pitch and roll are not transferred to the spring.
4. Although the spring loss is expected to be principally hysteretic, it has been represented by an equivalent viscous damping.
5. Nonlinear spring can be simulated by a "constant" spring constant, based on desired equilibrium length and helix angle, and a bias in the r equation, which results in static equilibrium about r_e .

The nomenclature, the energy and dissipation functions, and the eight-degrees-of-freedom equations of motion are in Appendix A.

As in GER-11502,² the independent-variable time was normalized to $\tau = \omega t$. It was this form of the equations that was further linearized to allow for the characteristic-equation and root-extraction analyses referred to in the following section on tuning theory, explaining why the imaginary part of the roots in Figure 7 are in terms of ω_0 .

SECTION III - DAMPER ANALYSIS AND TUNING THEORY

1. GENERAL

Optimum values for the damper parameters were developed under assumed limits of total damper weight, maximum outside dimensions, and other constraints imposed by payload capability. Optimization is achieved by setting the natural frequencies of the two modes of damper articulation at certain discrete frequencies that will be excited by librations of the satellite. The spring constants, masses, and inertias of the damper are selected to give the discrete frequencies at which the most energy will dissipate. The energy-dissipation in each of the two modes is adjusted for a compromise between high dissipations over a narrow band of frequencies and lower dissipations over a broader band of frequencies. The mechanical hysteresis of the plunging mode of the spring and the viscosity of the fluid in the torsional mode are the parameters varied to make this compromise.

The analysis indicates how the usual low rate limitation of viscous dampers in gravity-gradient systems is overcome by the high-articulation gain of the Rice/Wilberforce damper and resonant tuning that transform the low angular librations into relatively fast motion of the damping elements.

2. ANALYSIS OF DAMPER

a. General

Figure 3 is a schematic diagram and definition of symbols used in the analysis of the R/W damper. For an analysis of optimum tuning and energy-dissipation, it is convenient to work with rates of displacement as the basic variables, since the dissipative elements of the damper are treated as rate-sensitive. The damper alone, when in

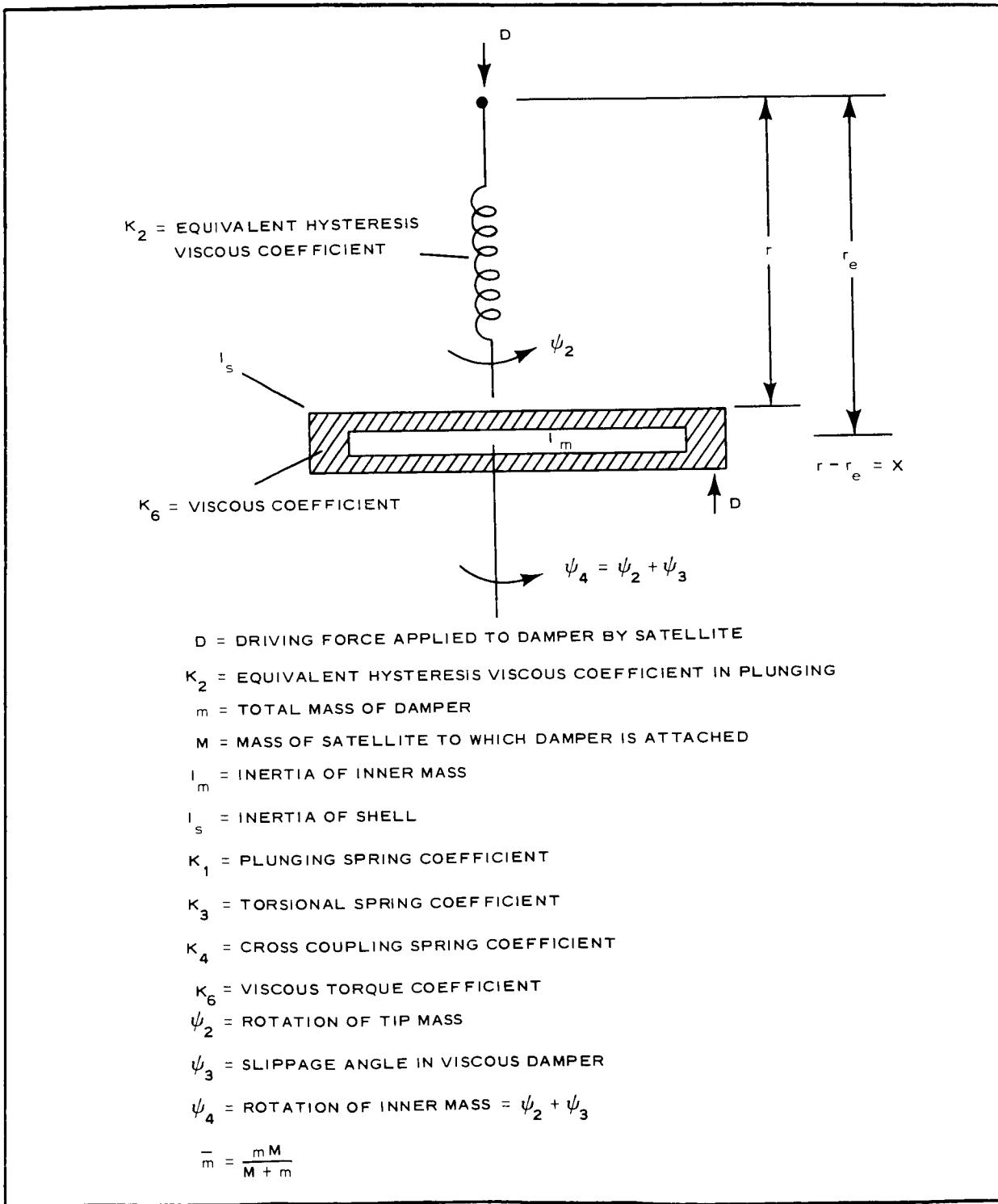


Figure 3 - Schematic Diagram and Definition of Symbols for R/W Damper

orbital deployment (but neglecting spring libration angles), is described mathematically by the following differential equations of motion:

$$\left[\bar{m}p + K_2 + \frac{1}{p} \left(K_1 - 3\bar{m}\omega_o^2 \right) \right] \dot{x} - \frac{K_4}{p} \dot{\psi}_2 = D, \quad (1)$$

$$-\frac{K_4}{p} \dot{x} + \left(I_s p + K_6 + \frac{K_3}{p} \right) \dot{\psi}_2 - K_6 \dot{\psi}_4 = 0, \quad (2)$$

and

$$(I_m p + K_6) \dot{\psi}_4 - K_6 \dot{\psi}_2 = 0, \quad (3)$$

where p is the Laplace operator signifying $d(\)/dt$. The properties of helical springs in the range of parameters required here are discussed in Appendix C. Note that the over-all spring constant, as modified by the gravity-gradient and centrifugal-force term, $K_1 - 3\bar{m}\omega_o^2$, must be positive.

Figure 4 is a mechanical impedance diagram for these equations of motion. Coefficient K_4 should be as large as practical, for maximum excitation of the torsional mode. If the plunging and torsional loop impedances are combined through Thevinin's theorem and set to equal zero, to match most nearly the conjugate of the load impedance, Equation 4 is obtained by making two reasonable assumptions:

$$I_m \gg \frac{K_6}{p},$$

and

$$K_2 = 0.$$

$$\left(K_3 + I_s p^2 \right) \left(K_1 + \bar{m}p^2 - 3\bar{m}\omega_o^2 \right) - K_4^2 = 0 \quad (4)$$

Equation 4 is of fourth order in the variable p , giving rise to two natural frequencies in the response of the damper. These natural frequencies are, of course, related to the isolated plunging and torsional modes of

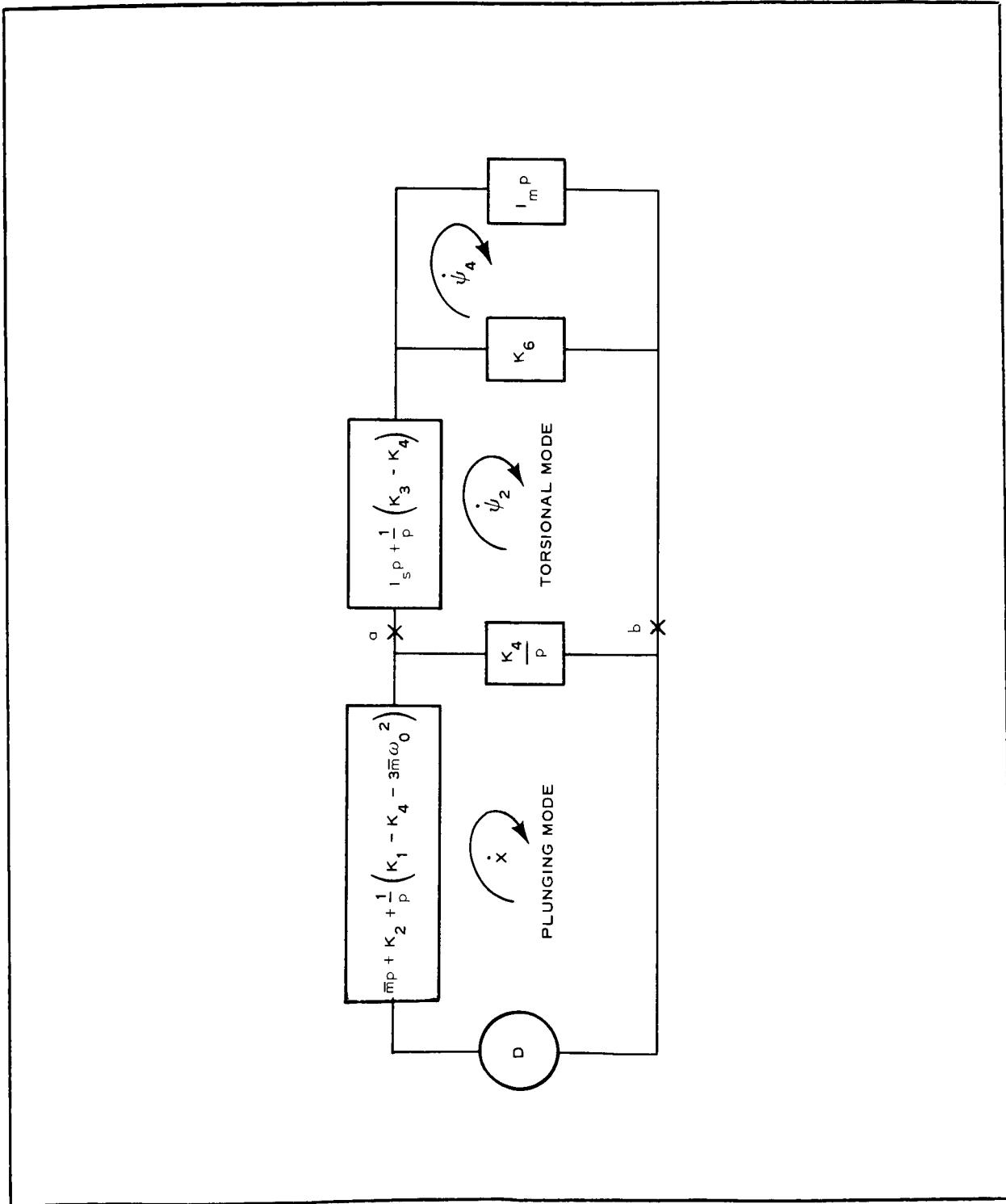


Figure 4 - Mechanical Impedance Diagram of Rice/Wilberforce Damper

the damper, depending on the magnitude of cross-coupling coefficient K_4 . If cross-coupling term K_4 is set to equal zero, the two isolated or uncoupled natural frequencies of the damper are

$$\omega_{n_{\text{torsion}}} = \sqrt{\frac{K_3}{I_s}} \quad (5)$$

and

$$\omega_{n_{\text{plunging}}} = \sqrt{\frac{K_1 - 3\bar{m}\omega_o^2}{\bar{m}}} \quad (6)$$

It is convenient to analyze the coupled natural frequencies that are the solution to Equation 4 in terms of the uncoupled natural frequencies. One result is shown in Figure 5 for a spring helix angle of 30 deg, where the cross-coupling is given by

$$K_4 = 0.34 \sqrt{K_1 K_3}.$$

When large values of fluid-damping coefficient K_6 are employed, and for which the assumption of small K_6 does not hold, tuning Equation 4 must be modified to include the reflected inertia of the inner member of the damper. The modification takes the form of substituting a new value, I_s' , for I_s into these equations. The new value is

$$I_s' = I_s + \frac{K_6^2 I_m}{K_6^2 - p^2 I_m^2}. \quad (7)$$

Use of tuning Equation 4 requires knowledge of the discrete frequencies at which the R/W damper accepts the librational energy of the satellite and dissipates that energy in the damping fluid and the hysteresis loss coating of the helical spring. Specifying the frequencies requires examination of the librational frequencies of the satellite and the way the librational motion excites the R/W spring. Basically, the spring is attached to the

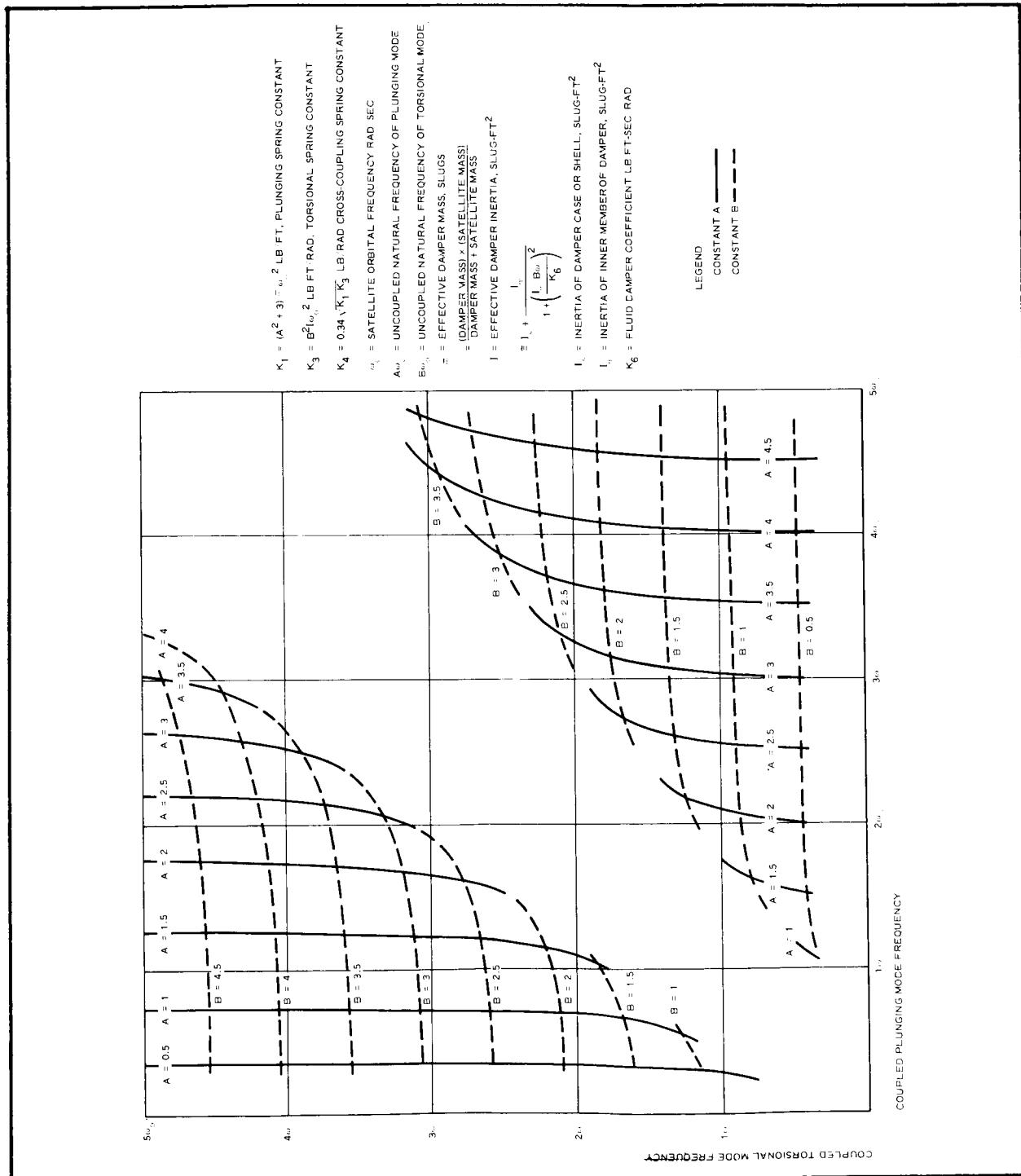


Figure 5 - Three-Degrees-of-Freedom Coupled versus Uncoupled Spring Natural Frequencies of R/W Damper for 30-Deg Helix Angle

satellite by a long gravity-gradient boom, so there will be tension forces in the spring due to centrifugal and gravity-gradient forces that excite the plunging and torsional modes of the damper. First, consider the centrifugal forces in the spring due to the orbital-plane or pitch-axis motion of the satellite. In the presence of pitch-axis librations, the total angular rate of concern is orbital rate, ω_o , plus pitch libration rate, $\dot{\phi}$. The resultant centrifugal force, producing tension in the plunging mode of the spring, is proportional to

$$(\omega_o + \dot{\phi})^2 = \omega_o^2 + 2\omega_o\dot{\phi} + \dot{\phi}^2. \quad (8)$$

Consideration of Equation 8 shows that tension forces in the spring due to centrifugal effects of pitch-axis motion are periodic at the fundamental and second harmonic of the satellite natural frequency in pitch plus a zero frequency or steady component. Centrifugal forces due to roll-axis or traverse-plane librations can be shown to contain a zero-frequency term plus a second harmonic of the roll-axis natural frequency. Thus, there is a significant difference in the frequency composition of tension forces in the spring between those due to centrifugal forces of pitch librations and those due to centrifugal forces of roll-axis librations; that is, the pitch librations cause fundamental and second-harmonic terms that excite the spring, whereas the roll librations generate only second-harmonic terms in the spring tension.

The discussion of the frequency composition of forces that excite the R/W spring has emphasized those forces originating by centrifugal action. Equally important are the forces in the spring that arise from differential gravity. The spring-tension forces due to gravity gradient are periodic at twice the natural libration frequencies of the satellite. (Recall that tension in a rod connecting the two masses of a dumbbell satellite is periodic at twice the libration frequency of the dumbbell.) Thus, there is excitation of the R/W spring at the second harmonic of the libration frequencies of the satellite because of centrifugal and differential gravity forces acting along the plunging axis of the spring.

Pitch-axis librations excite the spring tension at the fundamental and second harmonic of the pitch axis, whereas in roll, tension forces in the spring are periodic at only the second harmonic of the roll-libration natural frequency. The damper can dissipate no energy associated with steady or zero-frequency forces. Therefore, the tuning frequencies chosen must be constrained. For damping the roll-axis librations, either the plunging or torsional mode can be tuned to the second harmonic of the roll-axis natural frequency. There is somewhat more freedom in suppressing pitch-axis librations, with the choice of tuning the remaining plunging or torsion mode to either the fundamental or second harmonic of the pitch natural frequency. If certain practical aspects are considered, such as the minimum length and maximum stiffness of the spring, then the plunging mode should be tuned to the second harmonic of the satellite roll-axis frequency, and the wind-up mode of the damper should be tuned to the pitch-axis natural frequency of satellite libration. Another practical consideration would be to reverse the gyroscopic-precession torques of the damper as often as possible. This consideration leads to tuning the plunging mode to the second harmonic of the pitch-axis librations and the torsional mode to the second harmonic of the roll-axis librations. The latter tuning is not possible for large cross-coupling coefficients of the R/W spring, where the helix angle is in the region of 25 deg or more. However, if a low helix angle (15 to 20 deg) is used in the spring, such tuning is possible. Figure 5 gives insight into this constraint on the physically realizable tuning frequencies. In general, if spring cross-coupling is increased by use of a larger helix angle in the spring, then the two-mode frequencies are constrained to be farther apart.

The influence of the fluid viscosity and the hysteresis loss of the cadmium-coated spring is as follows. The energy dissipation or power loss in the damper fluid is

$$W_f = K_6 (\dot{\psi}_2 - \dot{\psi}_4)^2 , \quad (9)$$

where

K_6 = fluid-drag-torque coefficient, and

$(\dot{\Psi}_2 - \dot{\Psi}_4)$ = slip rate in the damper.

Similarly, the energy dissipation in the hysteresis of the cadmium coating of the spring is

$$W_h = K_2 \dot{X}^2 , \quad (10)$$

where

K_2 = equivalent viscous coefficient of the cadmium coating and

\dot{X} = rate of spring deflection in plunging.

The expression for K_2 used for analysis is

$$K_2 = \frac{bK_1}{2\omega\pi} , \quad (11)$$

where

b = fractional energy loss per cycle of plunging in the spring,

K_1 = plunging-spring constant, and

ω = plunging frequency.

Note that Equation 11 is valid at one frequency only, but since the plunging mode is excited dominantly at a single discrete frequency, this expression holds.

b. Analysis of Damping Spectrum

A damping-spectrum analysis was made to determine how the band width and relative dissipation capabilities vary with damper characteristics and how the undamped coupled frequencies obtained from Equation 4 are affected by fluid and hysteresis damping. Equations

1 through 3 were modified to four degrees of freedom and used to obtain the peak damping spectrums for the three damping sources as a function of input frequency for a sinusoidal rate input and various spring and damper characteristics.

A constant-amplitude sinusoidal rate input (one foot per second) was imparted to the top of the spring, and the lower end masses were free. Note that two translation variables, X_1 and X_2 , are now needed in the equations, one for each end of the spring. The rate input was used for direct comparison between the rate-sensitive damping sources, hysteresis damping in plunging, viscous damping in the end masses, and hysteresis damping in torsion.

Solutions to each of the three remaining variables were assumed to be of the form

$$\dot{X}_2 = B \sin \omega t + C \cos \omega t. \quad (12)$$

Substituting and considering the validity of the remaining equations at both $\omega t = 0$ and $\pi/2$, the three equations become six equations in six unknowns. The matrix form of these equations was solved by Crout's reduction method on the digital computer to obtain the unknowns, B, C, D, etc. In terms of these variables, the rates for damping are

$$\begin{aligned} (\dot{X}_2 - \dot{X}_1)_{\max}^2 &= (B - A)^2 + C^2 \\ \dot{\Psi}_2^2_{\max} &= D^2 + E^2 \\ \dot{\Psi}_3^2_{\max} &= (F - D)^2 + (G - E)^2 \end{aligned} \quad (13)$$

The peak dissipation for a sinusoidal displacement input is proportional to ω^3/ξ . Since this analysis gives the relative dissipation for a constant sinusoidal rate input, it is equivalent to dividing all dissipation values by ω^2 . The maximum dissipation as functions of input

frequency is plotted in Figure 6. These spectrums, with the characteristic roots, demonstrate the shifting of the poles (roots) as varying degrees of damping and cross-coupling are added. ω_T and ω_P are the frequencies for the coupled spring without damping, the spectrums show the slight shifting as damping is introduced, and ω_{ψ_2} and ω_r are the spring-torsion and plunging-characteristic frequencies for the completely coupled eight-degrees-of-freedom satellite-plus-damper system.

These two spectrum plots, with the performance of these tuning conditions in Section IV, Item 3, c, demonstrate the existence of two optimum tuning conditions as a result of the way the fluid viscosity influences the equivalent inertia in torsion. In the high-viscosity case, a large equivalent inertia exists with small slippage between masses, while in the low-viscosity case, a small inertia exists with more motion between the end masses. Section III, Item 1, explains the mechanics involved.

In a final choice between high- and low-viscosity fluids, the physical characteristics (including temperature independency and handling qualities) must be considered. Preliminary analyses based on Coutte flow show that the required viscosity can be obtained by using fluoro-hydrocarbon, chlorocarbon, or silicone fluids.

c. Characteristic-Equation Root-Extraction Analysis

The general eight-degrees-of-freedom equations of motion were simplified for digital-computer analysis as presented in Section IV, Item 3. A normalized time was introduced for convenience, reducing the orbital frequency to one. These normalized equations were then linearized for use in a digital-computer program to form the characteristic equation from polynomial matrix elements. The Muller root-extraction routine was then used to obtain the complex form of the roots.

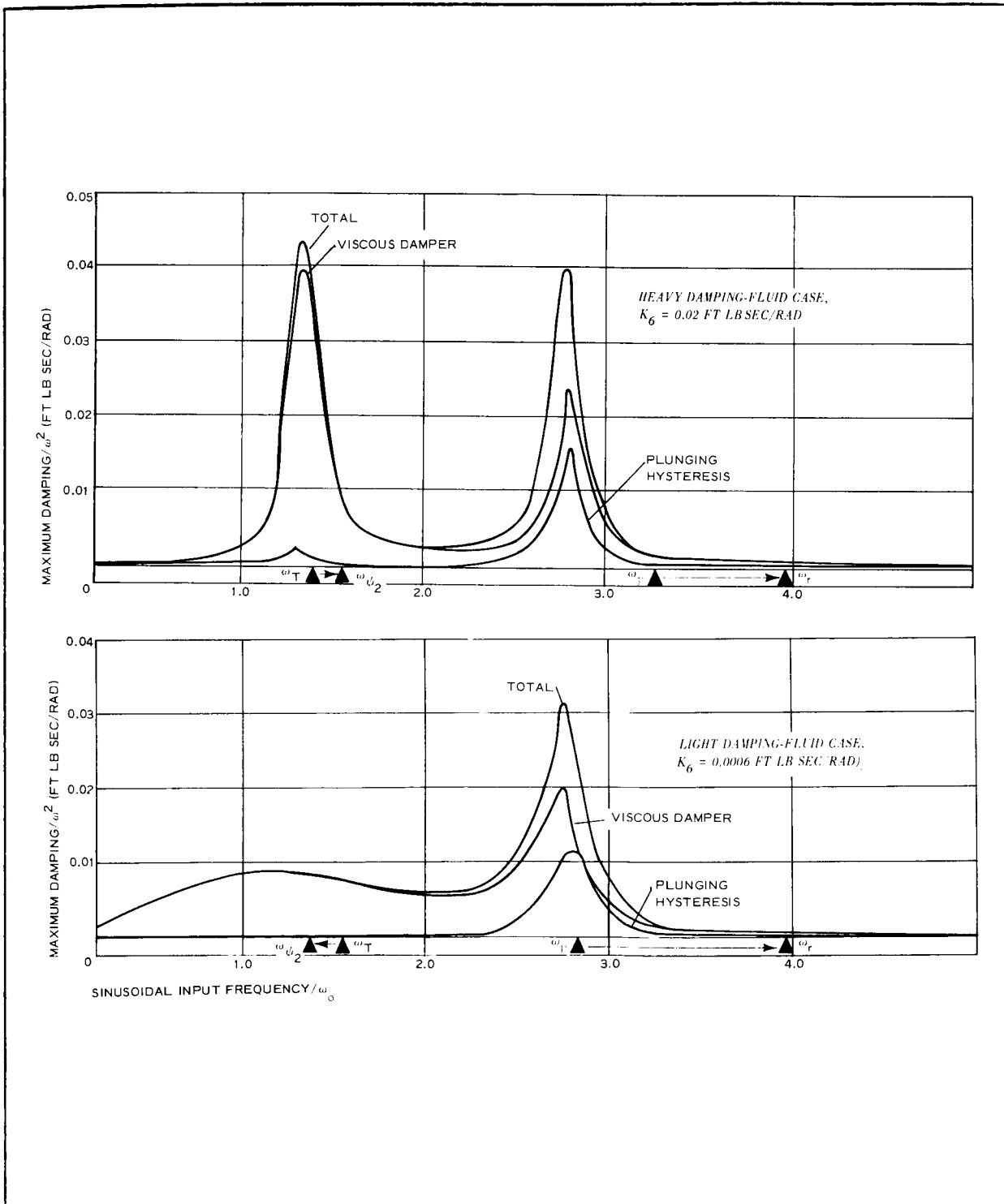


Figure 6 - Damping Spectrums for Preferred Configurations

These linearized equations in matrix form are presented in Appendix C for the lenticular satellite and R/W damper. The roots for the preferred satellite and two preferred dampers are shown in Figure 7. Note how the completely coupled plunging frequency of the spring, ω_r , equals twice the satellite roll frequency, ω_{θ_1} . The completely coupled torsional frequency of the spring, ω_Ψ , is slightly higher than the satellite pitch frequency, ω_{ϕ_1} , thus indicating a broader band for pitch tuning, as is confirmed by analog- and digital-computer data. Also, note how the roll frequency of the satellite is relatively independent of the pitch-damper. The roots of satellite roll are unstable with long time constants, since the roll mode is damped only through second-order terms that were eliminated in this linear analysis.

This root-extraction program became especially valuable when the criterion for evaluating damping shifted from initial large-angle to small-angle transient response (4 deg or less). At the small angles, the preferred tuning in plunging from digital-computer studies is less than one percent lower than that obtained by tuning the plunging frequency, ω_r , to exactly twice the roll frequency, ω_{θ_1} . This minute variation is due to the higher-order terms and coupling that exist in the satellite-motion computer programs and the slight downward variation of frequency with increase in amplitude.

3. TUNING THEORY

The preferred tuning theory consists of tuning the completely coupled plunging frequency of the damper to twice the roll frequency of the satellite. The torsional frequency of the damper tends to drive the pitch frequency of the satellite down, so the damper is tuned in torsion as close to the pitch frequency as possible (the resulting pitch frequency must not be resonated by the eccentricity-forcing frequency of approximately ω_o). Damping-spectrum data provided insight into the dynamics of the damper

alone and helped develop the tuning theory. The characteristic-equation root-extraction data helped confirm the tuning theory and corroborated the optimum tuning parameters obtained with computer simulations. The characteristic-equation data also showed how far a linearized analysis could be used to tune this damper (the best plunging-spring constant, according to the linearized analysis, is within one percent of the preferred digital-computer-simulation tuning). With all considered, the satisfactory band width for tuning the more-critical plunging-spring constant shows up as an allowable 4-percent variation. Further parameter-variation studies are needed to confirm the design and orbital tolerances involved. A method of increasing the tuning-band width, which requires study of its feasibility, is to increase the fractional energy loss per cycle, b , of the spring. Increasing factor b from 25 to 50 percent approximately doubles the tuning-band width.

HEAVY DAMPING-FLUID CASE, $K_6 = 0.02$ FT LB-SEC/RAD

1	REAL	0.03000000E+00	IMAGINARY	0.00000000E+00	$s = 0$
2	REAL	-0.38626807E+01	IMAGINARY	0.12058294E+01	ω_{ϕ_1}
3	REAL	-0.38626807E+01	IMAGINARY	-0.12058294E+01	ω_{ψ_1}
4	REAL	-0.58486264E+05	IMAGINARY	-0.93912025E+00	ω_{ϕ_1}
5	REAL	-0.58486264E+05	IMAGINARY	0.93912025E+00	ω_{ψ_1}
6	REAL	-0.58171697E+01	IMAGINARY	-0.15493374E+01	ω_{ϕ_2}
7	REAL	-0.58171697E+01	IMAGINARY	0.15493374E+01	ω_{ψ_2}
8	REAL	0.57896392E-06	IMAGINARY	-0.19912767E+01	ω_{θ_1}
9	REAL	0.57896409E-06	IMAGINARY	0.19912767E+01	ω_{θ_1}
10	REAL	-0.32116849E-01	IMAGINARY	-0.25085772E+01	ω_{θ_1}

SECTION III - DAMPER

11	REAL	-0.32116849E-01	IMAGINARY	0.25085772E 01	ϕ_2
12	REAL	0.29938850E-06	IMAGINARY	-0.34287430E 01	ω_{θ_2}
13	REAL	0.29938850E-06	IMAGINARY	0.34287430E 01	ω_{θ_2}
14	REAL	-0.34880181E-01	IMAGINARY	0.39718522E 01	ω_r
15	REAL	-0.34880181E-01	IMAGINARY	-0.39718522E 01	ω_r
16	REAL	-0.70666794E 02	IMAGINARY	0.11213000E-18	$\sigma\psi_3$

LIGHT DAMPING-FLUID CASE, $K_6 = 0.0006$ FT LB-SEC/RAD

1	REAL	0.00000000E-00	IMAGINARY	0.00000000E-00	$s = 0$
2	REAL	-0.60484026E-05	IMAGINARY	0.93915180E-00	$\omega\psi_1$
3	REAL	-0.60484026E-05	IMAGINARY	-0.93915180E-00	$\omega\psi_1$
4	REAL	-0.65181957E-01	IMAGINARY	0.13688342E 01	$\omega\psi_2$
5	REAL	-0.65181957E-01	IMAGINARY	-0.13688342E 01	$\omega\psi_2$
6	REAL	0.17591406E-05	IMAGINARY	-0.19912839E 01	$\omega\theta_1$
7	REAL	0.17591406E-05	IMAGINARY	0.19912839E 01	$\omega\theta_1$

Figure 7 - Roots of

8	REAL	-0.78549903E-00	IMAGINARY	-0.13308276E 01	ω_{ϕ_1}
9	REAL	-0.78549903E-00	IMAGINARY	0.13308276E 01	
10	REAL	-0.59502455E-01	IMAGINARY	-0.24971745E 01	ω_{ϕ_2}
11	REAL	-0.59502455E-C1	IMAGINARY	0.24971745E 01	
12	REAL	-0.33C31236E-00	IMAGINARY	-0.46393560E-17	$\sigma\psi_3$
13	REAL	-0.50688074E-06	IMAGINARY	-0.34271322E 01	
14	REAL	-0.50688074E-06	IMAGINARY	0.34271322E 01	ω_{θ_2}
15	REAL	-0.38664911E-01	IMAGINARY	-0.39733403E 01	
16	REAL	-0.38664911E-01	IMAGINARY	0.39733403E 01	ω_r

Characteristic Equation for Preferred Configuration

SECTION IV - PERFORMANCE OF DAMPER ON SATELLITE

1. GENERAL

The Langley Research Center lenticular satellite is a large-inertia satellite to which a passive damper can be applied. The damping capability presented here therefore applies to large satellites (passive communication satellites, space stations, etc.) as well as small ones. On the other hand, most of the passive dampers described in the literature have been for small satellites where the payload could be approximated by a point mass in comparison with the gravity-gradient booms.

In the lenticular satellite, the librational (transient) motion to be damped may come from either initial-attitude errors or attitude rates, or the steady-state motion may be forced by solar-pressure torques or orbital eccentricity. As indicated in the preceding sections, various degrees of simplification were made for analog- and digital-computer simulations and closed-solution analyses. The simulations were concerned with the capability of the R/W damper to suppress the transient and steady-state motion of the lenticular satellite.

2. LENTICULAR SATELLITE AND R/W DAMPER

The lenticular satellite used in these studies was based on an early design to fix the configuration for damper analyses. No significant changes have been made. The mass and inertia distribution for various degrees of photolyzation are listed in Table I.

The influence of payload weight and space limitation was considered in arriving at a damper configuration. For a lenticular satellite with, for example, a 1000-lb payload limit, it is reasonable to allow 10 percent for gravity-gradient damping, to make the total weight of the damper

TABLE I - MASS AND INERTIA FOR DEGREES OF PHOTOLYZATION

Configuration	Mass ratio, m	Pitch and roll inertias (slug-ft ²)	Yaw inertia (slug-ft ²)
Nonphotolyzed	0.9	1,094,088	479,547
Lens photolyzed	0.9	1,026,173	377,529
All photolyzed	0.9	897,872	122,091

100 lb. The parameter $M/(M + m)$ thus becomes 0.9. Assuming further that the maximum outside diameter of the payload container can accommodate a damper no larger than a disk with a radius of 18 in., for an orbital altitude of 2000 naut mi and an orbital rate of $\omega_o = 6.2 \times 10^{-4}$ rad per second, the total tip-mass inertia becomes 50 lb-in.-sec^2 . Also, in attempting to make I_m as large as possible and yet holding the total tip-mass inertia to no more than 50 lb-in.-sec^2 , the best design could obtain a shell inertia no less than $6.25 \text{ lb-in.-sec}^2$, and an inner-element inertia no greater than $I_m = 43.75 \text{ lb-in.-sec}^2$.

For the desired spring characteristics, beryllium-copper or carbon-steel springs must be wire 0.015 in. in diameter in a coil approximately 8 in. in diameter. According to a reliable manufacturer of springs, the wire diameter can be held to a tolerance of 0.0001 in. In the spring theory, Appendix B, the spring constants are proportional to diameter to the fourth power, so the spring constants can be obtained within tolerances of 2.5 percent.

3. STUDIES OF TRANSIENT AND STEADY-STATE RESPONSE

a. General

Transient-response studies were made to determine the preferable satellite-damper configuration, using the tuning criteria developed in Section III. The analog simulation was used extensively to search

for the optimum and to compare configurations, while the digital was used to verify the results. Both simulations were based upon the eight-degree-of-freedom equations discussed in Section II. The basic differences between the two simulations with respect to the equations were:

1. The analog simulation maintained the trigonometric functions as presented in the complete equations of Section II. However, certain yaw-acceleration terms were negligible and were omitted as noted in the equations.
2. The digital simulation contained linearizing assumptions with respect to the trigonometric functions of the pitch and roll displacements, and third-order and higher terms were neglected ($\sin \theta = \theta$, $\cos \theta = 1 - \theta^2/2$, $\sin \theta \cos \theta = \theta$).

The results of the two simulations corroborated one another and the basic tuning criteria as shown in the computer runs.

b. Analog-Computer Simulation of Transient and Steady-State Response

The equations mechanized in the analog simulation are presented in Appendix A. Terms were rearranged, using trigonometric identities to improve their accuracy at low amplitudes and to reduce hardware requirements. Sine-cosine diode-function generators were used to develop the trigonometric functions. The circuitry reported in GER-11537³ simulated the required angular resolution of satellite yaw.

The simulation was checked for static accuracy by comparing all computer variables with calculated values for nominal sets of initial-condition rates and displacements, and the static error was less than one percent. Dynamic accuracy was checked by allowing each simulated position variable to oscillate with all cross-coupling terms

disconnected and the simulation frequency compared with the calculated value. Again, the static error was below one percent, and no convergence or divergence could be noted in any of the oscillations. The entire simulation was also examined for divergence at zero equilibrium; the very small divergence noted could be attributed to computer-equipment noise and accumulated electronic multiplier zero accuracy.

c. Results of Transient-Response Study

The results of the transient-response study are shown in Table II and Appendix D. The preferred configuration has the damper-spring plunging mode tuned to the second harmonic of the roll frequency and the torsional mode tuned near the pitch frequency. A relatively heavy damping-fluid coefficient was selected on the basis of the roll transient response and practical hardware considerations. A 12-percent asymmetry gives the system a preferred orientation about the yaw axis that results in the smallest steady-state yaw oscillation, and improves the low-amplitude damping for high initial roll errors. A photolyzed satellite was selected on the basis of reduced attitude errors induced by orbital eccentricity and solar pressure.

The criterion for optimum tuning of the R/W damper was low-amplitude transient response. The gains thus obtained from the digital-computer simulation and gains obtained by tuning the plunging mode to twice the satellite roll according to the linearized characteristic-root-extraction program are within 0.6 percent of each other. This agreement with slight difference is to be expected, because the second-order terms, including damping terms, are included in the digital simulation, and the criterion is based on response at small angles. The plunging gain obtained from the analog simulation is within 4 percent of the digital-simulation gain. The roots presented were obtained from the linearized root-extraction program, but for the gains as obtained from either the analog- or digital-computer simulation. Notice

Chart	Purpose of run	Inertias of satellite body axes (10^5 slug-ft 2)					Spring equilibrium length, r_e (ft)	Plunging spring constant K 10^{-3}
		Pitch	Roll	Yaw	Asymmetry (percent)	Extent of photolyzation		
1	Optimum configuration - demonstrate damping capability for large initial errors							
1	Pitch (25 deg)	9.5177	8.4403	1.221	12	Complete	206	1.1145
2	Roll (25 deg)	9.5177	8.4403	1.221	12		206	1.1145
3	Pitch (25 deg), roll (25 deg) and yaw (100 deg)	9.5177	8.4403	1.221	12		206	1.1145
4	Optimum digital configuration - digital verification of damping capability							
4	Pitch (25 deg), roll (25 deg) and yaw (0 deg)	9.5177	8.4403	1.221	12	Complete	218.7	1.077
5	Comparison of analog and digital simulation results							
5	Pitch (25 deg), yaw (90 deg)	9.1574	8.7982	1.221	4	Complete		
6	Analog	9.1574	8.7982	1.221	4		267	0.965
6	Digital 103	9.1574	8.7982	1.221	4		267	0.965
7	Roll (25 deg), yaw (90 deg)	9.1574	8.7982	1.221	4		267	0.965
7	Analog	9.1574	8.7982	1.221	4		267	0.965
8	Digital 115 and 118	9.1574	8.7982	1.221	4		267	0.965
8	Roll (25 deg), yaw (0 deg)	9.1574	8.7982	1.221	4		267	0.965
9	Analog	9.1574	8.7982	1.221	4		267	0.965
10	Configuration with hysteresis damping only							
10	Pitch (25 deg)	9.5177	8.4403	1.221	12	Complete	206	1.1145
11	Roll (25 deg)	9.5177	8.4403	1.221	12		206	1.1145
12	Pitch (20 deg), roll (20 deg) and yaw (0 deg)	9.5177	8.4403	1.221	12		206	1.1145
13	Light fluid damping configuration							
13	Pitch (25 deg)	9.5177	8.4403	1.221	12	Complete	207	1.1118
14	Roll (25 deg)	9.5177	8.4403	1.221	12		207	1.1118
15	Pitch (25 deg), roll (25 deg) and yaw (0 deg)	9.5177	8.4403	1.221	12		207	1.1118
16	Unphotolyzed satellite							
16	Pitch (25 deg)	11.560	10.322	4.7955	12	None	289	0.9251
17	Roll (25 deg)	11.560	10.322	4.7955	12		289	0.9251
18	Symmetrical satellite							
18	Pitch (25 deg)	8.979	8.979	1.221	0	Complete		
19	Roll (25 deg)	8.979	8.979	1.221	0		233	1.0382
20	Roll (4 deg)	8.979	8.979	1.221	0		233	1.0382
21	Optimum configuration							
21	Roll (4 deg)	9.5177	8.4403	1.221	12	Complete	206	1.1145
22	Optimum configuration with plunging spring constant K_1 increased by 4 percent	-						
22	Roll (4 deg)	9.5177	8.4403	1.221	12	Complete	193.2	1.1591
23	Roll (25 deg)	9.5177	8.4403	1.221	12		193.2	1.1591
24	Optimum configuration with plunging spring constant K_1 decreased by 4 percent							
24	Roll (4 deg)	9.5177	8.4403	1.221	12	Complete	220.7	1.070
25	Roll (25 deg)	9.5177	8.4403	1.221	12		220.7	1.070
26	Optimum configuration with torsional spring constant K_3 increased by 23 percent							
26	Pitch (25 deg)	9.5177	8.4403	1.221	12	Complete	206	1.1145
27	Roll (25 deg)	9.5177	8.4403	1.221	12		206	1.1145
28	Optimum configuration with torsional spring constant K_3 decreased by 42 percent							
28	Pitch (25 deg)	9.5177	8.4403	1.221	12	Complete	206	1.1145
29	Roll (25 deg)	9.5177	8.4403	1.221	12		206	1.1145

All runs except 5 through 9 and 22 through 29 have optimum tuning ratio between spring plunging and satellite roll modes. Transient

3LE II - ANALOG-COMPUTER STU

Rice/Wilberforce damper - parameters					
Ring ant., lb	Torsion spring constant, K_3 10^{-6} ft-lb rad	Cross- couple spring constant, K_4 10^{-6} lb rad	Plunging equivalent viscous hysteresis loss coefficient, K_2 10^{-4} lb-sec ft	Torsional equivalent viscous hysteresis loss coefficient, K_5 10^{-5} ft-lb-sec rad	Fluid damping viscous coefficient K_6 10^{-3} ft-lb-s rad
3.645	2.166		1.77	0	20
3.645	2.166		1.77	0	20
3.645	2.166		1.77	0	20
3.645	2.130		1.77	0	20
0.92	1.01		2.57	3.4	0.6
0.92	1.01		2.57	3.4	0.6
0.92	1.01		2.57	3.4	0.6
0.92	1.01		2.57	3.4	0.6
0.92	1.01		2.57	3.4	0.6
3.645	2.166		1.77	15.6	0
3.645	2.166		1.77	15.6	0
3.645	2.166		1.77	15.6	0
0.965	0.965		1.757	0	0.6
0.965	0.965		1.757	0	0.6
0.965	0.965		1.757	0	0.6
4.0095	2.0708		1.757	0	20
4.0095	2.0708		1.757	0	20
3.645	2.092		1.733	0	20
3.645	2.092		1.733	0	20
3.645	2.092		1.733	0	20
3.645	2.166		1.77	0	20
3.645	2.2089		1.77	0	20
3.645	2.2089		1.77	0	20
3.645	2.1239		1.77	0	20
3.645	2.1239		1.77	0	20
4.5	2.4078		1.77	0	20
4.5	2.4078		1.77	0	20
2.5	1.795		1.77	0	20
2.5	1.795		1.77	0	20

Time constants taken from approximate exponential curve drawn to transient response.

2

SECTION IV - PERFORMANCE OF DAMPER ON SATELLITE GER-11790

UDY OF TRANSIENT RESPONSE

Rec	System performance										Comments	
	Transient response											
	Time constants (number of orbits)											
	High amplitude (25 deg)			Low amplitude (4 deg)			Time to decay of 16 percent of initial error		Roll error at 100 orbits			
	β_1	β_2	θ_1	θ_2	ψ_1	ψ_2	r	β_1	θ_1	β_1	θ_1	
	1.22	2.54	1.99	3.47	0.94	1.55	4.03	2.5	4.5	33	4.3	These are used as reference runs
	1.22	2.54	1.99	3.47	0.94	1.55	4.03	3	5	22	36	Roots from digital program are ~1 percent from theoretical ideal of $\omega_r = 2\omega_{\theta_1}$. Frequencies on analog runs appear to be in exact 2:1 ratio.
	1.22	2.54	1.99	3.47	0.94	1.55	4.03	13	28	0.6	0.65	
	1.21	2.51	1.99	3.43	0.94	1.55	3.97	3.5	6	22	33	Plunging constant K_1 returned to best 4-deg roll transient response on digital simulation. Note: plunging frequency equals twice satellite roll frequency.
	1.29	2.44	1.96	3.26	0.54	1.63	3.82	1.4			3	Digital runs initially had satellite in a nonpreferred yaw orientation ($\psi_1 = 90$ deg).
	1.29	2.44	1.96	3.26	0.54	1.63	3.82	1.5				Preferred orientation run made (Chart 9) to note long-time roll damping
	1.29	2.44	1.96	3.26	0.54	1.63	3.82	4.5				Initial roll damping appears good, but long-time damping is poor when roll ≤ 4 deg.
	1.29	2.44	1.96	3.26	0.54	1.63	3.82	2.5				Yaw rate appears lightly damped for nonpreferred orientation.
	1.29	2.44	1.96	3.26	0.54	1.63	3.82	6		37.5	110	Analog runs show less roll damping than digital runs.
	1.21	2.54	1.99	3.47	0.94	1.55	4.02	2.5				Fluid damper replaced by solid mass. Roots show fluid damper reflects inner inertia in wind-up mode according to theory. Pitch damping is slightly poorer than optimum. Although runs are not shown here, pitch response is more sensitive to K_3 variations than with R/W damper
	1.21	2.54	1.99	3.47	0.94	1.55	4.02	5		45	30	
	1.21	2.54	1.99	3.47	0.94	1.55	4.02	4	5.5	26	50	1.3
	1.32	2.52	1.99	3.47	0.94	1.38	4.02	1.4			4.5	Pitch response improved with torsional mode tuned to pitch mode.
	1.32	2.52	1.99	3.47	0.94	1.38	4.02	4		50	46	This tuning is possible only with light-fluid damping coefficient. This coefficient is very difficult to mechanize. Damping of roll at low amplitude appears poorer than optimum.
	1.32	2.52	1.99	3.47	0.94	1.38	4.02	3	5.3		2.2	
	1.10	2.20	1.84	3.09	0.49	1.52	3.71	3.2		10	8	High-amplitude roll damping appears good, but low-amplitude appears poor. This configuration is more sensitive to steady-state torque disturbances.
	1.10	2.20	1.84	3.09	0.49	1.52	3.71	3.5		80	28	
	1.19	2.54	1.94	3.33	0	1.57	3.93	2.2			3.2	
	1.19	2.54	1.94	3.33	0	1.57	3.93	5				Poor roll damping at low amplitudes for large initial roll errors.
	1.19	2.54	1.94	3.33	0	1.57	3.93	22				Low-initial-roll-error run as good as optimum (21) yaw spin developed in all response runs
	21	2.54	1.99	3.47	0.94	1.55	4.02			21		Reference low-amplitude roll response
	23	2.58	1.99	3.52	0.94	1.55	4.086			200	220	
	23	2.58	1.99	3.52	0.94	1.55	4.086	27		55	60	Roll response at low amplitudes degraded by detuning plunging mode.
								4.5				Pitch response unaffected - very little change in pitch and torsional-mode frequencies.
	20	2.50	1.99	3.42	0.94	1.55	3.96			90	200	
	20	2.50	1.99	3.42	0.94	1.55	3.96	32		35	37	Results similar to +4 percent K_1 variation although roots show ideal tuning.
	7	2.55	1.99	3.47	0.94	1.64	4.03	3		4.5	6	
	7	2.55	1.99	3.47	0.94	1.64	4.03	6		34	45	Pitch response slightly degraded by large change in K_3 . R/W damper has very broad band with respect to pitch-input frequencies. Roll response and r and θ_1 roots not sensitive to K_3 variation.
	7	2.53	1.99	3.47	0.94	1.46	4.02	2.8		5.5	11	
	7	2.53	1.99	3.47	0.94	1.46	4.02	6.5		31	36	Same results as $+K_3$ variation. Note that K_3 variation has not brought ψ_2 root closer to β_1 root in either case. Exact 1:1 tuning not possible. Lower values of fluid-damper coefficient did bring roots closer together but low-amplitude roll response was degraded.

that the plunging frequency of the spring in all but the digital cases is about 2 percent high, or in other words, the preferred K_1 obtained from the analog computer is about 4 percent high.

Table II lists the important parameters for each group of histories and the associated natural frequencies for each set of parameters. An approximate damping-time constant is shown at high and low amplitudes for the various responses, for comparison. Since each response is a combination of several frequencies, the time constants were taken from the slope of an exponential curve approximately fitted to the response. The response error at 100 orbits is also noted for the longer roll runs.

Histories 1 through 4 (Figures D-1 through D-4) show the transient response of the optimum configuration for separate and combined pitch and roll errors. Figure D-4 is a digital-simulation run of the same configuration and corroborates the analog results. These digital-run parameters (Figure D-4) were selected by comparing several digital roll responses for low-amplitude roll errors and interpolating the results for the optimum plunging-spring constant. As the table shows, the two-to-one ratio here was approximately 0.30 percent off. These digital roll responses are in Appendix E. Examination of the natural frequencies obtained from the digital root-extraction program show that the desired two-to-one frequency ratio between the damper-spring plunging mode and the satellite roll mode for the preferred analog configuration differ approximately one percent. This discrepancy is believed to be due either to error accumulation in the analog components or to the combined effect of noise and slight negative damping, which could cause a slight frequency shift. It is important to note that this effect is consistent throughout the tabulation of the optimum roll and plunging-mode frequencies.

Figures D-5 through D-8 are digital-analog comparison runs for near-optimum tuning and a satellite with four-percent asymmetry. It is

important to note here that the yaw is primarily due to an initial non-preferred orientation. Figure D-9 shows the response with the preferred yaw orientation. Although the analog simulation shows less damping capability than the digital simulation does, the similarity between the runs is obvious.

Figures D-10 through D-12 show the use of hysteresis damping only with the preferred configuration. Roll response is like that of the preferred configuration, while the pitch response is slightly degraded. The poorer pitch response is due to the superiority of the R/W damper. The similarity of the roots for this case and the optimum indicates that the heavy-fluid-damper coefficient does effectively couple the inner inertia to the outer inertia of the R/W damper, as in theory. Variations in the torsional-spring constant degraded the pitch response, indicating this tuning was the best available with this configuration. The same variations for the R/W damper also degraded the pitch performance but not as seriously, indicating a broader band-pass with the R/W damper as compared to hysteresis damping only.

Figures D-13 through D-15 show the use of a light-fluid damping coefficient rather than the heavy, and the pitch response is definitely improved. The desired one-to-one frequency ratio between the damper-spring torsional mode and the pitch mode has been attained, but roll has very poor damping at relatively low amplitudes (≤ 5 deg).

Figures D-16 and D-17 show the response of an unphotolyzed satellite. Pitch and roll performance is degraded. The main effect is that this configuration is more sensitive to perturbing torques as shown in the steady-state results.

A photolyzed symmetrical satellite (Figures D-18 and D-19) has very poor roll damping after the first large roll error has decayed to a lower amplitude. The yaw-axis spin appears to be lightly damped. Roll damping for a low initial roll error, 4 deg in the spring and

satellite roll axes, is shown in Figure D-20. Both initial errors were used here to develop a more-uniform sinusoidal response. It has the same damping characteristics as in Figure D-21, which is a similar response for the optimum configuration, except for the motion of the satellite yaw axis.

Figures D-22 through D-29 show the effect of varying the plunging and torsional-spring constants from the optimum. Figures D-22 through D-25 show the roll response for a variation of four percent of the plunging-spring constant for large and small initial roll errors. The large initial errors are well damped at high amplitudes and are poorer at lower amplitudes in comparison with the nominal optimum. Pitch response was not affected by this variation, and the frequency variations of the torsional and pitch modes are not appreciably affected. Figures D-26 through D-29 show the pitch and roll response for large variations in the torsional-spring constant. The variations here do not bring the torsional or pitch frequencies closer together. The resulting pitch-response runs also show that the broad band of the R/W damper in this mode makes the pitch response relatively insensitive to these variations. Note that the plunging and roll frequencies are not greatly affected by this variation, and the large roll-error transient responses are only slightly degraded at low amplitudes.

Table III is a summary chart of the digital simulation transient response runs. The transient-response histories obtained at Philco are in Appendix E.

4. STUDIES OF STEADY-STATE RESPONSE

a. General

A knowledge of the steady-state response of the optimum satellite-and-damper system to solar-pressure torque and orbital eccentricity is necessary to determine the magnitude of the libration angles from

the vertical and to determine whether there is any critical combination of orbital conditions and steady-state disturbances. The solar-torque equations show the forcing frequencies at one and two times orbital frequency and the eccentricity effect at orbital frequency. The critical nature occurs because these forcing frequencies are close to the natural frequencies of the satellite librations.

The effects of eccentricity and solar torque were investigated on the complete eight-degrees-of-freedom analog-computer simulation at GAC, and solar torque was investigated at Philco Western Development Laboratories on the Transac 2000 digital computer.

The derivation of the solar-torque equations relative to the satellite-fixed-coordinate system, in Reference 2, are repeated here. A discussion of the relative torque due to eccentricity is also presented.

b. Moments Due to Solar Radiation Pressure

The torque expressions presented here were used in obtaining the forcing functions for the steady-state-response studies of the lenticular satellite.

The satellite comprises four subsystems: lens, torus (nonphotolyzed), booms, and canisters. The respective moments, added, determine the composite moment. Because of the complexity of the exact derivations, simplifying assumptions are made. An order-of-magnitude analysis led to the conclusion that all subsystem moments are approximately the same order of magnitude and must be included in the study.

The general simplifying assumptions are:

1. All material partially transmits or reflects incident light, or both (as for example, Mylar and wire screen). This property will be represented by the ratio of reflecting-to-total surface area, μ , and independent of angle of incidence.

TABLE III - DIGITAL-COMPUTER STUD

Run no.	Purpose of run	Satellite					R/W damper					
		Inertias of satellite body axes (10^5 slug-ft 2)				Extent of photolyzation of satellite film	Spring equilibrium length, r_e (ft)	Plunging spring constant K_1 (10^{-5} lb/ft)	Torsion spring constant K_3 (10^{-6} ft-lb/rad)	Cross-couple spring constant K_4 (10^{-6} lb/rad)	Plunging equivalent viscous hysteresis loss coefficient K_2 (10^{-4} lb-sec/ft)	Torsional equivalent viscous hysteresis loss coefficient K_5 (10^{-4} ft-lb-sec/rad)
		Pitch	Roll	Yaw	Percent asymmetry							
	Confirm five-degree-of-freedom analog simulation optimum											
113	Pitch 25 deg	8.979	8.979	1.221	0	Complete	94.4	1.904	4.605	3.184	3.33	0
114	Roll 25 deg	8.979	8.979	1.221	0	Complete	94.4	1.904	4.605	3.184	3.33	0
115 and 118	Run 104 rerun with damping added to plunging mode - same parameters as run 103											
	Roll 25 deg	9.1574	8.79815	1.221	- 4	Complete	267	0.965	0.92	1.01	2.57	3.4
	Attempt to improve roll damping by increasing plunging spring constant K_1											
116	Roll 25 deg	9.1574	8.79815	1.221	- 4	Complete	228.5	1.05	4.98	2.46	2.445	0
	Attempt to improve roll damping by increasing plunging spring constant K_1											
117	Roll 25 deg	9.1574	8.79815	1.221	- 4	Complete	162.6	1.292	4.69	2.67	2.68	0
	Determine optimum plunging spring constant K_1 for low amplitude roll response and compare with analog results											
127	Roll, satellite and spring, 4 deg	9.5177	8.4403	1.221	12	Complete	216	1.084	3.645	2.127	3.54	0
128	Roll, satellite and spring, 4 deg	9.5177	8.4403	1.221	12	Complete	211	1.0992	3.645	2.155	3.54	0
129	Roll, satellite and spring, 4 deg	9.5177	8.4403	1.221	12	Complete	206	1.1145	3.645	2.166	3.54	0
135	Roll, satellite and spring, 4 deg	9.5177	8.4403	1.221	12	Complete	221.3	1.0688	3.645	2.120	3.54	0
136	Roll, satellite and spring, 4 deg	9.5177	8.4403	1.221	12	Complete	227	1.0535	3.645	2.107	3.54	0
130	Optimum verification	9.5177	8.4403	1.221	12	Complete	218.7	1.077	3.645	2.130	1.77	0

STUDY OF TRANSIENT RESPONSE

Fluid damping viscous coefficient K_6 (3 ft-lb-sec) rad	System Performance											
	System natural frequencies (multiples of orbital frequency)							Transient time constants number of orbits				
	ϕ_1	ϕ_2	θ_1	θ_2	ψ_1	ψ_2	r	ϕ_1	θ_1	Comments		
20	1.47	3.37	1.93	4.25	0	1.65	4.99	2	50+	This run did not confirm the earlier analog-simulation roll-response results. Analog 8-degree-of-freedom simulation runs corroborated these runs and showed that plunging was not tuned to second harmonic of roll as it had been in five-degree simulation but was actually tuned to $5\omega_o$. Simulation was retuned to optimize roll and program initiated to develop characteristic root extraction.		
20	1.47	3.37	1.93	4.25	0	1.65	4.99			Pitch response very good.		
0.6	1.29	2.44	1.96	3.26	0.54	1.63	3.82		50+	Companion run to pitch response (103) and run with hysteresis damping only (105). Run made to narrow search before eight-degree-of-freedom analog simulation. Used as analog-digital comparison run. Roll damping poor at low amplitudes.		
20										Run made to investigate roll response for K_1 value between 115-118 and 113 values and provide insight to tuning before analog simulation. Roll response degraded - very poor.		
20									50+	Same as results in 116.		
20									50+	50 percent power loss per cycle used in spring hysteresis damping to increase plunging-mode band width. Runs used to obtain optimum tuning for digital simulation. Spring and satellite roll attitude initial errors set at 4 deg to obtain uniform sinusoidal response.		
20	1.21	2.52	1.99	3.44	0.94	1.55	3.98		34.1			
20									35.5			
20									40.8			
20									37.2			
20									37.2			
20	1.22	2.54	1.99	3.47	0.94	1.55	3.97	3.5	5-8	Results confirm optimum configuration damping capability. Note as in previous runs that the initial (large-angle) time constant < (small-angle) time constant.		

2. Shadow effects of one subsystem on another are neglected.
3. Only direct radiation from the sun will be considered (no reflections considered)

The coordinate systems used in the analysis of each subsystem with nomenclature and solar-torque expressions are shown in Figures 8 through 11. The basic equations used in obtaining the moment equations for the subsystems are presented here. These equations, integrated over a particular subsystem (lens, torus, etc.) surface area, result in the moment equations for each subsystem.

The force on an element of area for a partially transmissive and partially specularly reflective surface is

$$\begin{aligned}\bar{dF}_{\text{total}} &= \bar{dF}_{\text{outer surface}} + \bar{dF}_{\text{inner surface}} \\ &= -\mu \frac{2P^i dA}{C} (\hat{\xi} \cdot \hat{\eta})^2 \hat{\eta} - \mu \frac{2(1-\mu)P^i dA}{C} (\hat{\xi} \cdot \hat{\eta})^2 \hat{\eta}.\end{aligned}\quad (14)$$

Symbols used here and in later equations are defined in Figures 8 through 11 or in the general simplifying assumptions.

The moments for various subsystems are

$$\begin{aligned}1. \quad \bar{dM}_{\text{lens}} &= \bar{r} \times \bar{dF}_{\text{lens}} \\ &= -\mu^2 \frac{2P^i dA}{C} (\hat{\xi} \cdot \hat{\eta})^2 \left(-R \cos \rho_{\max} \times \hat{\eta} \right)\end{aligned}$$

or

$$\begin{aligned}\bar{M}_{\text{lens}} &= \int_0^{\rho_{\max}} \int_{-\pi}^{\pi} -\mu^2 \frac{2P^i}{C} (\hat{\xi} \cdot \hat{\eta})^2 \times \\ &\quad \left(-R \cos \rho_{\max} \times \hat{\eta} \right) R^2 \sin \rho d\lambda d\rho,\end{aligned}\quad (15)$$

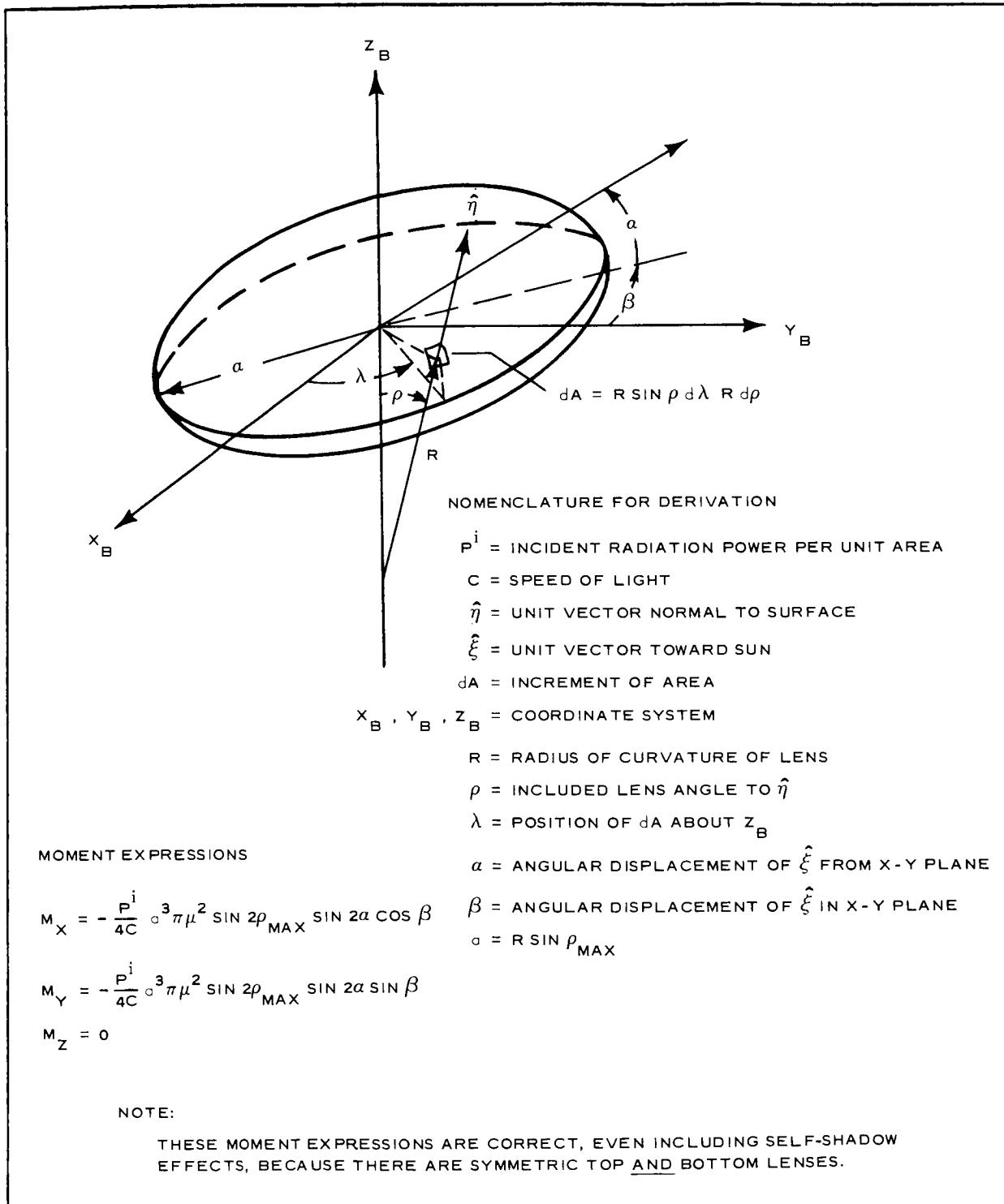
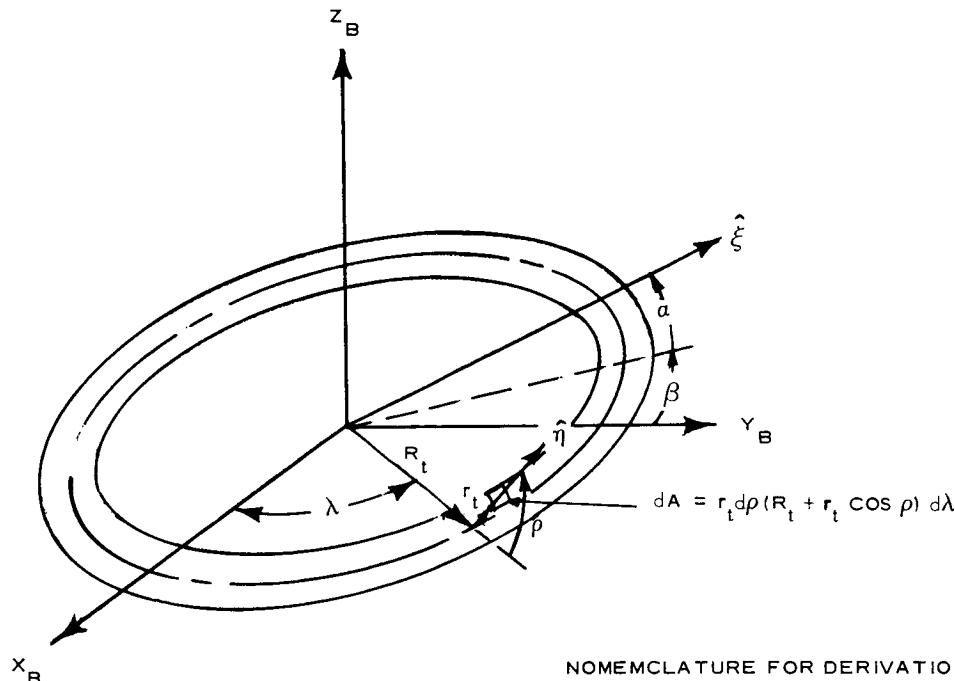


Figure 8 - Lens Subsystem



R_t = RADIUS OF TORUS ABOUT Z_B

r_t = RADIUS OF TORUS

ρ = ANGLE OF $\hat{\eta}$ ABOUT TORUS ξ

MOMENT EXPRESSIONS

$$M_X = -\mu \frac{(2-\mu)P^i}{4C} r_t^2 R_i \pi^2 \sin 2\alpha \cos \beta$$

NOTE:

$$M_Y = -\mu \frac{(2-\mu)P^i}{4C} r_t^2 R_i \pi^2 \sin 2\alpha \sin \beta$$

ALL OTHER NOMENCLATURE HAS BEEN
PRESENTED.

$$M_Z = 0$$

NOTE:

TO OBTAIN A SIMPLER CLOSED-SOLUTION, AND BECAUSE IT IS CONSERVATIVE,
THE LIMITS OF ρ FOR INTEGRATION PURPOSES ARE $0 \leq \rho \leq 180$ DEG.

Figure 9 - Torus Subsystem

where

$$\hat{\xi} = (-\cos \alpha \sin \beta, \cos \alpha \cos \beta, \sin \alpha)$$

$$\hat{\eta} = (\sin \rho \cos \lambda, \sin \rho \sin \lambda, \cos \rho).$$

$$2. \quad \overline{dM}_{\text{canisters}} = \sum_{n=1}^2 \left[-\mu^2 \frac{2P^i dA_n}{C} (\hat{\xi}_n \cdot \hat{\eta}_n)^2 (\bar{L}_n \times \hat{\eta}_n) \right] \quad (\beta = 0)$$

or

$$\bar{M}_{\text{cans}} = \sum_{n=1}^2 \left[\int_{-\pi/2}^{\pi/2} \int_{\rho_{1n}}^{\rho_{2n}} -\mu^2 \frac{2P^i}{C} (\hat{\xi}_n \cdot \hat{\eta}_n)^2 (\bar{L}_n \times \hat{\eta}_n) \times R_C^2 \cos \lambda d\rho d\lambda \right], \quad (16)$$

where

$$\hat{\xi} = (0, \cos \alpha, \sin \alpha)$$

$$\hat{\eta} = (-\sin \lambda, \cos \lambda \cos \rho, \cos \lambda \sin \rho).$$

For $\beta \neq 0$, the X_B and Y_B components of \bar{M}_{cans} are easily obtained by rotation through β . For the canisters, the μ^2 factor is equivalent to a reflectance coefficient.

$$3. \quad \bar{M}_{\text{booms}} = \left[\sum_{n=1}^3 \left(-F_{Y_n} \frac{L_n}{2} + F_{Z_n} \frac{\alpha \cos \gamma_n}{2} \right) \text{ or} \right. \\ \left. \sum_{n=4}^6 \left(F_{Y_n} \frac{L_n}{2} + F_{Z_n} \frac{\alpha \cos \gamma_n}{2} \right) \right] \hat{i} +$$

NOMENCLATURE FOR DERIVATION

r_b = RADIUS OF BOOMS

$$M_x = \sum_{n=1}^3$$

L = HEIGHT OF UPPER BOOMS

L_L = HEIGHT OF LOWER BOOMS

$$M_y = \sum_{n=1}^3$$

σ_u = ANGLE OF INCLINATION OF UPPER BOOMS

$$M_z = \sum_{n=1}^3$$

σ_L = ANGLE OF LOWER BOOMS (NEGATIVE)

γ_n = POSITION OF BOOM n TO y_B

$$M_z = \sum_{n=1}^3$$

ρ = ANGLE TO $\hat{\eta}$ FROM $\hat{\xi}$

δ_n = ANGLE FROM y_B' TO $\hat{\xi}'$ FOR BOOM n

WHERE

$$M_{x_n} = -\frac{F_x}{\mu}$$

$$M_{y_n} = -\frac{F_y}{\mu}$$

$$M_{z_n} = -\frac{F_z}{\mu}$$

$$F_{x_n} = -\mu$$

$$F_{y_n} = -\mu$$

$$F_{z_n} = -\mu$$

$$\delta_n = TA$$

$$C = CC$$

SECTION IV - P

$$M_{X_n}(\gamma_n, \sigma_n, L) + \sum_{n=4}^6 M_{X_n}(\gamma_n, \sigma_n, L_L)$$

$$M_{Y_n}(\gamma_n, \sigma_n, L) + \sum_{n=4}^6 M_{Y_n}(\gamma_n, \sigma_n, L_L)$$

$$M_{Z_n}(\gamma_n, \sigma_n, L) + \sum_{n=4}^6 M_{Z_n}(\gamma_n, \sigma_n, L_L)$$

$$\frac{r_n L}{2} |_{n=1, 2, 3} + \frac{F_{Y_n} L}{2} |_{n=4, 5, 6} + F_Z \frac{\alpha \cos \gamma_n}{2}$$

$$\frac{r_n L}{2} - \frac{F_{Z_n} \alpha \sin \gamma_n}{2}$$

$$\frac{x_n \alpha \cos \delta_n}{2} + \frac{F_{Y_n} \alpha \sin \gamma_n}{2}$$

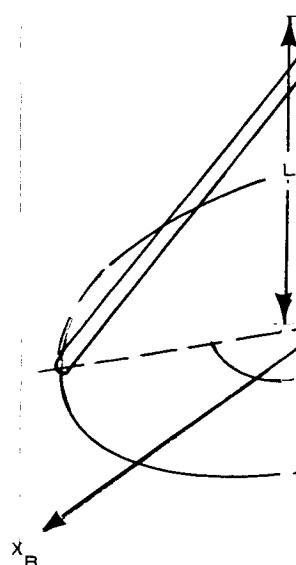
$$\frac{(2-\mu)P^i L}{3C \cos \sigma_n} r_b \left\{ A \left[\cos \sigma_n \sin \gamma_n \cos^3 \delta_n - \cos \gamma_n \sin \delta_n (\cos^2 \delta_n + 2) \right] + B \left[\cos \sigma_n \sin \gamma_n \cos \delta_n (\sin^2 \delta_n + 2) \right] \right\}$$

$$\frac{4(2-\mu)P^i L}{3C \cos \sigma_n} r_b \left\{ A \left[\cos \sigma_n \cos \gamma_n \cos^3 \delta_n + \sin \gamma_n \sin \delta_n (\cos^2 \delta_n + 2) \right] + B \left[\cos \sigma_n \cos \gamma_n \cos \delta_n (\sin^2 \delta_n + 2) \right] \right\}$$

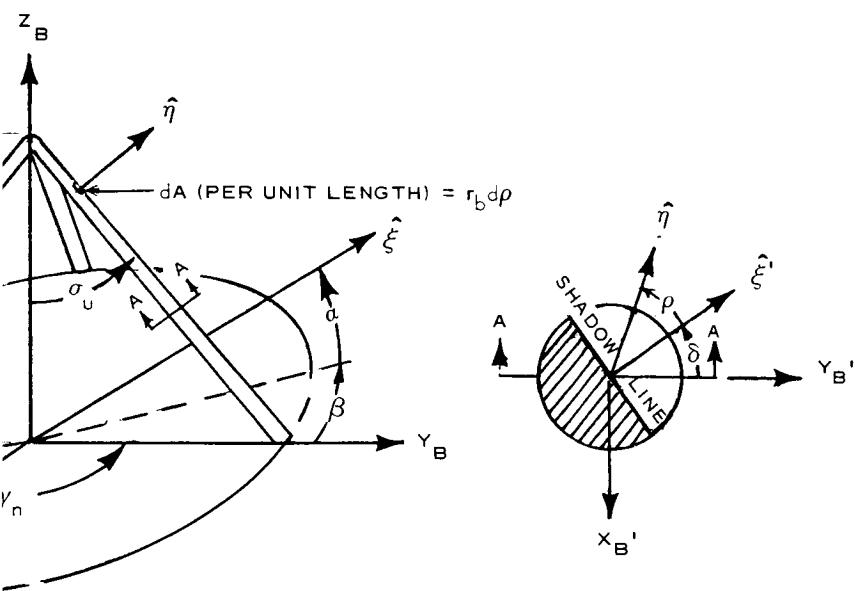
$$\frac{4(2-\mu)P^i L}{3C \cos \sigma_n} r_b \left[A \sin \sigma_n \cos^3 \delta_n + B \sin \sigma_n \cos \delta_n (\sin^2 \delta_n + 2) + C \sin \sigma_n \sin^3 \delta_n \right]$$

$$\sqrt{-1} \left[\frac{\cos \alpha \sin (\beta + \gamma_n)}{\cos \alpha \cos (\beta + \gamma_n) \cos \sigma_n + \sin \alpha \sin \sigma_n} \right], A = \cos^2 \alpha \sin^2 (\beta + \gamma_n), B = \left[\begin{array}{l} \cos \sigma_n \cos \alpha \\ \cos \sigma_n \sin \alpha \end{array} \right]$$

$$; \alpha \left[\cos \sigma_n \cos \alpha \sin 2(\gamma_n + \beta) + 2 \sin \alpha \sin \sigma_n \sin (\beta + \gamma_n) \right]$$



2



$$\left. \begin{aligned} & \delta_n (\sin^2 \delta_n + 2) - \cos \gamma_n \sin^3 \delta_n \Big] + C \left[\cos \sigma_n \sin \gamma_n \sin^3 \delta_n - \cos \gamma_n \cos^3 \delta_n \right] \Big\} \\ & \sin \delta_n (\sin^2 \delta_n + 2) + \sin \gamma_n \sin^3 \delta_n \Big] + C \left[\cos \sigma_n \cos \gamma_n \sin^3 \delta_n + \sin \gamma_n \cos^3 \delta_n \right] \Big\} \\ & \cos(\beta + \gamma_n) + \sin \sigma_n \sin \alpha \Big], \end{aligned} \right.^2$$

3

Figure 10 - Booms Subsystem

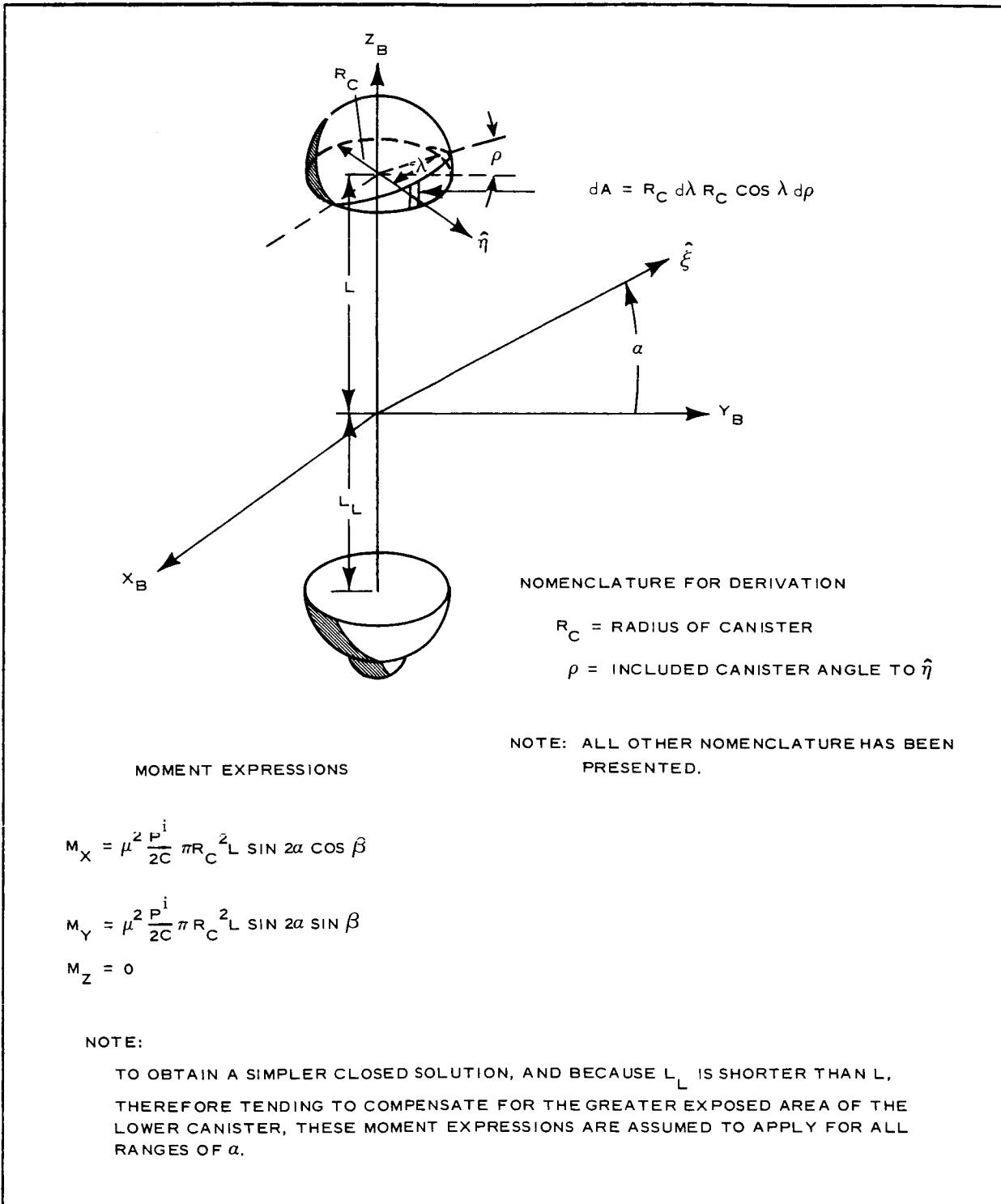


Figure 11 - Canister Subsystem

$$\left[\sum_{n=1}^3 \left(F_{X_n} \frac{L_n}{2} - F_{Z_n} \frac{\alpha \sin \gamma_n}{2} \right) \text{ or} \right.$$

$$\left. \sum_{n=4}^6 \left(-F_{X_n} \frac{L_n}{2} - F_{Z_n} \frac{\alpha \sin \gamma_n}{2} \right) \right] \hat{j} +$$

$$\left[\sum_{n=1}^6 \left(-F_{X_n} \frac{\alpha \cos \gamma_n}{2} + F_{Y_n} \frac{\alpha \sin \gamma_n}{2} \right) \right] \hat{k}, \quad (17)$$

where

$$\bar{F}_{\text{booms}} = \frac{L_n}{\cos \sigma_n} \int_{-\frac{\pi}{2}}^{\frac{\pi}{2}} -\mu \frac{2(2-\mu)P^i}{C} r_b (\hat{\xi}_n \cdot \hat{\eta}_n)^2 \hat{\eta}_n d\rho$$

and

$$\hat{\xi}_n = (-\cos \alpha \sin \beta, \cos \alpha \cos \beta, \sin \alpha)$$

$$\begin{aligned} \hat{\eta} = & \left[-\sin(\rho + \delta_n) \cos \gamma_n + \cos(\rho + \delta_n) \times \right. \\ & \cos \sigma_n \sin \gamma_n, \cos(\rho + \delta_n) \cos \sigma_n \cos \gamma_n + \\ & \left. \sin(\rho + \delta_n) \sin \gamma_n, \cos(\rho + \delta_n) \sin \sigma_n \right]. \end{aligned}$$

$$4. \quad \bar{dM}_{\text{torus}} = -\mu \frac{2(2-\mu)P^i dA}{C} (\hat{\xi} \cdot \hat{\eta})^2 (\bar{R}_t \times \hat{\eta})$$

or

$$\bar{M}_{\text{torus}} = \int_{+\pi}^{-\pi} \int_{\tan^{-1} \left[\frac{\sin \alpha}{\cos \alpha \cos (\lambda + \beta)} \right] - \frac{\pi}{2}}^{\tan^{-1} \left[\frac{\sin \alpha}{\cos \alpha \cos (\lambda + \beta)} \right] + \frac{\pi}{2}} -\mu \frac{2(2-\mu)P^i}{C} r_t (\hat{\xi} \cdot \hat{\eta})^2 (\bar{R}_t \times \hat{\eta}) \times \\ (R_t + r_t \cos \rho) d\rho d\lambda, \quad (18)$$

where

$$\begin{aligned}\hat{\xi} &= (-\cos \alpha \sin \beta, \cos \alpha \cos \beta, \sin \alpha) \\ \hat{\eta} &= (\cos \rho \sin \lambda, \cos \rho \cos \lambda, \sin \rho).\end{aligned}$$

The total moment or body-axis components of the total moment can be obtained by adding these subsystem contributions. These contributions in terms of body-axis coordinates have been presented in Figures 8 through 11. Note that in the satellite equations of motion presented in Appendix A, the input torques (L_{θ_1} , L_{ϕ_1} , L_{ψ_1}) are about Euler rotational axes. Therefore, these body-axis solar-pressure moments must be rotated back through the angles ψ_1 , and θ_1 and ϕ_1 , as applicable to obtain L_{ϕ_1} and L_{θ_1} .

c. Solar-Torque Forcing Functions

The varying solar torques about body axes $\hat{\xi}$, $\hat{\eta}$, and $\hat{\zeta}$ are presented in Figure 12 for the two extreme satellite configurations and with the sun line in the orbit plane. These satellites are the preferred all-photolyzed satellite and the nonphotolyzed satellite, both with 12-percent asymmetry about the yaw axis. Figure 13 presents the solar-torque forcing functions about body axes for these satellites with the sun line 45 deg from the orbit plane. These forcing functions were

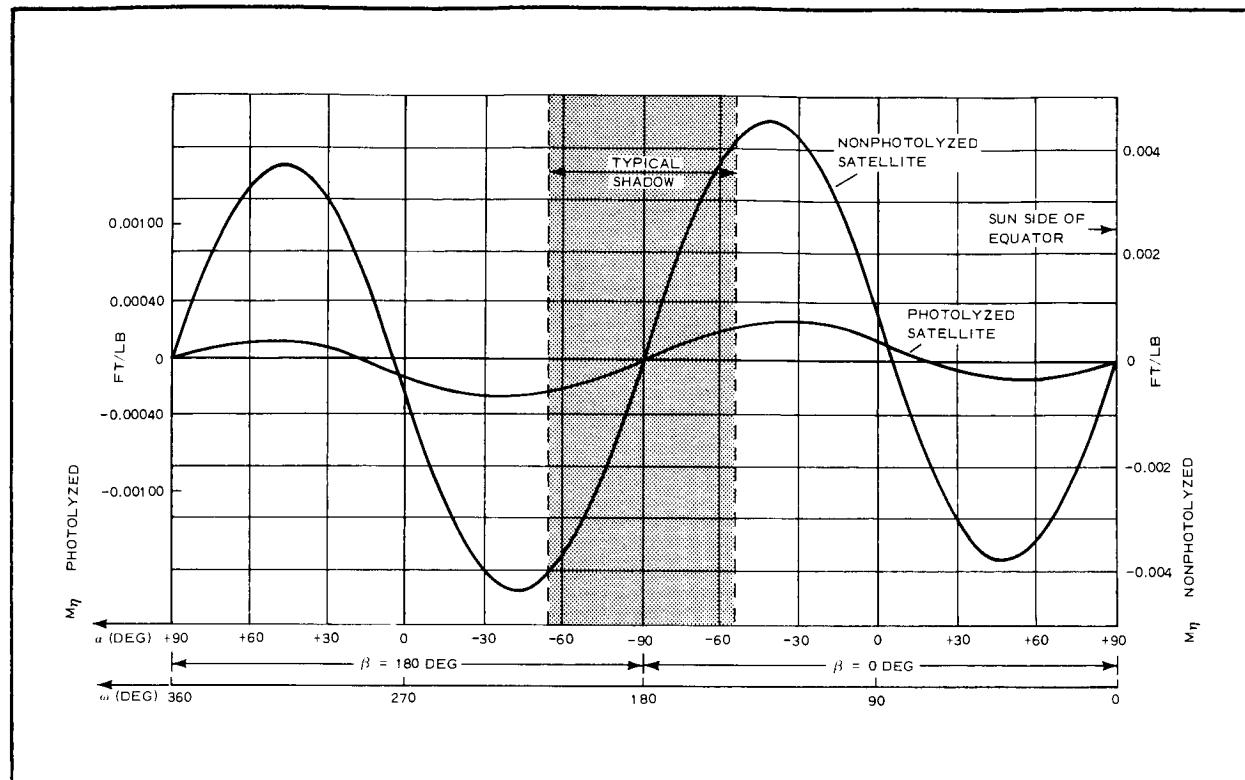


Figure 12 - Solar Torques About Body Axes (Sun Line in Plane of Orbit)

mechanized as sinusoidal functions at one and two times orbital frequency, independent of libration angles, by Fourier series expansions for the analog-computer study.

The corroborating digital-computer study included the complete solar-torque equations of the previous section in the computer program.

d. Effects of Orbital Eccentricity

Depending upon initial orbital parameters and solar-pressure effects upon the orbit, the perigee of an eccentric orbit will oscillate, causing a variation in eccentricity after injection.

This eccentricity appears at orbital frequency as near-sinusoidal forcing functions about the satellite axes. For small eccentricities, these forcing functions can be simulated by

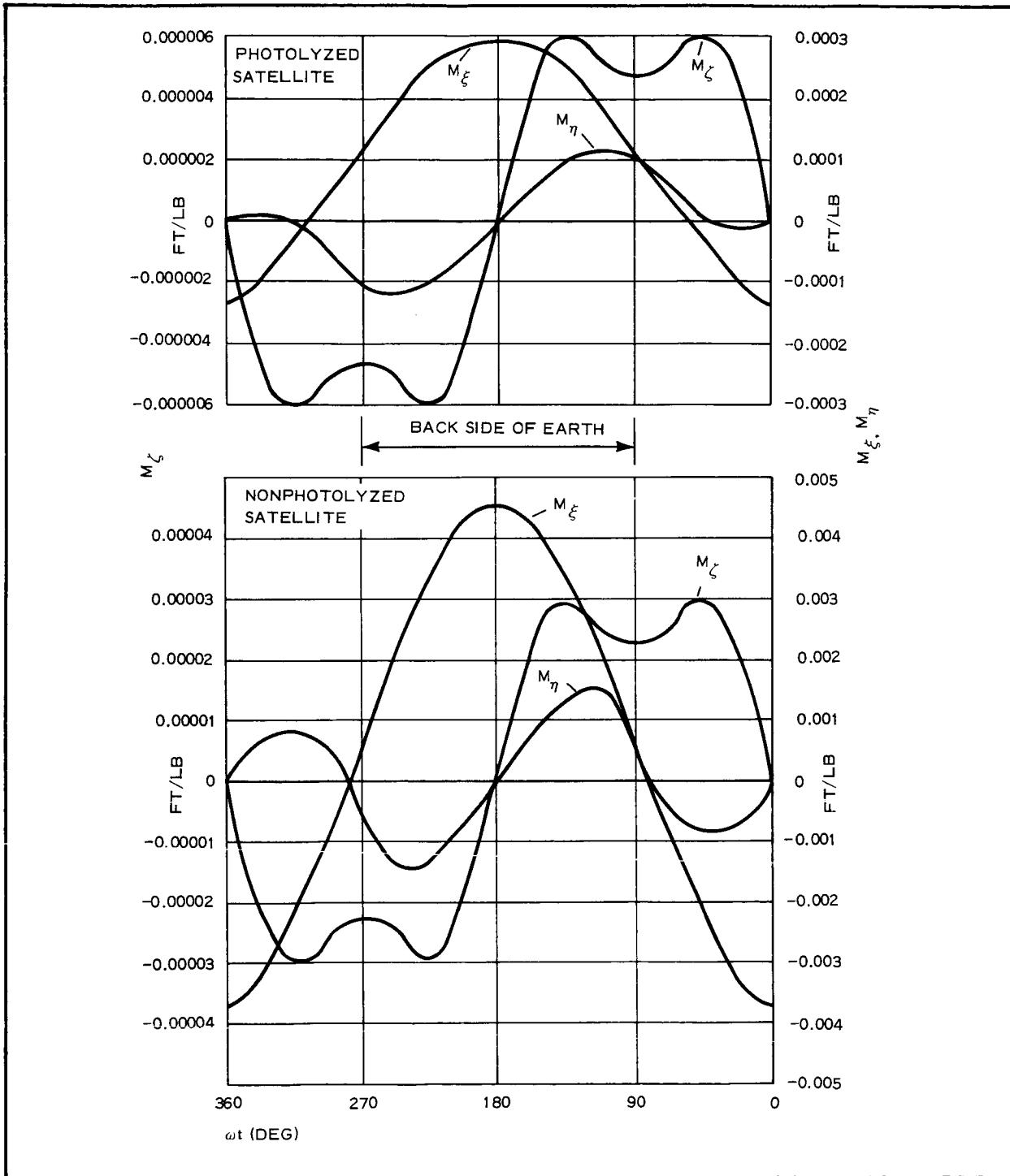


Figure 13 - Solar-Torque Forcing Functions (Sun Line 45 Deg from Plane of Orbit)

$$L_\eta = 2eI_\eta \bar{\omega}^2 \sin \bar{\omega}t \text{ ft lb ,}$$

$$L_\xi = (2eI_\xi \bar{\omega}^2 \sin \bar{\omega}t) \psi_1, \quad (19)$$

$$L_\zeta = -(2eI_\zeta \bar{\omega}^2 \sin \bar{\omega}t) \theta_1 .$$

where

e = eccentricity and

$\bar{\omega}$ = average orbital frequency.

e. Results of Study

Results from the study of steady-state response for the preferred all-photolyzed satellite and damper, and nonphotolyzed satellite and damper, are in Table IV and in Figures D-30 through D-35. Damper tuning is based on the best transient-response performance. Satellites with 12-percent asymmetry were used because of improved low-amplitude roll transient and steady-state yaw responses.

Table IV presents the steady-state amplitude and frequency of oscillation for an eccentricity of approximately 0.01 and solar torques for sun line in orbit and 45 deg to orbit. These data are taken from Figures D-30 through D-35 and from other runs not reported here. The eccentricity about the pitch axis causes the only sizable oscillation. For the nonphotolyzed satellite, this oscillation approaches the nominal small-angle limit of 3 deg. Note that there are no resonant build-ups about any of the axes.

Because of the amplitude of oscillation from eccentricity and undeterminacy of accurate solar torques, and because of the unknown deterioration properties of the Mylar surfaces of the satellite with time in orbit, as much of the satellite as possible should be photolyzable material.

Table V presents, for comparison, the results of the digital-computer

SECTION IV - PERFORMANCE OF DAMPER ON SATELLITE GER-11790

study of steady-state response. Except for the different frequencies in pitch and roll for the preferred configuration with the sun line 45 deg from the orbit plane, the agreement is quite good. In these cases, where the frequencies do not match, note that the digital-run frequency is a natural frequency, indicating that the transient response still dominates.

The steady-state-response histories obtained from the Transac 2000 digital computer at Philco Western Development Laboratories are in Appendix E.

TABLE IV - ANALOG-COMPUTER STUDY OF ST

Run no.	Type of damper	System natural frequency (multiples of orbital frequency)							Type of disturbance	
		ϕ_1	ϕ_2	θ_1	θ_2	ψ_1	ψ_2	r	Type	Shape
1	R/W light fluid completely photolyzed	1.32	2.52	1.99	3.47	0.94	1.38	4.02	Eccentricity = 0.011	None
2	R/W light fluid completely photolyzed	1.32	2.52	1.99	3.47	0.94	1.38	4.02	Solar torque (sun line)	70 deg
3	R/W light fluid completely photolyzed	1.32	2.52	1.99	3.47	0.94	1.38	4.02	Solar torque (45 deg to sun line)	...
4 (Chart 33)	R/W heavy fluid completely photolyzed	1.22	2.54	1.99	3.47	0.94	1.55	4.03	Eccentricity = 0.011	...
5 (Chart 34)	R/W heavy duty completely photolyzed	1.22	2.54	1.99	3.47	0.94	1.55	4.03	Solar torque (sun line)	70 deg
6 (Chart 35)	R/W heavy fluid completely photolyzed	1.22	2.54	1.99	3.47	0.94	1.55	4.03	Solar torque (45 deg to sun line)	...
7	Hysteresis only completely photolyzed	1.21	2.54	1.99	3.47	0.94	1.55	4.02	Eccentricity = 0.011	...
8	Hysteresis only completely photolyzed	1.21	2.54	1.99	3.47	0.94	1.55	4.02	Solar torque (sun line)	70 deg
9	Hysteresis only completely photolyzed	1.21	2.54	1.99	3.47	0.94	1.55	4.02	Solar torque (45 deg to sun line)	...
10	R/W heavy fluid lens only	1.14	2.28	1.88	3.18	0.54	1.54	3.78	Eccentricity = 0.011	...
11	R/W heavy fluid lens only	1.14	2.28	1.88	3.18	0.54	1.54	3.78	Solar torque (sun line)	70 deg
12 (Chart 33)	R/W heavy fluid nonphotolyzed	1.10	2.20	1.84	3.09	0.49	1.52	3.71	Eccentricity = 0.01	...
13 (Chart 34)	R/W heavy fluid nonphotolyzed	1.10	2.20	1.84	3.09	0.49	1.52	3.71	Solar torque (sun line)	70 deg
14 (Chart 35)	R/W heavy fluid nonphotolyzed	1.10	2.20	1.84	3.09	0.49	1.52	3.71	Solar torque (45 deg to sun line)	...
15	R/W light fluid nonphotolyzed	1.15	2.17	1.84	3.10	0.49	1.21	3.73	Eccentricity = 0.01	...
16	R/W light fluid nonphotolyzed	1.15	2.17	1.84	3.10	0.49	1.21	3.73	Solar torque (sun line)	70 deg
17	R/W light fluid nonphotolyzed	1.15	2.17	1.84	3.10	0.49	1.21	3.73	Solar torque (45 deg to sun line)	...

EADY-STATE RESPONSE

ce ow	Response					
	ϕ_1		θ_1		ψ_1	
	Ampli- tude (deg)	Fre- quency (ω_o)	Ampli- tude (deg)	Fre- quency (ω_o)	Ampli- tude (deg)	Fre- quency (ω_o)
e	1.0	1	0.017	2	0.05	0.96
eg	0.025	4	0.01	3.5	0.10	0.94
.	0.022	4	0.017	3.5	0.10	1
.	1.0	1	0.02	2	0.08	1
eg	0.036	4	0.02	3.7	0.10	0.98
.	0.024	3.9	0.023	3.6	0.05	0.95
.	1.0	1	0.02	2	0.05	1
eg	0.03	4	0.01	3.3	0.08	0.9
.	0.032	4	0.027	3.5	0.05	0.95
.	1.8	1	0.01	3.0	0.05	0.55
eg	0.05	2	0.017	3.2	0.05	0.55
.	2.3	1	.08-.60	0.5	2-16	0.5
eg	0.19	2	0.05	3.1	0.10	0.5
.	0.10	2	0.30	2	0.22	1
.	1.9	1	.08-.60	0.5	2-14	0.5
eg	0.3	2	0.01	3	0.05	0.5
.	0.13	2	0.21	1	0.20	1



TABLE V - DIGITAL-COMPUTER STUDY OF STEADY-STATE RESPONSE

Run no.	Type of damper	Type of disturbance	System natural frequencies (multiples of orbital frequency)						Response						
			ϕ_1	ϕ_2	θ_1	θ_2	ψ_1	ψ_2	r	ϕ_1	Frequency (ω_o)	θ_1	Frequency (ω_o)		
131	R/W heavy fluid nonphotolyzed	Solar torque, sun line 45° deg to orbit	1.09	2.19	1.84	3.06	0.49	1.53	3.68	0.13	2	0.30	1.9	0.80	0.5
132	R/W heavy fluid completely photolyzed	Solar torque, sun line 45° deg to orbit	1.21	2.51	1.99	3.43	0.94	1.55	3.97	0.01	1	0.03	2	0.07	1
133	R/W heavy fluid nonphotolyzed	Solar torque, sun line in orbit	1.09	2.19	1.84	3.06	0.49	1.53	3.68	0.20	2	0.008	3	0.025	0.5
134	R/W heavy fluid completely photolyzed	Solar torque, sun line in orbit	1.21	2.51	1.99	3.43	0.94	1.55	3.97	0.01	4	0.002	2	0.11	1

SECTION V - CONCLUSIONS AND RECOMMENDATIONS

The Rice/Wilberforce damper provides satisfactory three-axis stabilization for the large-inertia NASA lenticular communication satellite. Settling-time constants of transient librations will be approximately three orbits in pitch and six in roll. Steady-state oscillations due to eccentricity and solar pressure will be less than 2 deg. The studies of steady-state response demonstrated that photolyzation of the film on the lens and torus is not required.

Physical realizability of the spring is within manufacturing capability. Tuning tolerances of 4 percent in plunging, although stringent, are practical. For torsional tuning, allowable tolerances greater than 10 percent present no problem.

It has been demonstrated conclusively through close corroboration with an independent digital-computer simulation, that the analog computer can simulate the gravity-gradient stabilization problem, given enough detail and care.

Laboratory testing is necessary for detailed design. Studies to determine the limit of energy loss per cycle for hysteresis damping are required, to increase the band width and to relax spring tolerances. Laboratory and analytical studies are required, to ensure successful damper deployment during the initial motion of the satellite. The mathematical model of the satellite-damper system should be extended to include gyroscopic effects on the spin axis of the damper. Alternate types of damping elements, such as magnetic hysteresis rods, should be considered for this damper because of the possibility of fluid-seal problems on long missions.

LIST OF REFERENCES

1. TG-502: Dynamic Analysis of Gravity-Gradient Satellite with Passive Damping. Baltimore, Md., The Johns Hopkins University, Applied Physics Laboratory, June 1963.
2. GER-11502: Feasibility Study and Preliminary Design of Gravity-Gradient-Stabilized Lenticular Test Satellite. Akron, Ohio, Goodyear Aerospace Corporation, 1 June 1964
3. GER-11537: Demonstration of an Unlimited Angle Resolution Capability in Analog Computer Simulation. Akron, Ohio, Goodyear Aerospace Corporation, 1 April 1964.

APPENDIX A - NOMENCLATURE, ENERGY, AND DISSIPATION
FUNCTIONS AND EIGHT-DEGREES-OF-FREEDOM EQUATIONS

1. NOMENCLATURE

$$(\dot{ }) = d(\) / dt$$

ω = constant orbital angular velocity, rad per sec

R = distance from system C. M. to earth center, ft

L = distance from satellite c. g. to spring attachment, ft

r, r_e = instantaneous and equilibrium length of spring, ft

M, m = mass of satellite, combined weights on end of spring, slugs

\bar{m} = modified mass of spring weights, $\bar{m} = mM/m + M$

X, Y, Z = basic rectangular coordinate system, rotating about Y at orbital speed

X_M , X_m , etc = rectangular coordinates of M, m

ξ , η , ζ = principal body axes of satellite

I_ξ , I_η , I_ζ = principal moments of inertia of satellite, slug-ft²

I_S , I_m = spin moment of inertia of fixed mass at end of spring, inner mass, slug-ft²

ϕ_1 , θ_1 , Ψ_1 = Euler angles for satellite, rad

ϕ_2 , θ_2 = first two Euler angles for fixed mass, rad

Ψ_2 = spin angle of spring and outer mass relative to attachment, rad

Ψ_3 = spin angle of inner mass relative to the fixed
(container) mass, rad

K_1 = Hooke's constant of spring, lb/ft

K_2 = equivalent viscous damping constant of spring,
lb-sec/ft

K_3 = torsional spring constant, ft-lb/rad

K_4 = spring cross-coupling extension and wind-up,
ft-lb/ft or lb/rad

K_5 = spring torsional damping, ft-lb-sec/rad

K_6 = torsional (viscous) damping constant acting on
inner mass, ft-lb-sec/rad

L_{ϕ_1} , L_{θ_1} , L_{Ψ_1} = external torques acting on satellite about Euler
axes 1, 2, 3, ft-lb

T, V, D = system kinetic, potential, and dissipation func-
tions

N = ratio of masses ($m \pm M$)/M

s(), c() = sine and cosine of (), respectively

Subscripts 0, 1, 2, 3 = orderly rotations in a 3-Euler angle rotation

2. ENERGY EQUATIONS

a. Kinetic Energy

$$\begin{aligned} T = & \frac{\overline{m}}{2} \left[L^2 (\dot{\theta}_1^2 + \dot{\phi}_1^2 c^2 \theta_1^2) + r^2 (\dot{\theta}_2^2 + \dot{\phi}_2^2 c^2 \theta_2^2) + \dot{r}^2 + \right. \\ & 2 L r [\dot{\theta}_1 \dot{\theta}_2 (c \theta_1 c \theta_2 + s \theta_1 s \theta_2 c(\phi_2 - \phi_1)) + \\ & \left. \dot{\theta}_1 \dot{\phi}_2 s \theta_1 c \theta_2 s(\phi_2 - \phi_1) - \dot{\theta}_2 \dot{\phi}_1 c \theta_1 s \theta_2 s(\phi_2 - \phi_1) \right] \end{aligned}$$

$$\begin{aligned}
& \dot{\phi}_1 \dot{\phi}_2 c \theta_1 c \theta_2 c(\phi_2 - \phi_1) \Big] + 2L \dot{r} \left[\dot{\theta}_1 (c \theta_1 s \theta_2 - s \theta_1 c \theta_2 c(\phi_2 - \phi_1)) + \right. \\
& \dot{\phi}_1 c \theta_1 c \theta_2 s(\phi_2 - \phi_1) \Big] + 2\omega \left[L^2 \dot{\phi}_1^2 \theta_1 + L r (\dot{\theta}_1 s \theta_1 c \theta_2 s(\phi_2 - \phi_1) - \right. \\
& \dot{\theta}_2 c \theta_1 s \theta_2 s(\phi_2 - \phi_1) + \dot{\phi}_1 c \theta_1 c \theta_2 c(\phi_2 - \phi_1) + \dot{\phi}_2 c \theta_1 c \theta_2 c(\phi_2 - \phi_1) \Big] + \\
& r^2 \dot{\phi}_2^2 \theta_2 + L \dot{r} c \theta_1 c \theta_2 s(\phi_2 - \phi_1) \Big] + \omega^2 \left[L^2 c^2 \theta_1 + \right. \\
& 2L r c \theta_1 c \theta_2 c(\phi_2 - \phi_1) + r^2 c^2 \theta_2 \Big] + \omega^2 R^2 \frac{(m + M)}{2} + \frac{1}{2} \left\{ I_\xi \left[\dot{\theta}_1^2 c^2 \Psi_1 + \right. \right. \\
& \dot{\theta}_1 (\omega + \dot{\phi}_1) c \theta_1 s^2 \Psi_1 + (\omega + \dot{\phi}_1)^2 c^2 \theta_1 s^2 \Psi_1 \Big] + I_\eta \left[\dot{\theta}_1^2 s^2 \Psi_1 - \right. \\
& \dot{\theta}_1 (\omega + \dot{\phi}_1) c \theta_1 s^2 \Psi_1 + (\omega + \dot{\phi}_1)^2 c^2 \theta_1 c^2 \Psi_1 \Big] + I_\zeta \left[(\omega + \dot{\phi}_1)^2 s^2 \theta_1 - \right. \\
& \left. \left. 2 \dot{\Psi}_1 (\omega + \dot{\phi}_1) s \theta_1 + \dot{\Psi}_1^2 \right] + I_s (\dot{\Psi}_1 + \dot{\Psi}_2)^2 + I_m (\dot{\Psi}_1 + \dot{\Psi}_2 + \dot{\Psi}_3)^2 \right\} \quad (A-1)
\end{aligned}$$

b. Potential Energy

$$\begin{aligned}
V = & \frac{1}{2} \left[K_1 \frac{r^2}{2} + 2K_1 (r - r_e) \Psi_2 + K_3 \Psi_2^2 \right] + \frac{\bar{m}\omega^2}{2} \left[L^2 \left(1 - 3c^2 \theta_1 c^2 \phi_1 \right) + \right. \\
& 2Lr(c \theta_1 c \theta_2 s \phi_1 s \phi_2 - 2c \theta_1 c \theta_2 c \phi_1 c \phi_2 + s \theta_1 s \theta_2) + \\
& r^2 \left(1 - 3c^2 \theta_2 c^2 \phi_2 \right) \Big] - \frac{3}{4} \omega^2 \left\{ I_\xi \left[\left(c^2 \phi_1 s^2 \theta_1 - s^2 \phi_1 \right) c^2 \Psi_1 + \right. \right. \\
& s^2 \phi_1 s \theta_1 s^2 \Psi_1 + c^2 \phi_1 c^2 \theta_1 \Big] + I_\eta \left[- \left(c^2 \phi_1 s^2 \theta_1 - s^2 \phi_1 \right) c^2 \Psi_1 - \right. \\
& \left. \left. s^2 \phi_1 s \theta_1 s^2 \Psi_1 + c^2 \phi_1 c^2 \theta_1 \right] - I_\zeta \left[2c^2 \phi_1 c^2 \theta_1 \right] \right\} \quad (A-2)
\end{aligned}$$

c. Dissipation Function

$$D = \frac{1}{2} \left(K_2 \dot{r}^2 + K_5 \dot{\Psi}_2^2 + K_6 \dot{\Psi}_3^2 \right) \quad (A-3)$$

3. SYSTEM DIFFERENTIAL EQUATIONS (8 DEG OF FREEDOM)

$$\left[\left(\bar{m}L^2 + I_\xi s^2 \Psi_1 + I_\eta c^2 \Psi_1 \right) c^2 \theta_1 + I_\zeta s^2 \theta_1 \right] \dot{\phi}_1 -$$

$$\begin{aligned}
& \bar{m}L \left[r\ddot{\theta}_2 + 2\dot{r}\dot{\theta}_2 \right] c\theta_1 s\theta_2 s(\phi_2 - \phi_1) + \bar{m}L \left[r\ddot{\phi}_2 + 2\dot{r}\dot{\phi}_2 + \right. \\
& \left. 2\omega_o \dot{r} \right] c\theta_1 c\theta_2 s(\phi_2 - \phi_1) + \\
& \bar{m}L \left[\ddot{r} - r\dot{\theta}_2^2 - r\dot{\phi}_2^2 - 2\omega_o r\dot{\phi}_2 \right] c\theta_1 c\theta_2 s(\phi_2 - \phi_1) - \\
& 2\bar{m}Lr \left[\dot{\theta}_2 \dot{\phi}_2 + \omega_o \dot{\theta}_2 \right] c\theta_1 s\theta_2 c(\phi_2 - \phi_1) - 2\bar{m}L^2 \left[\dot{\phi}_1 \dot{\theta}_1 + \omega_o \dot{\theta}_1 \right] c\theta_1 s\theta_1 + \\
& 3\bar{m}\omega^2 L \left[Lc\theta_1 c\phi_1 + r c\theta_2 c\phi_2 \right] c\theta_1 s\phi_1 + \\
& (I_\xi - I_\eta) \left[\ddot{\theta}_1 c\theta_1 - \dot{\theta}_1^2 s\theta_1 \right] s\Psi_1 c\Psi_1 - I_\zeta s\theta_1 \ddot{\Psi}_1 + \\
& \left[(I_\xi - I_\eta) c2\Psi_1 - I_\zeta \right] \dot{\theta}_1 \dot{\Psi}_1 c\theta_1 - 2 \left[I_\xi s^2 \Psi_1 + I_\eta c^2 \Psi_1 - \right. \\
& \left. I_\zeta \right] \dot{\theta}_1 (\omega_o + \dot{\phi}_1) c\theta_1 s\theta_1 + 2 \left[I_\xi - I_\eta \right] \dot{\Psi}_1 (\omega_o + \dot{\phi}_1) c^2 \theta_1 s\Psi_1 c\Psi_1 + \\
& 3\omega^2 \left[I_\xi c^2 \Psi_1 + I_\eta s^2 \Psi_1 - I_\zeta c^2 \theta_1 \right] c\phi_1 s\phi_1 - \\
& 3\omega^2 \left[I_\xi s^2 \Psi_1 + I_\eta c^2 \Psi_1 \right] s^2 \theta_1 c\phi_1 s\phi_1 - \\
& 3\omega^2 (I_\xi - I_\eta) (1 - 2s^2 \phi_1) s\theta_1 s\Psi_1 c\Psi_1 = L\phi_1 \quad (A-4) \\
& \left[\bar{m}L^2 + I_\xi c^2 \Psi_1 + I_\eta s^2 \Psi_1 \right] \ddot{\theta}_1 + \left[\bar{m}L^2 \dot{\phi}_1^2 \right] c\theta_1 s\theta_1 + \\
& \bar{m}L \left[r\ddot{\theta}_2 + 2\dot{r}\dot{\theta}_2 \right] \left[c\theta_1 c\theta_2 + s\theta_1 s\theta_2 c(\phi_2 - \phi_1) \right] + \\
& \bar{m}L \left[r\ddot{\phi}_2 + 2\dot{r}\dot{\phi}_2 + 2\omega_o \dot{r} \right] s\theta_1 c\theta_2 s(\phi_2 - \phi_1) + \\
& \bar{m}L \left[\ddot{r} - r\dot{\theta}_2^2 \right] \left[c\theta_1 s\theta_2 - s\theta_1 c\theta_2 c(\phi_2 - \phi_1) \right] + \\
& \bar{m}Lr \left[\dot{\phi}_2^2 + 2\omega_o \dot{\phi}_2 \right] s\theta_1 c\theta_2 c(\phi_2 - \phi_1) - \\
& 2\bar{m}Lr \left[\dot{\theta}_2 \dot{\phi}_2 + \omega_o \dot{\theta}_2 \right] s\theta_1 s\theta_2 s(\phi_2 - \phi_1) + 2\bar{m}L^2 \omega_o \dot{\phi}_1 s\theta_1 c\theta_1 +
\end{aligned}$$

$$\begin{aligned}
& \bar{m}\omega_o^2 L \left[(Ls\theta_1 + rs\theta_2)c\theta_1 + 3(Lc\theta_1 c\phi_1 + rc\theta_2 c\phi_2)s\theta_1 c\phi_1 \right] + \\
& (I_\xi - I_\eta) \ddot{\phi}_1 c\theta_1 s\Psi_1 c\Psi_1 + \\
& \left[I_\xi s^2 \Psi_1 + I_\eta c^2 \Psi_1 - I_\zeta \right] \left[(\omega_o + \dot{\phi}_1)^2 + 3\omega_o^2 c^2 \phi_1 \right] s\theta_1 c\theta_1 + \\
& \left[(I_\xi - I_\eta) c^2 \Psi_1 + I_\zeta \right] (\omega_o + \dot{\phi}_1) \dot{\Psi}_1 c\theta_1 - \\
& \left[I_\xi - I_\eta \right] \left[2\dot{\theta}_1 \dot{\Psi}_1 + 3\omega_o^2 s\phi_1 c\phi_1 c\theta_1 \right] s\Psi_1 c\Psi_1 = L_{\theta_1} \quad (A-5)
\end{aligned}$$

$$\begin{aligned}
& \left[I_\zeta + \underline{(I_s + I_m)} \right] \ddot{\Psi}_1 - I_\zeta \ddot{\phi}_1 s\theta_1 - I_\zeta (\omega + \dot{\phi}_1) \dot{\theta}_1 c\theta_1 + \left[\underline{(I_s + I_m)} \ddot{\Psi}_2 + \right. \\
& \underline{I_m \ddot{\Psi}_3} \left. \right] + (I_\xi - I_\eta) \left[\dot{\theta}_1^2 s\Psi_1 c\Psi_1 - \dot{\theta}_1 (\omega + \dot{\phi}_1) c\theta_1 c^2 \Psi_1 - \right. \\
& \left. (\omega + \dot{\phi}_1)^2 c^2 \theta_1 s\Psi_1 c\Psi_1 \right] + 3\omega^2 (I_\xi - I_\eta) \left[(c^2 \phi_1 s^2 \theta_1 - s^2 \phi_1) s\Psi_1 c\Psi_1 - \right. \\
& \left. s\phi_1 c\phi_1 s\theta_1 c^2 \Psi_1 \right] = L_{\Psi_1} \quad (A-6)
\end{aligned}$$

NOTE

Underlined terms were found to be negligible and therefore omitted from the analog simulation.

$$\begin{aligned}
& \bar{m}r^2 c^2 \theta_2 \ddot{\phi}_2 + \bar{m}Lr \left[\ddot{\phi}_1 c\theta_1 c(\phi_2 - \phi_1) + \ddot{\theta}_1 s\theta_1 s(\phi_2 - \phi_1) c\theta_2 + \right. \\
& \bar{m}Lr \left[\dot{\theta}_1^2 + \dot{\phi}_1^2 + 2\omega_o \dot{\phi}_1 \right] c\theta_1 c\theta_2 s(\phi_2 - \phi_1) - \\
& 2\bar{m}Lr \left[\dot{\theta}_1 \dot{\phi}_1 + \omega_o \dot{\theta}_1 \right] s\theta_1 c\theta_2 c(\phi_2 - \phi_1) + \\
& 2\bar{m}r \left[\dot{r} \dot{\phi}_2 c^2 \theta_2 + \omega_o \dot{r} c^2 \theta_2 - r \dot{\phi}_2 \dot{\theta}_2 c\theta_2 s\theta_2 - \omega_o r \dot{\theta}_2 c\theta_2 s\theta_2 \right] + \\
& 3\bar{m}\omega_o^2 r \left[Lc\theta_1 c\phi_1 + rc\theta_2 c\phi_2 \right] c\theta_2 s\phi_2 = 0 \quad (A-7)
\end{aligned}$$

$$\begin{aligned}
& \bar{m}r^2\ddot{\theta}_2 + \bar{m}Lr\ddot{\theta}_1 [c\theta_1 c\theta_2 + s\theta_1 s\theta_2 c(\phi_2 - \phi_1)] - \bar{m}Lr\dot{\phi}_1 c\theta_1 s\theta_2 s(\phi_2 - \phi_1) + \\
& \bar{m}Lr [\dot{\theta}_1^2 + \dot{\phi}_1^2 + 2\omega_o \dot{\phi}_1] c\theta_1 s\theta_2 c(\phi_2 - \phi_1) + \\
& \bar{m}Lr [2\dot{\theta}_1 \dot{\phi}_1 + 2\omega_o \dot{\theta}_1] s\theta_1 s\theta_2 s(\phi_2 - \phi_1) + \\
& 2\bar{m}r\dot{r}\dot{\theta}_2 + 2\bar{m}r^2\omega_o \dot{\phi}_2 c\theta_2 s\theta_2 - \bar{m}Lr\dot{\theta}_1^2 s\theta_1 c\theta_2 + \bar{m}r^2 \frac{\dot{\phi}_2^2}{2} c\theta_2 s\theta_2 + \\
& \bar{m}r\omega_o^2 [rc\theta_2 s\theta_2 + Ls\theta_1 c\theta_2 + 3(r c\theta_2 c\phi_2 + L c\theta_1 c\phi_1) s\theta_2 c\phi_2] = 0
\end{aligned}
\tag{A-8}$$

$$\begin{aligned}
& \bar{m}\ddot{r} + K_2\dot{r} + K_1r - \bar{m}r [2\omega_o \dot{\phi}_2 c^2\theta_2 + \dot{\phi}_2^2 c^2\theta_2 + \dot{\theta}_2^2] + K_4\Psi_2 - \\
& \bar{m}\omega_o^2 [(3rc\phi_2 c\theta_2 + 3Lc\phi_1 c\theta_1) c\phi_2 c\theta_2 - (rs\theta_2 + Ls\theta_1) s\theta_2] + \\
& \bar{m}L [\ddot{\phi}_1 c\theta_1 c\theta_2 s(\phi_2 - \phi_1) + \dot{\theta}_1 [c\theta_1 s\theta_2 - s\theta_1 c\theta_2 c(\phi_2 - \phi_1)] - \\
& (\dot{\phi}_1^2 + 2\omega_o \dot{\phi}_1 + \dot{\theta}_1^2) c\theta_1 c\theta_2 c(\phi_2 - \phi_1) - \dot{\theta}_1^2 s\theta_1 s\theta_2 - \\
& 2(\omega_o \dot{\theta}_1 + \dot{\theta}_1 \dot{\phi}_1) s\theta_1 c\theta_2 s(\phi_2 - \phi_1)] + (3\bar{m}\omega_o^2)(L + r_e) - K_1r_e = 0
\end{aligned}
\tag{A-9}$$

$$I_s [\ddot{\Psi}_2 + \underline{\ddot{\Psi}_1}] - K_6 \dot{\Psi}_3 + K_5 \dot{\Psi}_2 + K_3 \dot{\Psi}_2 + K_4(r - r_e) = 0 \tag{A-10}$$

$$I_m [\dot{\Psi}_3 + \dot{\Psi}_2 + \underline{\dot{\Psi}_1}] + K_6 \dot{\Psi}_3 = 0 \tag{A-11}$$

APPENDIX B - RICE/WILBERFORCE SPRING EQUATIONS

1. GENERAL

The basic concept of the Rice/Wilberforce damper involves use of the cross-coupling characteristics of the helical spring to convert plunging motion into rotary motion. At the beginning of this study, the literature and classic textbooks on spring characteristics did not adequately cover properties of helical springs in the region of parameters needed in this application.

For this reason, the necessary equations were developed as a part of the study. Later, a Russian paper^a reported work nearly identical to the work summarized here and corroborated the validity of the analysis.

The analysis that follows is not intended to be an all-encompassing treatise on helical springs, but is reasonably broad within the following constraints:

1. It is assumed that the spring is wire with uniform, symmetrical cross section and that the helix angle and radius of the coil are uniform throughout the spring.
2. The wire diameter is small compared with the radius of the coil, so that curved-beam effects on stress distribution and stiffness are negligible.
3. It is assumed that all spring deflections result from bending and torsion of the wire (deflections

^aChenyshev, N. A.: Nonlinear Theory of Elastic Deformation of Cylindrically Wound Springs. Governmental Scientific Technical Publications on Machine Construction, Moscow, 1958.

due to direct stresses, axial and shear, are negligible).

4. The wire behaves elastically.

The general expressions for the axial load and rotational moment are developed as a function of the wire characteristics and shape (including initial unloaded shape).

The stiffness coefficients (spring constants) are evaluated by taking appropriate partial derivatives of the force equations. Note that the nomenclature used to denote these stiffness coefficients in this derivation differs from the nomenclature used in the equations of motion, for convenience.

Special cases of particular interest in this study are evaluated in more detail, and curves are plotted to facilitate the choice of parameters for the dynamic study. Figure B-1 is included to show the result of linearization of the spring characteristics.

Further study of spring characteristics is desirable in the following areas:

1. Theoretical and practical implications of utilizing springs with various unloaded lengths
2. Effects of using wire of noncircular cross sections (flattened wire, for example). The equations indicate that the cross-coupling can be enhanced this way. Associated characteristics need more study.
3. Practical design considerations of the connection between the spring and the canister
4. Behavior of wire springs coated with inelastic materials
5. Stability characteristics and associated vulnerability to entanglement

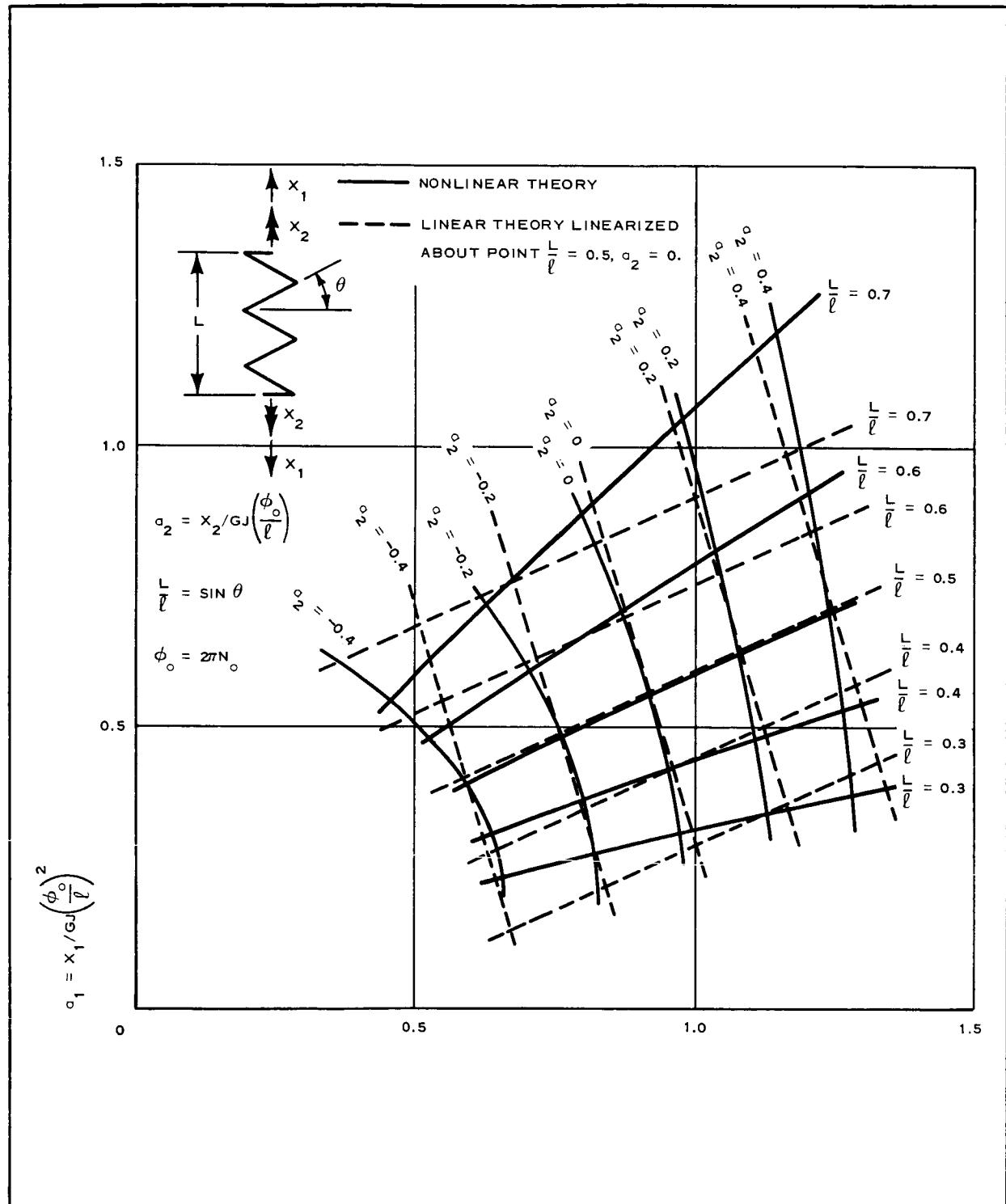


Figure B-1 - Comparison of Spring Parameters

2. HELICAL-SPRING SHAPE RELATIONSHIPS

A helical spring may be interpreted as the shape that results from the bending and twisting of a straight uniform wire around a cylinder at constant bending and twisting rates, so that the same longitudinal filament on the wire surface is always in contact with the surface of the cylinder.

Figure B-2 shows a helical spring with its geometric parameters.

The bending and twisting of the wire around the cylinder gives rise to the following relationships between:

1. The internal torque in the wire, T
2. The internal bending moment in the wire, M
3. The unit twist in the wire, α
4. The radius of curvature of the wire, ρ , associated with the moment, M (the subscript zero refers to initial unstressed conditions):

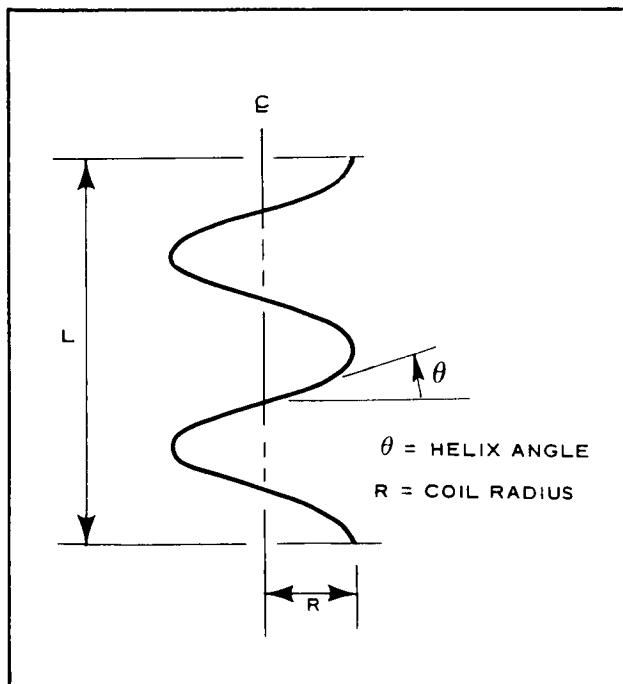
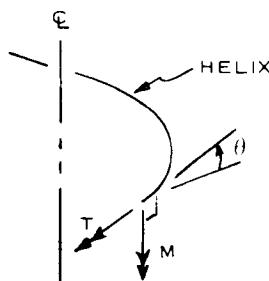


Figure B-2 - Geometric Parameters
of Helical Spring

$$\frac{1}{\rho} = \frac{M}{EI} + \frac{1}{\rho_0}, \quad (B-1)$$

and

$$\alpha = \frac{T}{JG} + \alpha_0. \quad (B-2)$$



Note: Right-hand rule for moments

The following derivation gives the relationship of the helical-spring geometrical parameters R and θ to α .

Problem:

Determine the unit twist required to keep a longitudinal filament of the round wire of a helix spring in contact with the cylinder enclosed by the helix for any given helix angle and radius.

Definitions:

R = radius of helix

θ = helix angle

\overline{EC} is a line in a plane tangent to the helix cylinder and perpendicular to the helix.

A and C are two points on the helix.

Analysis:

The total twist of the helix between points A and C is the angle, α , defined by the angle \overline{EC} makes with the plane perpendicular to \overline{OA} as ϕ approaches zero.

The following relations are obtained from geometry:

$$\text{true angle } CEF = \theta$$

$$\tan \gamma = \tan \theta \sin \phi$$

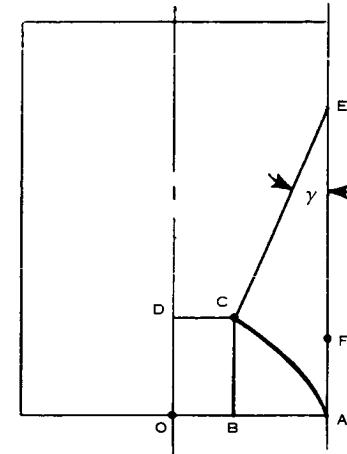
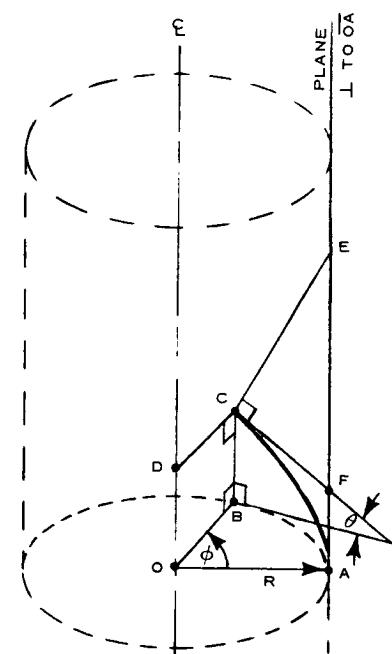
$$\text{as } \phi \rightarrow 0 \sin \phi \rightarrow \phi$$

Therefore,

$$\tan \gamma = \phi \tan \theta , \quad (B-3)$$

and

$$\text{arc CA} = \frac{R\phi}{\cos \theta} . \quad (B-4)$$



PROJECTION ON PLANE AOB

Since γ is the vector component of $\bar{\alpha}$ in the vertical direction, it follows that

$$\tan \bar{\alpha} = \tan \gamma \cos \theta . \quad (B-5)$$

Since

$$\begin{aligned} \tan \bar{\alpha} &= \phi \tan \theta \cos \theta \\ &= \phi \sin \theta , \end{aligned} \quad (B-6)$$

for small angles

$$\tan \bar{\alpha} \approx \bar{\alpha} . \quad (B-7)$$

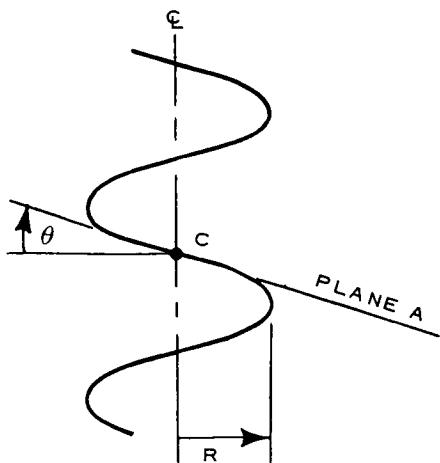
Therefore,

$$\bar{\alpha} = \phi \sin \theta . \quad (B-8)$$

Since the unit twist is the total twist divided by the length, it follows that

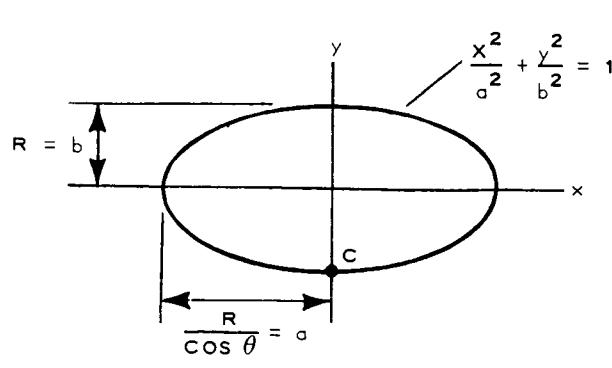
$$\begin{aligned} \text{unit twist} &= \alpha E \frac{\bar{\alpha}}{CA} \\ &= \frac{\phi \sin \theta}{R \phi} \\ &= \frac{\sin \theta \cos \theta}{R} . \end{aligned}$$

The following derivation gives the relationship of R and θ to ρ .



Problem:

Determine the radius of curvature, ρ , in the helix wire at point C on the helix. Point C is where plane A is tangent to the helix.

Analysis:

The projection of the cylinder on plane A results in the ellipse shown here. The radius of curvature in general terms is

$$\rho = \frac{(1 + y'^2)^{3/2}}{y''}. \quad (B-9)$$

For the ellipse of the above sketch,

$$y' = -\frac{b}{a} \left(\frac{x}{\sqrt{a^2 - x^2}} \right), \quad (B-10)$$

and

$$y'' = -\left(\frac{b}{a}\right) \left[\frac{a^2}{(a^2 - x^2)^{3/2}} \right]. \quad (B-11)$$

The radius of curvature then equals

$$\rho = \frac{\left[1 + \left(\frac{b}{a}\right)^2 \left(\frac{x^2}{a^2 - x^2} \right) \right]^{3/2}}{-\left(\frac{b}{a}\right) \left[\frac{a^2}{(a^2 - x^2)^{3/2}} \right]}. \quad (B-12)$$

Evaluating the radius of curvature at point C for $x = 0$ gives

$$\rho = -\frac{a^2}{b} = -\frac{R}{\cos^2 \theta}. \quad (B-13)$$

3. ELASTIC CHARACTERISTICS OF A HELICAL SPRING

Note: Right-hand rule for moments

R = radius of helix

R_o = radius of helix for unstressed state

L = length of helix

L_o = length of helix for unstressed state

ℓ = total length of wire in helix

θ = helix angle

θ_o = helix angle in unstressed state

ϕ = helix rotation about centerline of cylinder

ϕ_o = helix rotation, unstressed state

T = internal torque in helix wire

M = internal bending moment in helix wire

X_1 = external load applied along helix

X_2 = external torque applied along helix

I = moment of inertia of wire cross section

J = torsional stiffness factor

E = Young's modulus

G = shear modulus

In the following analysis of the elastic characteristics of helical springs (see Figure B-3), the following assumptions are made:

1. The helix is made from a wire with a constant symmetrical cross section, a bending stiffness, EI, and a torsional stiffness, JG.
2. Deflections caused by axial and shear energies are negligible.

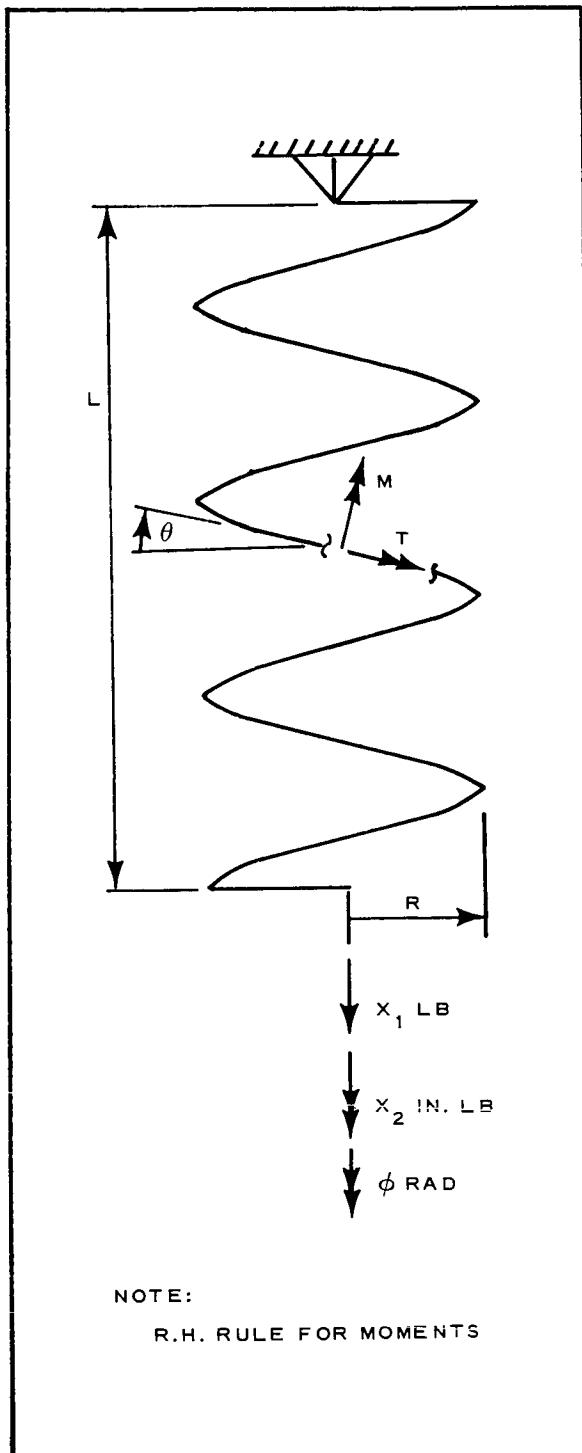


Figure B-3 - Helical Spring -
Elastic Characteristics

3. The external loads, X_1 and X_2 , and their reactions are applied by infinitely rigid brackets.

From Equations B-1, B-2, B-11, and B-12, the relationships between the internal force system in the wire and the geometry of the helix spring can be found by substituting Equations B-11 and B-12 into Equations B-1 and B-2. The result is

$$M = EI \left(\frac{\cos^2 \theta}{R} \right) - \frac{1}{\rho_o} \quad (B-14)$$

and

$$T = JG \left(\frac{\sin \theta \cos \theta}{R} \right) - \alpha_o \quad (B-15)$$

Application of the external loads X_1 and X_2 will cause the spring to go from its initial unstressed state to some other equilibrium stress state. Equations B-14 and B-15 can then be written

$$M = EI \left(\frac{\cos^2 \theta}{R} - \frac{\cos^2 \theta_o}{R_o} \right), \quad (B-16)$$

and

$$T = JG \left(\frac{\sin \theta \cos \theta}{R} - \frac{\sin \theta_o \cos \theta_o}{R_o} \right). \quad (B-17)$$

Statics give the following relationships:

$$X_1 = \frac{T \cos \theta}{R} - \frac{M \sin \theta}{R} \quad (B-18)$$

and

$$X_2 = T \sin \theta + M \cos \theta. \quad (B-19)$$

Solving Equations B-18 and B-19 for T and M gives

$$M = X_2 \cos \theta - X_1 R \sin \theta, \quad (B-20)$$

and

$$T = X_2 \cos \theta + X_1 R \cos \theta. \quad (B-21)$$

Substituting Equations B-20 and B-21 into Equations B-16 and B-17 and solving for X_1 and X_2 give the following equations:

$$X_1 = \frac{GJ \cos \theta}{R} \left(\frac{\sin \theta \cos \theta}{R} - \frac{\sin \theta_o \cos \theta_o}{R_o} \right) - \frac{EI \sin \theta}{R} \left(\frac{\cos^2 \theta}{R} - \frac{\cos^2 \theta_o}{R_o} \right), \quad (B-22)$$

and

$$X_2 = GJ \sin \theta \left(\frac{\sin \theta \cos \theta}{R} - \frac{\sin \theta_o \cos \theta_o}{R_o} \right) + EI \cos \theta \left(\frac{\cos^2 \theta}{R} - \frac{\cos^2 \theta_o}{R_o} \right). \quad (B-23)$$

X_1 and X_2 can also be written in terms of L and ϕ with the aid of the following relationships:

$$\sin \theta = \frac{L}{\ell}, \quad (B-24)$$

$$\cos^2 \theta = 1 - \left(\frac{L}{\ell} \right)^2, \quad (B-25)$$

and

$$R = \frac{\ell \cos \theta}{\phi}. \quad (B-26)$$

Substituting the above relationships into Equations B-21 and B-22 gives

$$X_1 = \frac{GJ}{\ell^3} (\phi L - \phi_o L_o) \phi - \frac{EI}{\ell^3} \left(\phi L \left[1 - \left(\frac{L}{\ell} \right)^2 \right]^{\frac{1}{2}} \left\{ \phi \left[- \left(\frac{L}{\ell} \right)^2 \right]^{\frac{1}{2}} - \phi_o \left[1 - \left(\frac{L_o}{\ell} \right)^2 \right]^{\frac{1}{2}} \right\} \right) \quad (B-27)$$

and

$$X_2 = \frac{GJ}{\ell^3} (\phi L - \phi_o L_o) L + \frac{EI}{\ell} \left[1 - \left(\frac{L}{\ell} \right)^2 \right]^{\frac{1}{2}} \left\{ \phi \left[1 - \left(\frac{L}{\ell} \right)^2 \right]^{\frac{1}{2}} - \phi_o \left[1 - \left(\frac{L_o}{\ell} \right)^2 \right]^{\frac{1}{2}} \right\} . \quad (B-28)$$

Since both X_1 and X_2 are functions of the same two independent variables, L and ϕ , the total differentials of X_1 and X_2 are

$$dX_1 = \frac{\partial X_1}{\partial L} dL + \frac{\partial X_1}{\partial \phi} d\phi , \quad (B-29)$$

and

$$dX_2 = \frac{\partial X_2}{\partial L} dL + \frac{\partial X_2}{\partial \phi} d\phi . \quad (B-30)$$

The stiffness coefficients are

$$K_{11} = \frac{\partial X_1}{\partial L} , \quad (B-31)$$

$$K_{12} = \frac{\partial X_1}{\partial \phi} = K_{21} = \frac{\partial X_2}{\partial L} , \quad (B-32)$$

and

$$K_{22} = \frac{\partial X_2}{\partial \phi} . \quad (B-33)$$

Partial differentiation yields the following equations for the stiffness coefficients:

$$K_{11} = \frac{GJ}{\ell^3} \phi^2 - \frac{EI}{\ell^3} \left(\phi^2 - \phi \phi_o \left[1 - \left(\frac{L_o}{\ell} \right)^2 \right] \left\{ \left[- \left(\frac{L}{\ell} \right)^2 \right]^{\frac{1}{2}} + \left(\frac{L}{\ell} \right)^2 \left[1 - \left(\frac{L}{\ell} \right)^2 \right]^{-\frac{3}{2}} \right\} \right), \quad (B-34)$$

$$K_{12} = K_{21} = \frac{GJ}{\ell^3} (2L\phi - L_o\phi_o) - \frac{EI}{\ell^3} \left\{ 2L\phi - L\phi_o \left[1 - \left(\frac{L_o}{\ell} \right)^2 \right]^{\frac{1}{2}} \left[1 - \left(\frac{L}{\ell} \right)^2 \right]^{-\frac{1}{2}} \right\}, \quad (B-35)$$

and

$$K_{22} = \frac{GJ}{\ell} \left(\frac{L}{\ell} \right)^2 + \frac{EI}{\ell} \left[1 - \left(\frac{L}{\ell} \right)^2 \right]. \quad (B-36)$$

When converted to functions of R and θ , Equations B-34, B-35, and B-36 become

$$K_{11} = \frac{GJ}{\ell R^2} \cos^2 \theta - \frac{EI}{\ell R^2} \left(\cos^2 \theta - \frac{R}{R_o} \frac{\cos^2 \theta_o}{\cos^2 \theta} \right), \quad (B-37)$$

$$K_{12} = K_{21} = \frac{GJ}{\ell} \left(\frac{2 \sin \theta \cos \theta}{R} - \frac{\sin \theta_o \cos \theta_o}{R_o} \right) - \frac{EI}{\ell} \left[\frac{2 \sin \theta \cos \theta}{R} - \frac{\sin \theta \cos \theta_o}{R_o} \left(\frac{\cos \theta_o}{\cos \theta} \right) \right], \quad (B-38)$$

and

$$K_{22} = \frac{GJ}{\ell} \sin^2 \theta + \frac{EI}{\ell} \cos^2 \theta . \quad (B-39)$$

4. EVALUATION OF HELICAL-SPRING-STIFFNESS CHARACTERISTICS FOR UNSTRESSED CONDITION; $L_o = 0$, $\theta_o = 0$

The helical-spring characteristics of the most interest are those at an equilibrium length, L_e . This deflection of the spring results from the gravity-gradient attraction on the damper mass. Therefore, with $\theta_o = 0$, $\sin \theta_o = 0$, and $\cos \theta_o = 1$, Equations B-38 and B-39 reduce to the following equations, where the subscript e denotes the extended equilibrium position:

$$X_1 = GJ \frac{\cos \theta_e}{R_e^2} (\sin \theta_e \cos \theta_e) - EI \frac{\sin \theta_e}{R_e} \left(\frac{\cos^2 \theta_e}{R_e} - \frac{1}{R_o} \right) \quad (B-40)$$

and

$$X_2 = GJ \frac{\sin \theta_e}{R_e} (\sin \theta_e \cos \theta_e) + EI \cos \theta_e \left(\frac{\cos^2 \theta_e}{R_e} - \frac{1}{R_o} \right) . \quad (B-41)$$

$X_2 = 0$ for the gravity-gradient equilibrium. Solving Equation B-41 with $X_2 = 0$ gives

$$\frac{R_o}{R_e} = \frac{EI}{GJ \sin^2 \theta_e + EI \cos^2 \theta_e} . \quad (B-42)$$

Substituting Equation B-42 into Equations B-37, B-38, and B-39 with $\sin \theta_o = 0$ and $\cos \theta_o = 1$ gives the following equations for the spring-stiffness coefficients at the gravity-gradient equilibrium length:

$$\begin{aligned}
 K_{11} &= \left(\frac{\partial X_1}{\partial L} \right)_e \\
 &= \frac{GJ(\cos^2 \theta_e + \tan^2 \theta_e) + EI \sin^2 \theta_e}{\ell R_o^2 \left(\frac{GJ}{EI} \sin^2 \theta_e + \cos^2 \theta_e \right)^2} \\
 &= f_1 \frac{GJ}{\ell R_o^2} , \tag{B-43}
 \end{aligned}$$

$$\begin{aligned}
 K_{12} = K_{21} &= \left(\frac{\partial X_1}{\partial \phi} \right)_e = \left(\frac{\partial X_2}{\partial L} \right)_e \\
 &= \frac{GJ - EI}{R_o \ell} \left(\frac{2 \sin \theta_e \cos \theta_e}{\frac{GJ}{EI} \sin^2 \theta_e + \cos^2 \theta_e} \right) + \frac{EI}{R_o \ell} \tan \theta_e \\
 &= f_{12} \frac{GJ}{\ell R_o} , \tag{B-44}
 \end{aligned}$$

$$\begin{aligned}
 K_{22} &= \left(\frac{\partial X_2}{\partial \phi} \right)_e \\
 &= \frac{GJ}{\ell} \sin^2 \theta_e + \frac{EI}{\ell} \cos^2 \theta_e \\
 &= f_2 \frac{GJ}{\ell} . \tag{B-45}
 \end{aligned}$$

A plot of the spring-stiffness coefficients is shown in Figure B-4.

5. HELICAL-SPRING PARAMETERS FOR UNSTRESSED HELIX ANGLE $\theta_o = 0$ DEG

Equations B-27 and B-28 can be factored into the form shown below, if $\beta = GJ/EI = 0.77$ for round steel wire.

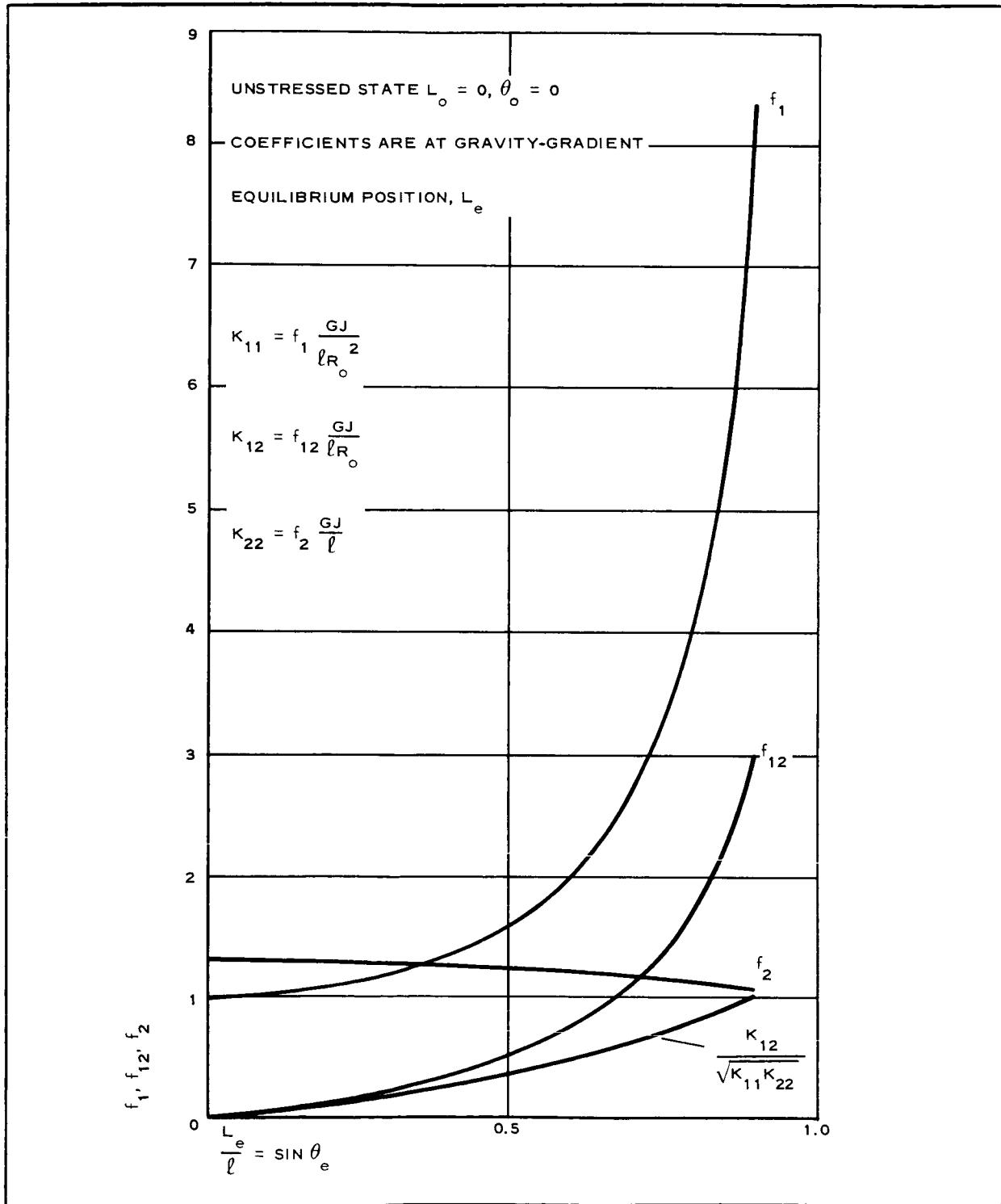


Figure B-4 - Helical-Spring Stiffness Coefficients

$$X_1 = GJ \left(\frac{\phi_o}{l} \right)^2 \left(\frac{\phi}{\phi_o} \right)^2 \frac{L}{l} \left(1 - \frac{1}{\beta} \left\{ 1 - \frac{\phi_o}{\phi} \left[1 - \left(\frac{L}{l} \right)^2 \right]^{-\frac{1}{2}} \right\} \right), \quad (B-46)$$

and

$$X_2 = GJ \left(\frac{\phi_o}{l} \right) \left[\frac{\phi}{\phi_o} \left(\frac{L}{l} \right)^2 \left(1 - \frac{1}{\beta} \left\{ 1 - \frac{\phi_o}{\phi} \left[1 - \left(\frac{L}{l} \right)^2 \right]^{-\frac{1}{2}} \right\} \right) + \frac{\phi}{\phi_o \beta} \left\{ 1 - \frac{\phi_o}{\phi} \left[1 - \left(\frac{L}{l} \right)^2 \right]^{-\frac{1}{2}} \right\} \right]. \quad (B-47)$$

Equations B-46 and B-47 can also be written

$$X_1 = GJ \left(\frac{\phi_o}{l} \right)^2 a_1 \quad (B-48)$$

and

$$X_2 = GJ \left(\frac{\phi_o}{l} \right) a_2 . \quad (B-49)$$

a_1 and a_2 are defined by Equations B-46 and B-47. Figure B-5 is a graphic presentation of X_1 , X_2 , a_1 , and a_2 .

6. STRESS-PARAMETER RELATIONSHIPS FOR HELICAL SPRINGS MADE FROM ROUND WIRE WITH UNSTRESSED HELIX ANGLE $\theta_o = 0$

The torsional shear stress, f_s , in the wire is

$$f_s = \frac{Td}{4I} . \quad (B-50)$$

The bending stress, f_b , in the wire is

$$f_b = \frac{Md}{2I} . \quad (B-51)$$

Equations B-16 and B-17 yield equations for T and M as follows:

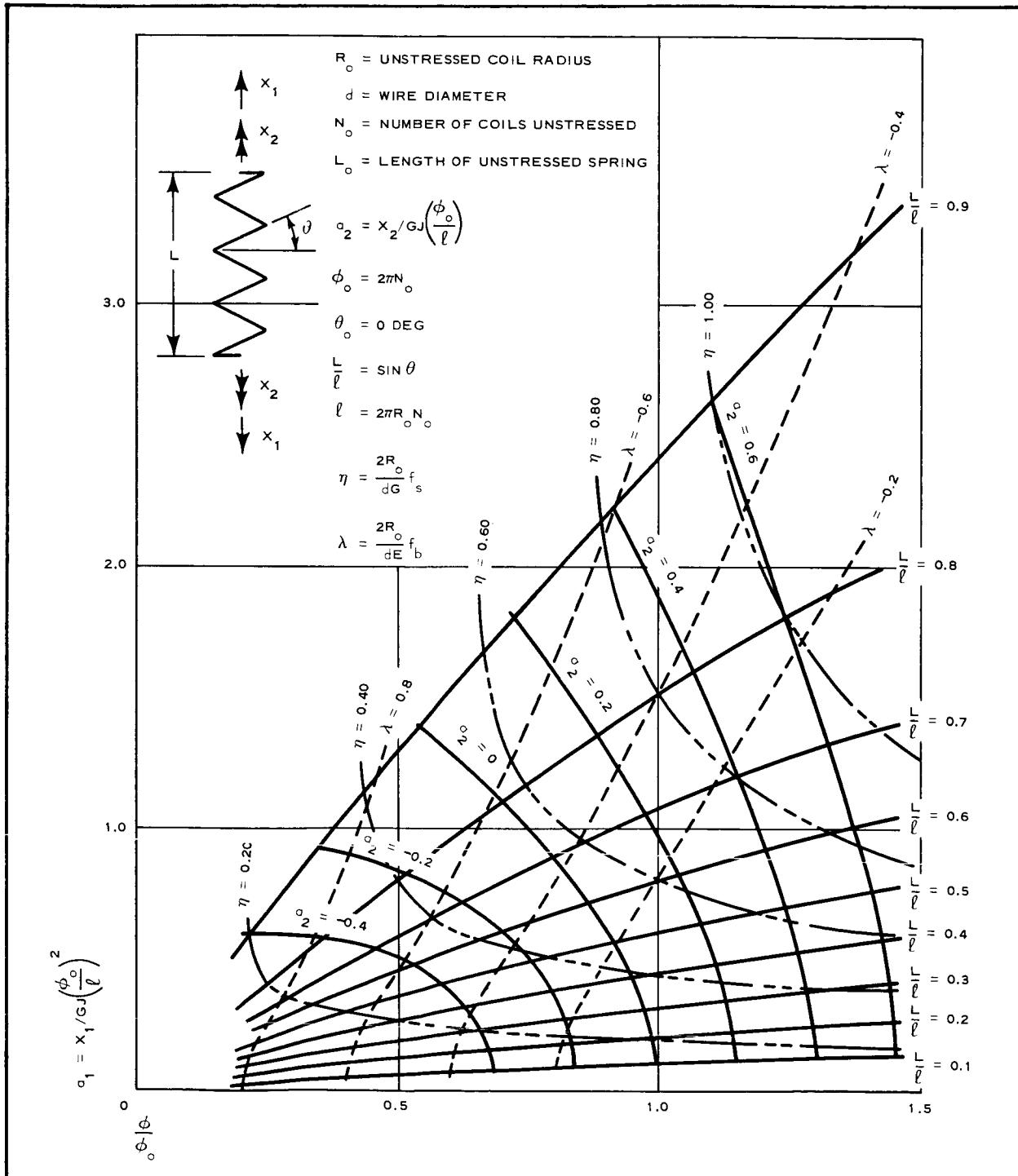


Figure B-5 - Helical-Spring Parameters for Unstressed Helical Angle
 $\theta_o = 0$ Deg

$$M = EI \left(\frac{\cos^2 \theta}{R} - \frac{1}{R_o} \right) \quad (B-52)$$

and

$$T = 2IG \frac{\sin \theta \cos \theta}{R} \quad (B-53)$$

Substituting Equations B-52 and B-53 into Equations B-50 and B-51 yields

$$f_s = \frac{dG}{2R} \sin \theta \cos \theta \quad (B-54)$$

and

$$f_b = \frac{dE}{2I} \left(\frac{\cos^2 \theta}{R} - \frac{1}{R_o} \right) \quad (B-55)$$

Equations B-54 and B-55 in terms of ϕ and L are

$$f_s = \frac{dGL\phi}{2\ell^2} \quad (B-60)$$

and

$$f_b = + \frac{dE}{2I} \left\{ \phi \left[1 - \left(\frac{L}{\ell} \right)^2 \right]^{\frac{1}{2}} - \phi_o \right\} \quad (B-61)$$

Written in nondimensional form, Equations B-60 and B-61 are

$$\frac{2R_o f_s}{dG} = \left(\frac{L}{\ell} \right) \left(\frac{\phi}{\phi_o} \right) = \eta \quad (B-62)$$

and

$$\frac{2R_o f_b}{dE} = -1 + \frac{\phi}{\phi_o} \left[1 - \left(\frac{L}{\ell} \right)^2 \right]^{\frac{1}{2}} = \lambda \quad (B-63)$$

The stress parameters in Equations B-62 and B-63 are shown graphically in Figure B-5.

APPENDIX C - LINEARIZED EIGHT-DEGREES-OF-FREEDOM EQUATIONS

$$\begin{bmatrix}
 0 & 2I_\zeta s^2 + 8[I_\eta - I_\zeta] + 6\bar{m}L[L + r_o] & 2[I_\xi - I_\eta + I_\zeta]s & 0 & -6\bar{m}L[L + r_o] & 0 & 0 & 0 & \varphi_1 & \frac{2L\varphi_1}{\omega^2} \\
 2I_\eta s^2 + 6[(I_\xi - I_\zeta) + \bar{m}L(L + r_o)] & 0 & 0 & -6\bar{m}L[L + r_o] & 0 & 0 & 0 & 0 & \theta_1 & \frac{2L\theta_1}{\omega^2} \\
 0 & -2[I_\xi - I_\eta + I_\zeta]s & 2[I_\zeta - I_s + I_m]s^2 & 0 & 0 & 2[I_s + I_m]s^2 & 0 & 2I_ms^2 & \psi_1 & \frac{2L\psi_1}{\omega^2} \\
 0 & Ls^2 + L & 0 & 0 & \frac{r_o s^2}{3L + 4r_o} & 0 & 0 & 0 & \varphi_2 & 0 \\
 Ls^2 & 0 & 0 & \frac{r_o s^2}{3[L + r_o]} & 0 & 0 & 2s & 0 & \theta_2 & 0 \\
 0 & 0 & [I_s + I_m]\omega_c^2 s^2 & 0 & 0 & \frac{[I_s + I_m]}{\omega_c^2 s^2} & K_4 & I_m \omega_c^2 s^2 & \psi_2 & 0 \\
 -2Im\omega_o^2 s & 0 & 0 & -2r_o m \omega_o^2 s & 0 & NK_4 & + NK_2 \omega_o s & 0 & r & 0 \\
 0 & 0 & I_m \omega_o s & 0 & 0 & I_m \omega_o s & 0 & \frac{m \omega_c^2 s^2}{-3m \omega_c^2} & \psi_3 & 0
 \end{bmatrix} = 0$$

APPENDIX D - TRANSIENT-RESPONSE AND STEADY-STATE-RESPONSE
HISTORIES FROM ANALOG-COMPUTER STUDY

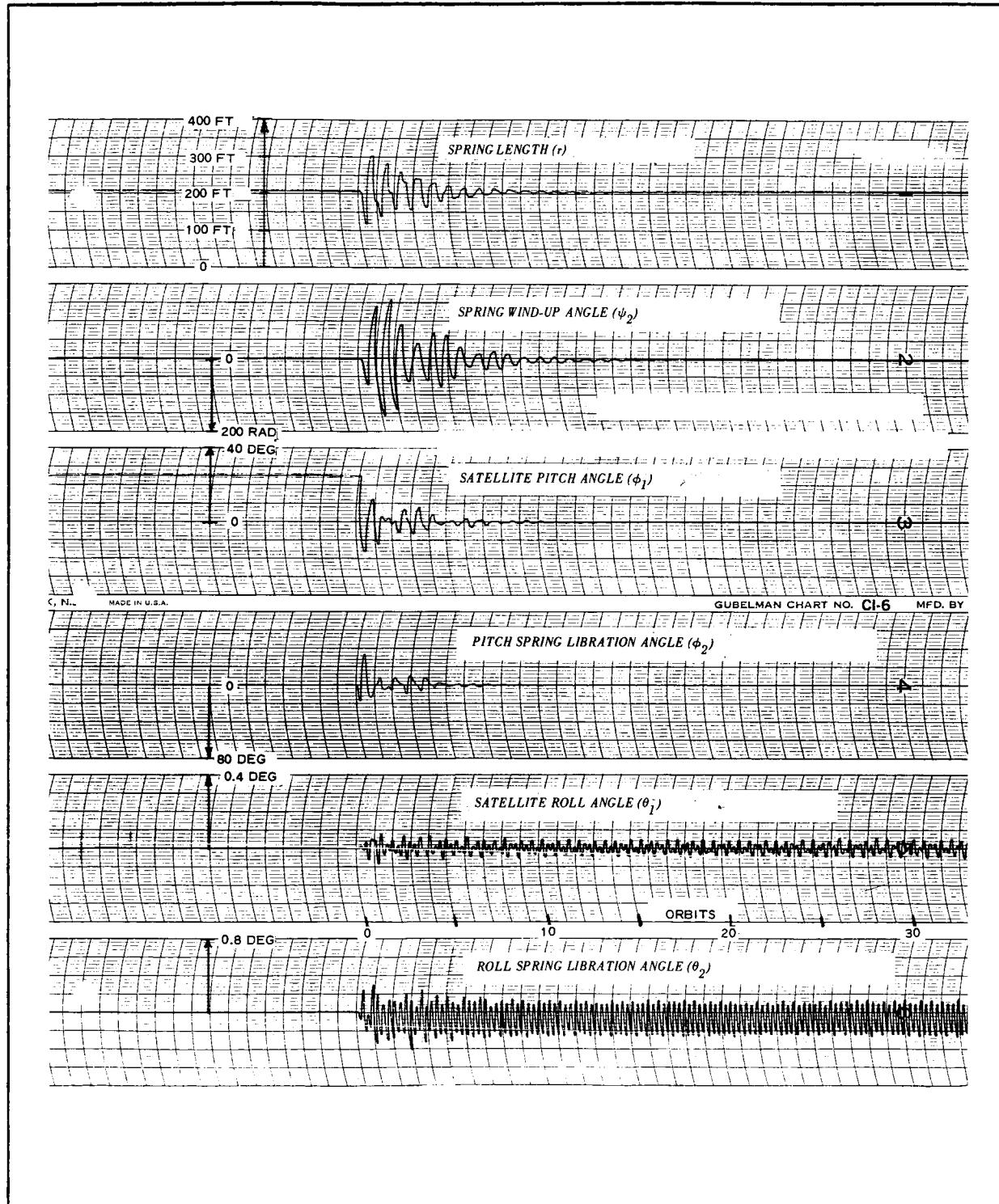


Figure D-1 - Optimum Configuration, Pitch Transient Response

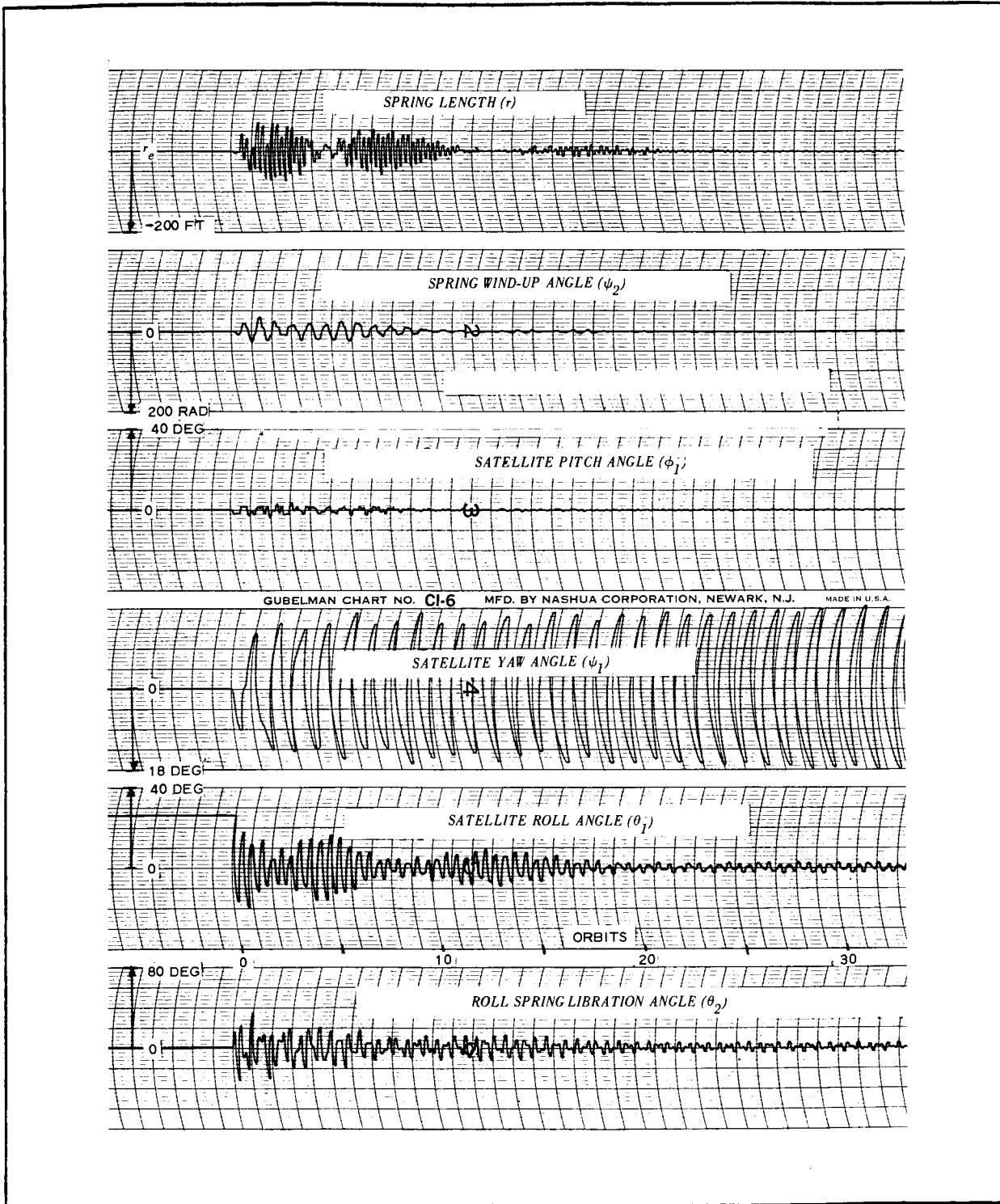
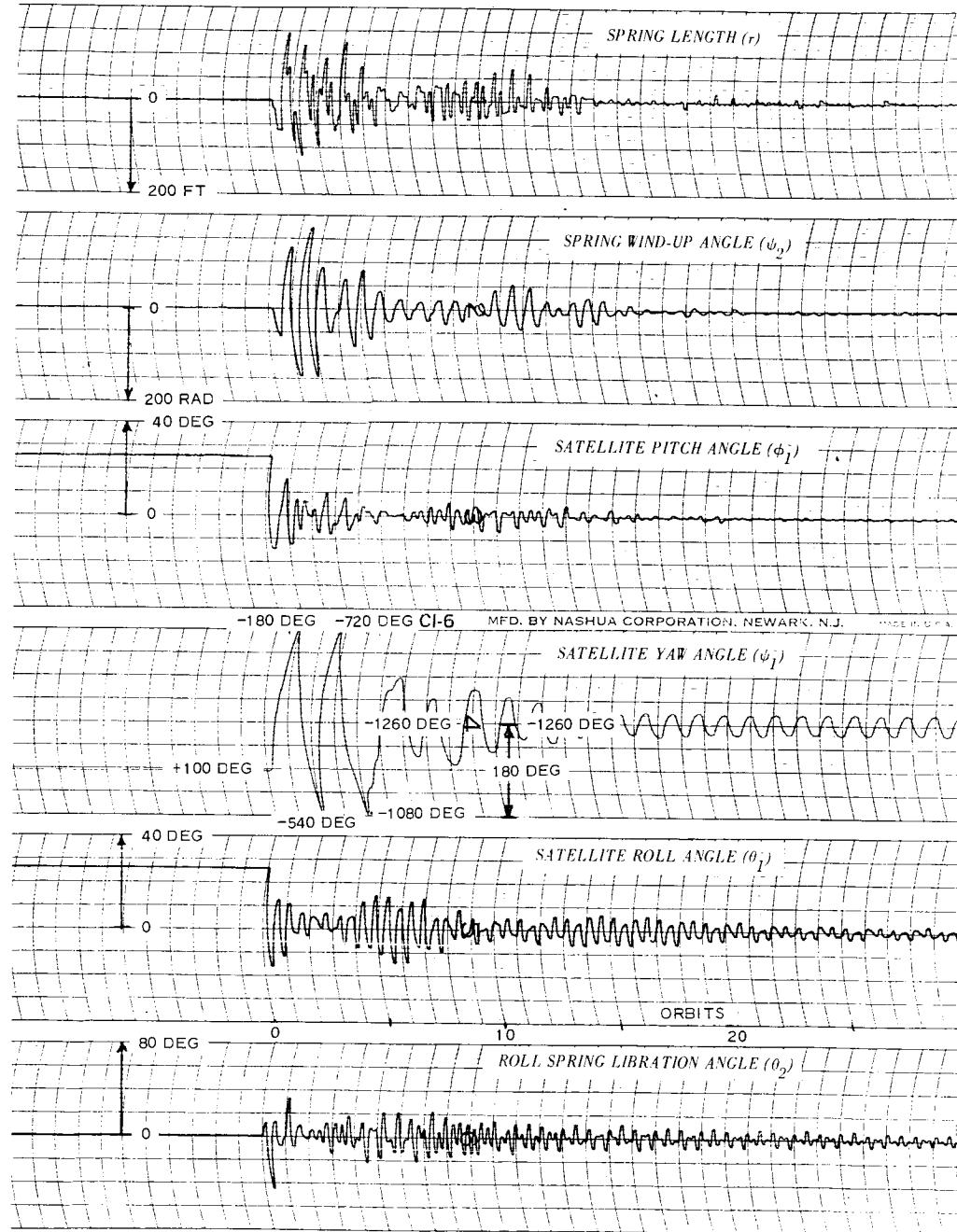


Figure D-2 - Optimum Configuration, Roll Transient Response



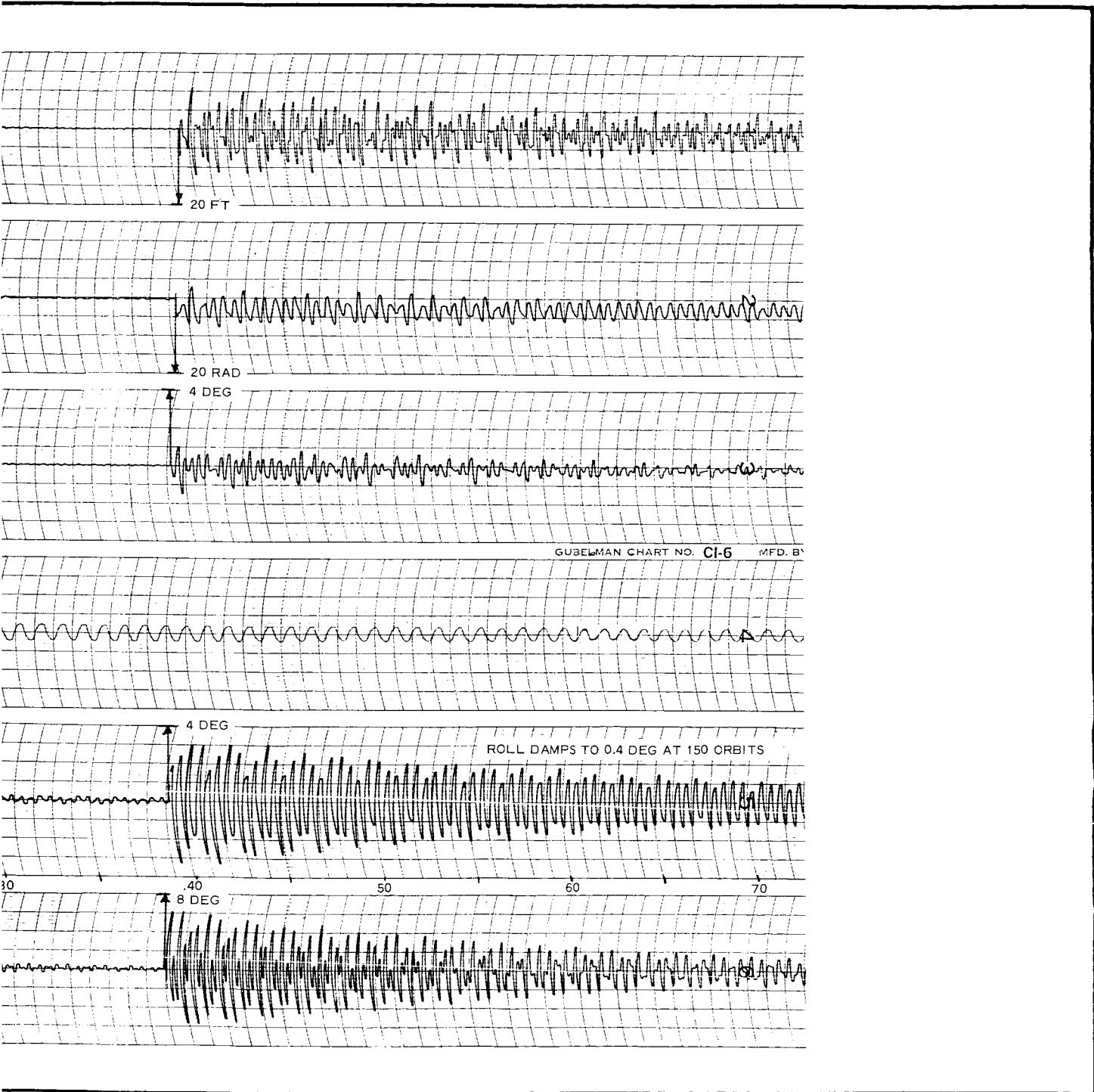


Figure D-3 - Optimum Configuration, Pitch, Roll, and Yaw
Transient Response

2

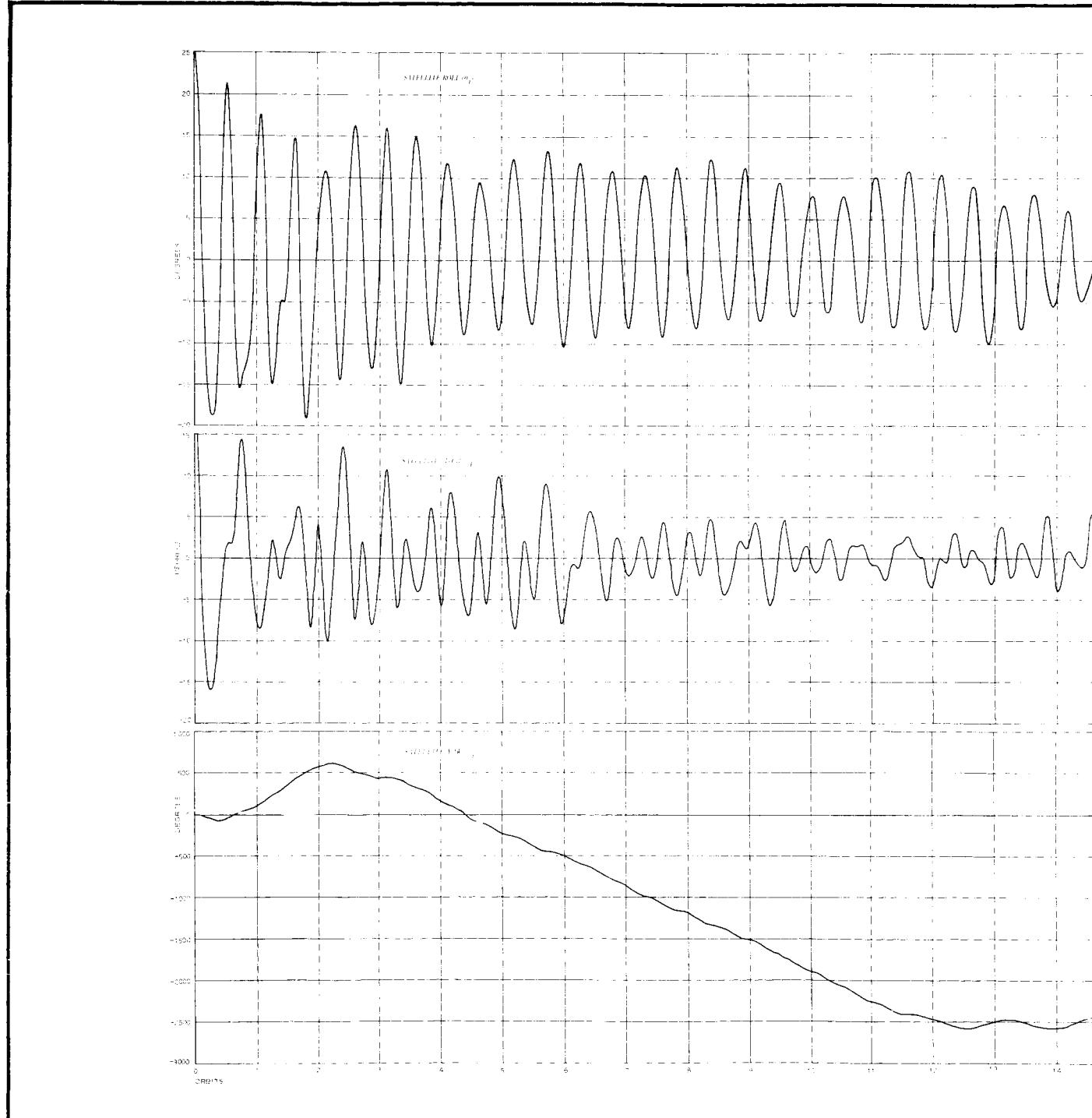
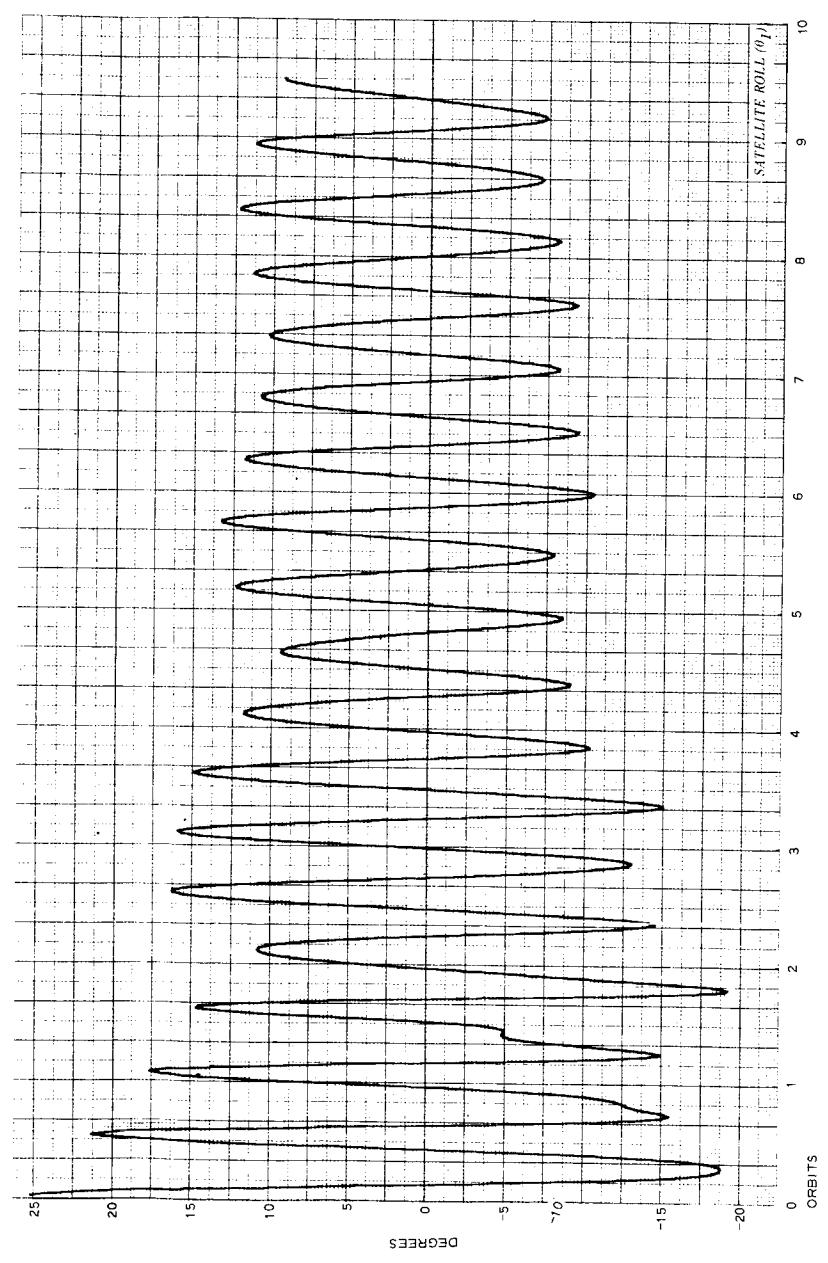




Figure D-4 - Optimum Configuration, Pitch and Roll Transient Response
(Sheet 1 of 9)

2



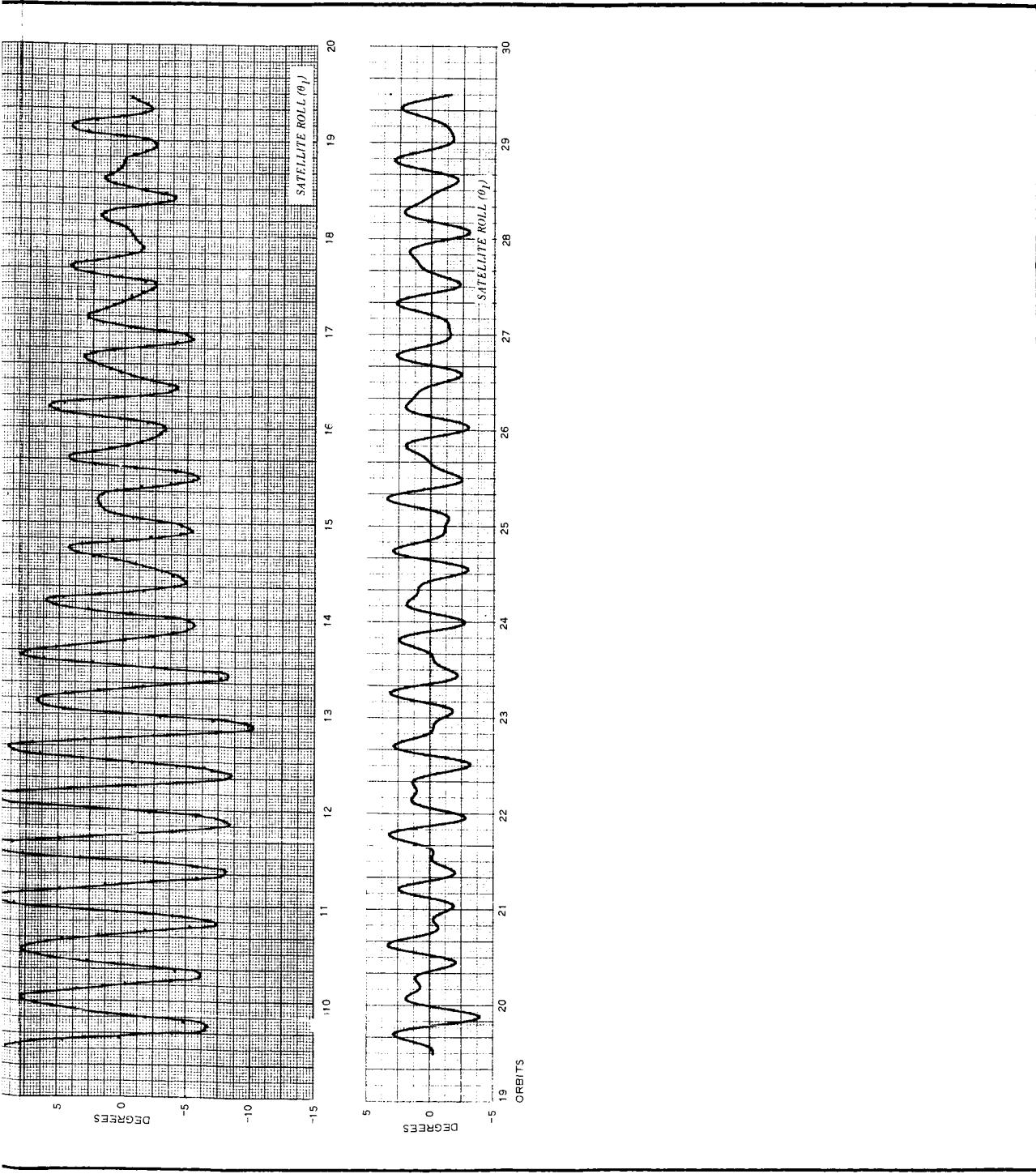
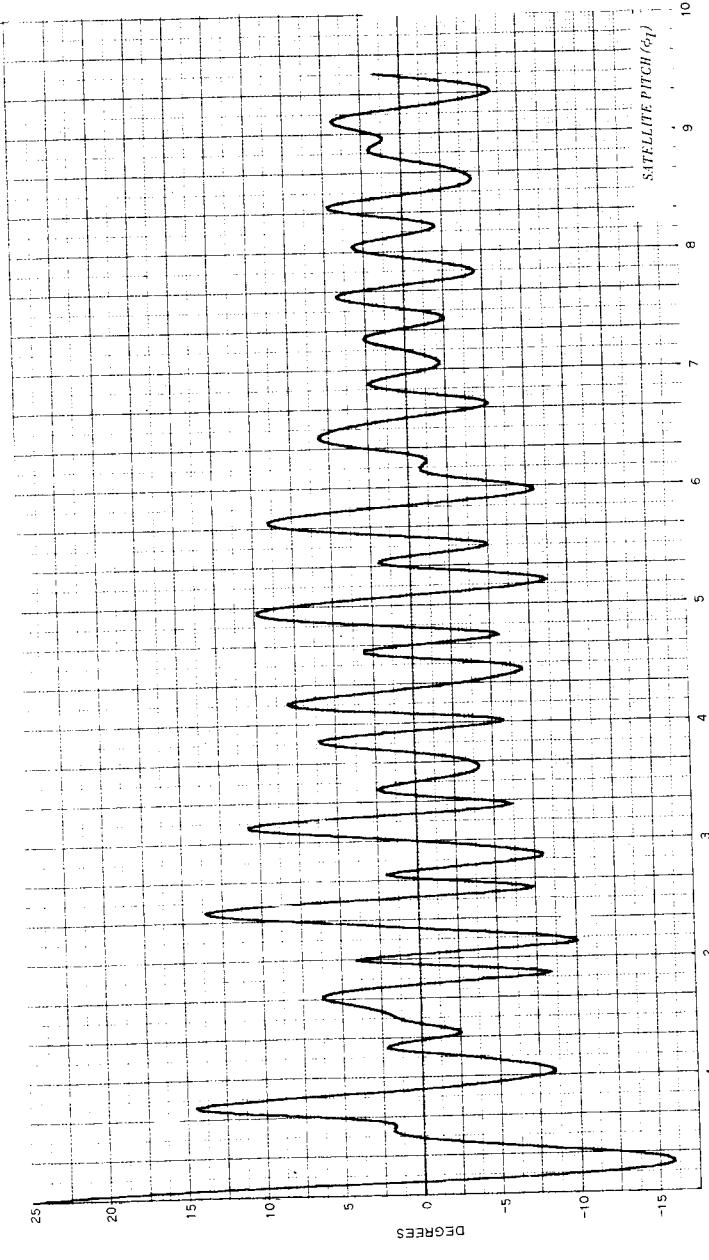


Figure D-4 - Optimum Configuration, Pitch and Roll Transient Response
(Sheet 2 of 9)



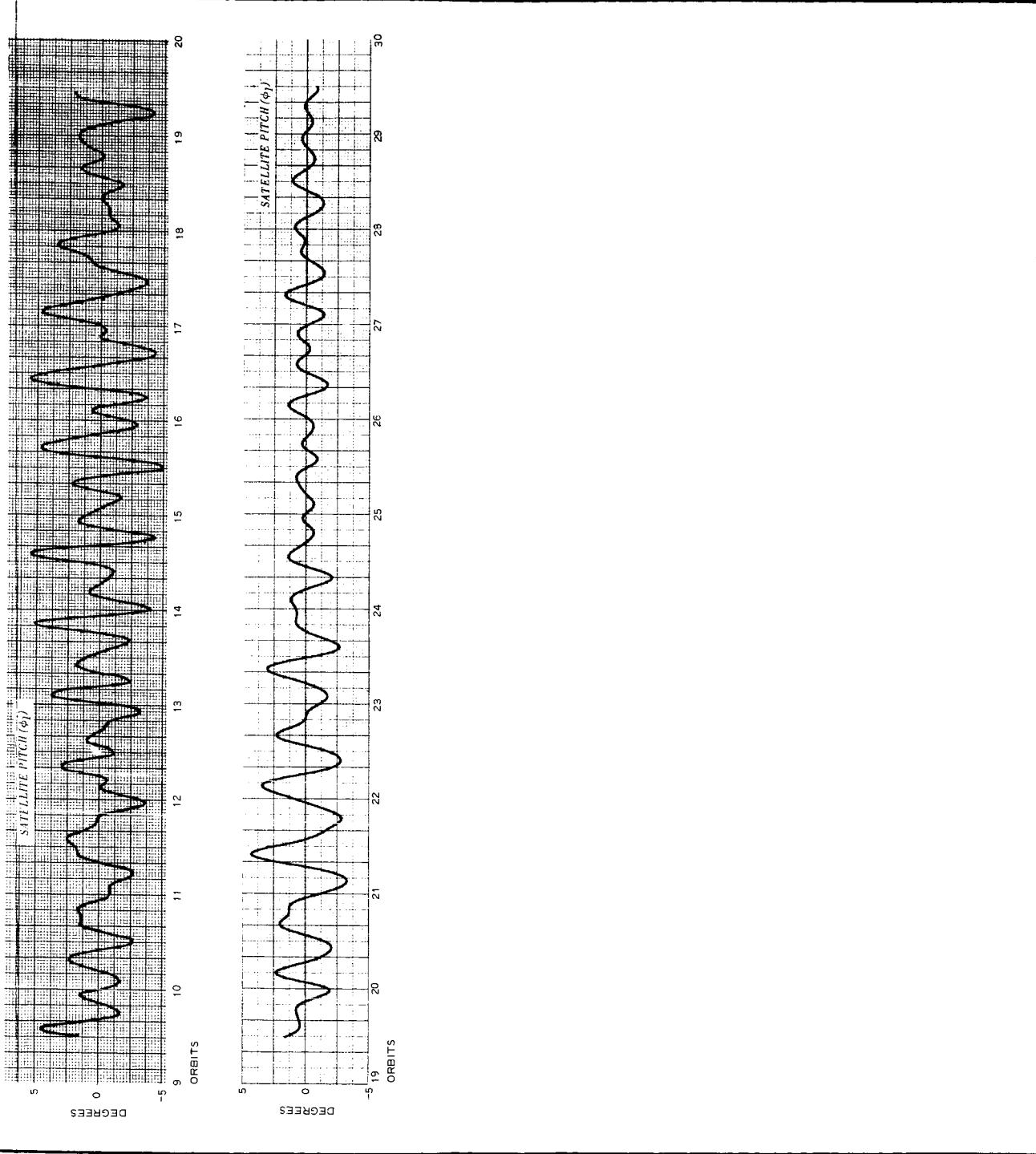
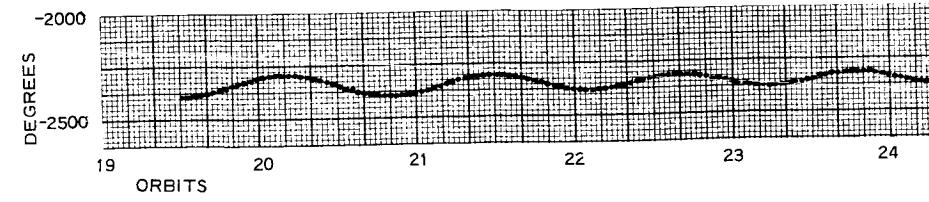
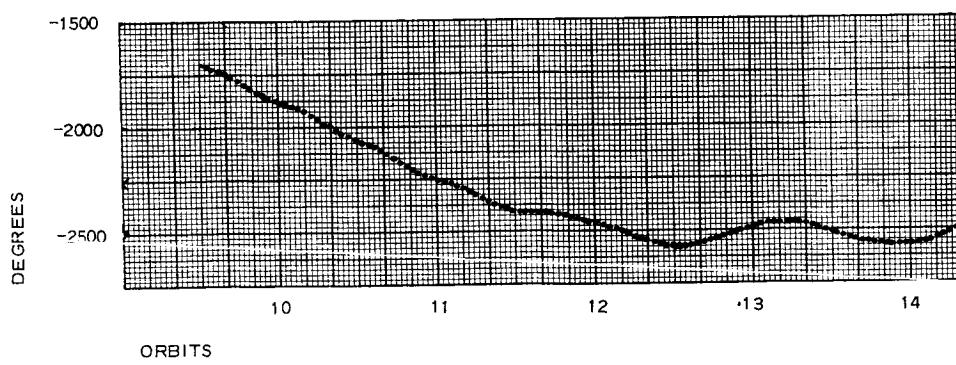
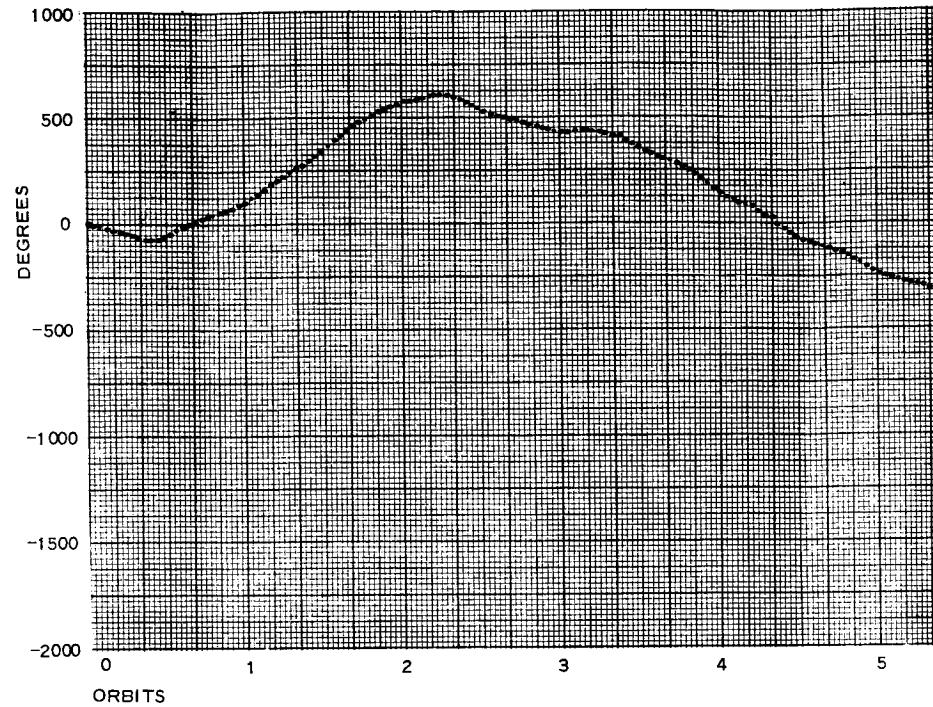


Figure D-4 - Optimum Configuration, Pitch and Roll Transient Response
(Sheet 3 of 9)



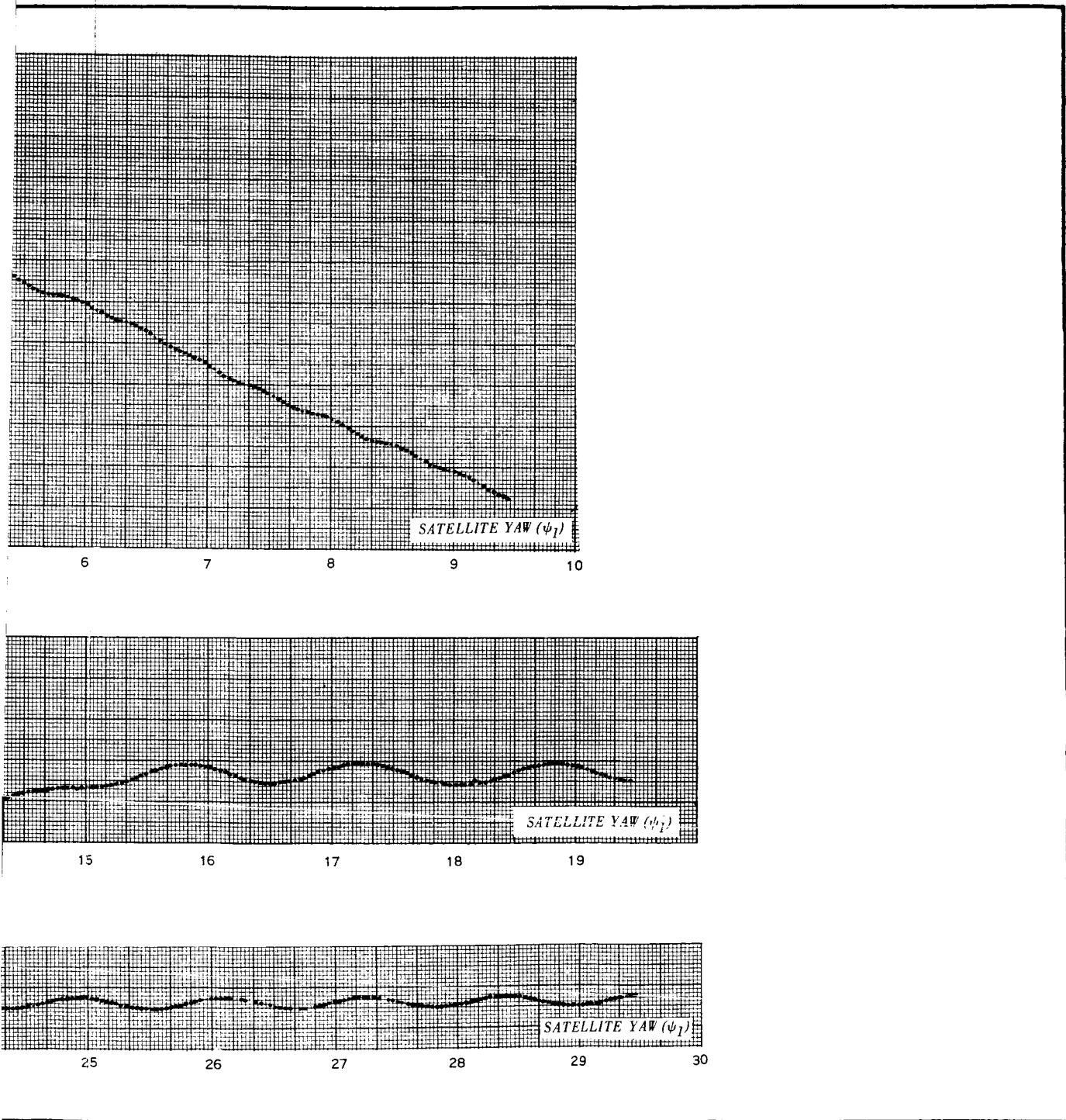
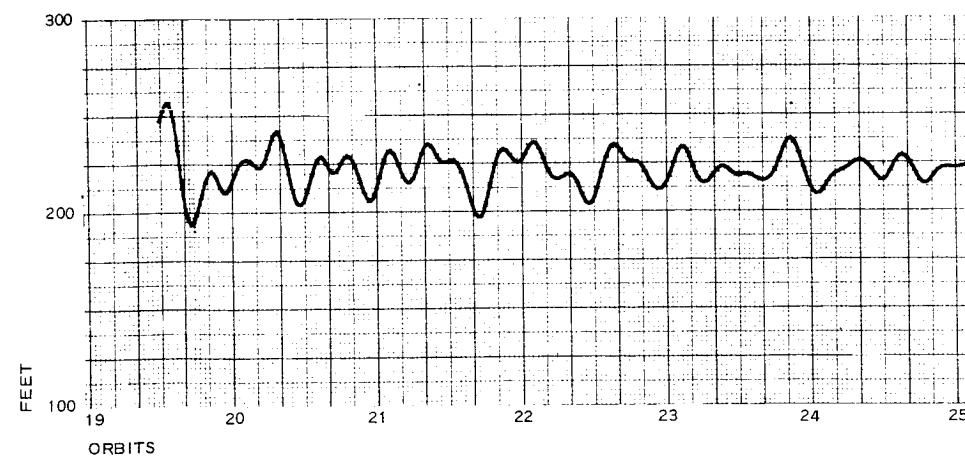
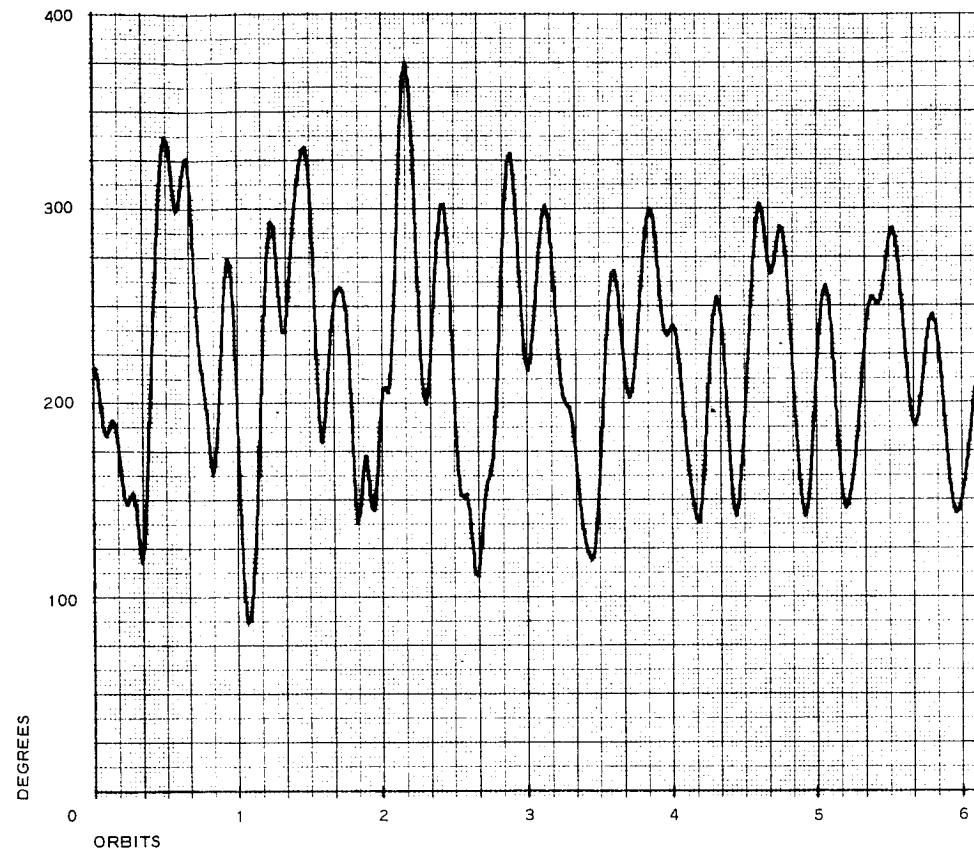


Figure D-4 - Optimum Configuration, Pitch and Roll Transient Response
(Sheet 4 of 9)





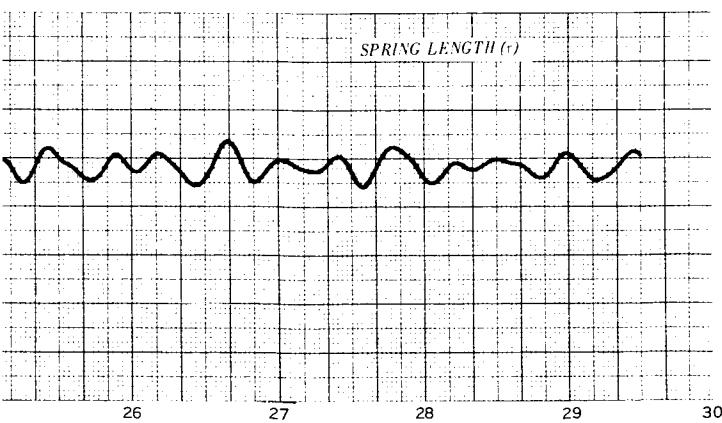
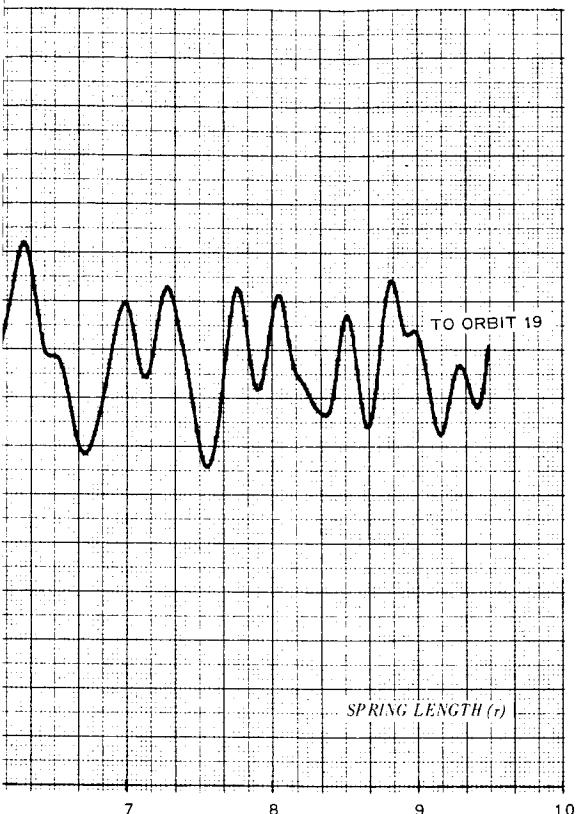
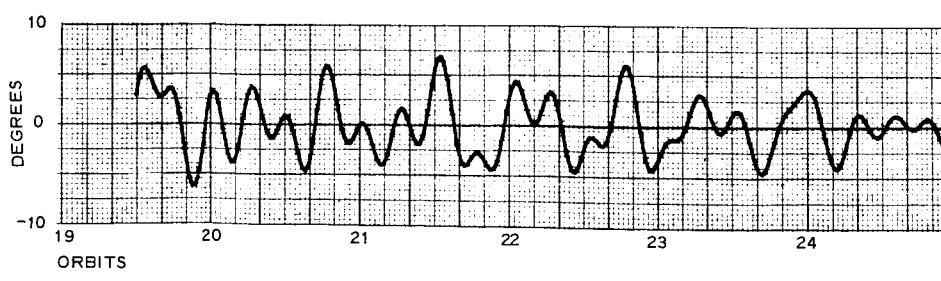
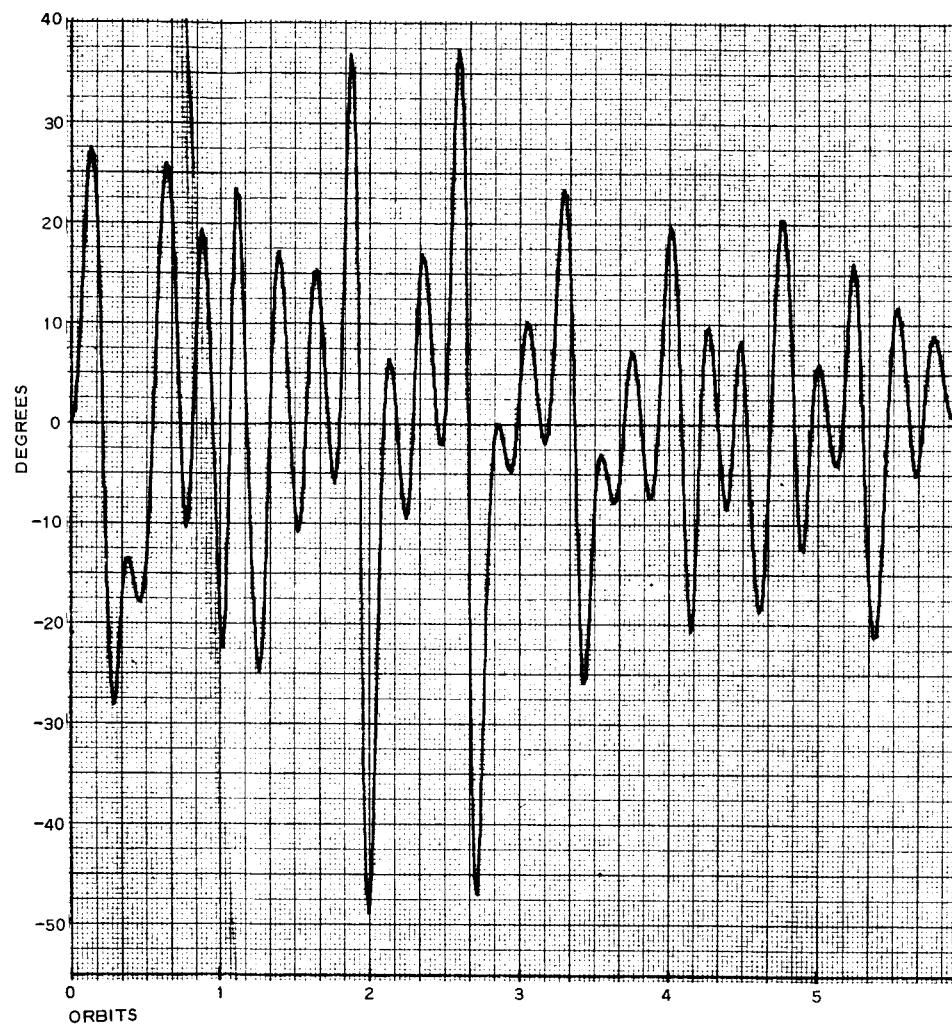


Figure D-4 - Optimum Configuration, Pitch and Roll Transient Response
(Sheet 5 of 9)

2



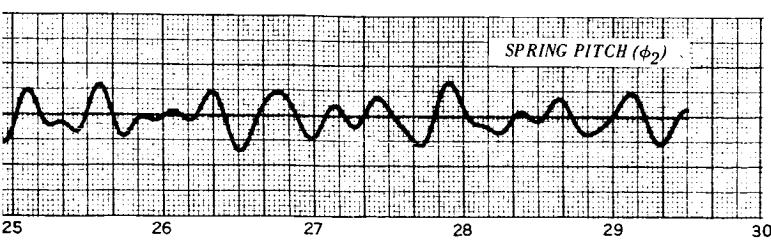
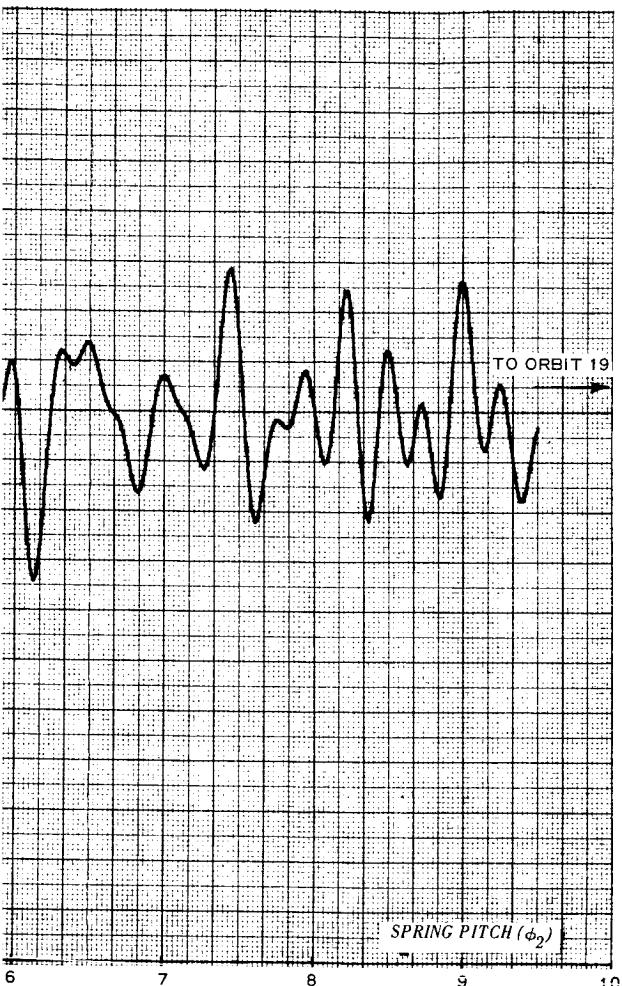
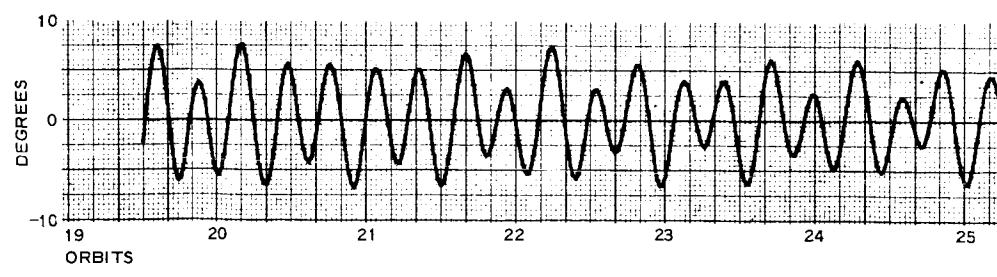
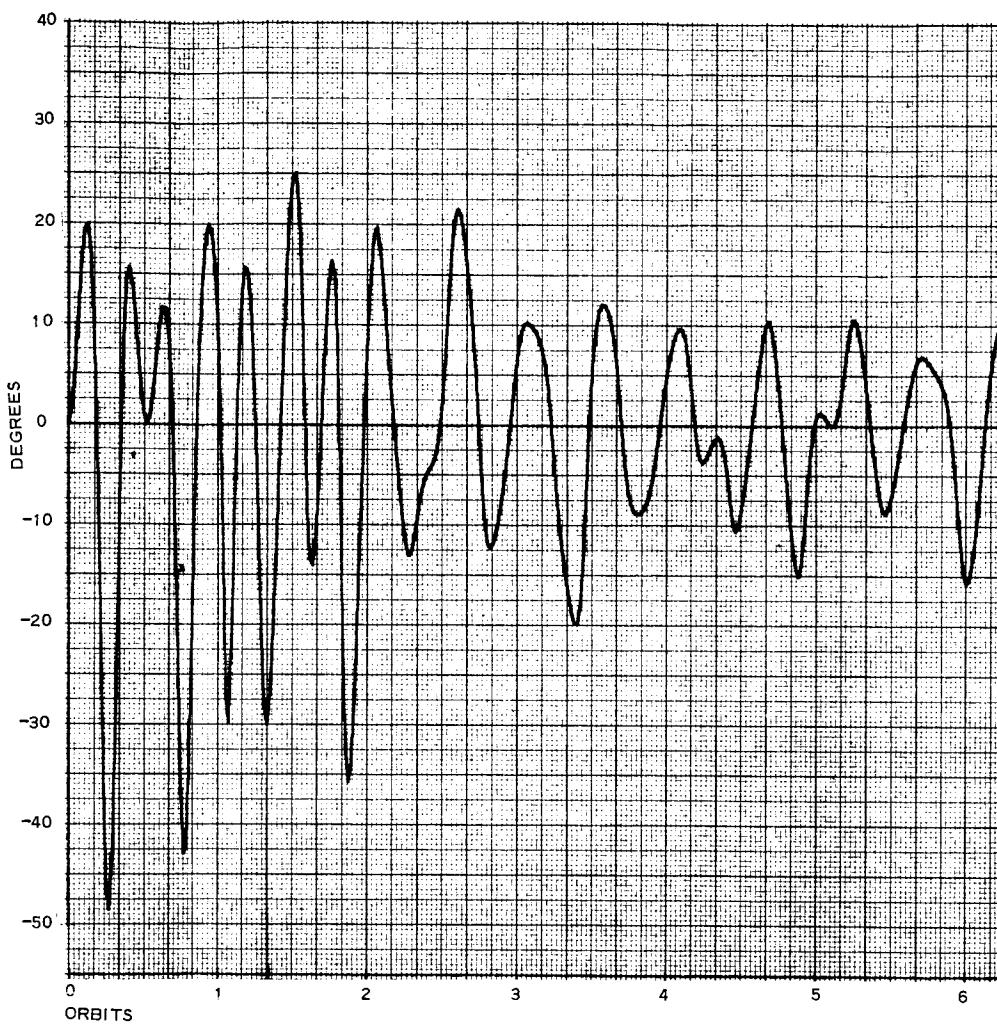


Figure D-4 - Optimum Configuration, Pitch and Roll Transient Response
(Sheet 6 of 9)

2



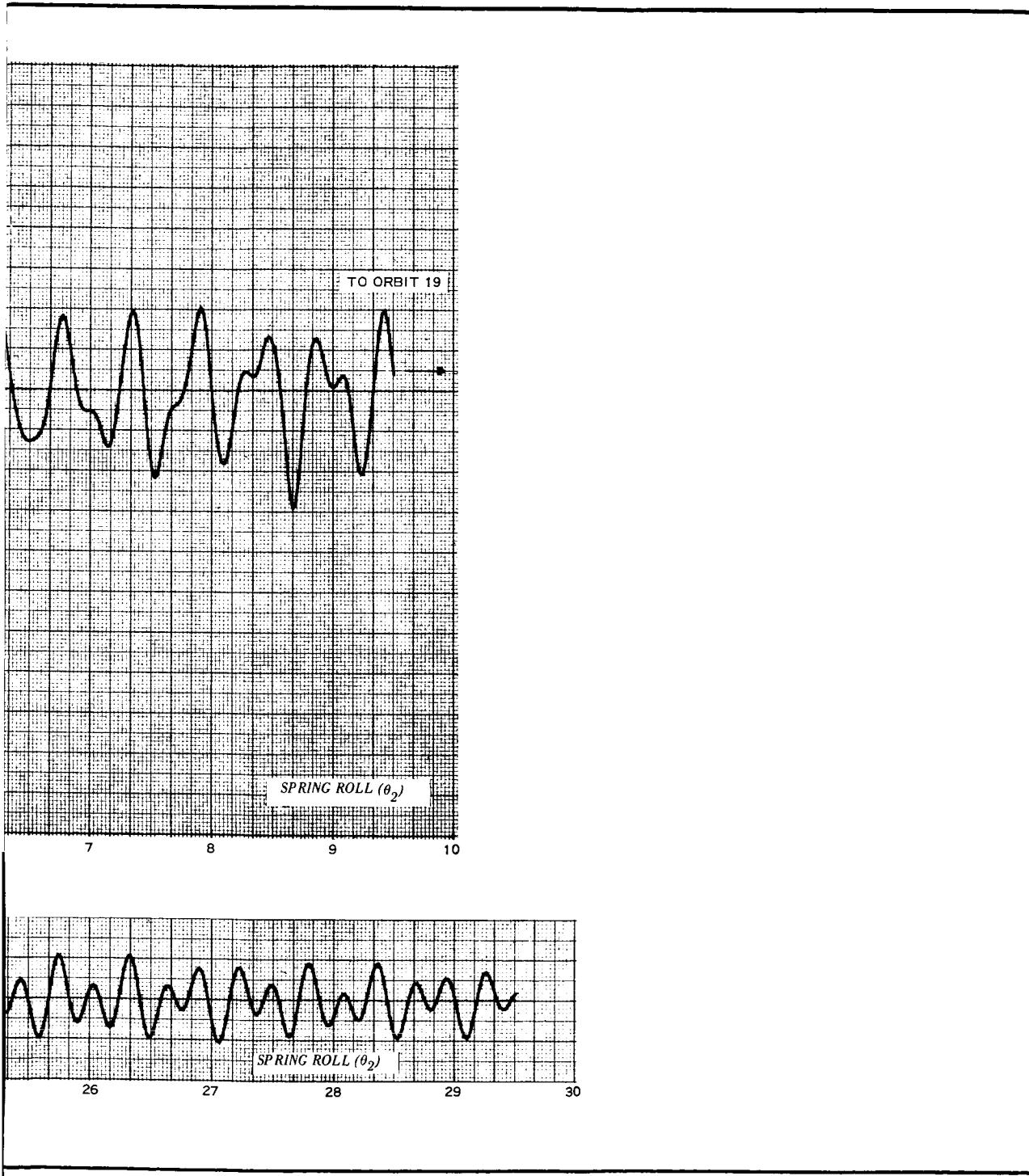
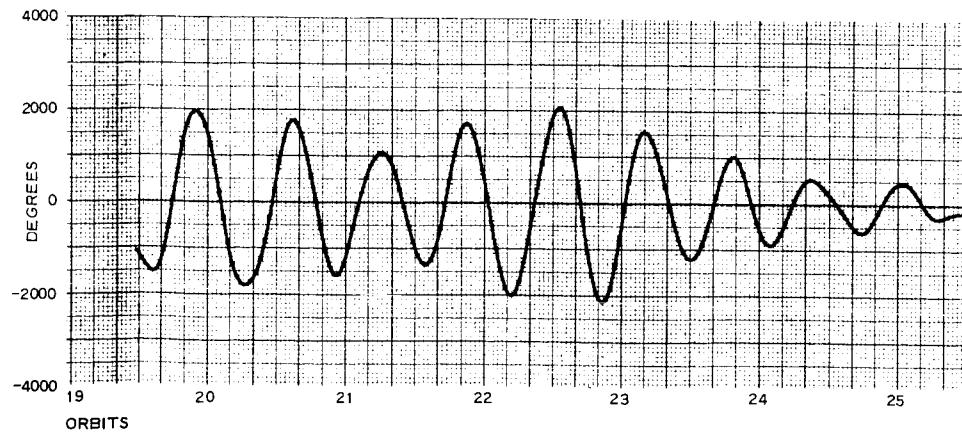
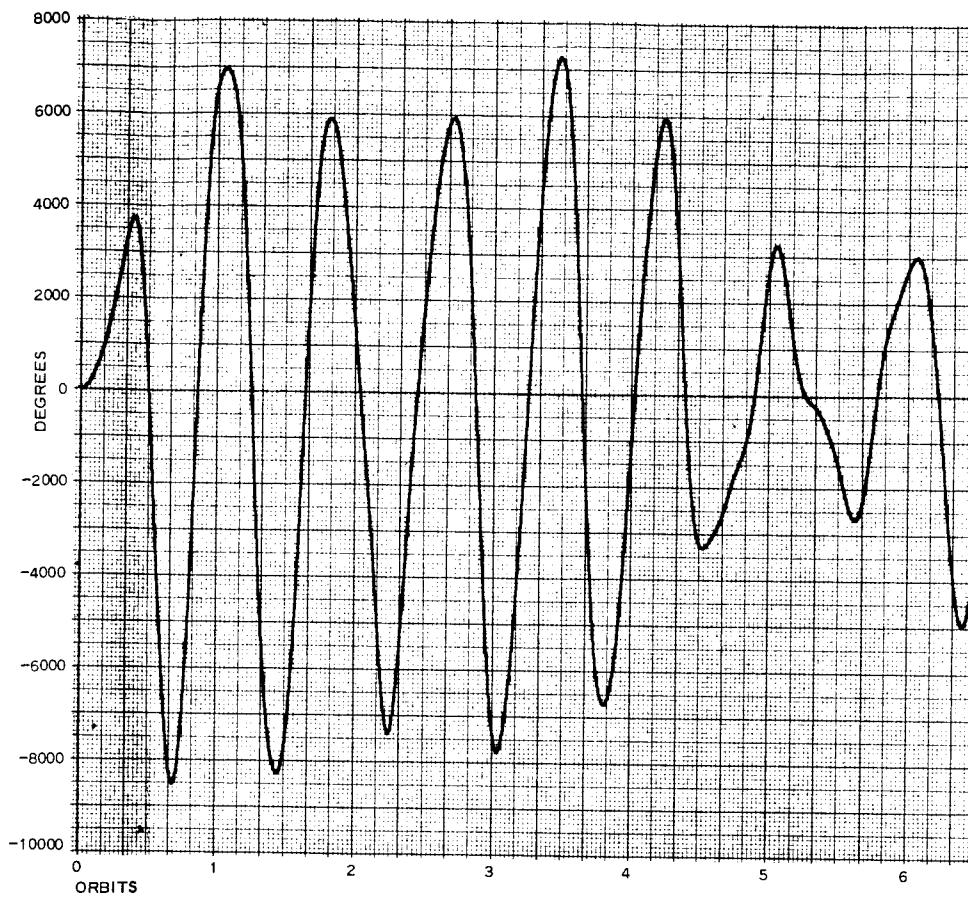


Figure D-4 - Optimum Configuration, Pitch and Roll Transient Response
(Sheet 7 of 9)

2



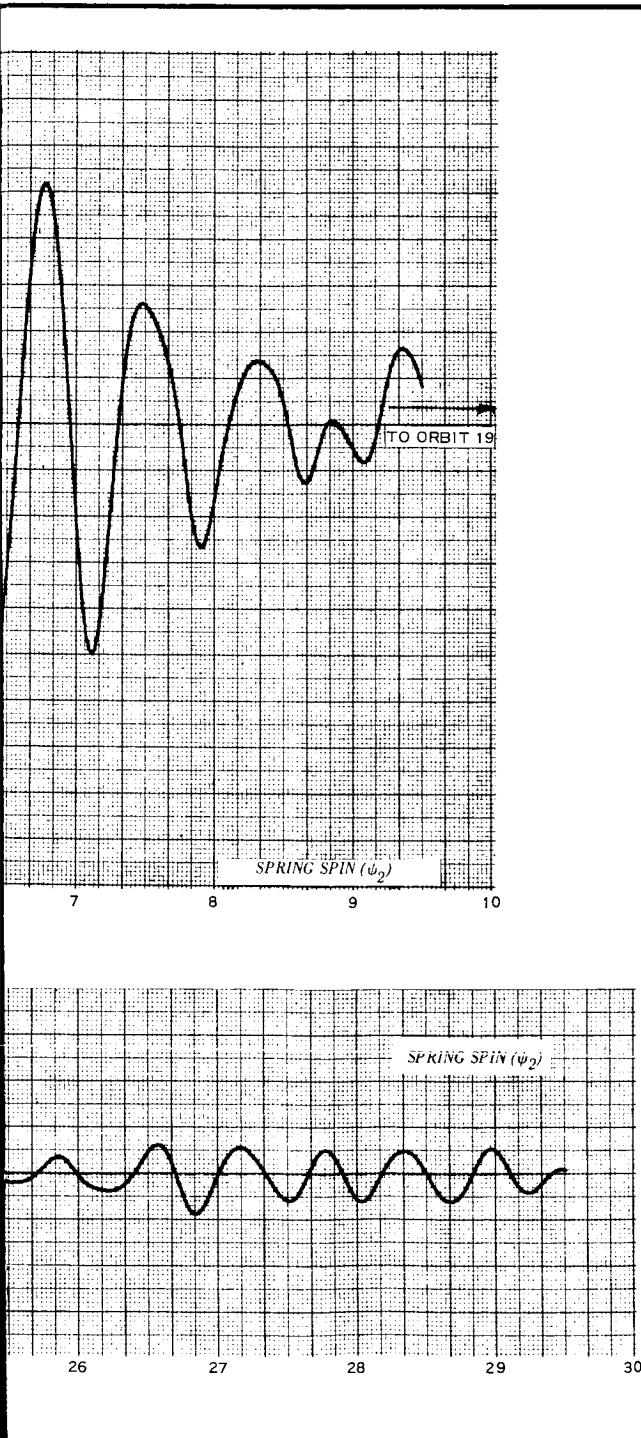
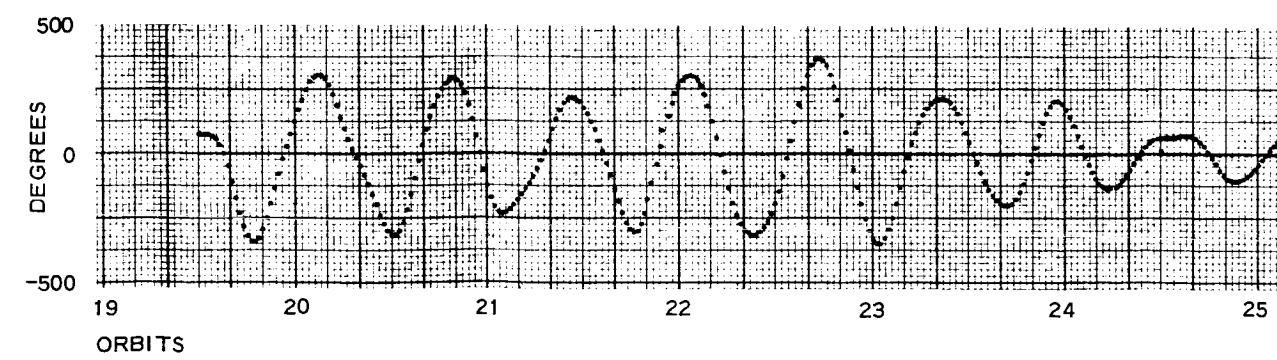
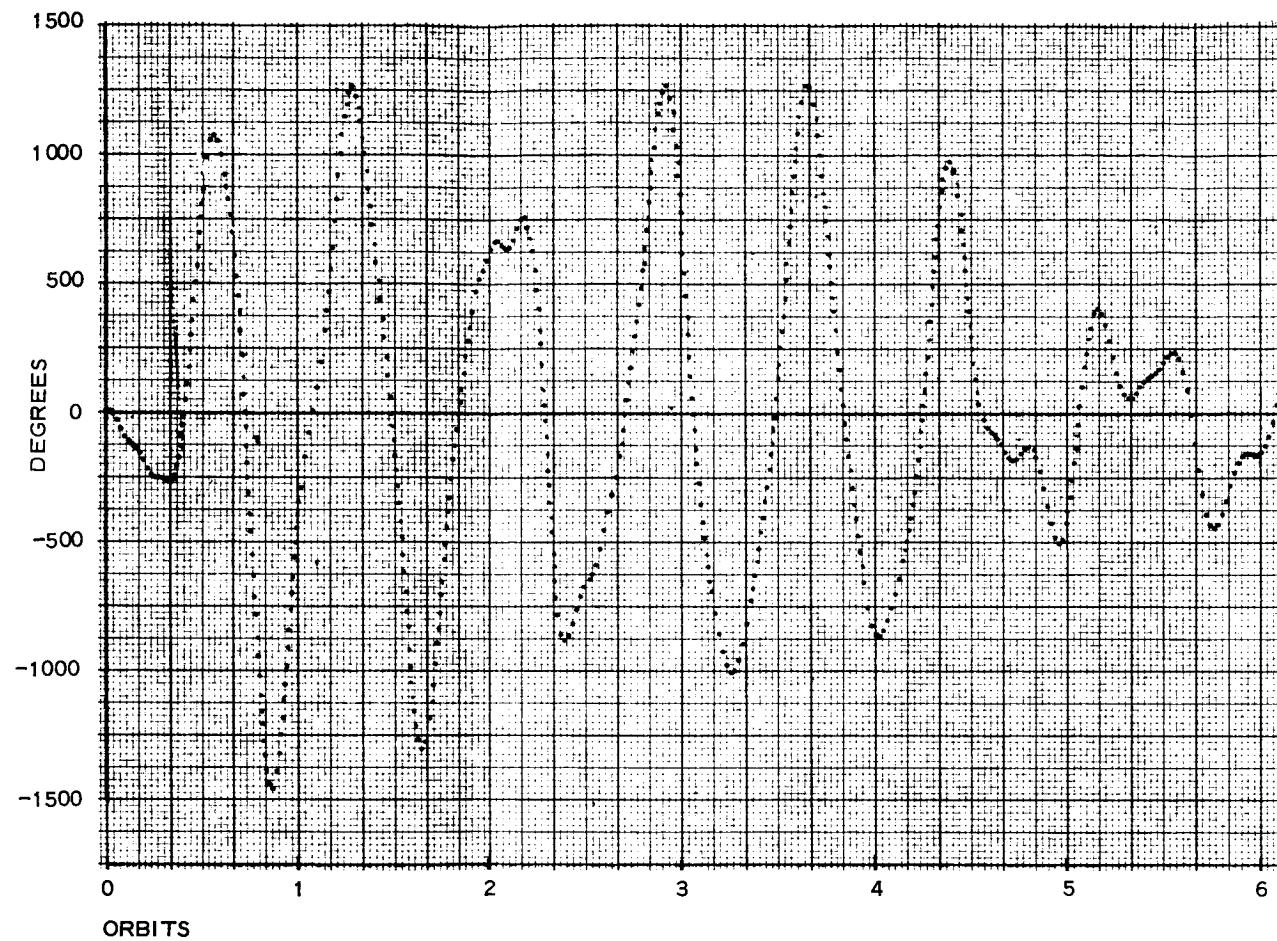


Figure D-4 - Optimum Configuration, Pitch and Roll Transient Response
(Sheet 8 of 9)

2



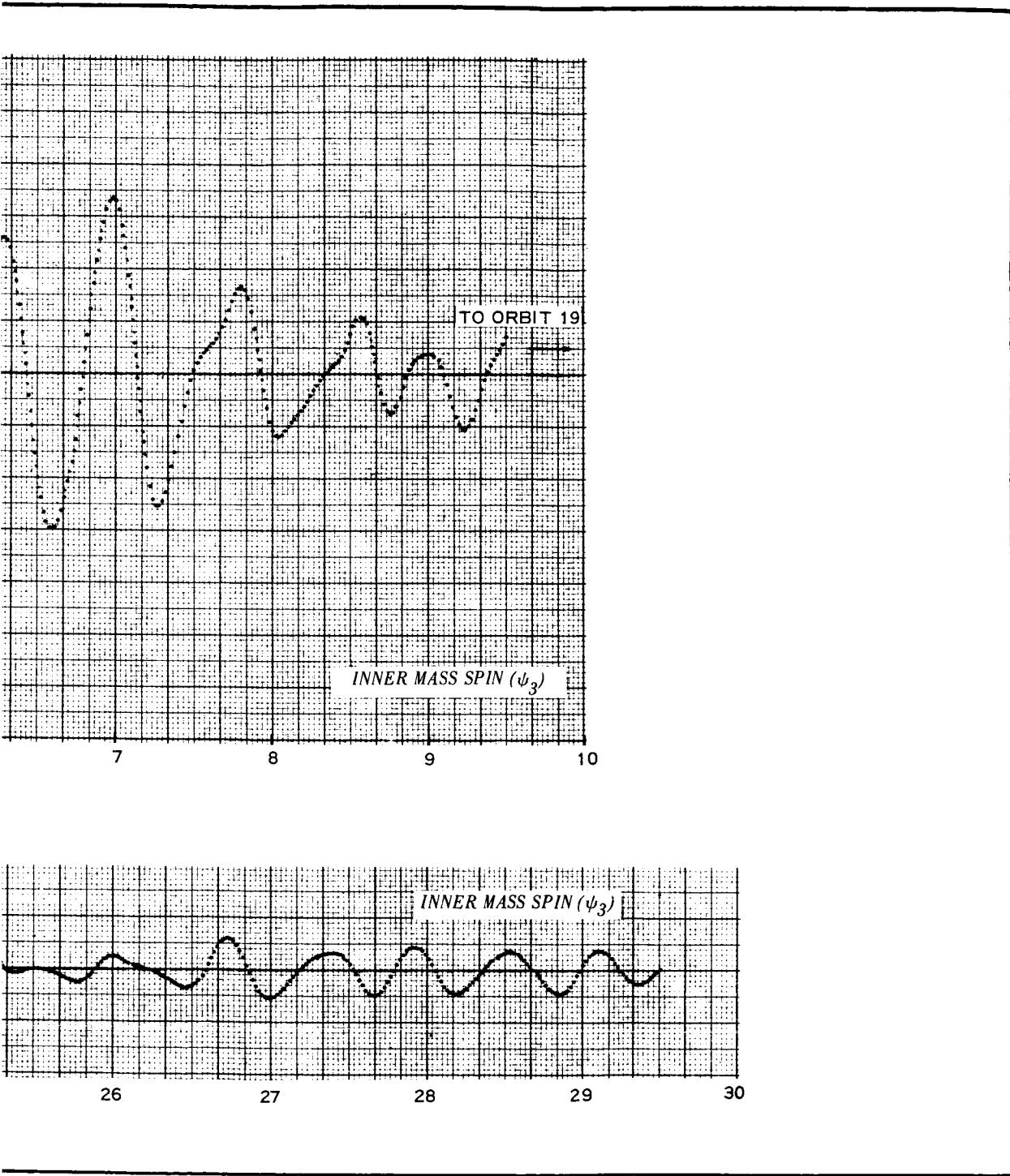
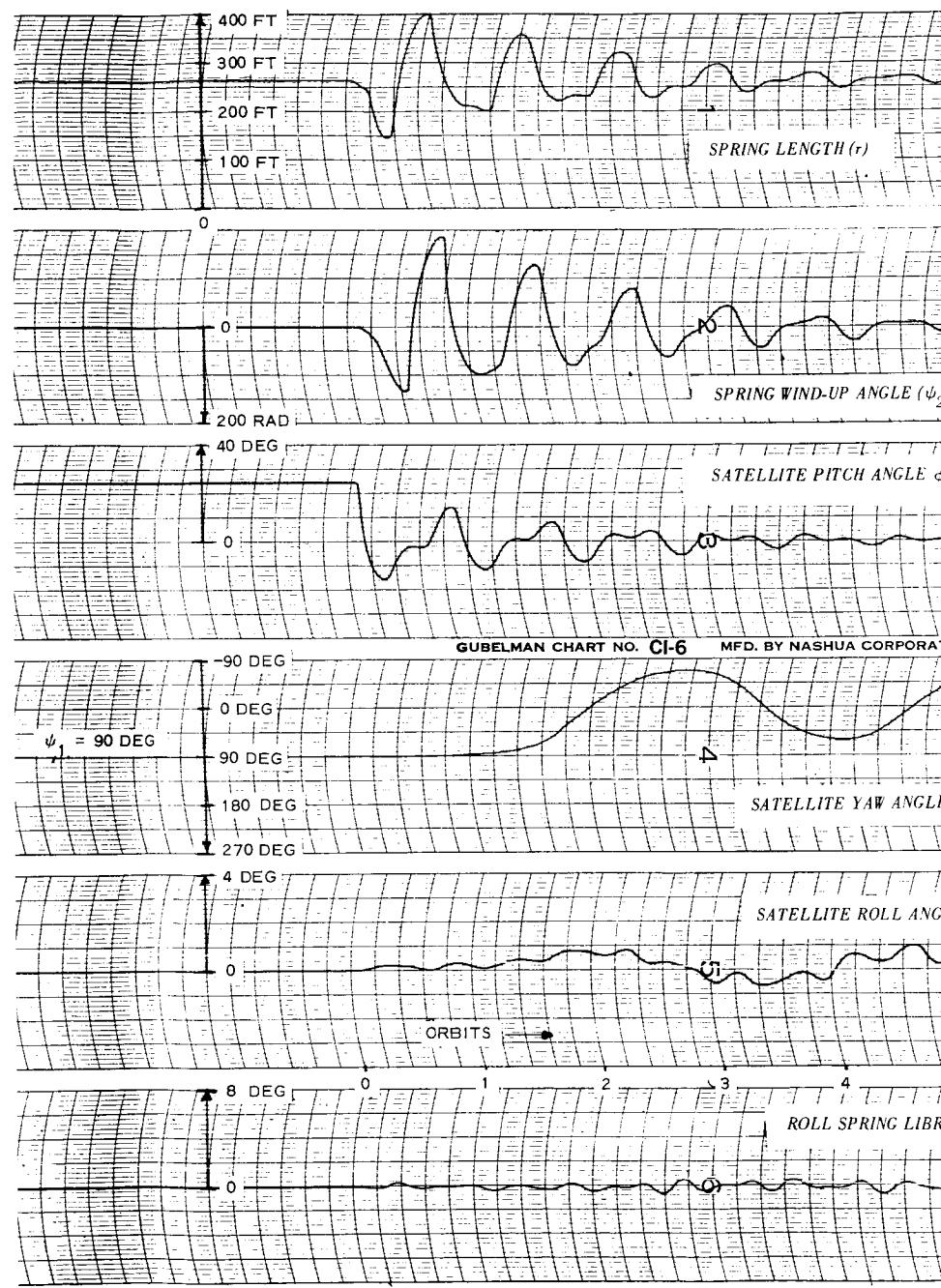


Figure D-4 - Optimum Configuration, Pitch and Roll Transient Response
(Sheet 9 of 9)

✓



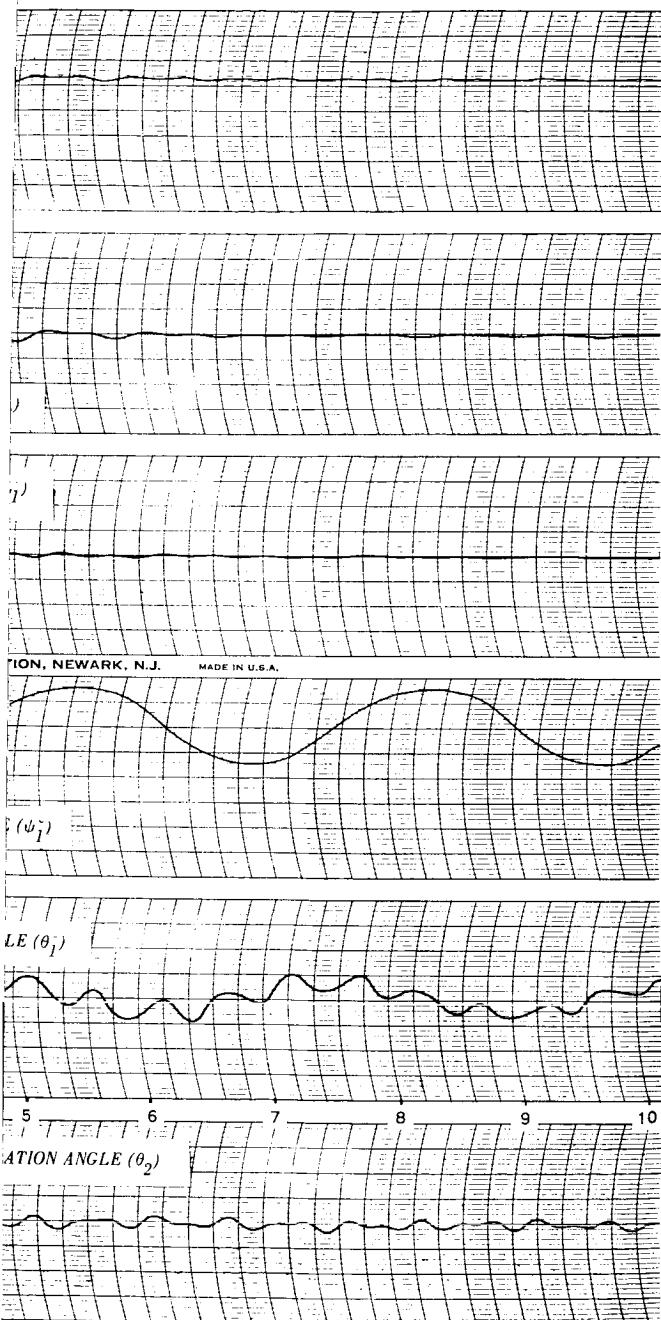


Figure D-5 - Analog-Digital Pitch Transient Response Comparison with Digital Run 103

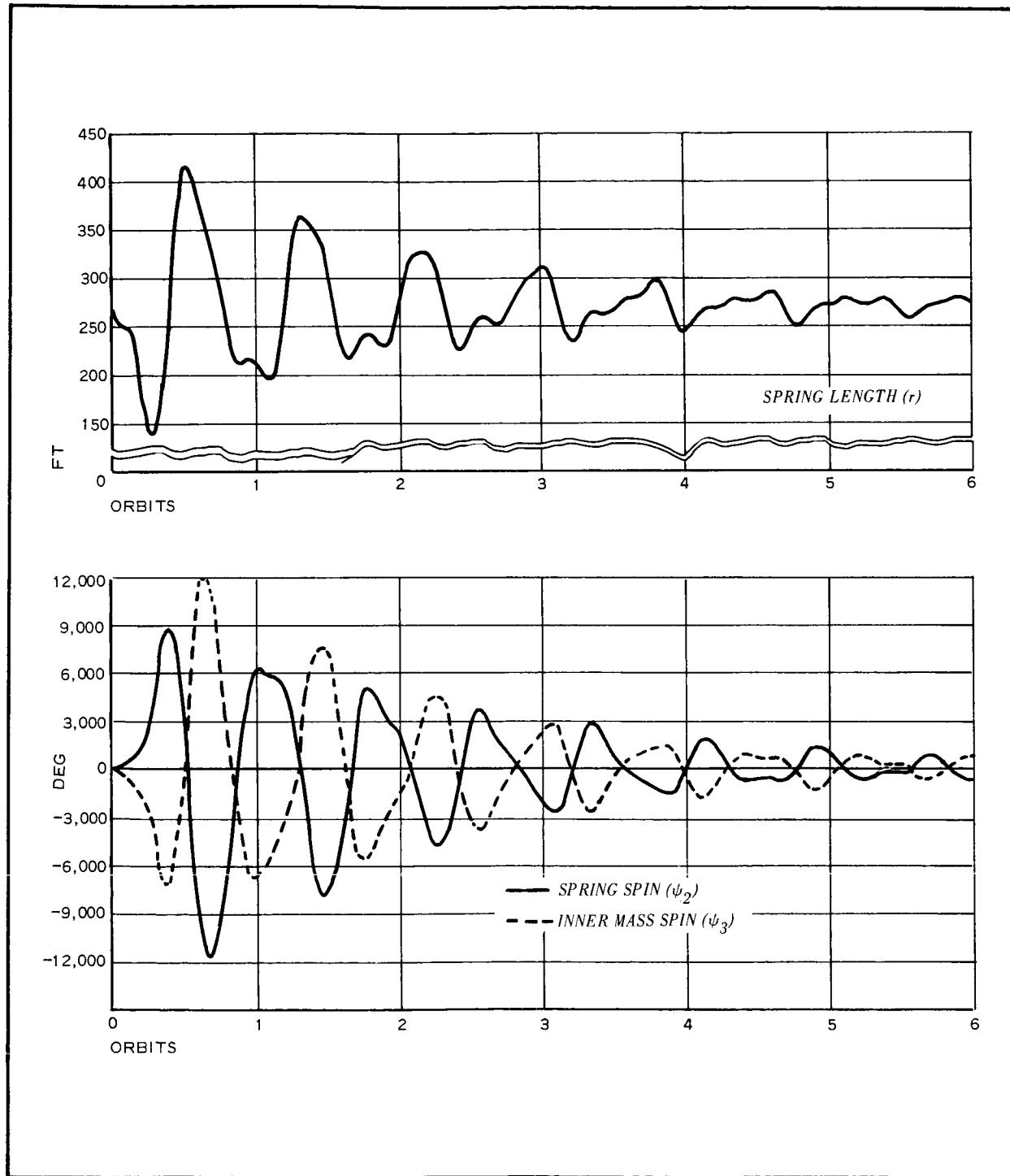


Figure D-6 - Digital-Analog Pitch Transient Response Comparison with Digital Run 103 (Sheet 4 of 4)

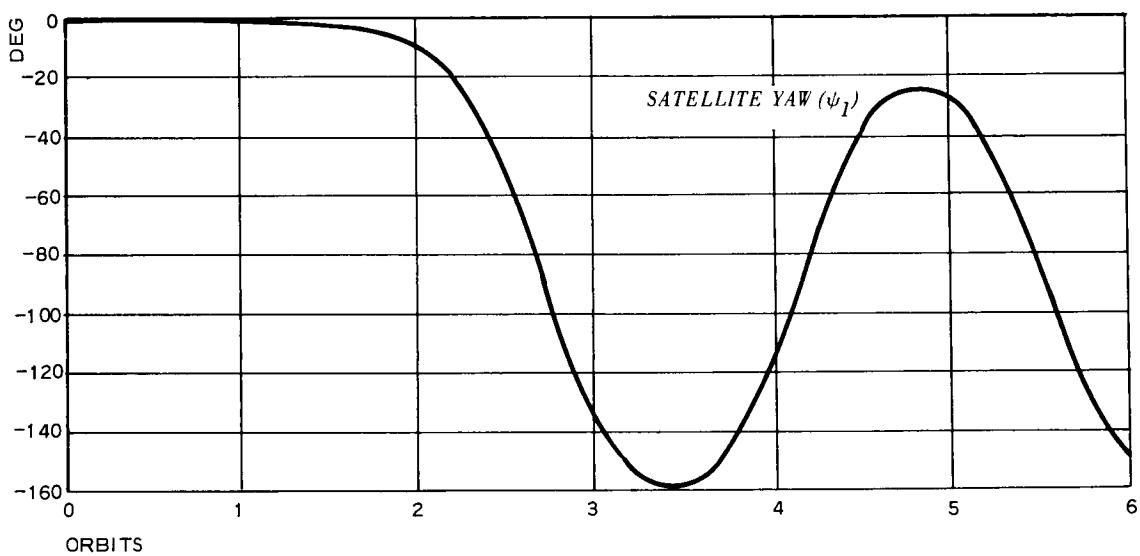


Figure D-6 - Digital-Analog Pitch Transient Response Comparison with
Digital Run 103 (Sheet 3 of 4)

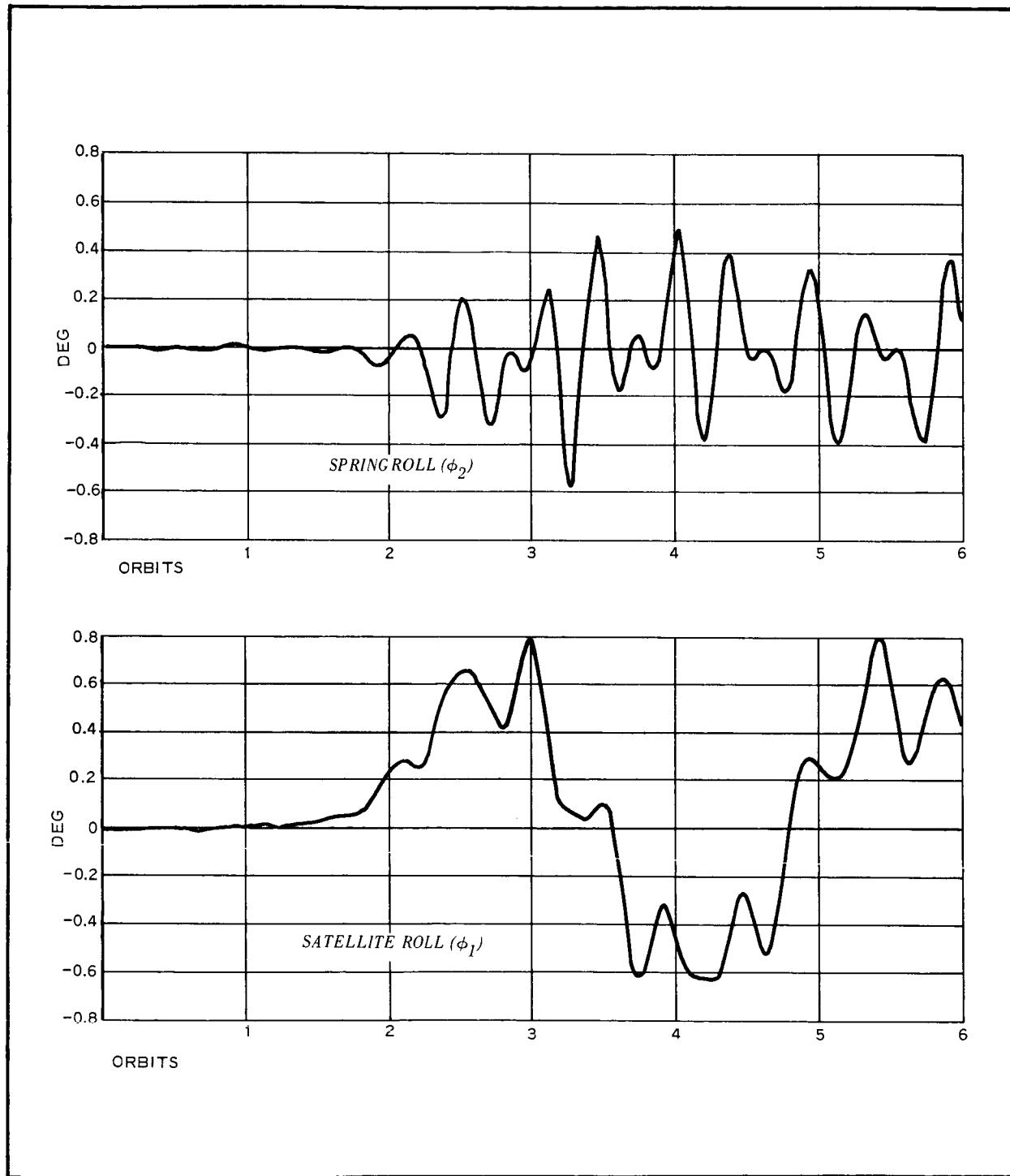


Figure D-6 - Digital-Analog Pitch Transient Response Comparison with
Digital Run 103 (Sheet 1 of 4)

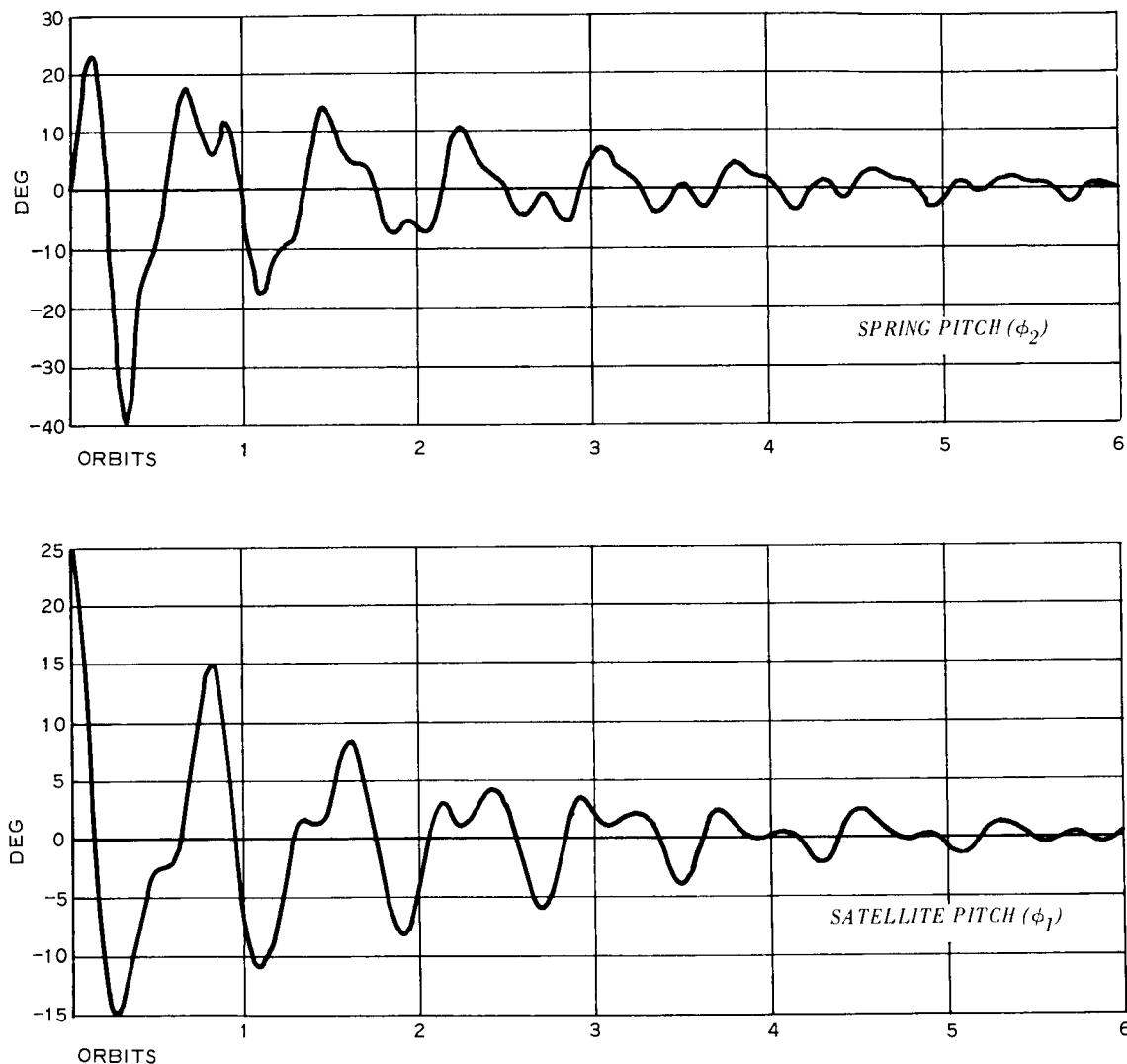
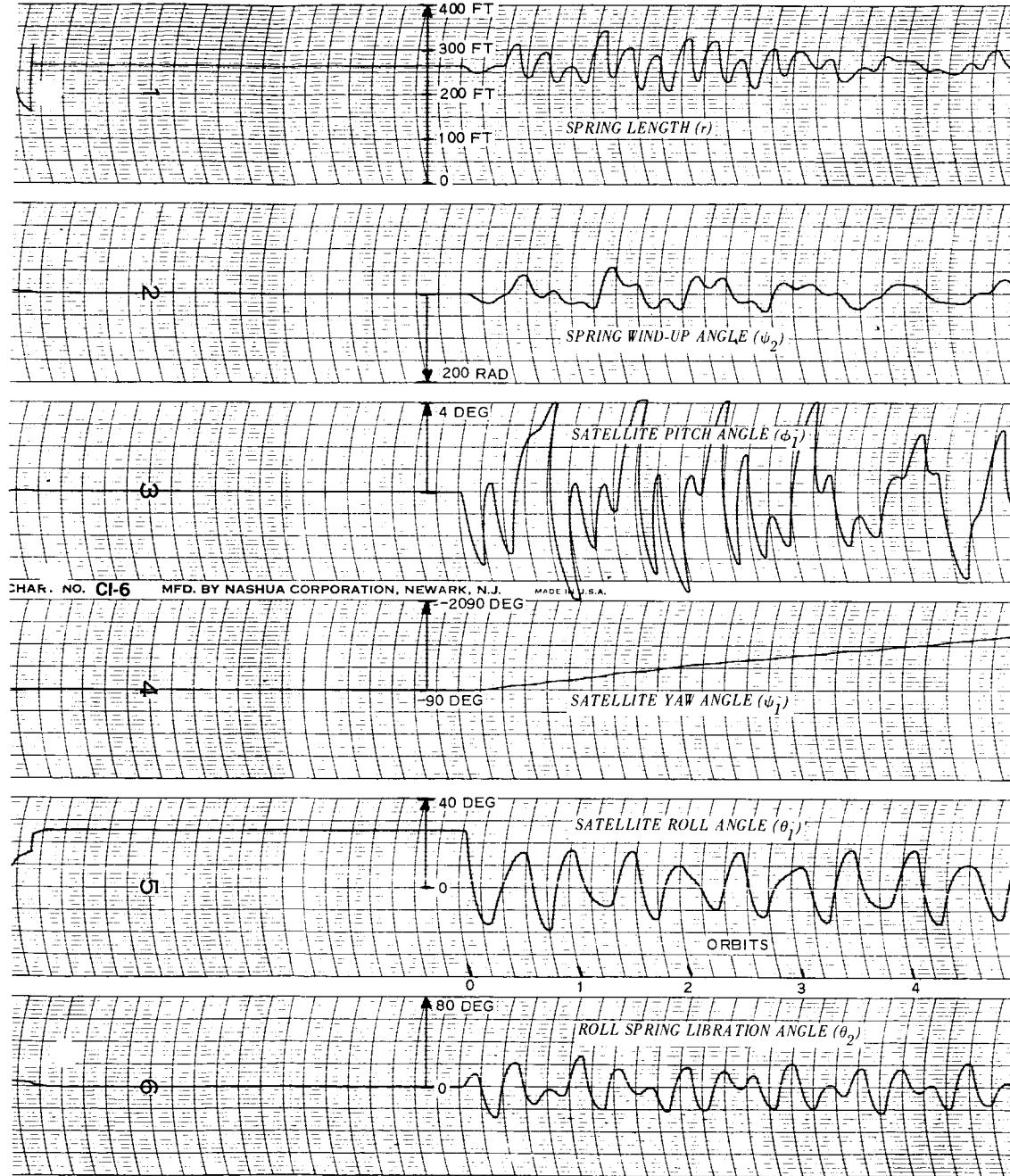


Figure D-6 - Digital-Analog Pitch Transient Response Comparison with Digital Run 103 (Sheet 2 of 4)



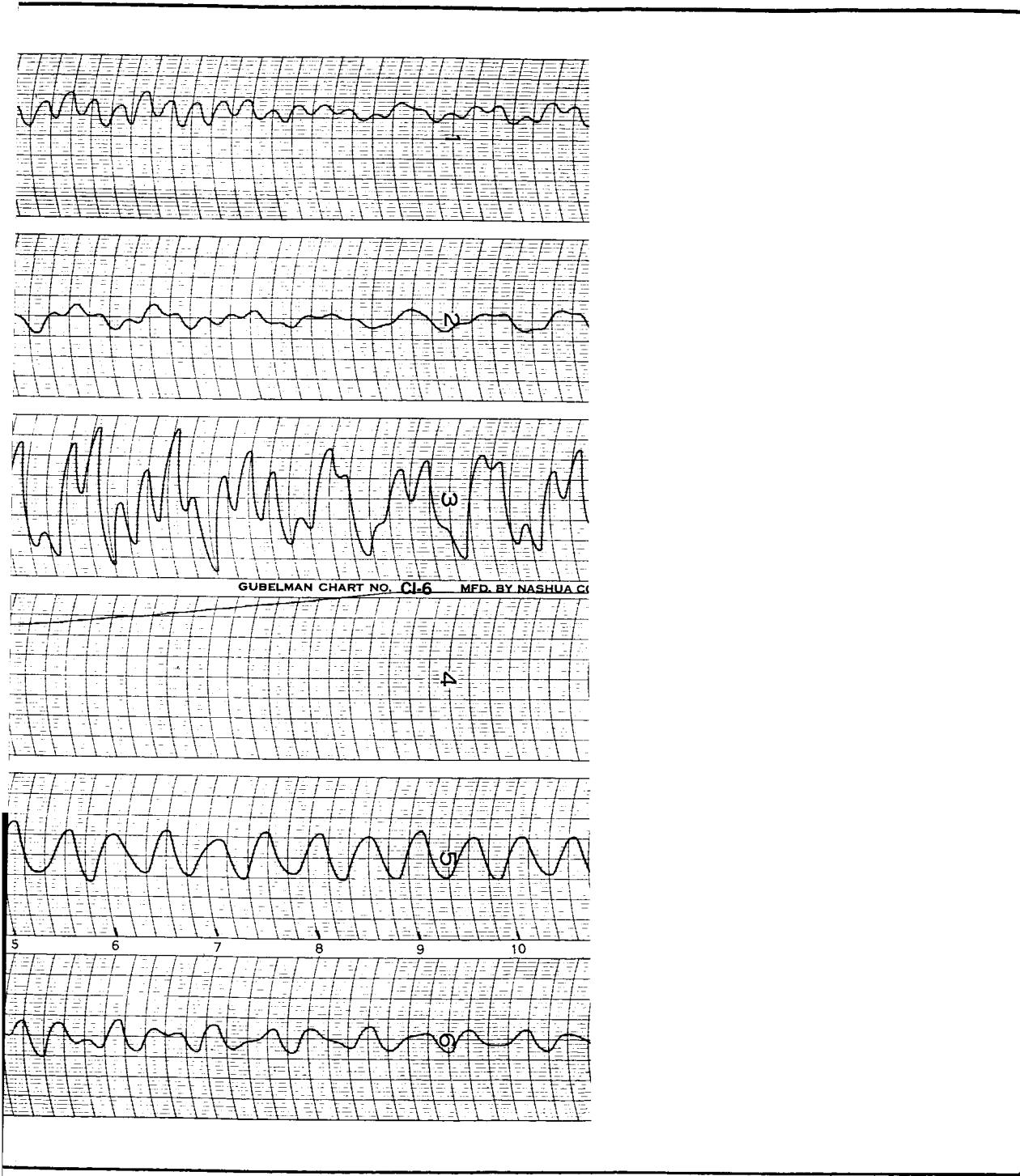
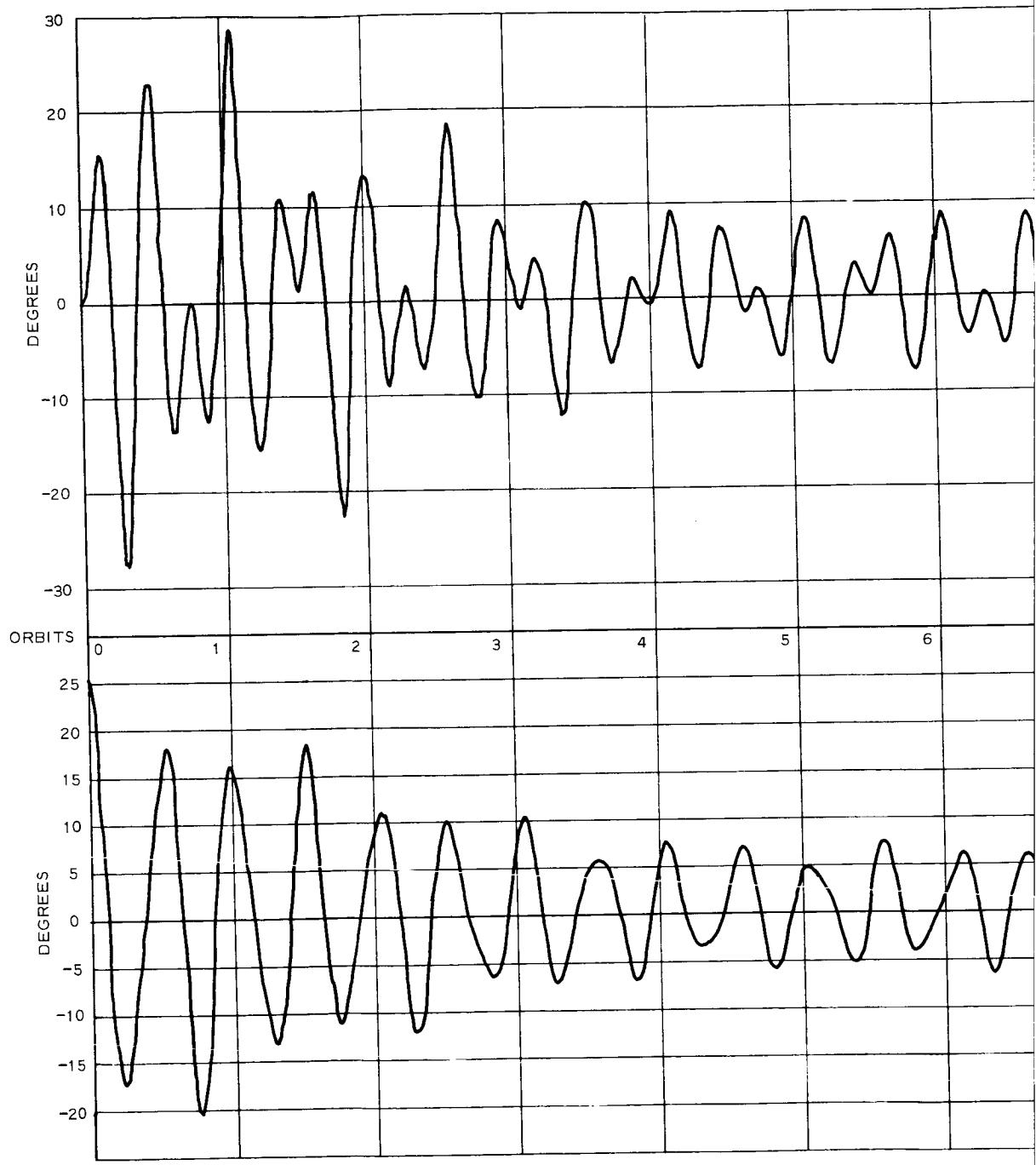


Figure D-7 - Analog-Digital Roll Transient Response Comparison with Digital Runs 115 and 118



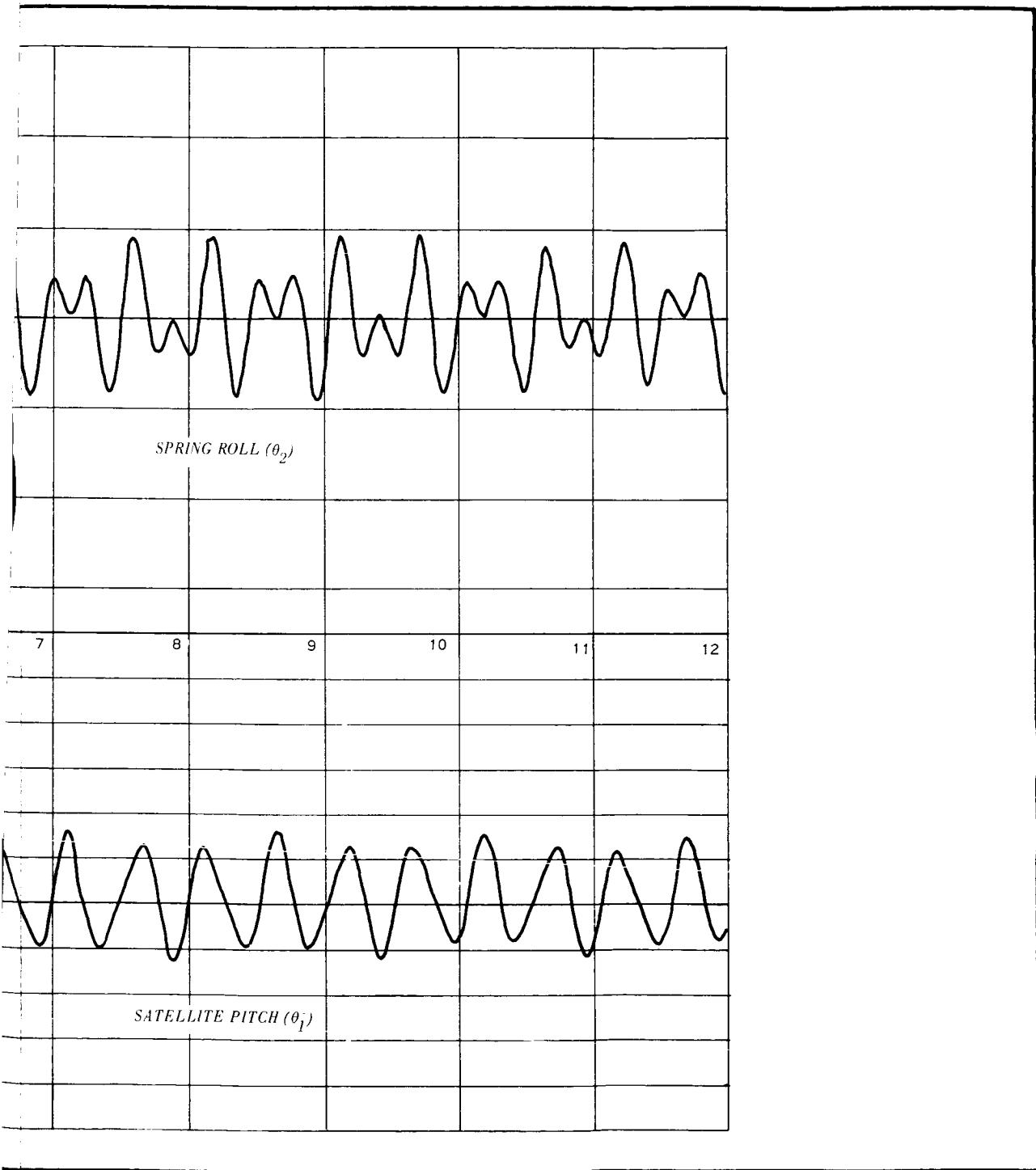
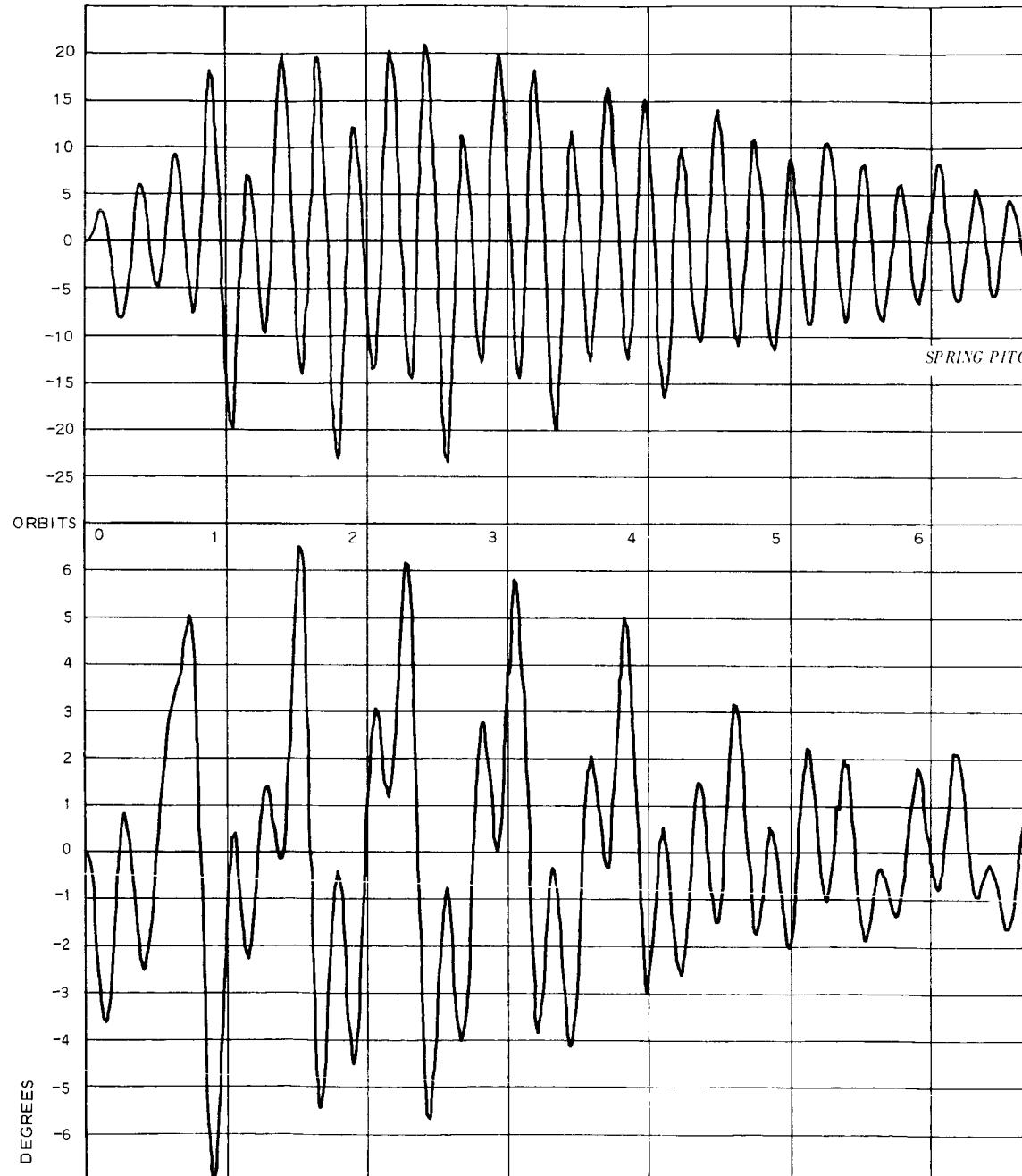


Figure D-8 - Digital-Analog Roll Transient Response Comparison with
Digital Runs 115 and 118 (Sheet 1 of 4)



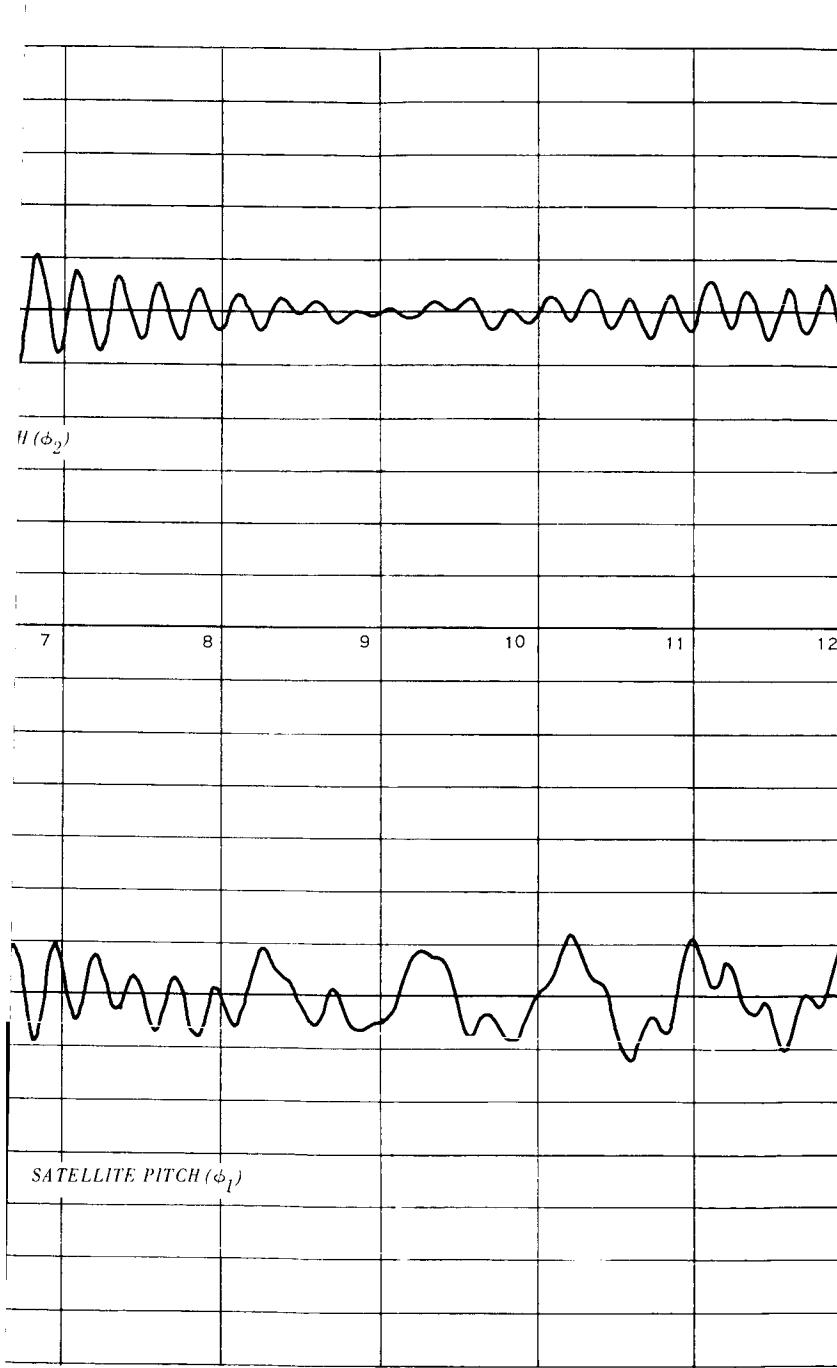
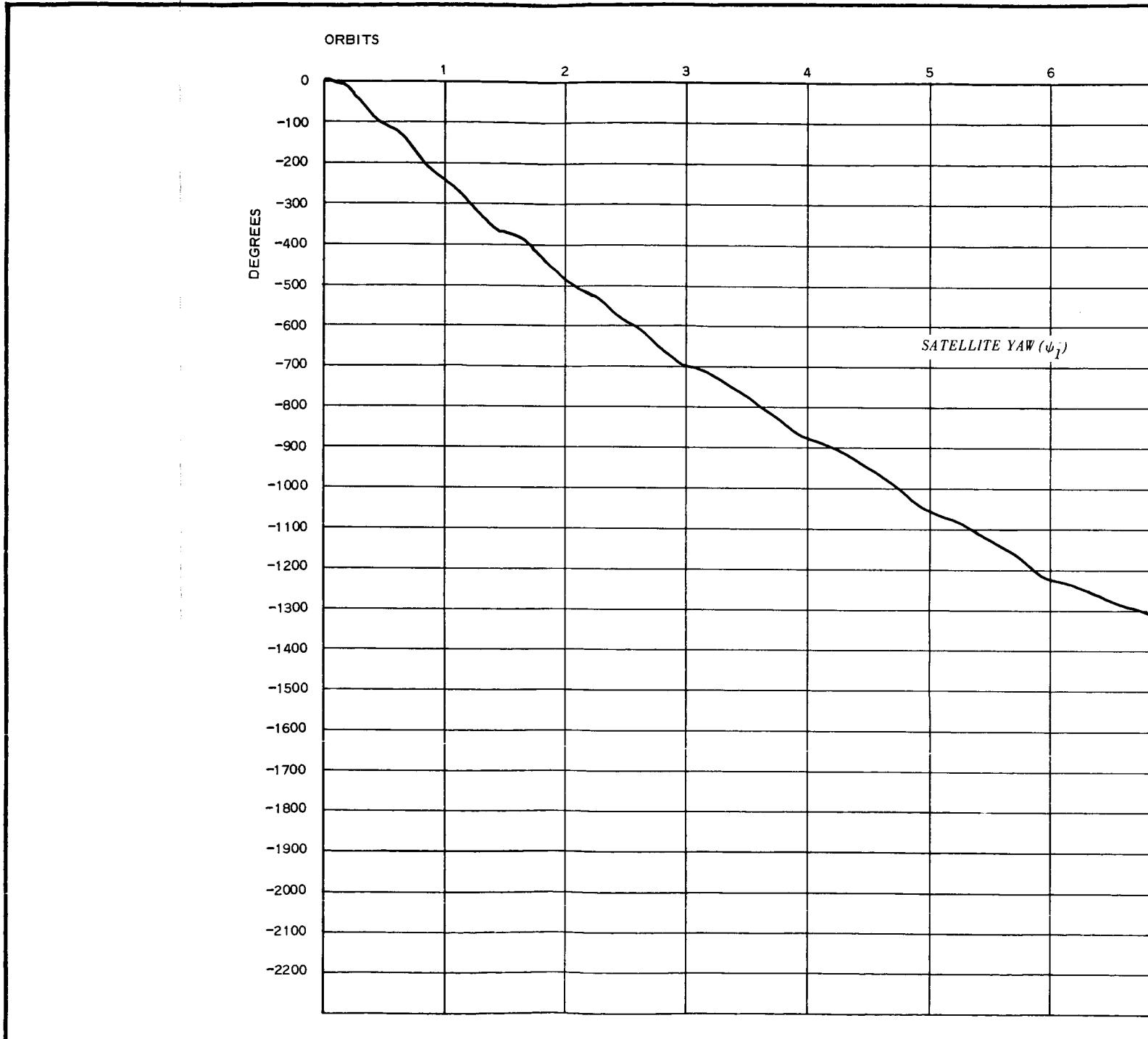


Figure D-8 - Digital-Analog Roll Transient Response Comparison with
Digital Runs 115 and 118 (Sheet 2 of 4)



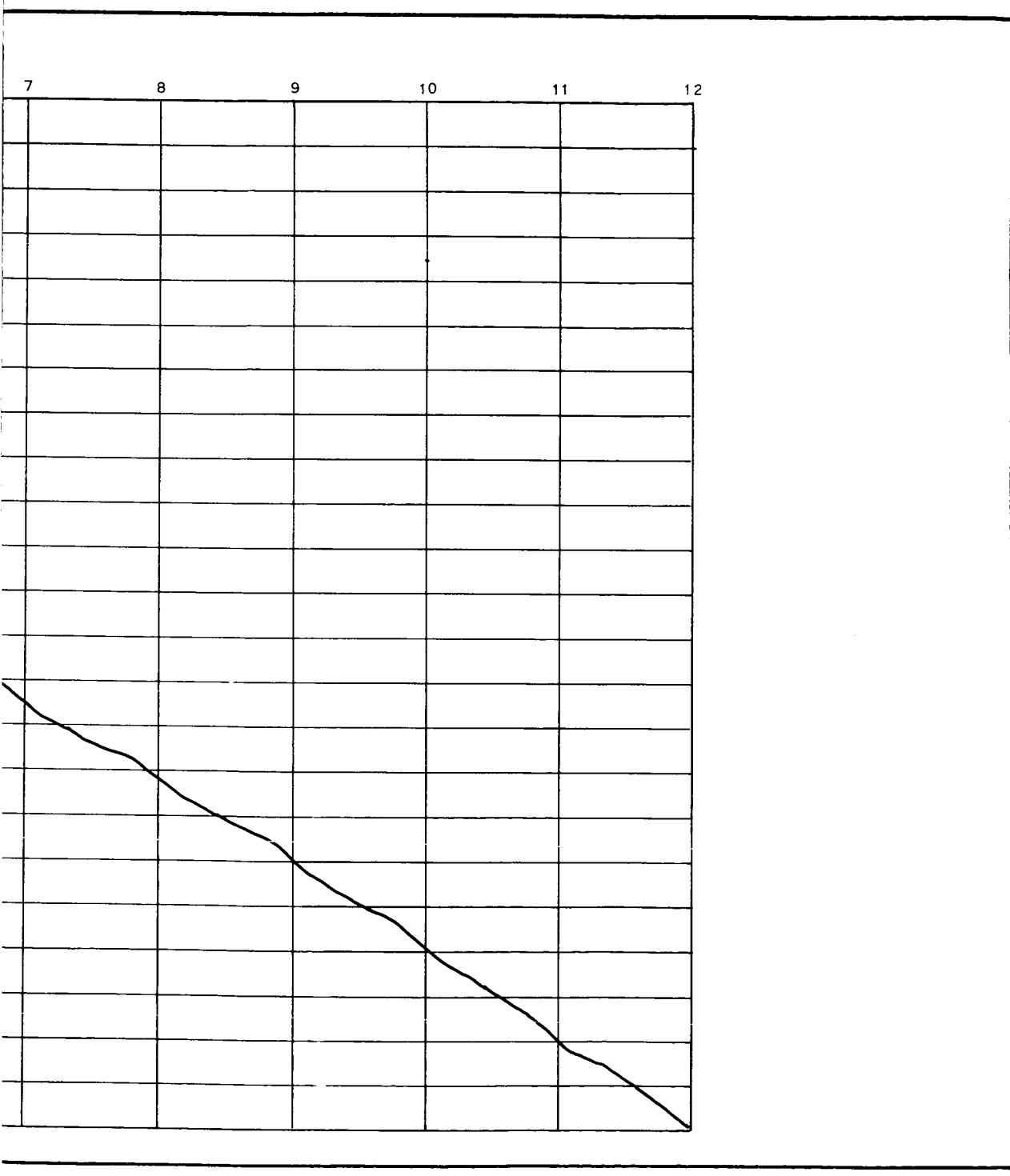
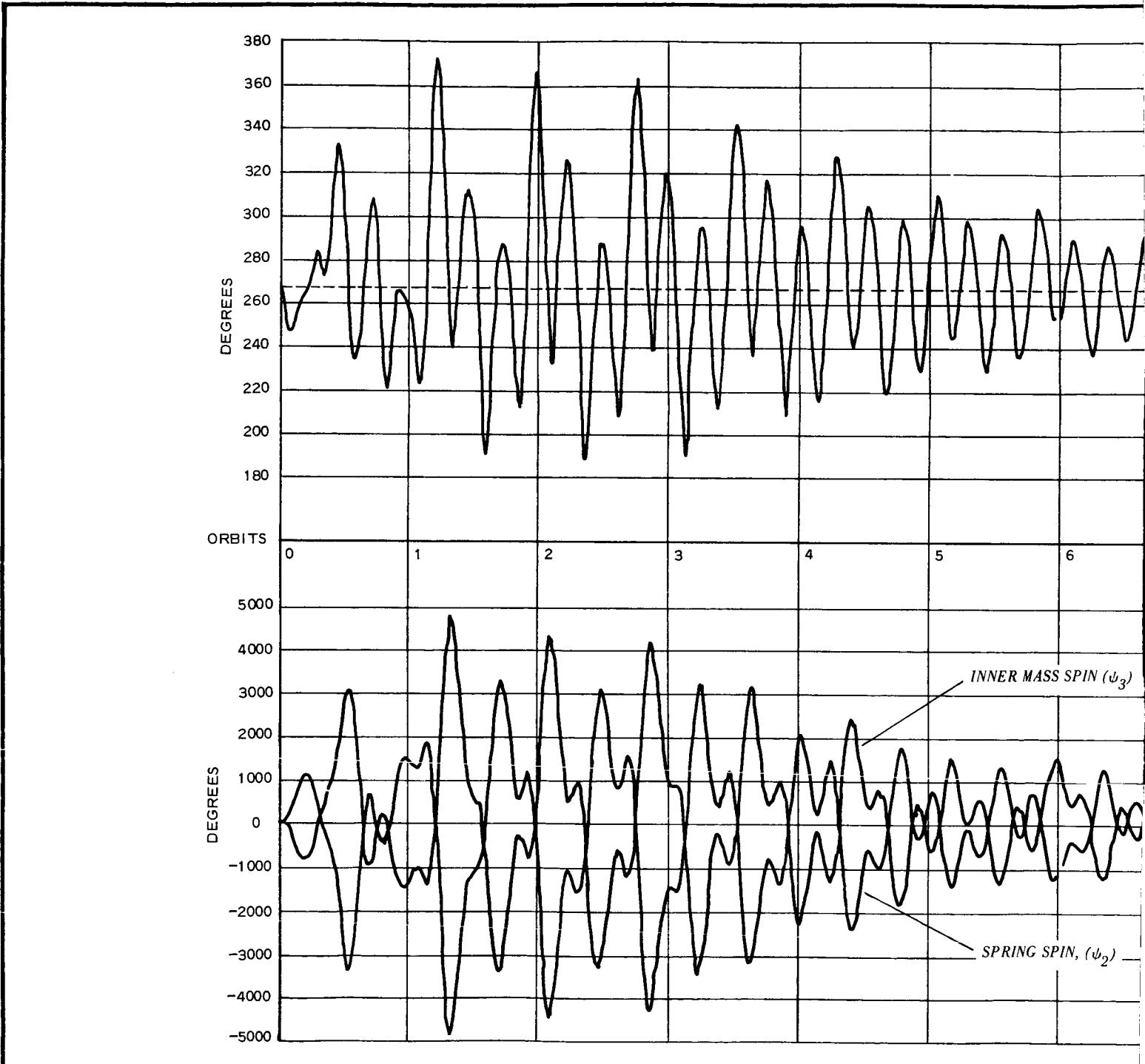


Figure D-8 - Digital-Analog Roll Transient Response Comparison with
Digital Runs 115 and 118 (Sheet 3 of 4)

2



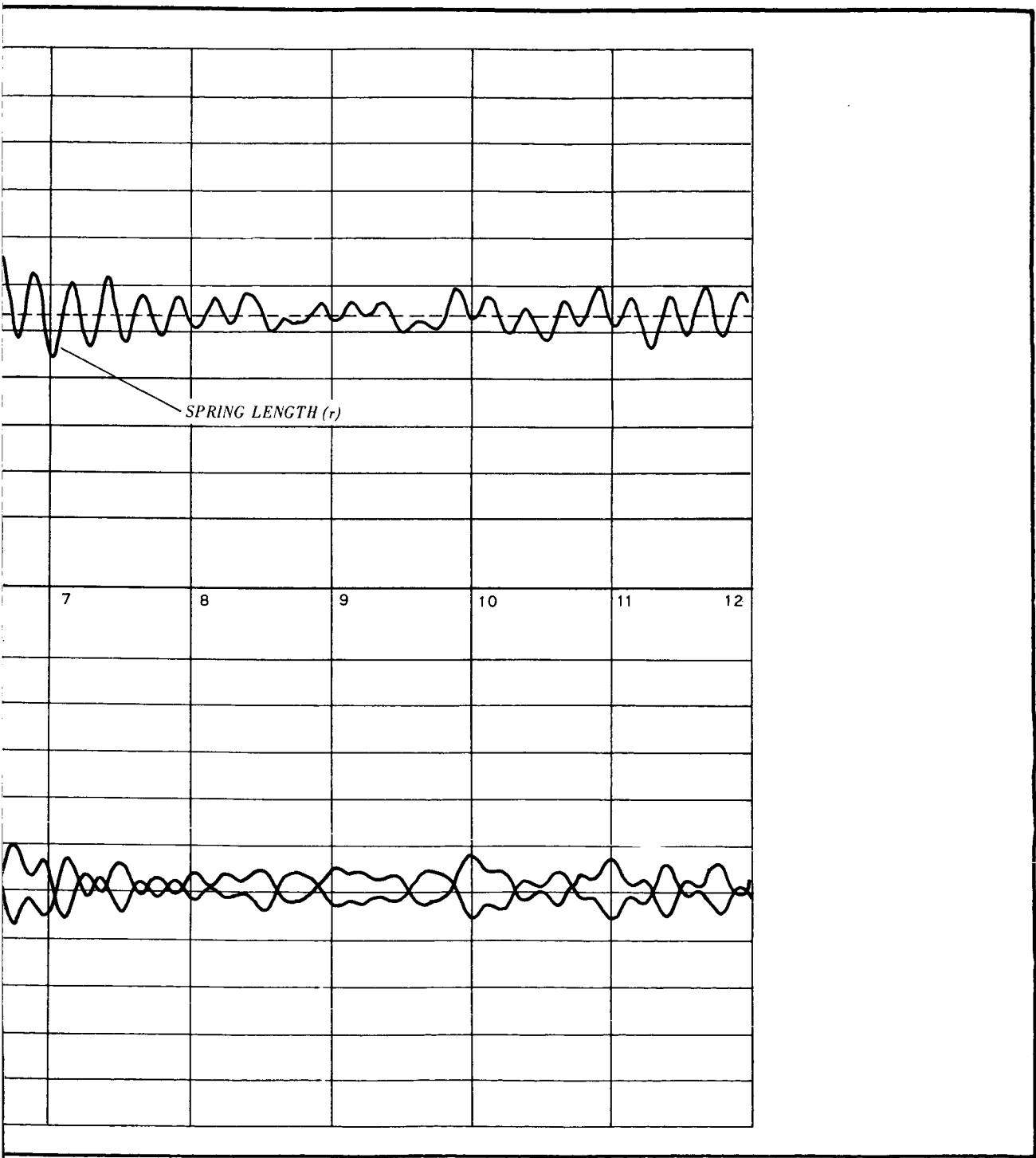
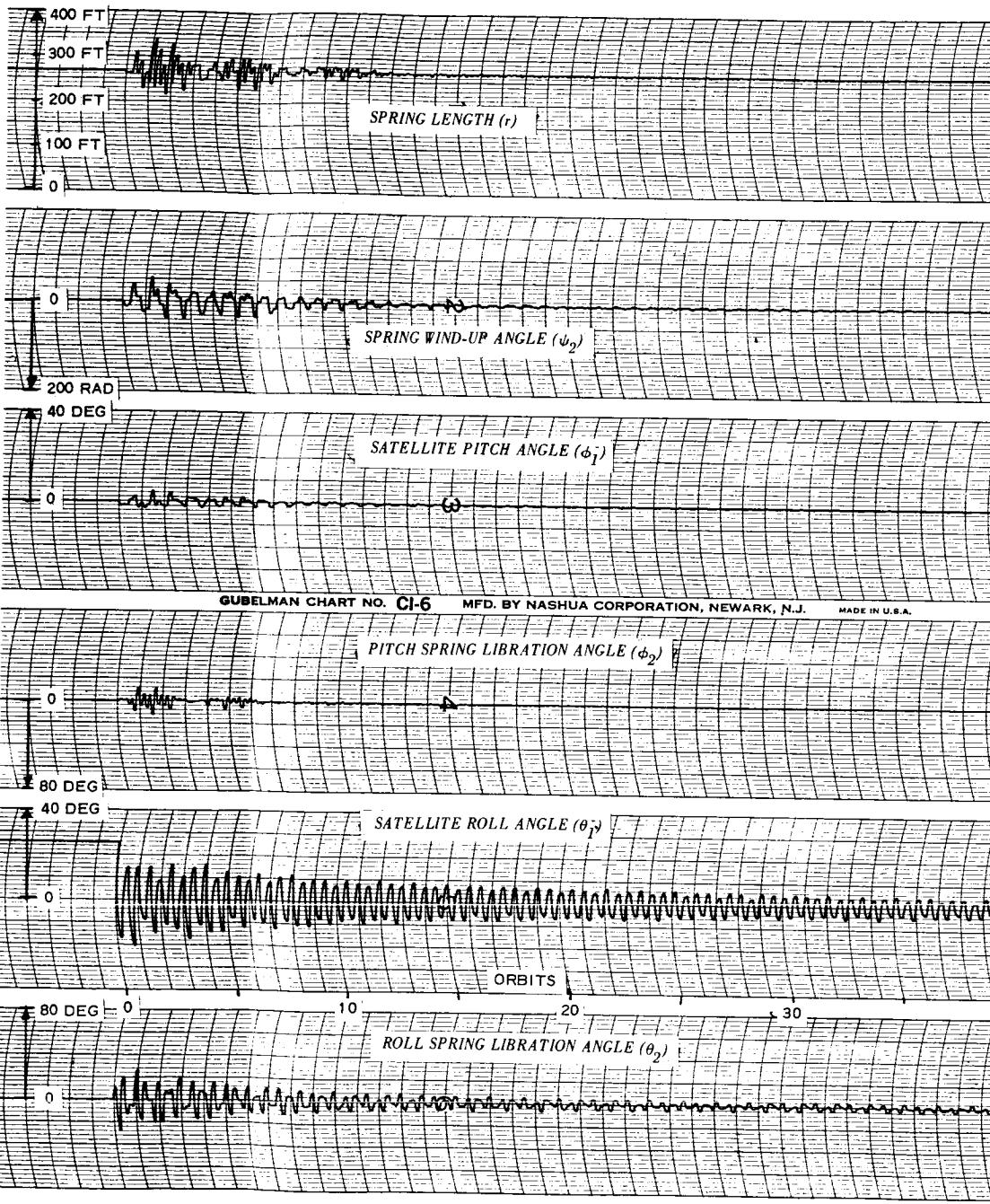


Figure D-8 - Digital-Analog Roll Transient Response Comparison with
Digital Runs 115 and 118 (Sheet 4 of 4)

2



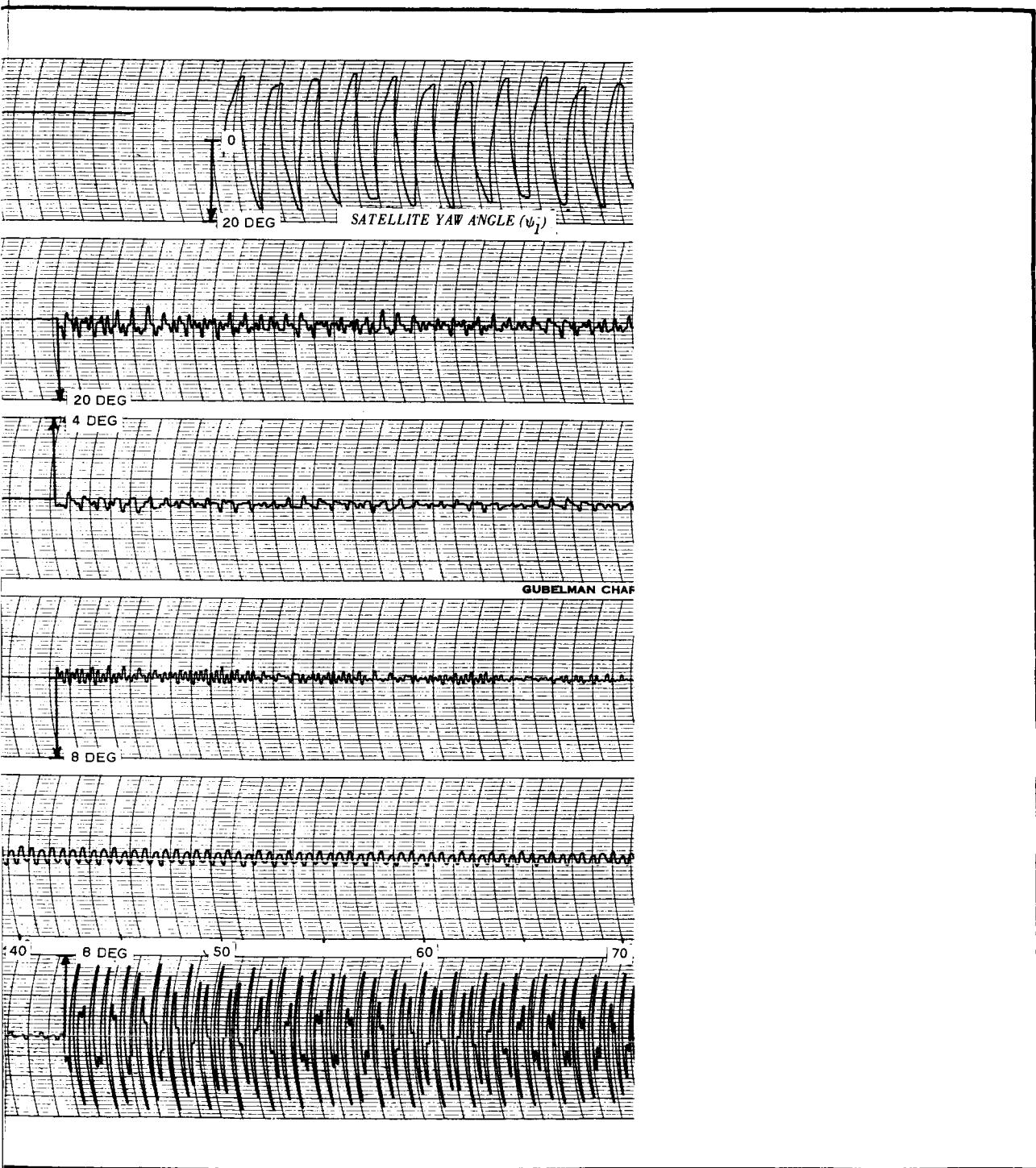
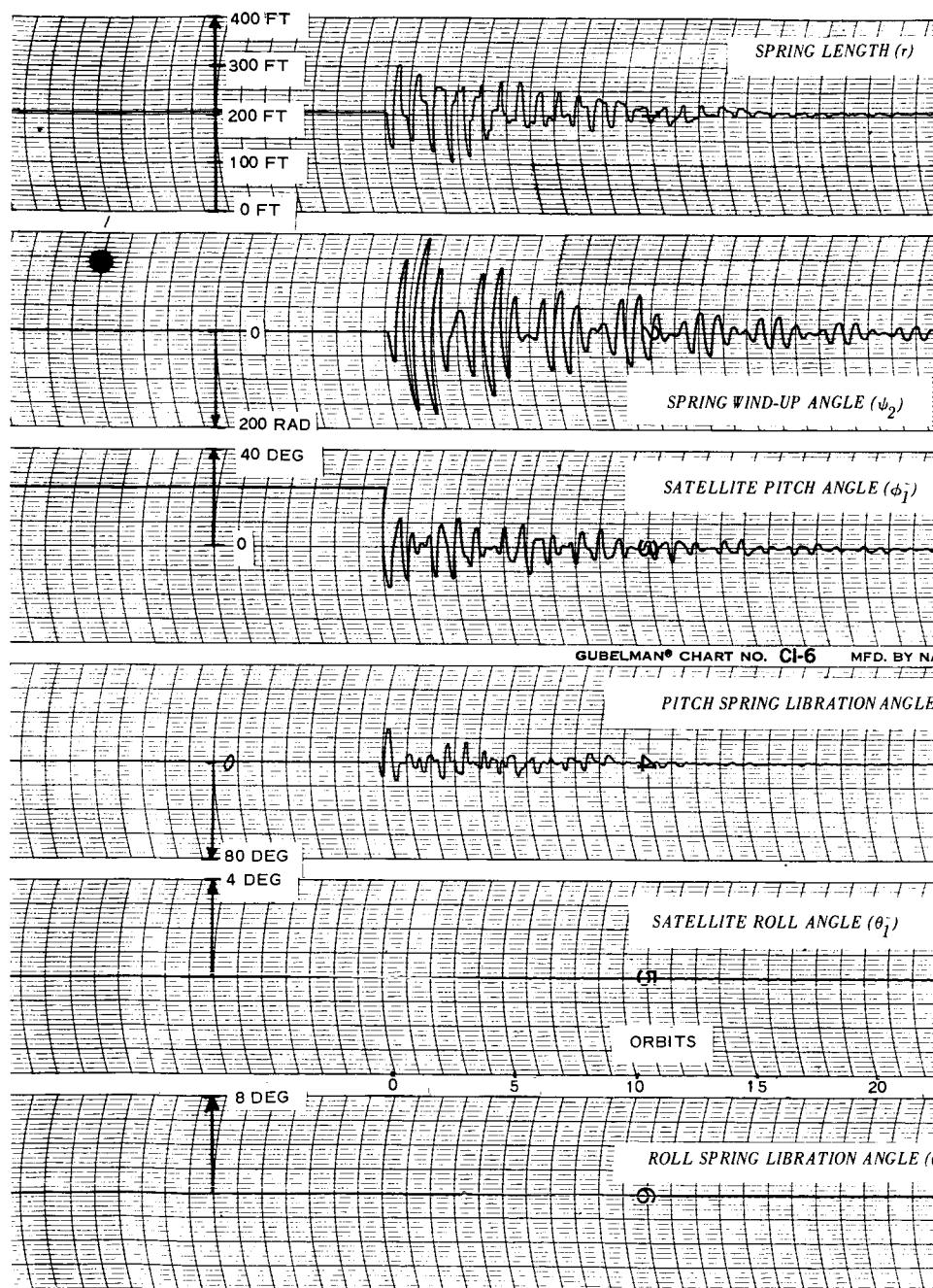


Figure D-9 - Analog-Digital Roll Transient Response Comparison with Digital Runs 115 and 118 (No Initial Yaw)

2



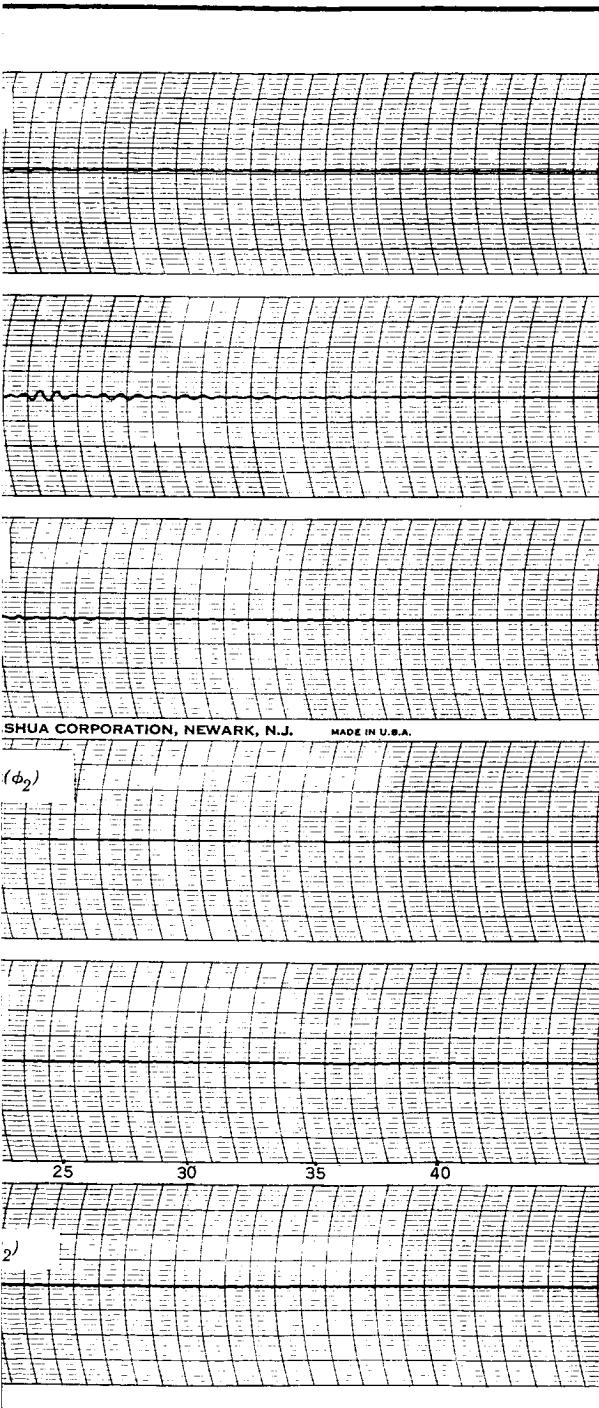
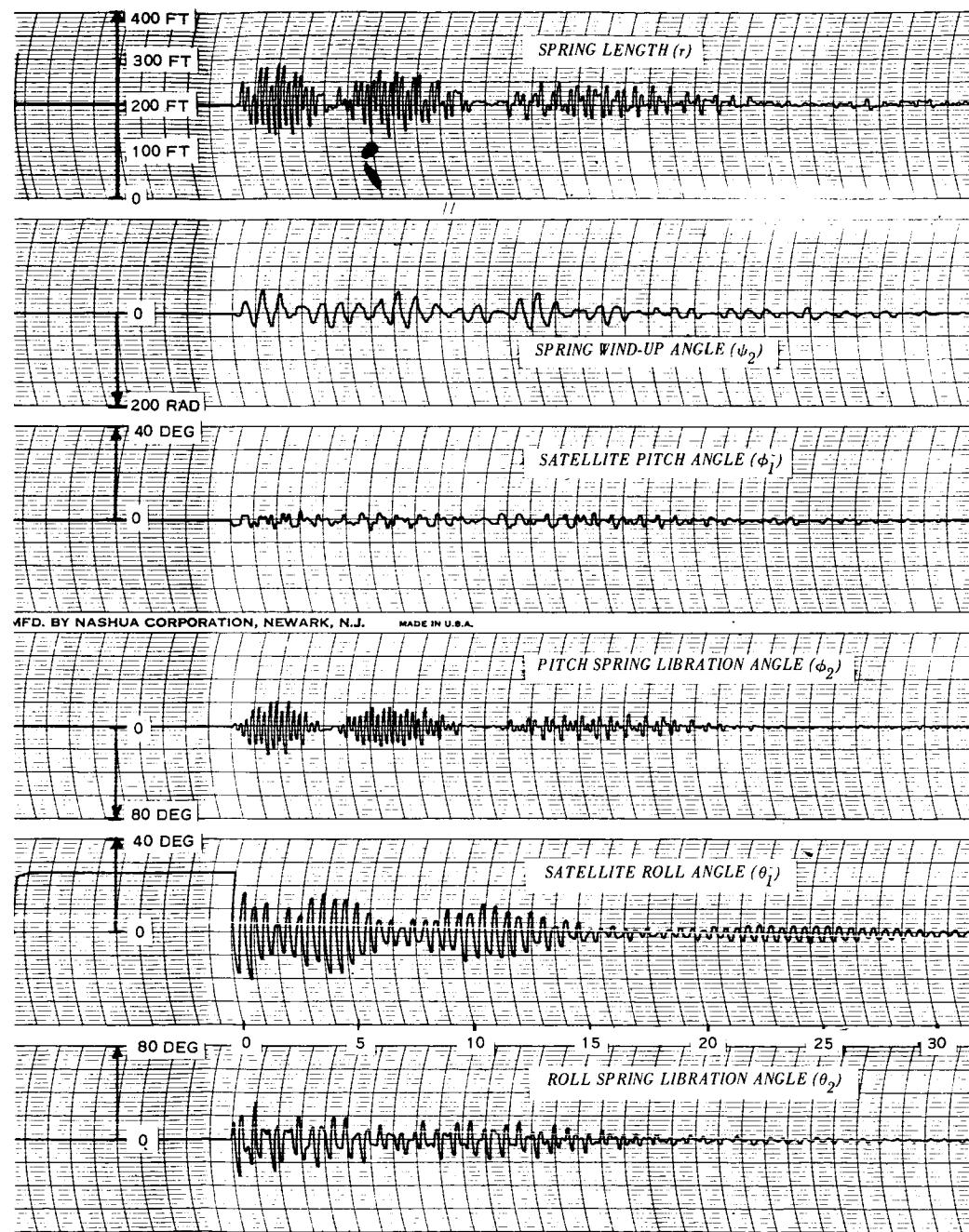


Figure D-10 - Preferred Configuration, Pitch Transient Response with Hysteresis Damping Only



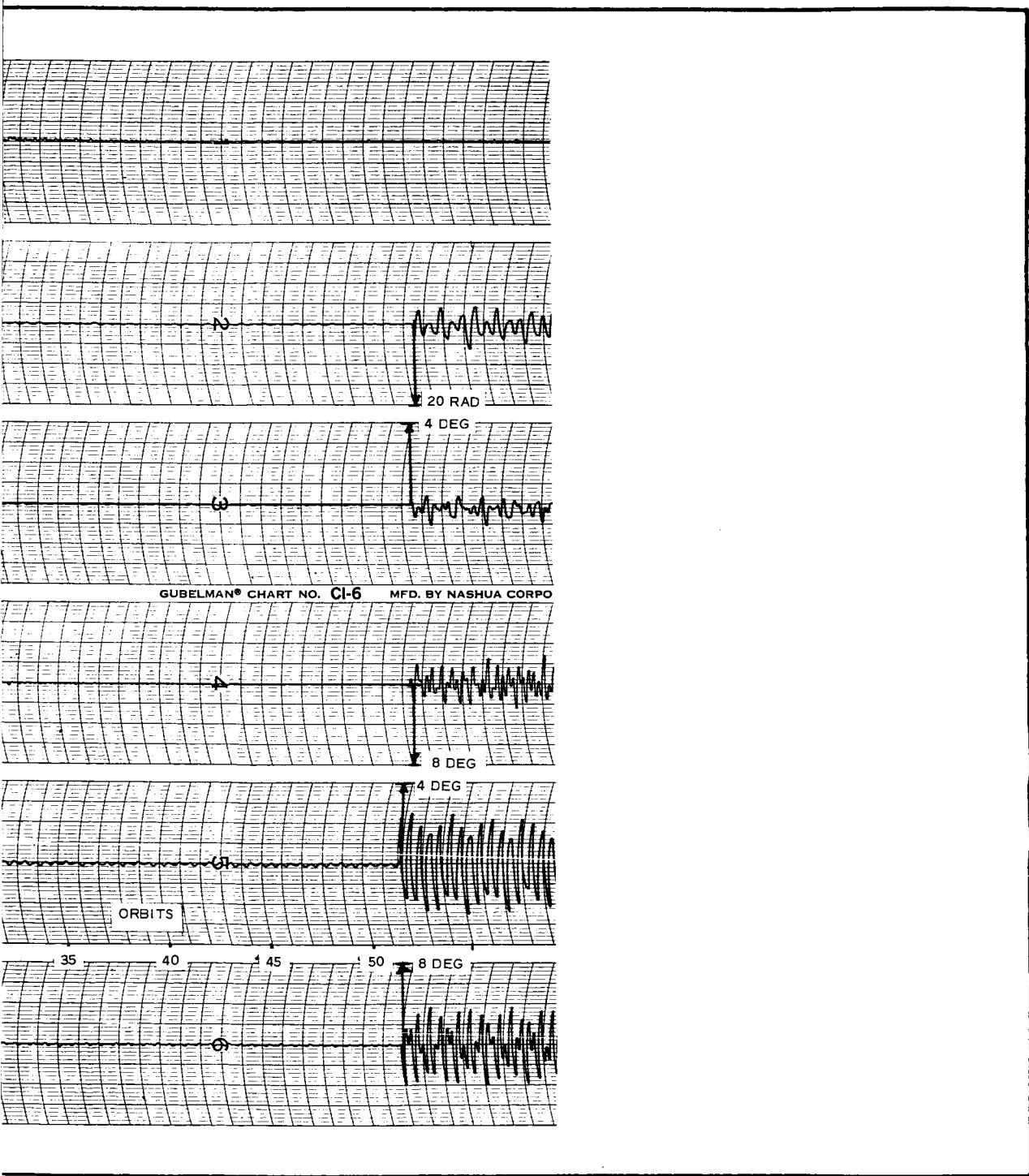
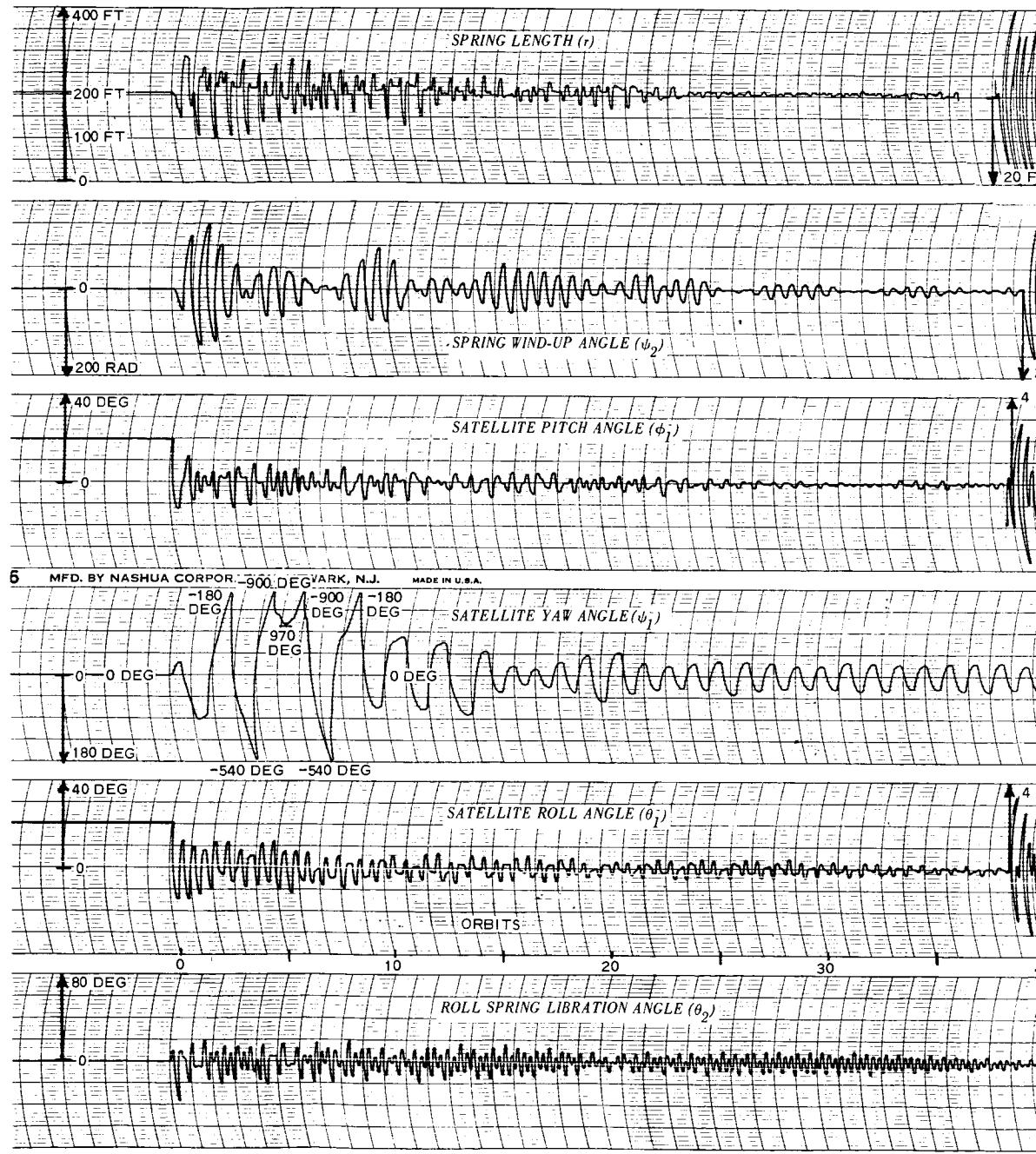


Figure D-11 - Preferred Configuration, Roll Transient Response with Hysteresis Damping Only



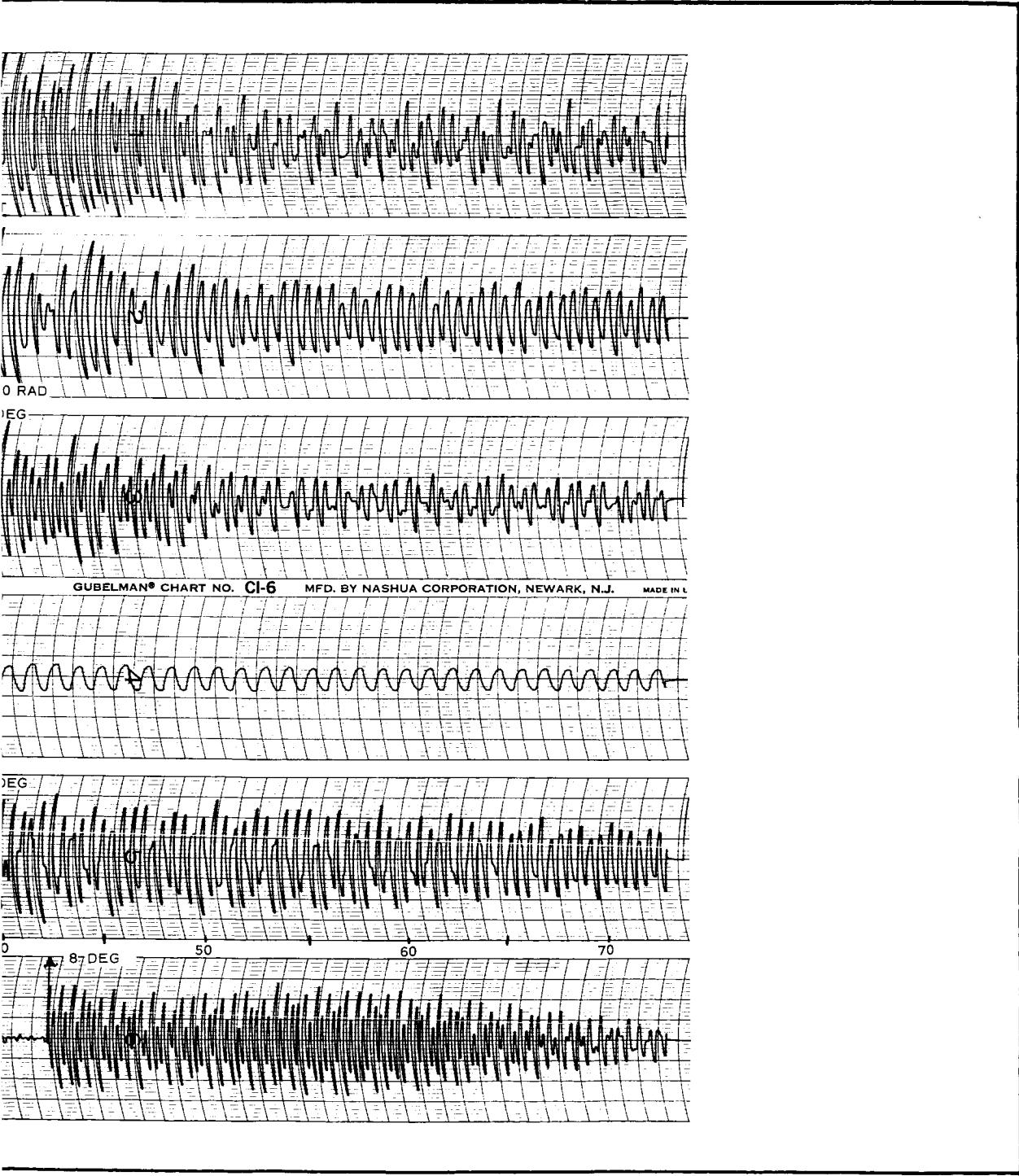
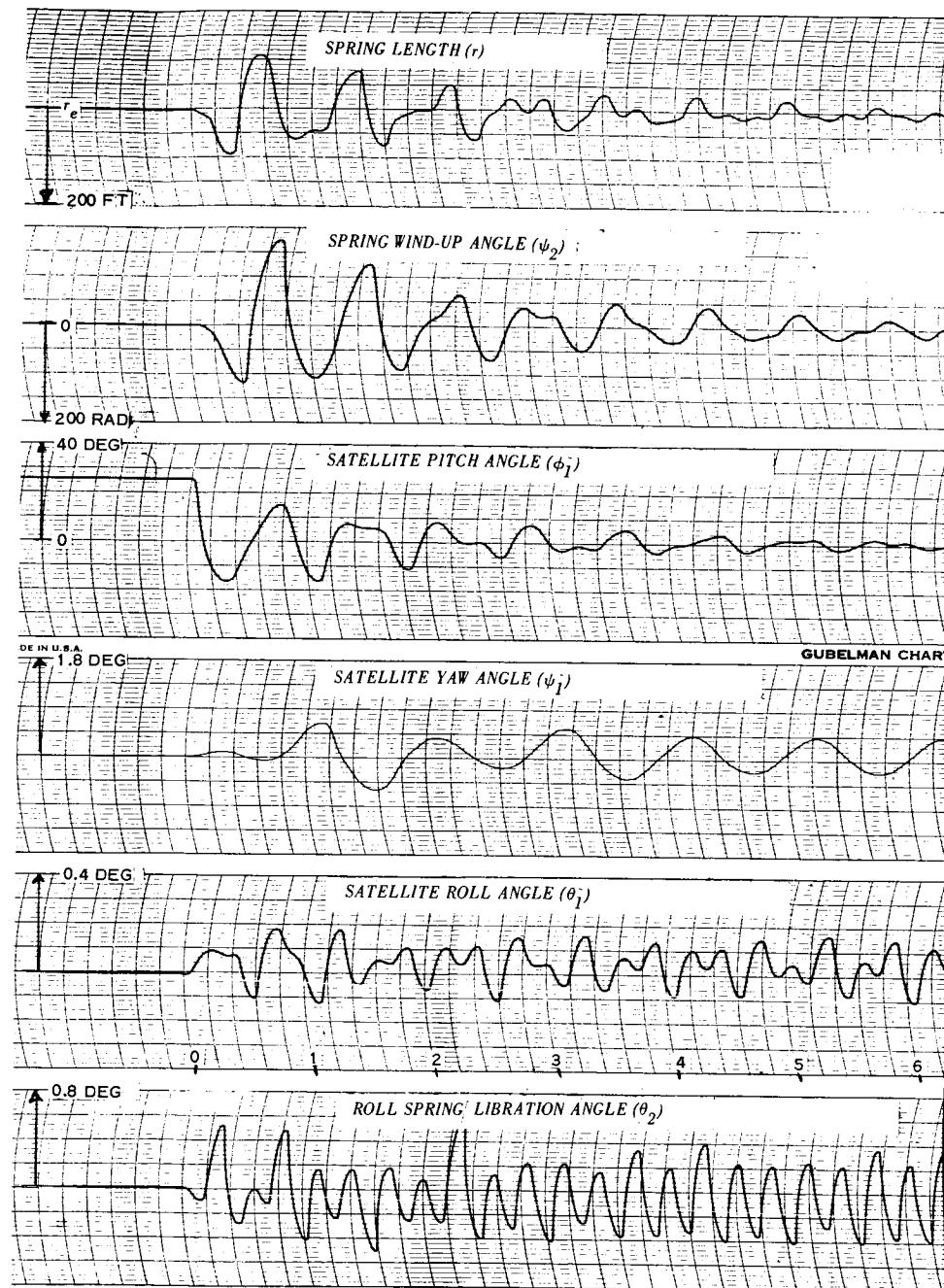


Figure D-12 - Preferred Configuration, Pitch and Roll Transient Response with Hysteresis Damping Only

2



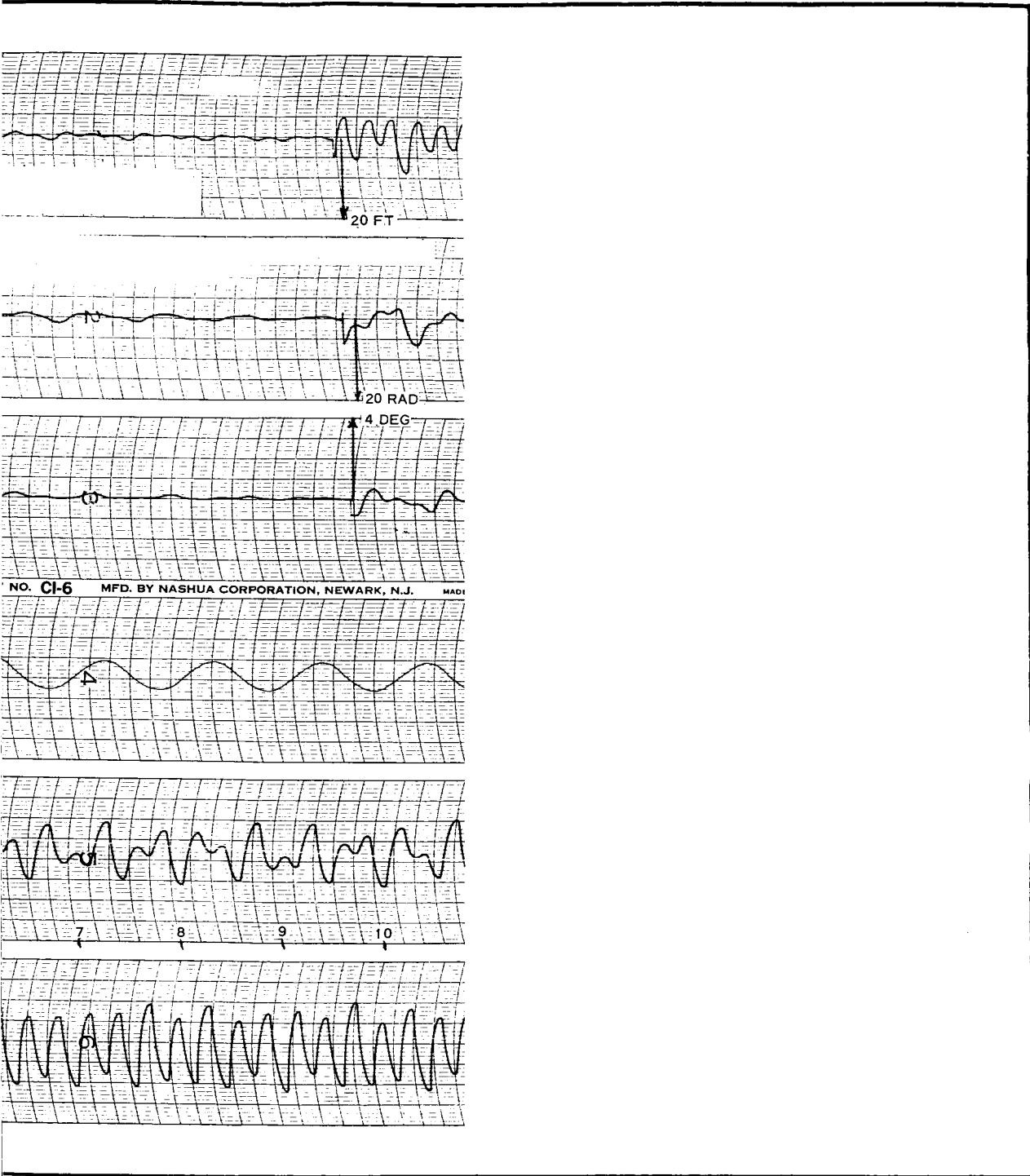
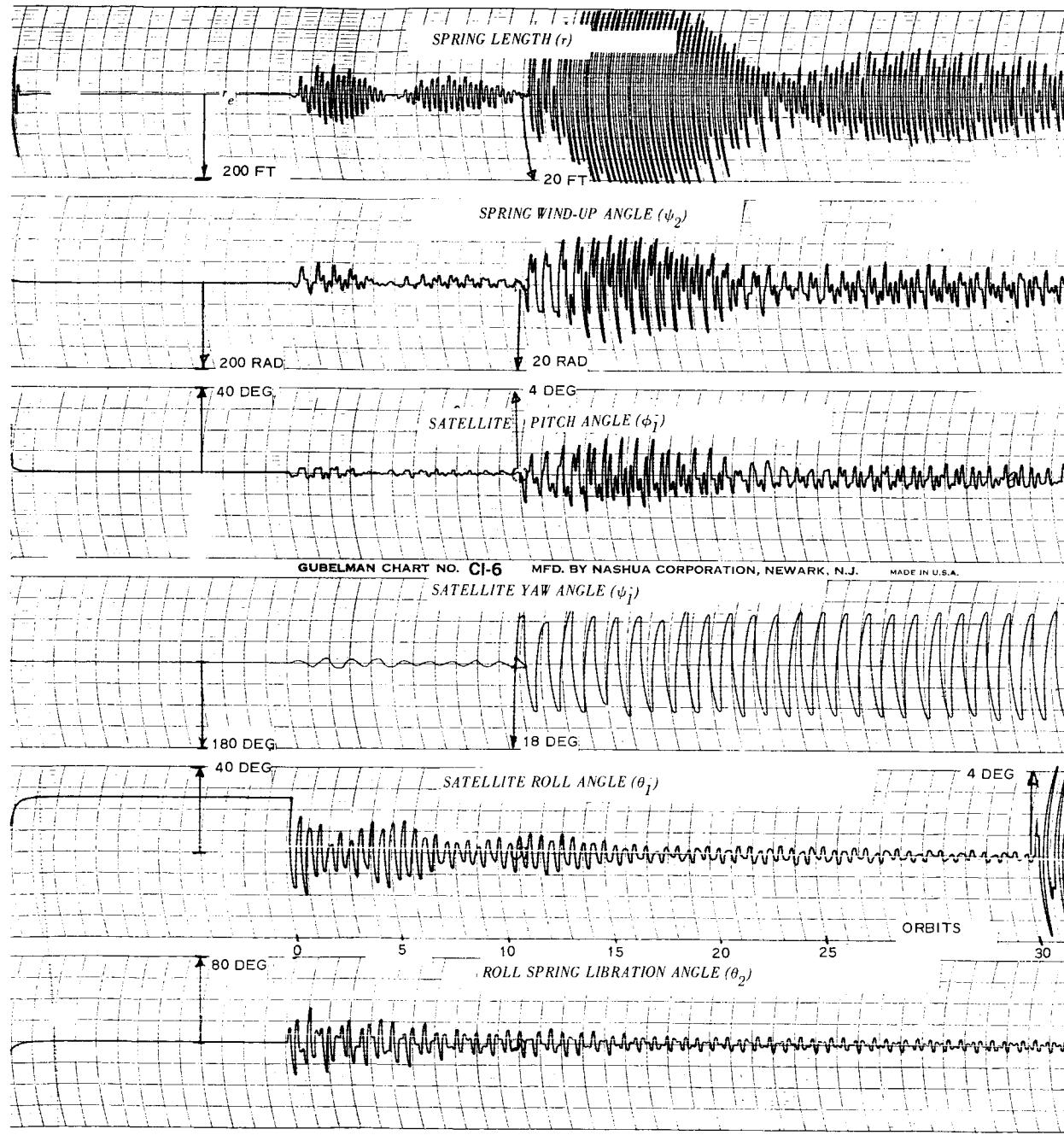


Figure D-13 - Preferred Configuration, Pitch Transient Response with Light Damping Fluid



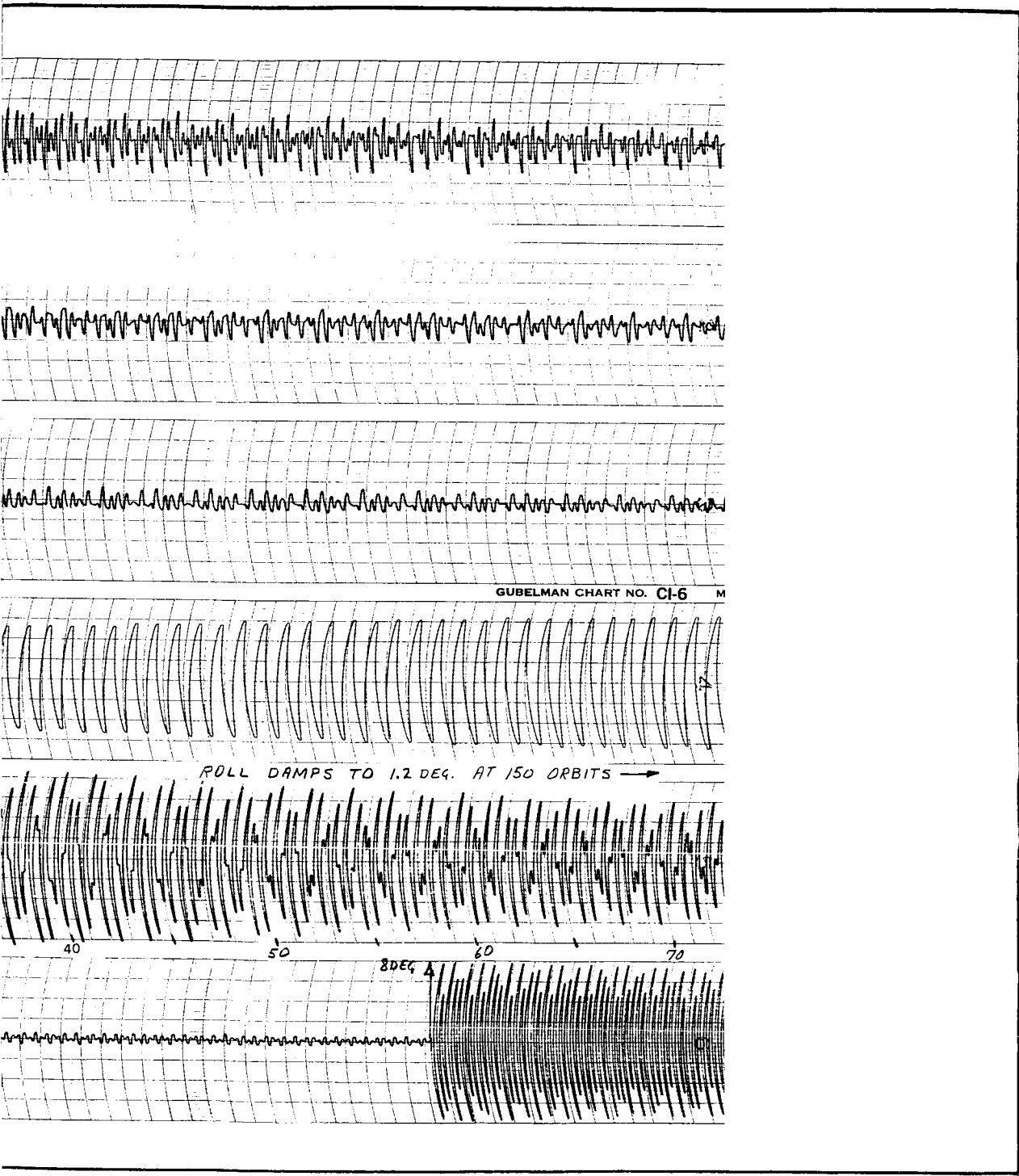
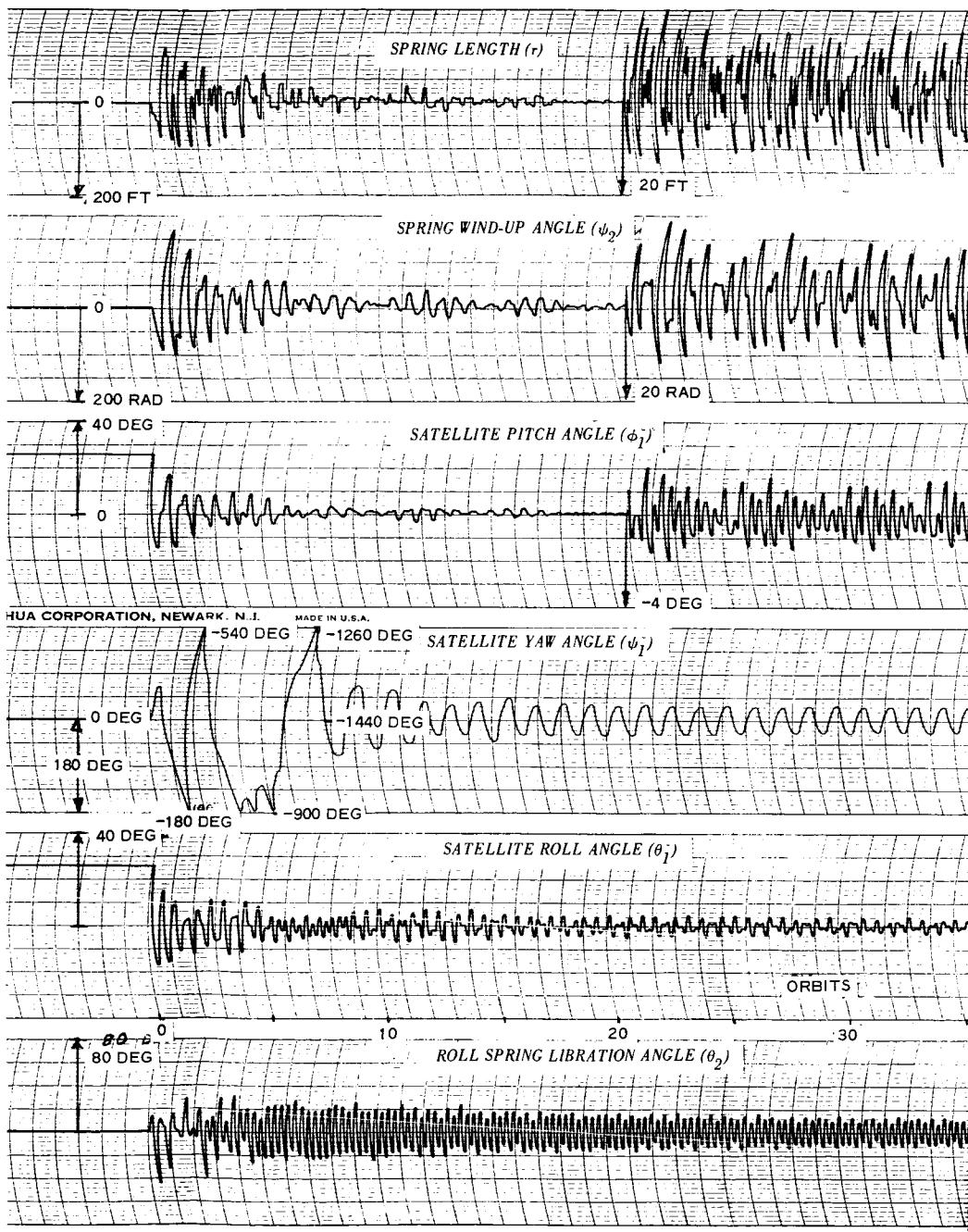


Figure D-14 - Preferred Configuration, Roll Transient Response with Light Damping Fluid

2



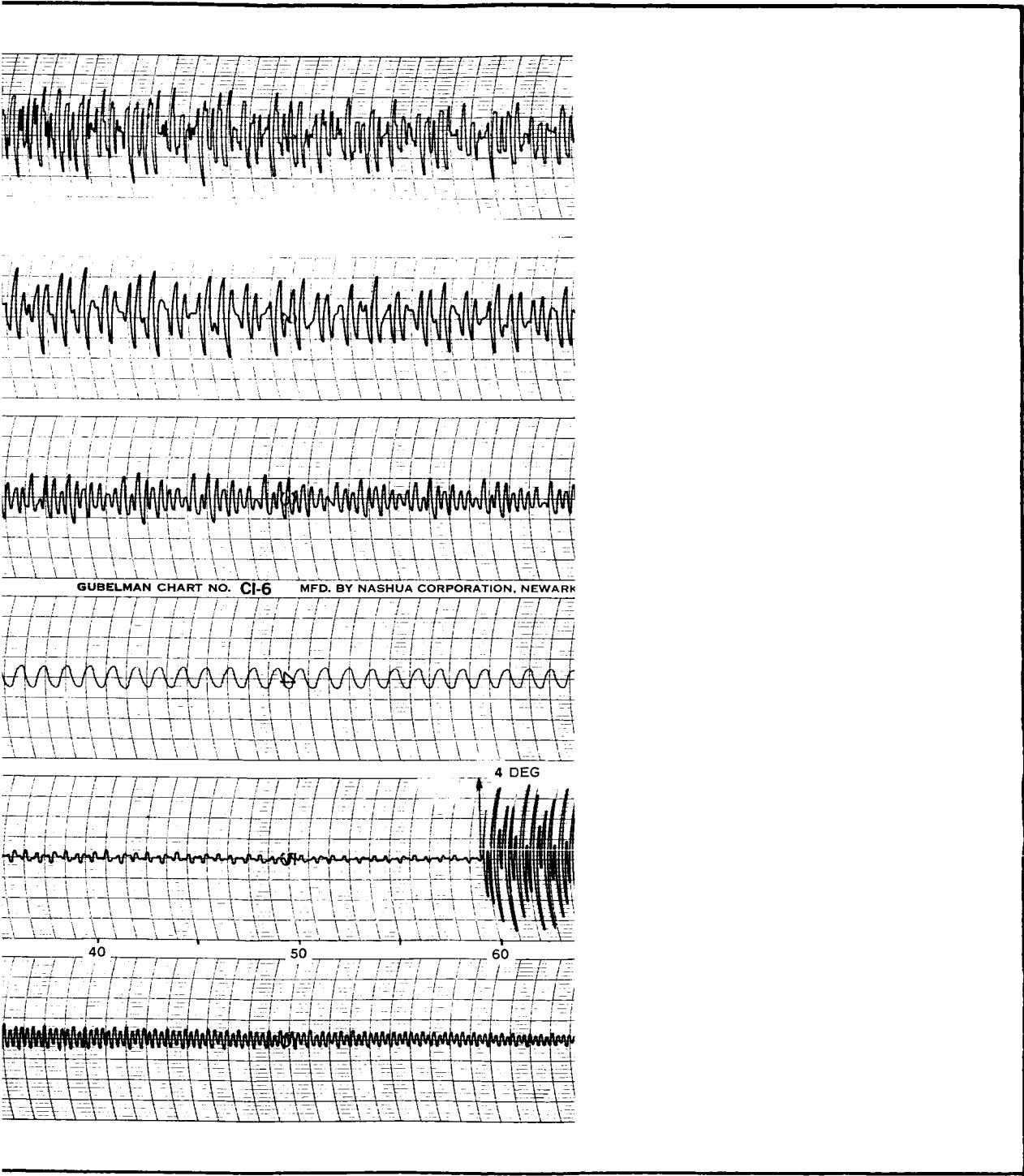


Figure D-15 - Preferred Configuration, Pitch and Roll Transient Response with Light Damping Fluid

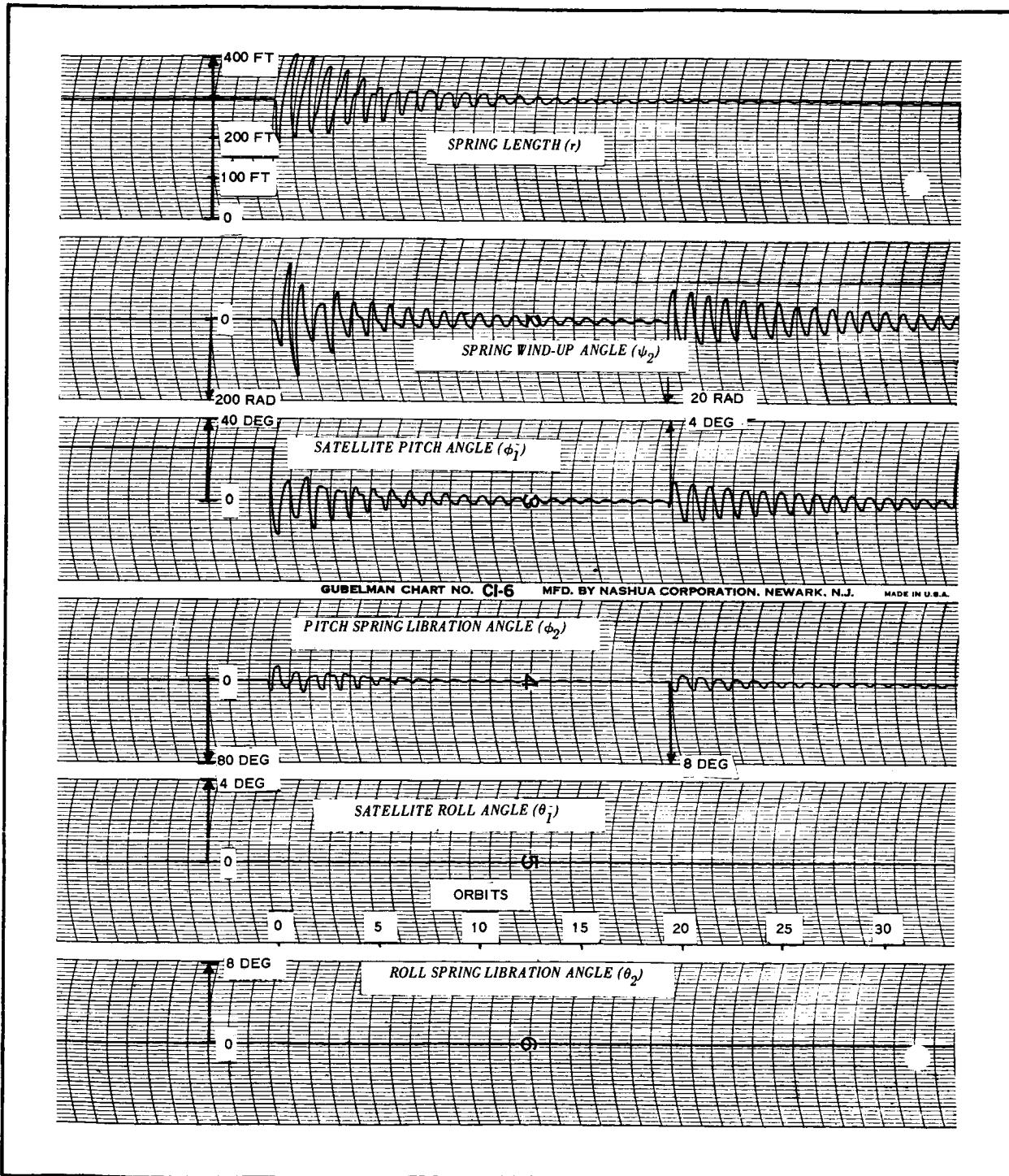
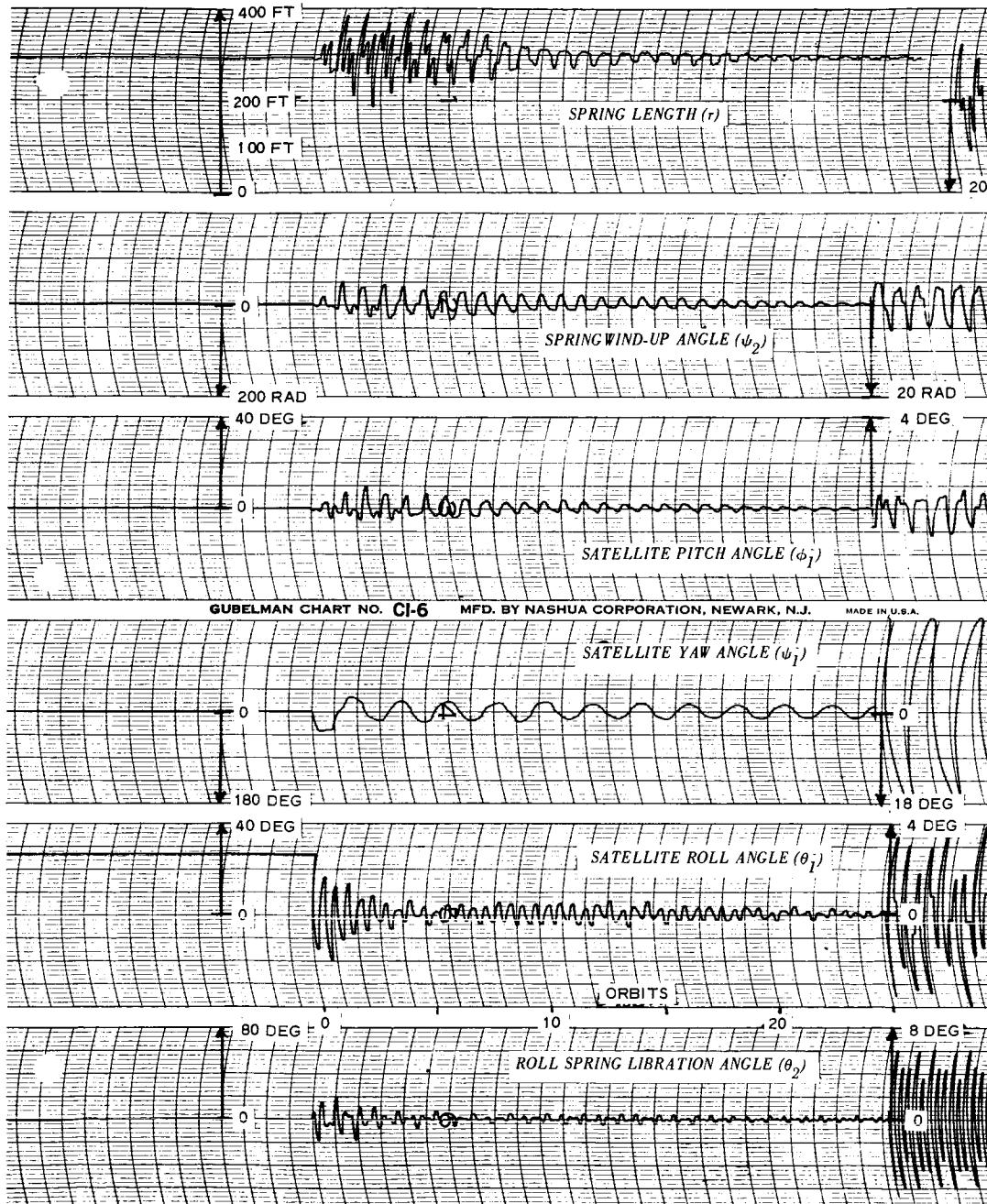


Figure D-16 - Preferred Configuration, Pitch Transient Response for Unphotolyzed Satellite



page 54 blank

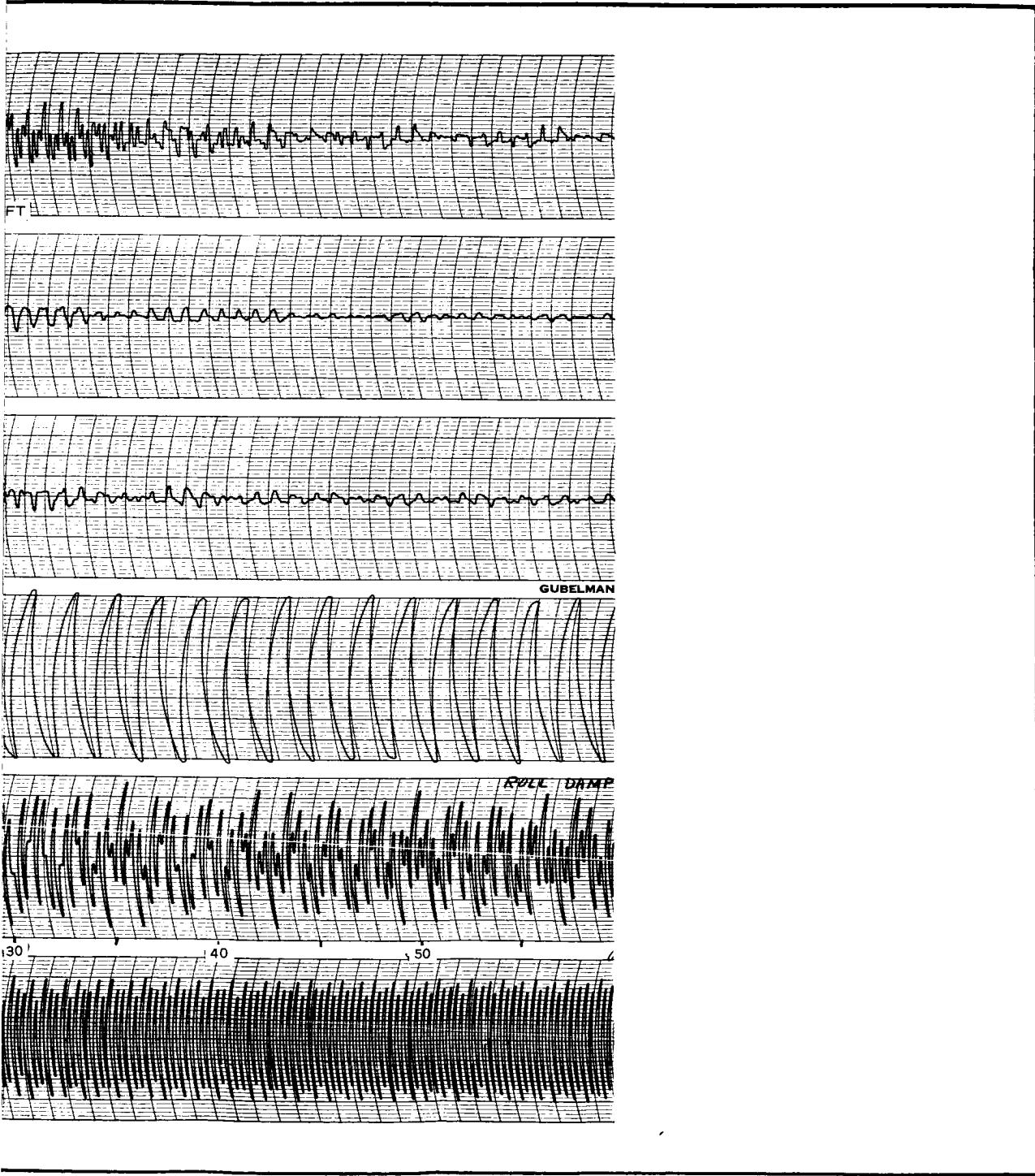


Figure D-17 - Preferred Configuration, Roll Transient Response for
Unphotolyzed Satellite

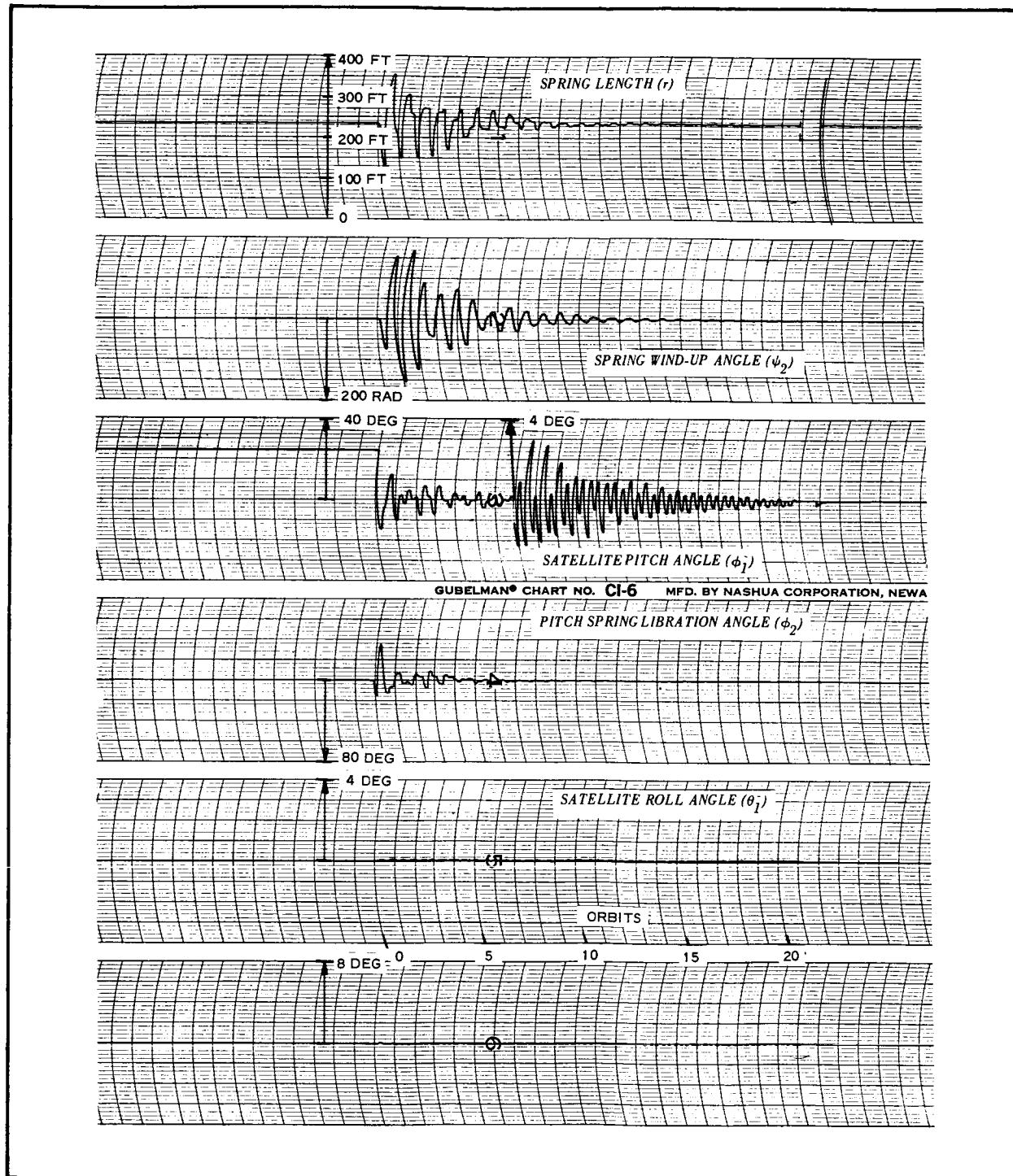
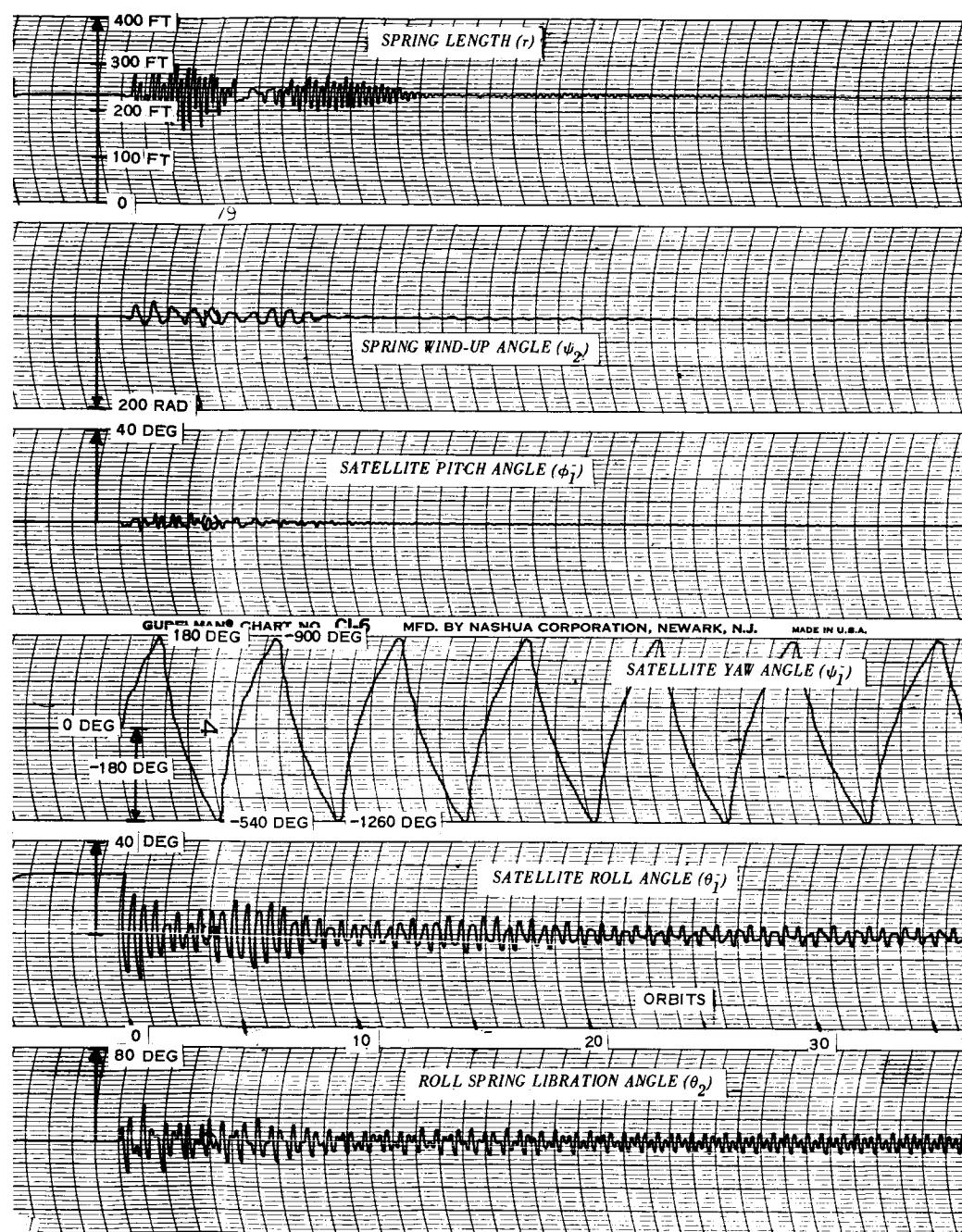


Figure D-18 - Preferred Configuration, Pitch Transient Response for Symmetrical Satellite



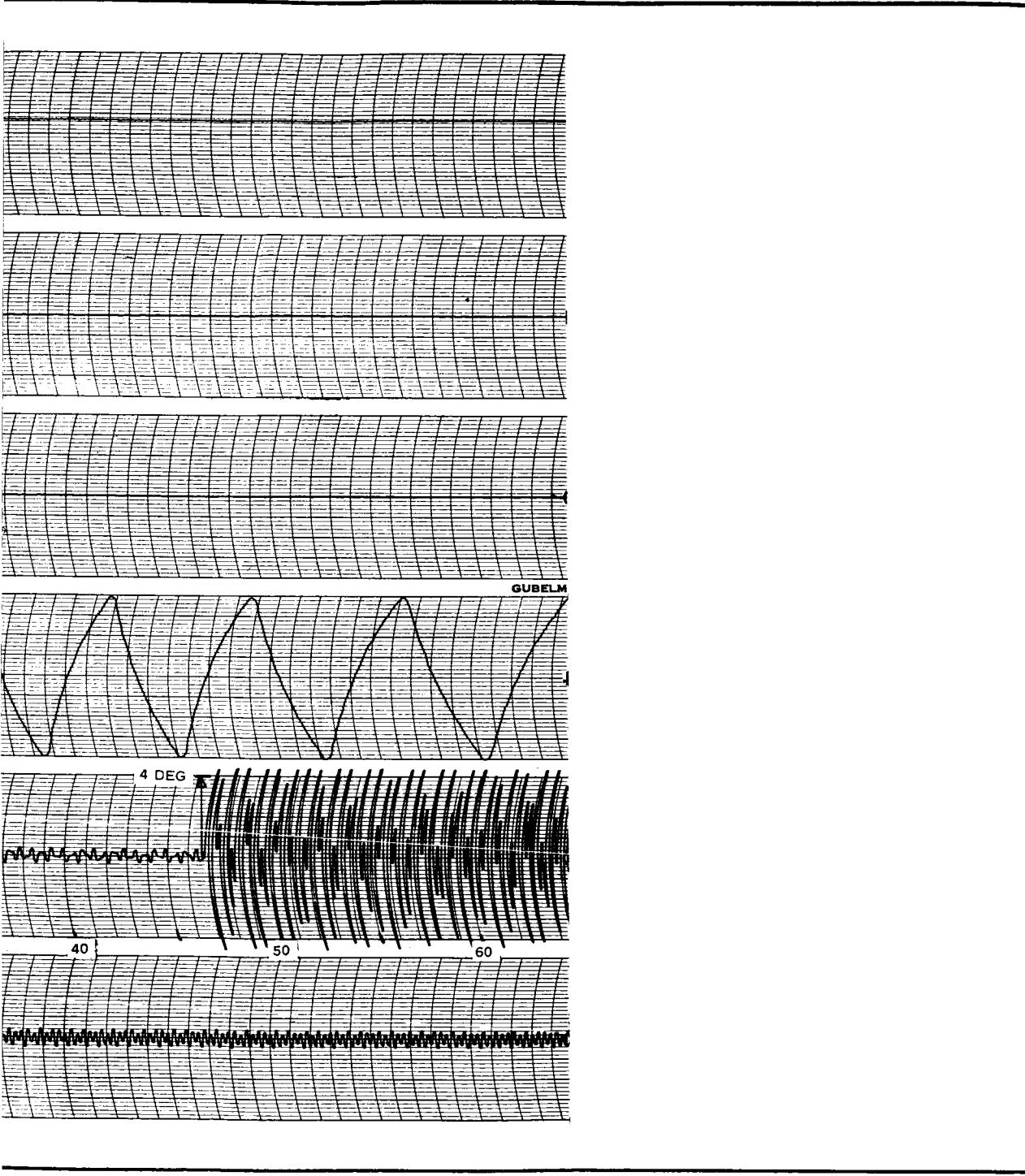


Figure D-19 - Preferred Configuration, Roll Transient Response for Symmetrical Satellite

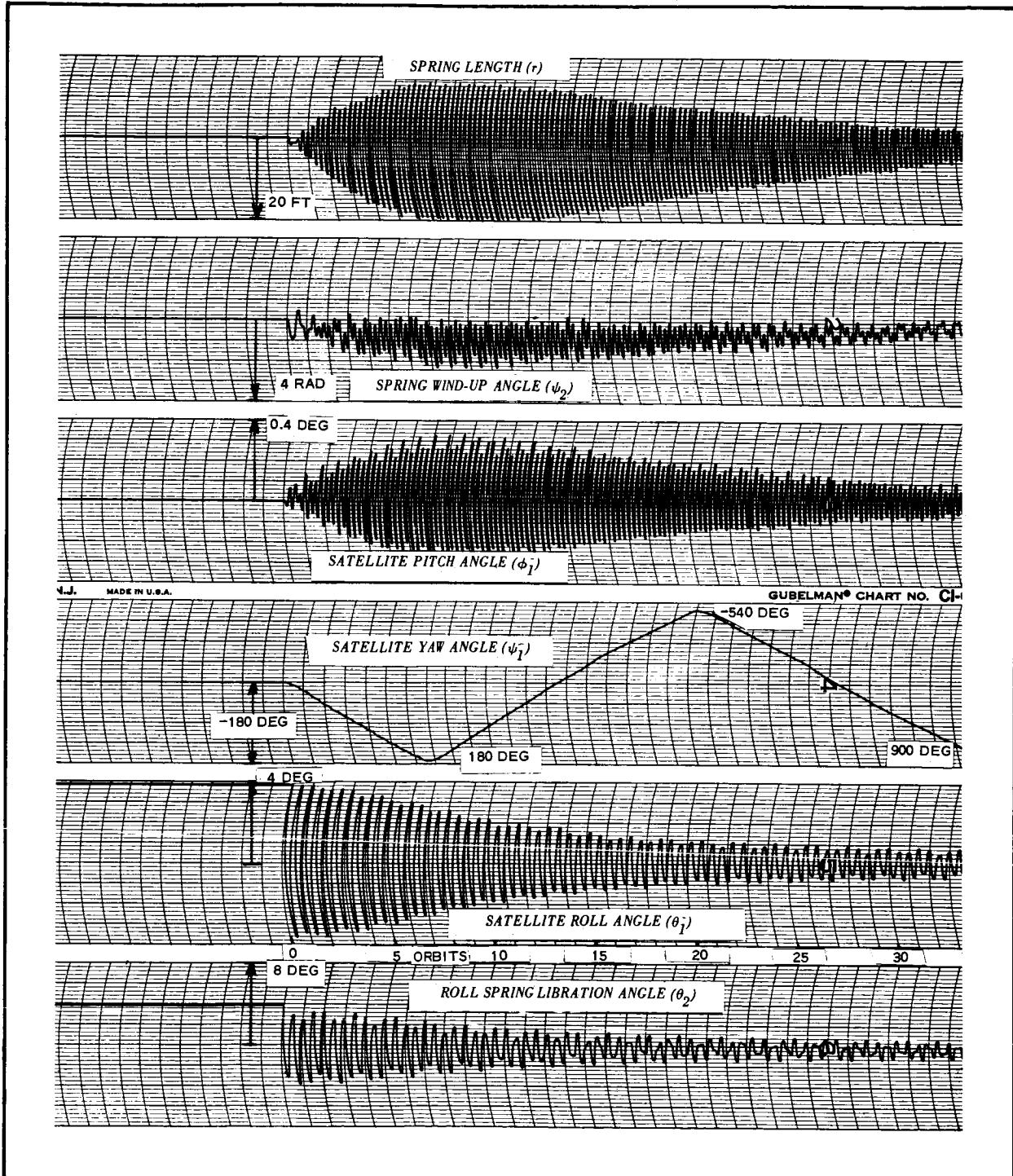


Figure D-20 - Preferred Configuration, Roll Transient Response for Symmetrical Satellite with Small Initial Roll

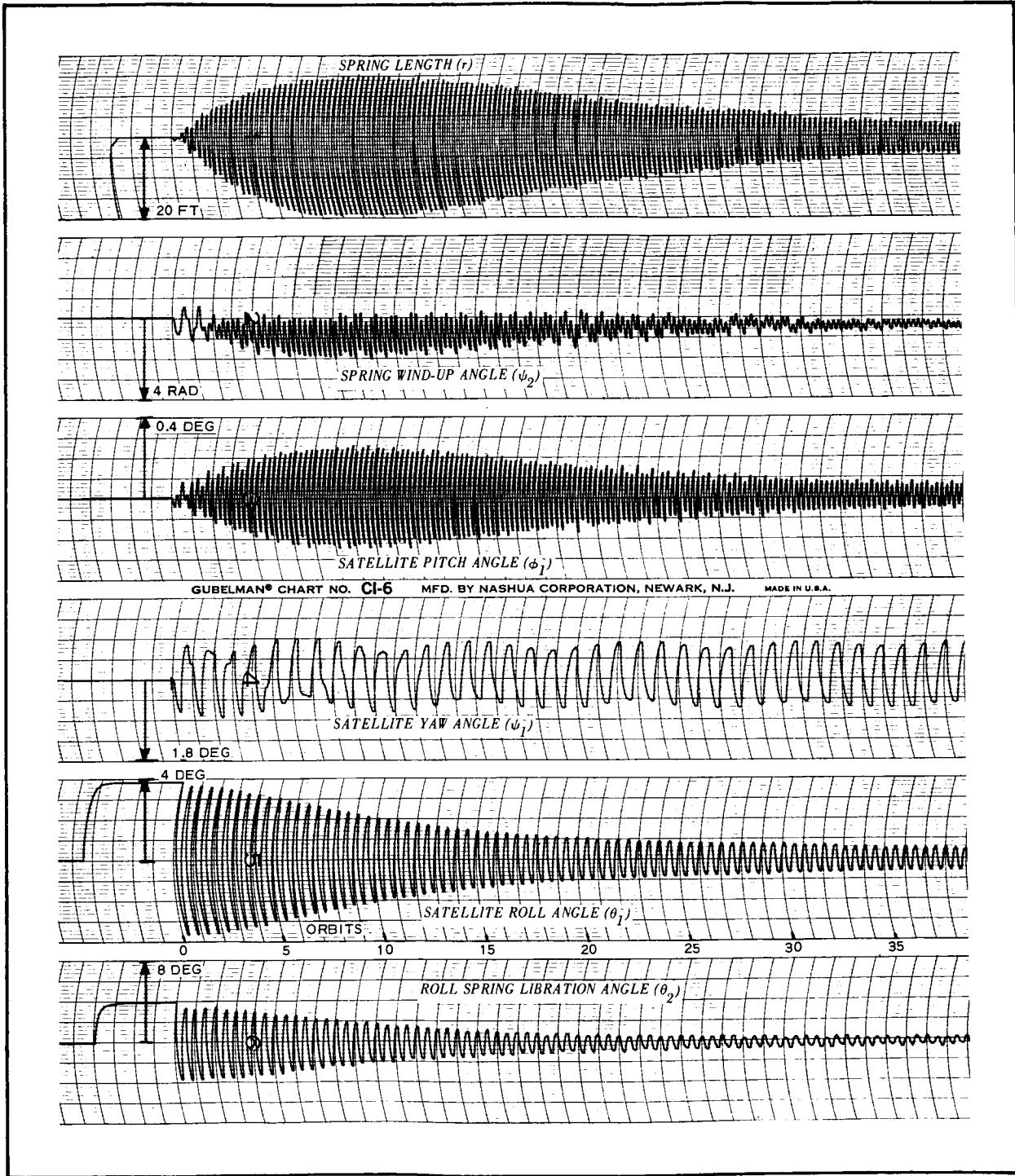


Figure D-21 - Optimum Configuration, Roll Transient Response with Small Initial Roll

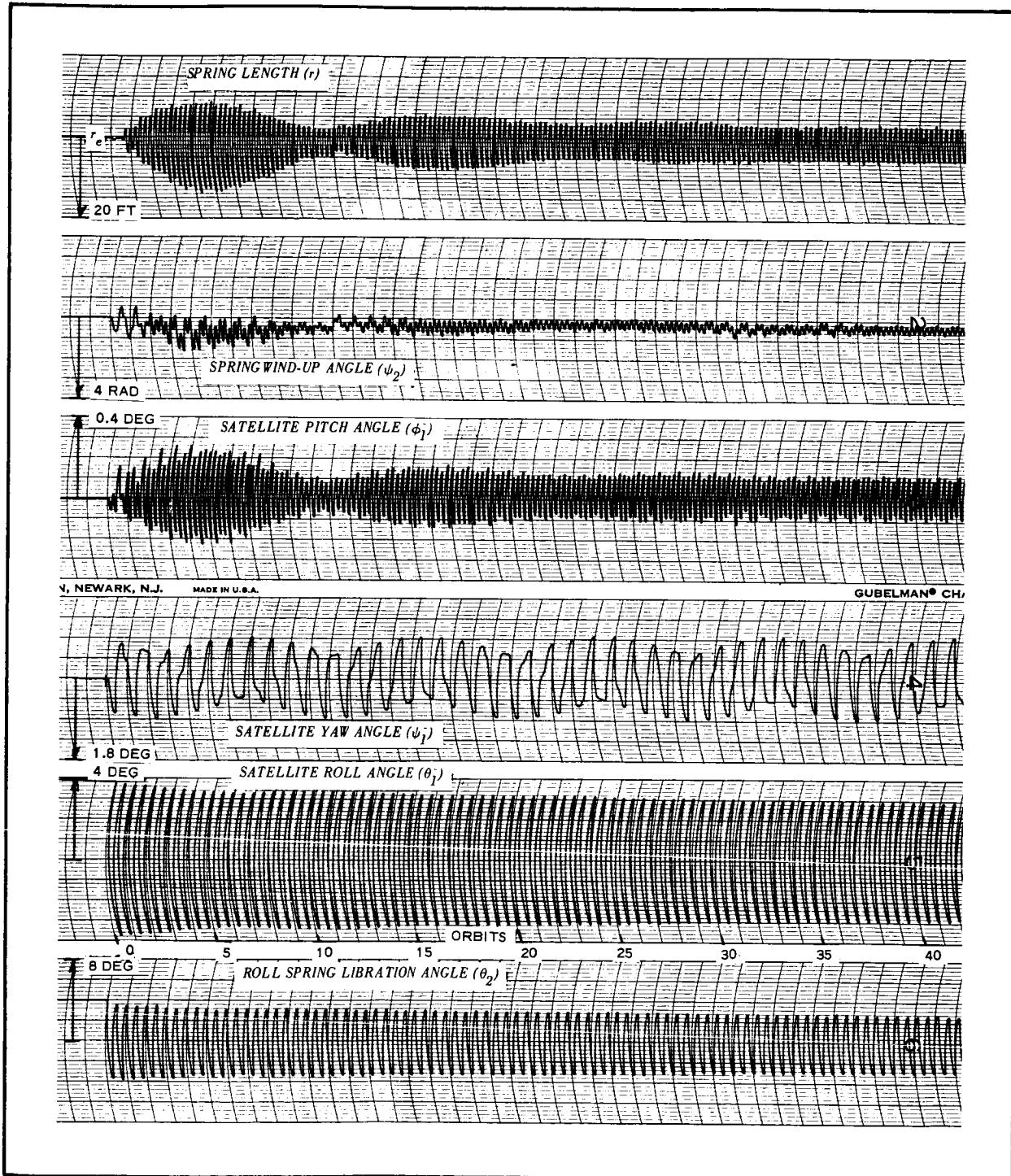
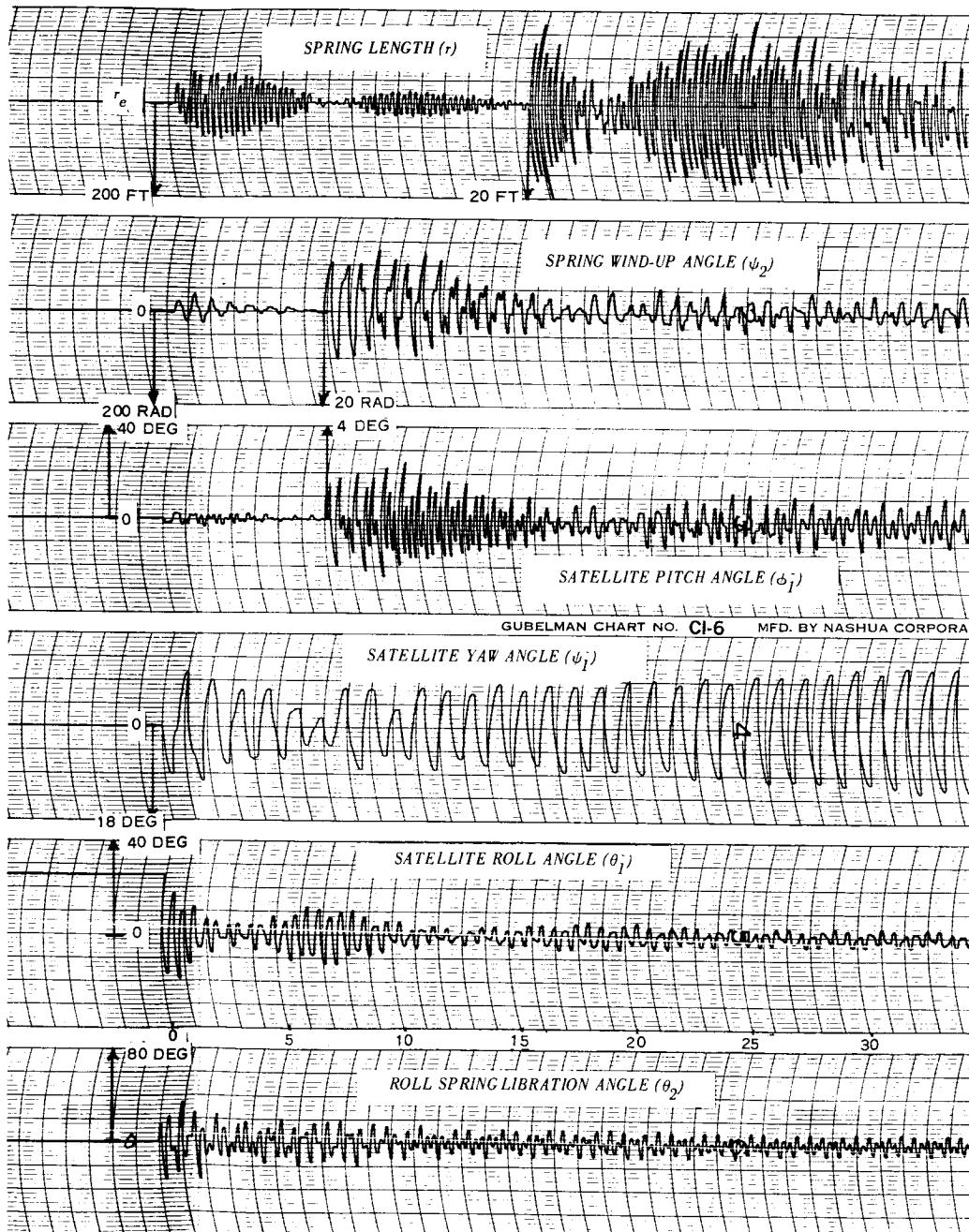


Figure D-22 - Optimum Configuration with Plunging-Spring Constant Increased Four Percent with Small Roll



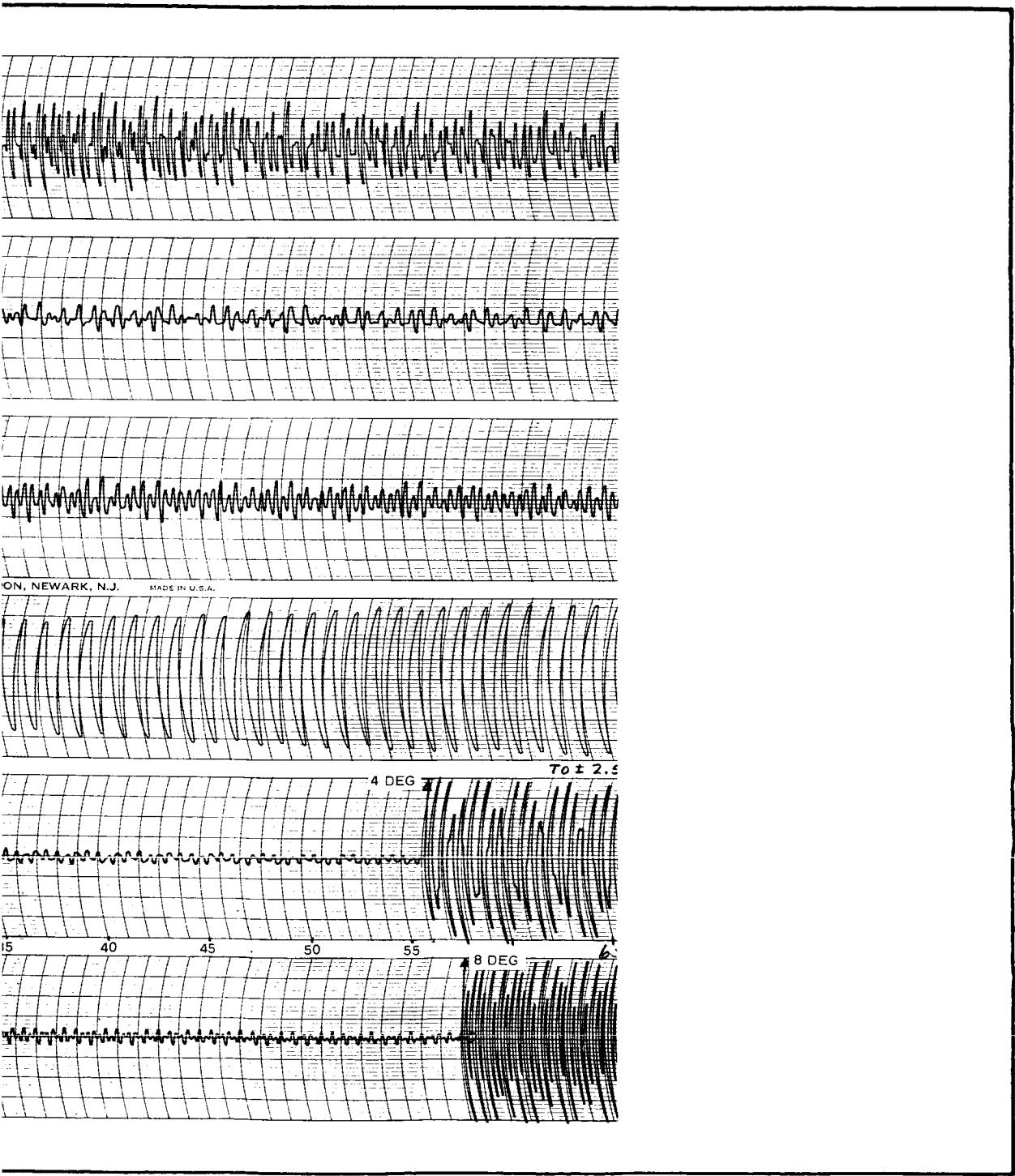


Figure D-23 - Optimum Configuration with Plunging-Spring Constant Increased Four Percent with Large Roll

2

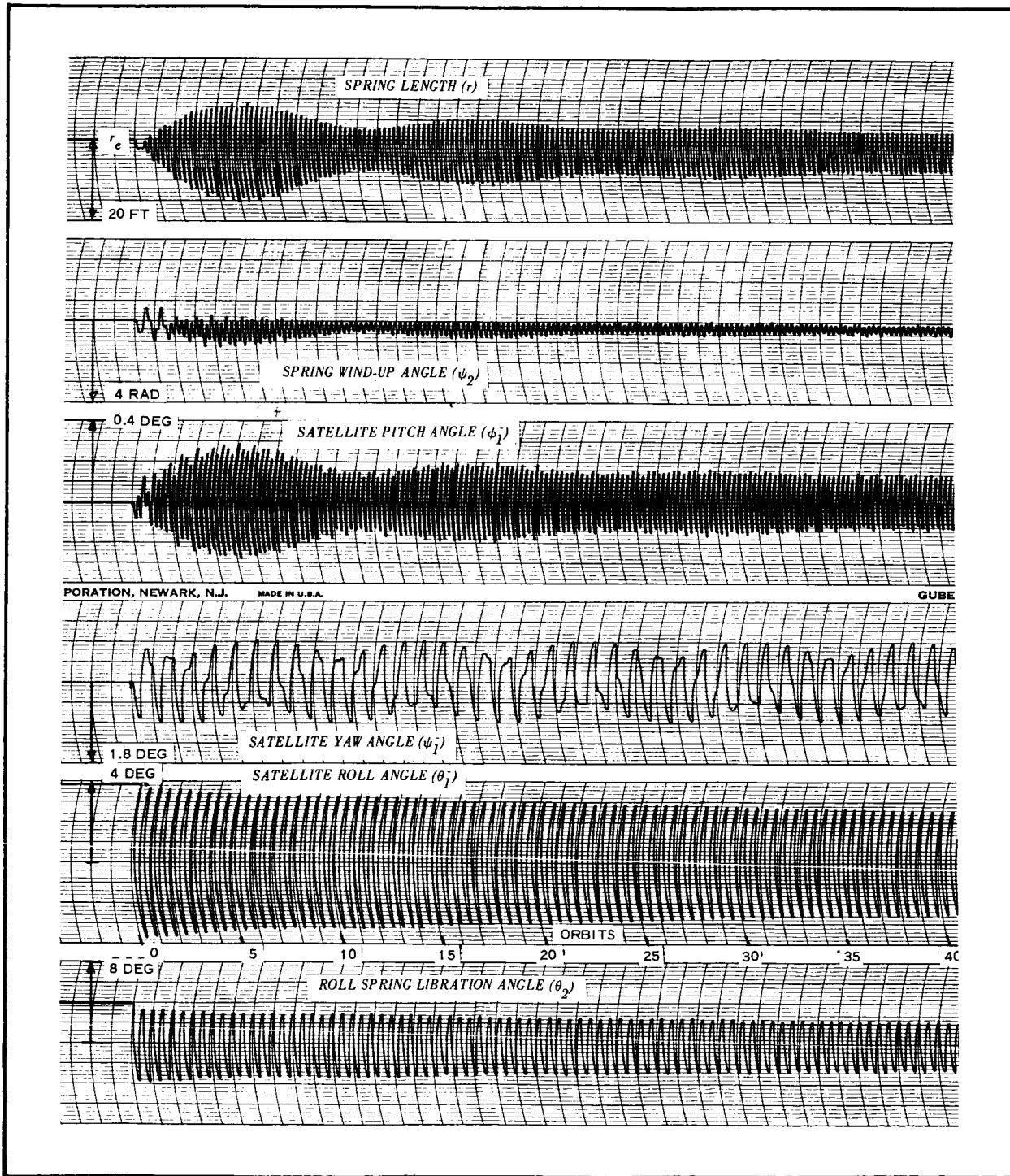
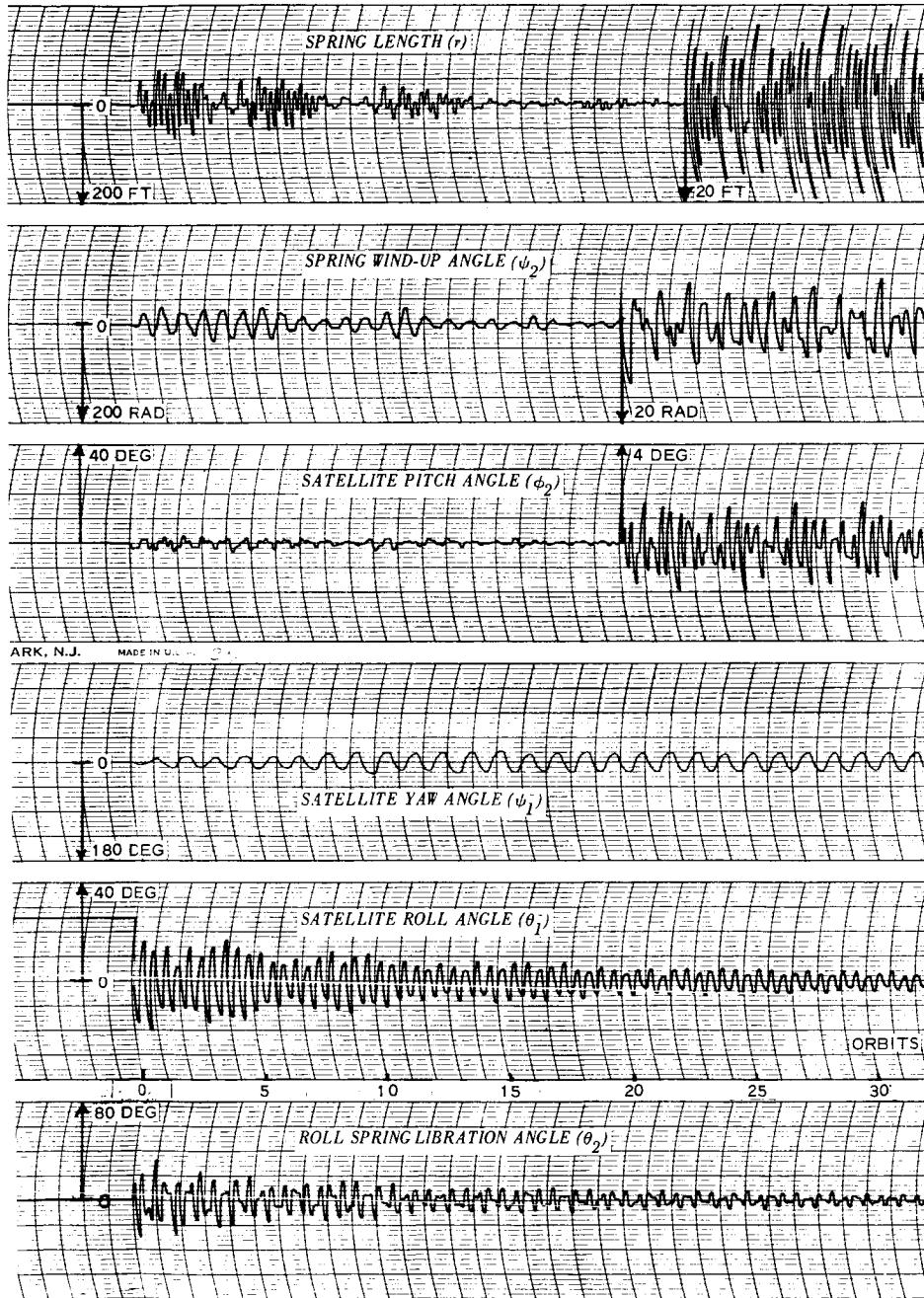


Figure D-24 - Optimum Configuration with Plunging-Spring Constant Decreased Four Percent with Small Roll



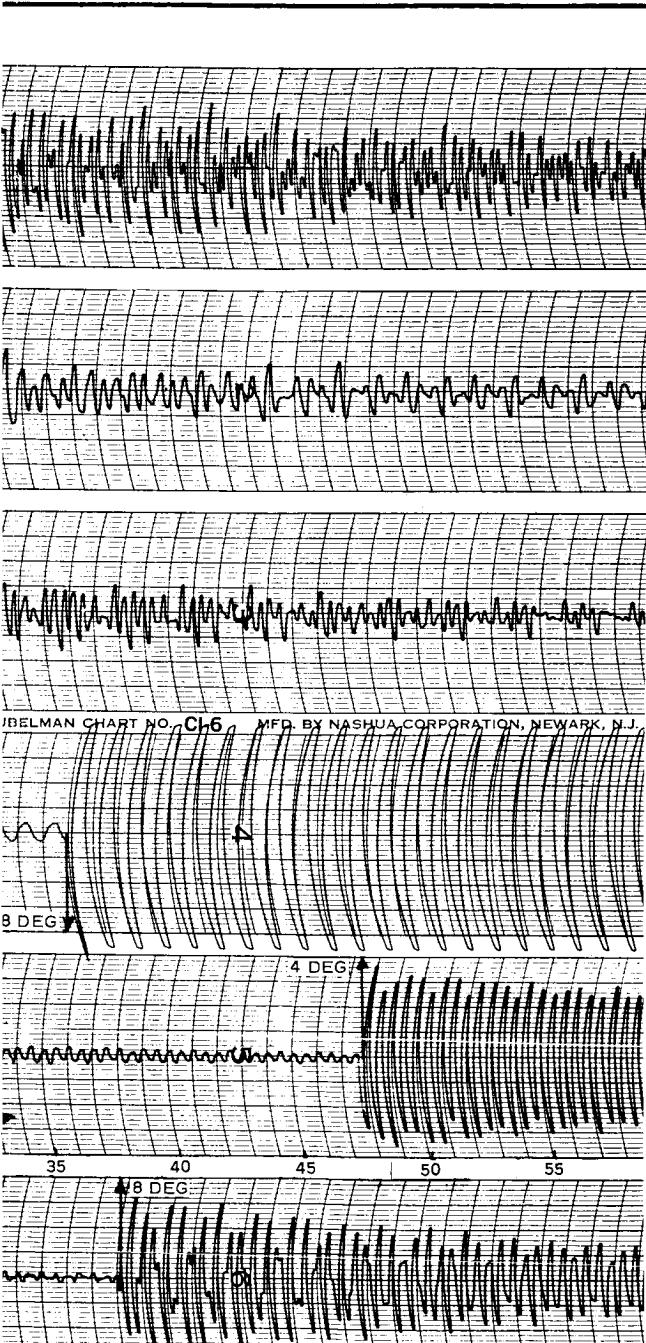


Figure D-25 - Optimum Configuration with Plunging-Spring Constant Decreased Four Percent with Large Roll

2

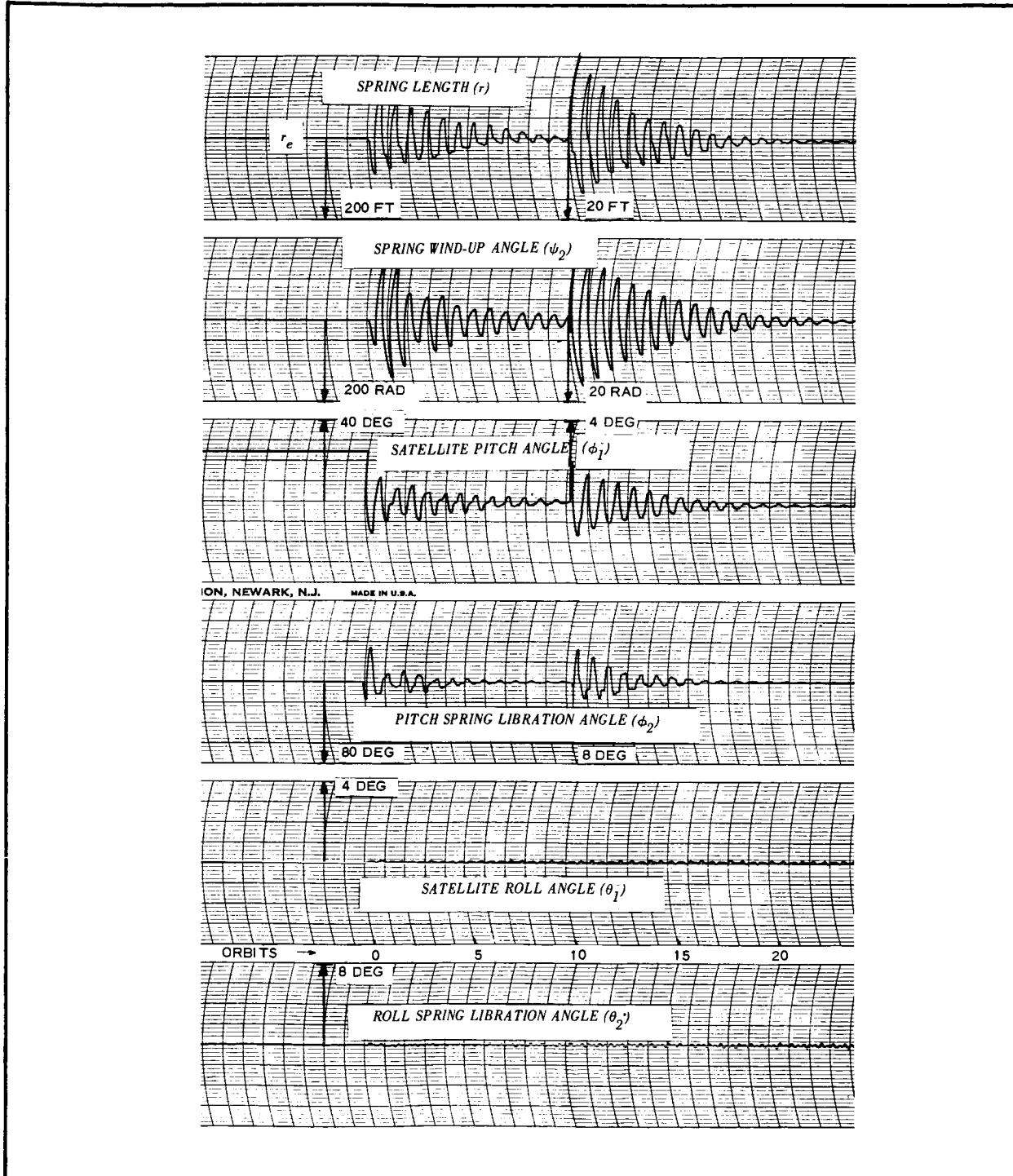


Figure D-26 - Optimum Configuration with Torsional-Spring Constant Increased 23 Percent with Large Pitch

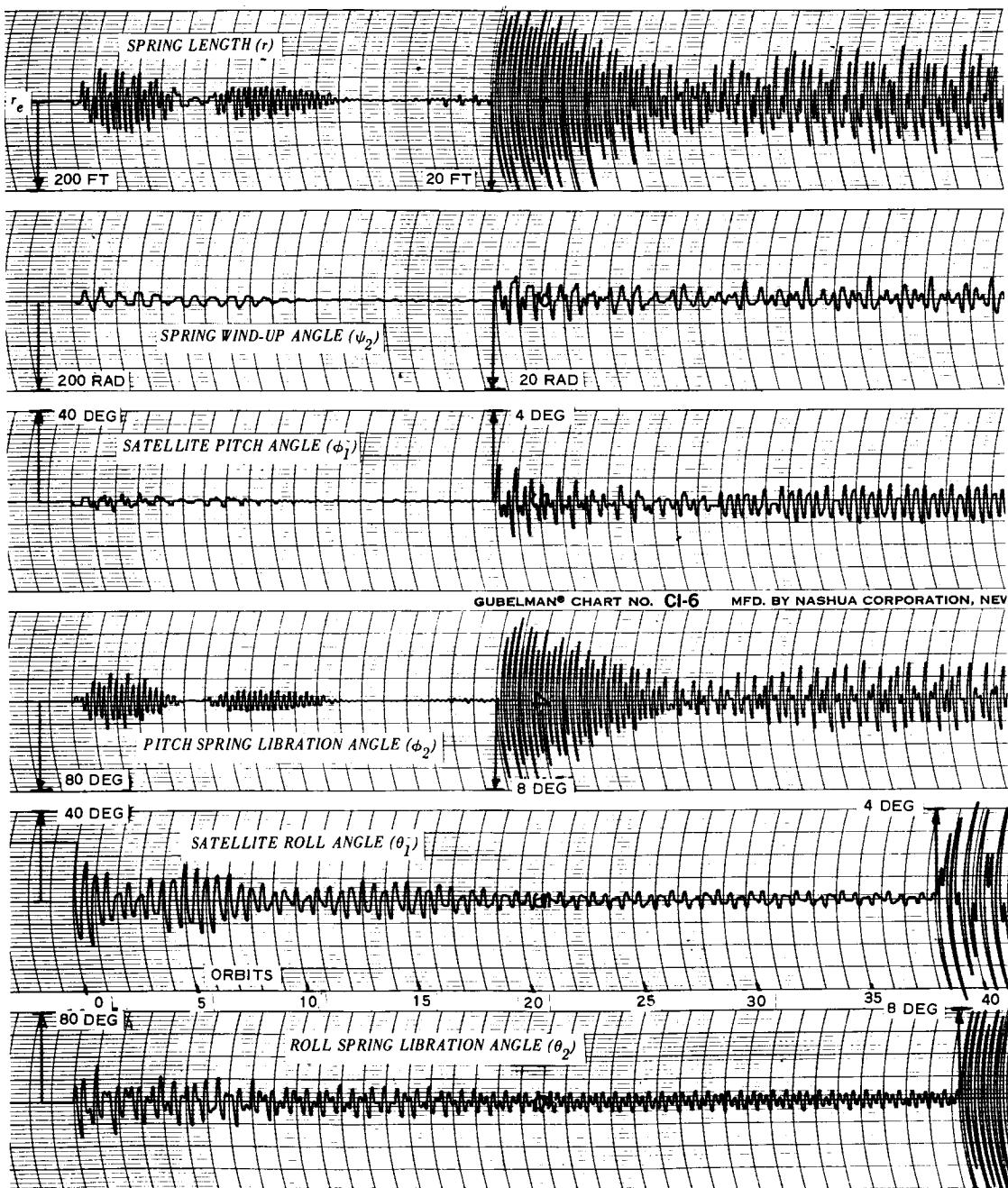


Figure D-27 - Optimum Configuration with Torsional-Spring Constant Increased 23 Percent with Large Roll

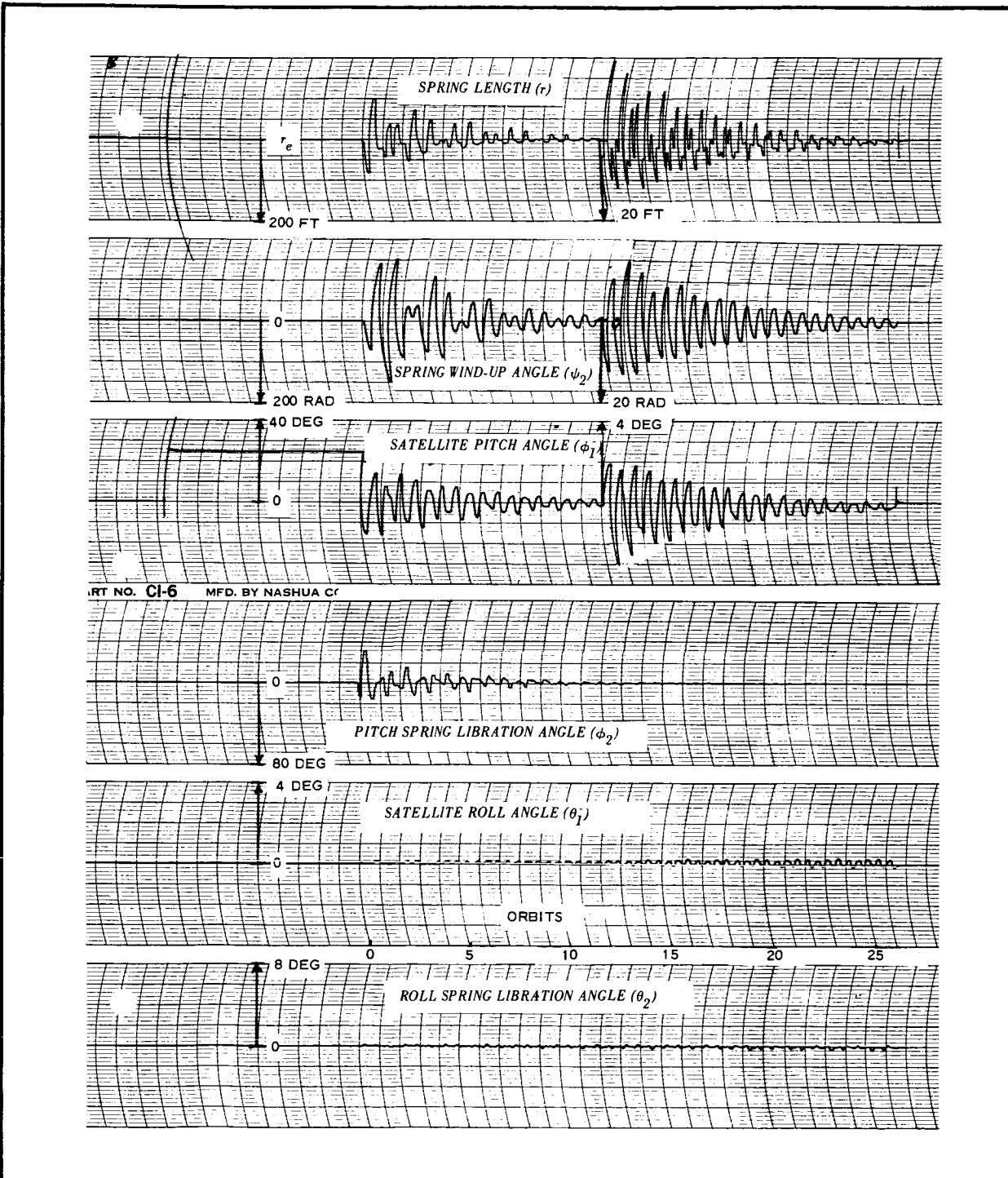


Figure D-28 - Optimum Configuration with Torsional-Spring Constant Decreased 42 Percent with Large Pitch

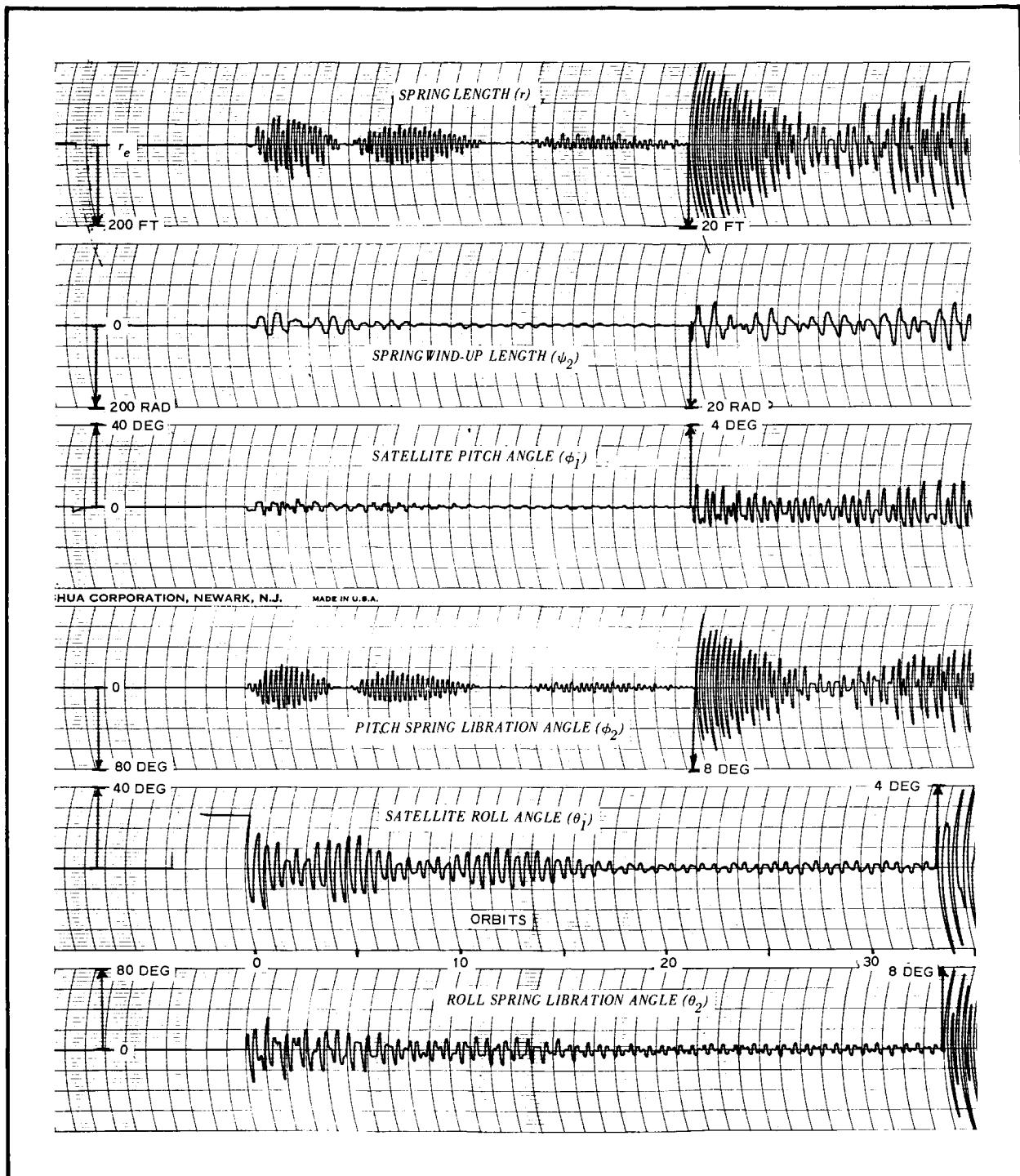


Figure D-29 - Optimum Configuration with Torsional-Spring Constant Decreased 42 Percent with Large Roll

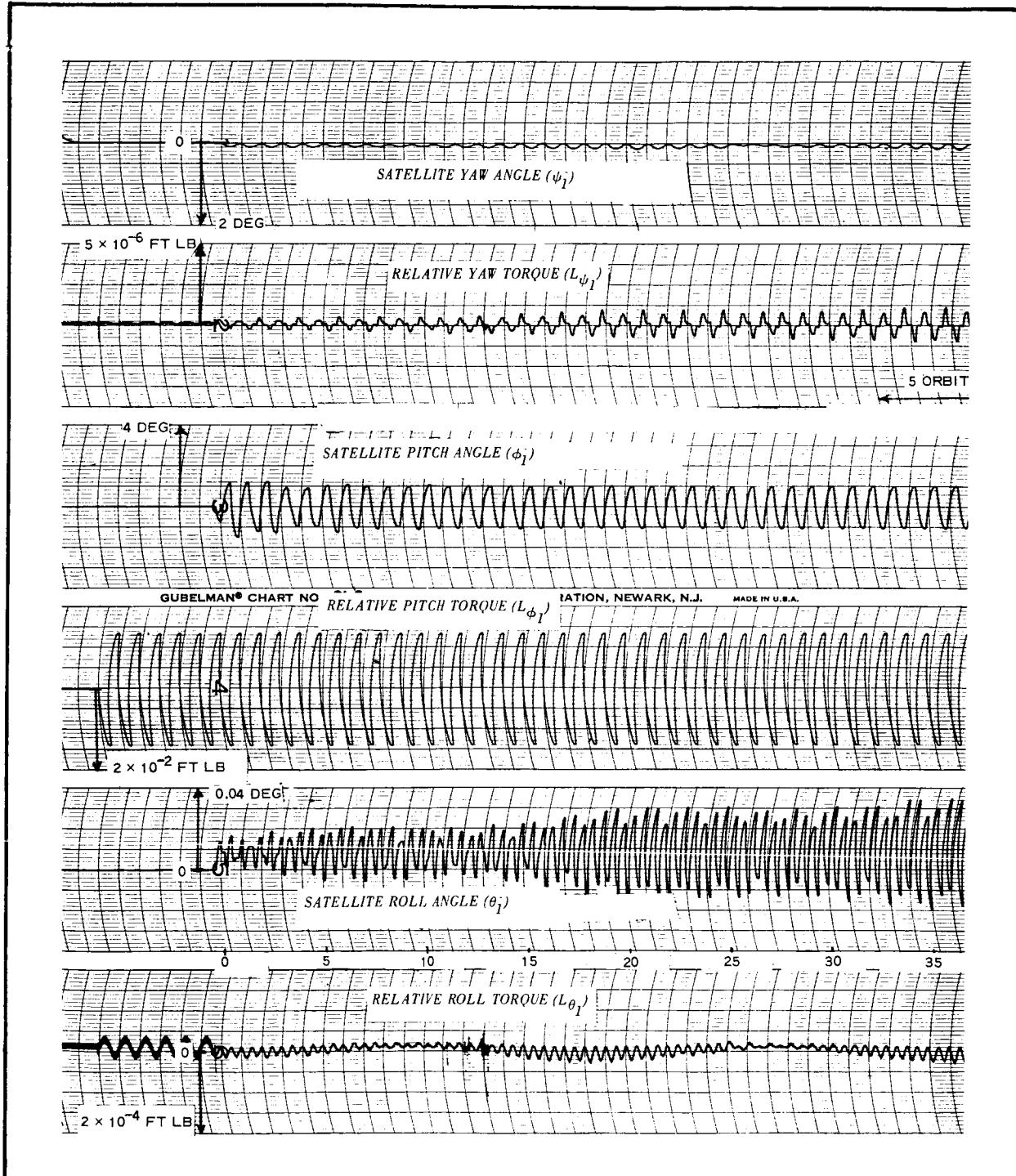


Figure D-30 - Optimum Configuration, Steady-State Response to 0.01 Eccentricity

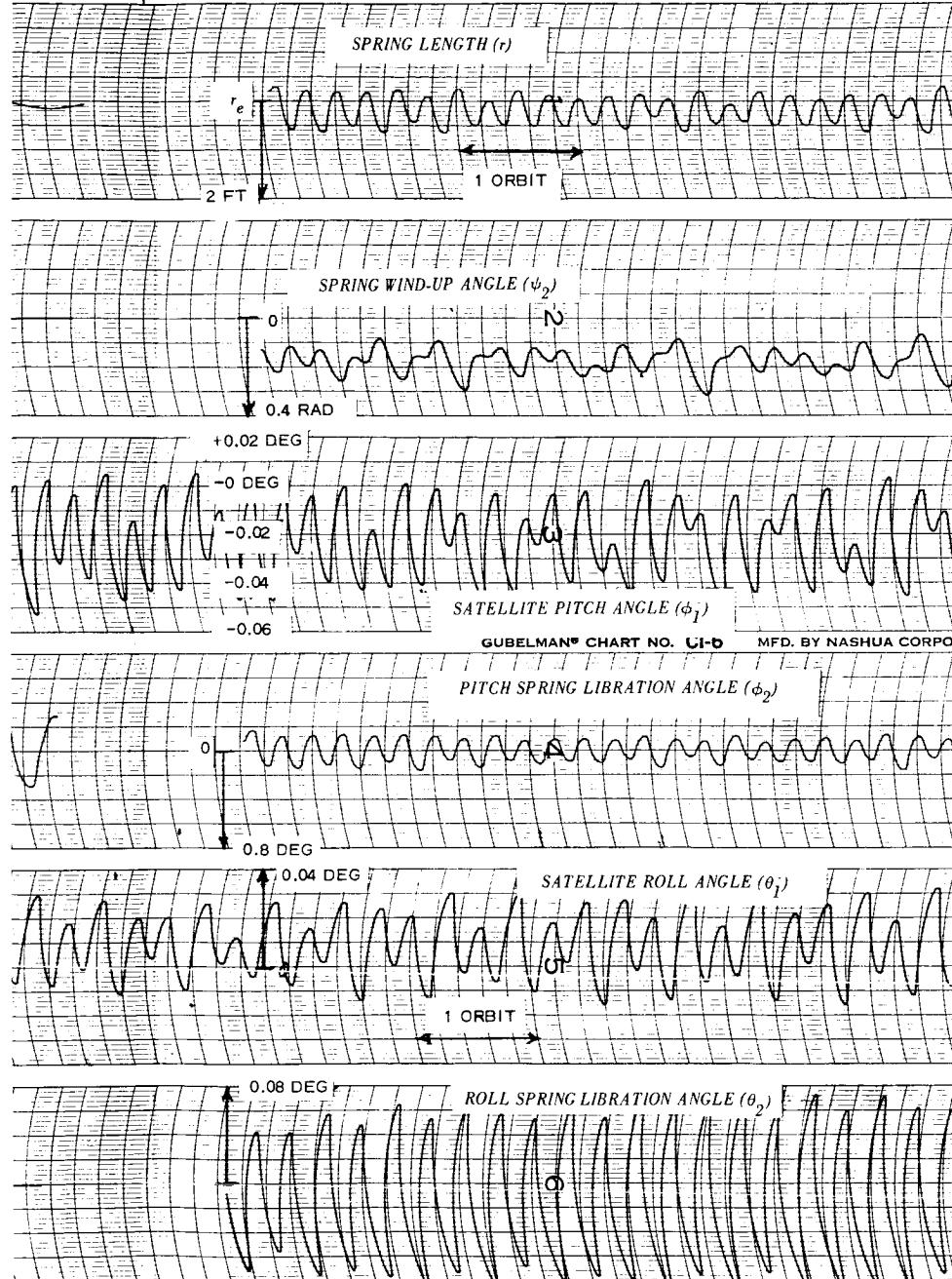




Figure D-31 - Optimum Configuration, Steady-State Response to Sun in Orbital Plane

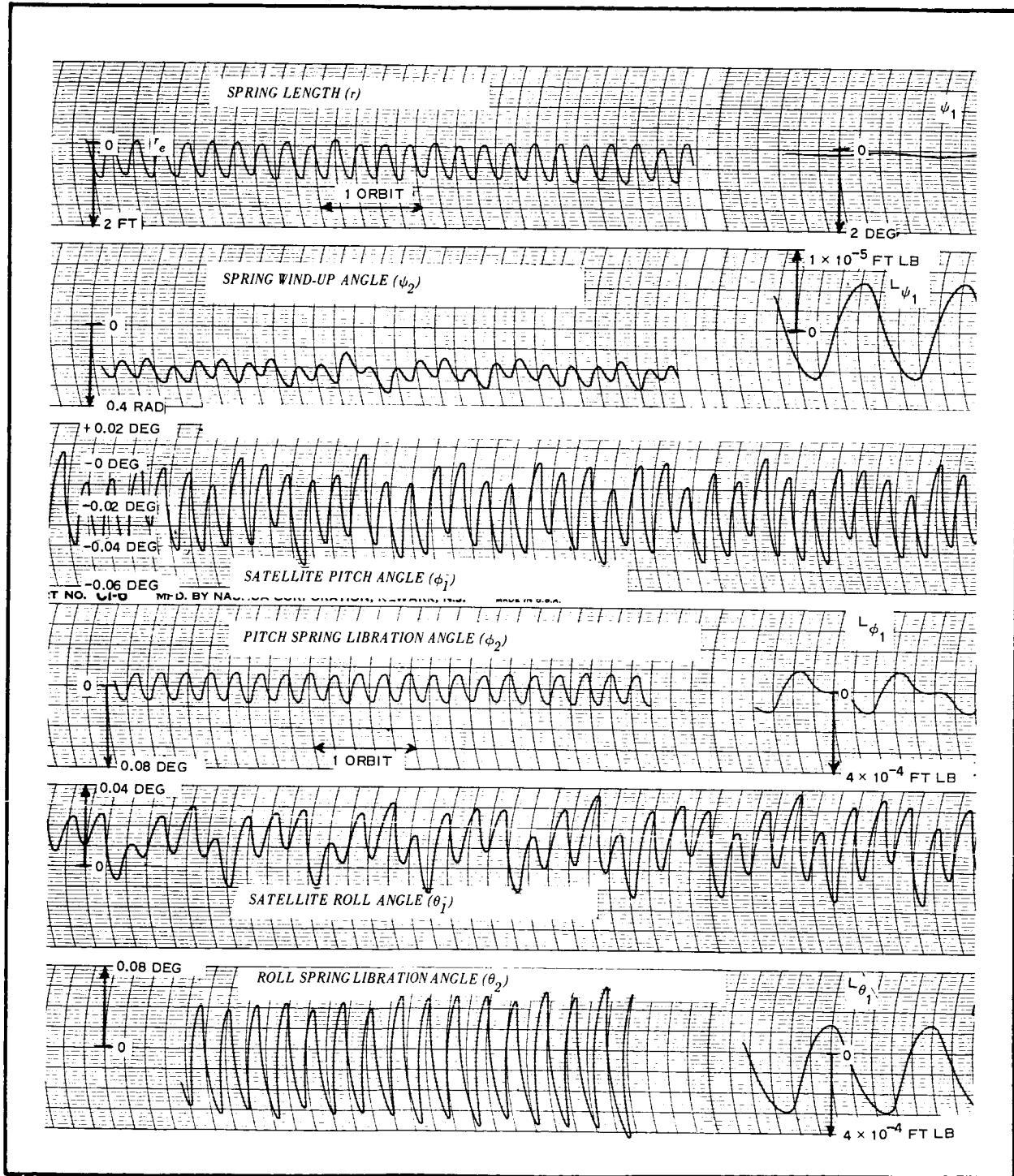
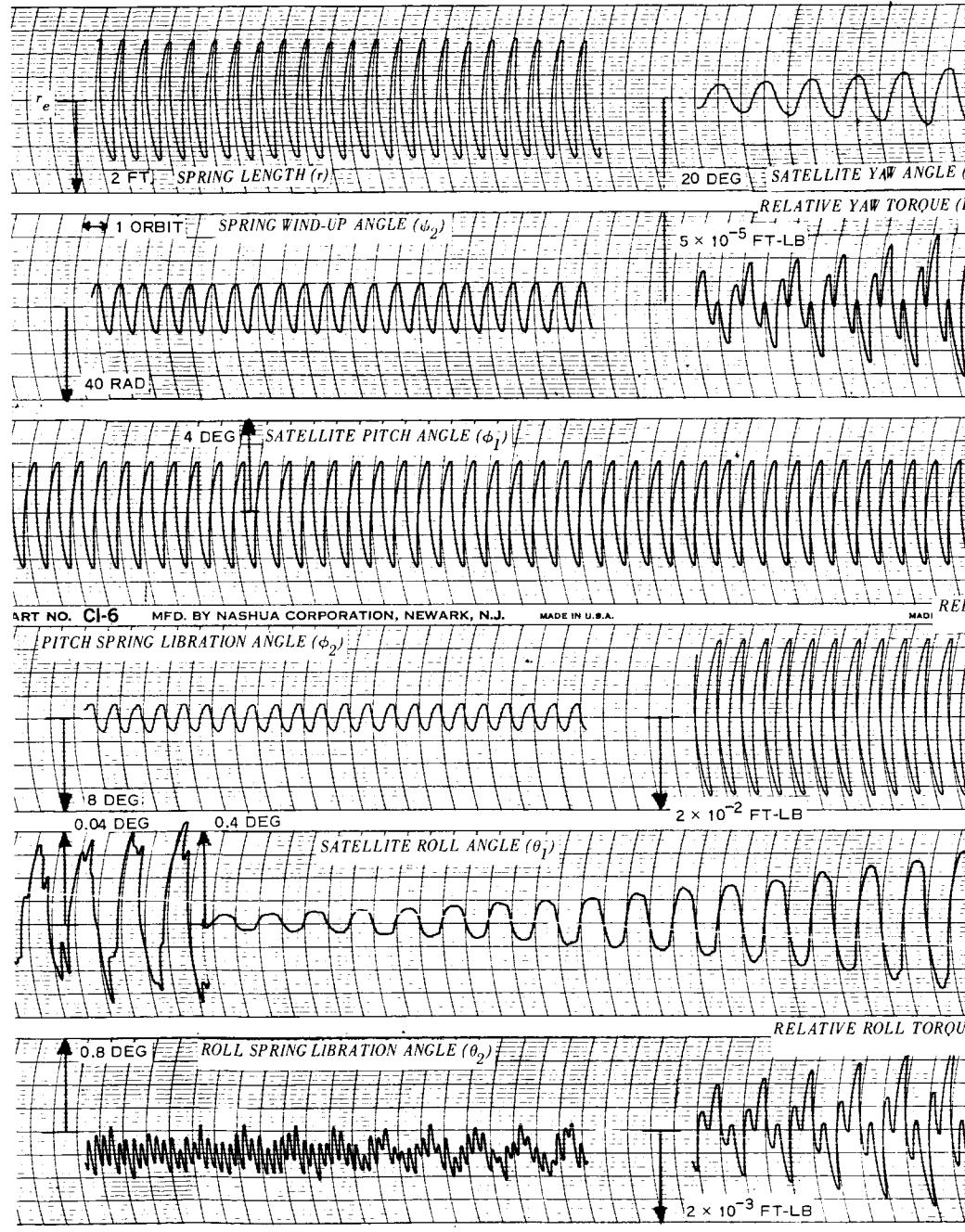


Figure D-32 - Optimum Configuration, Steady-State Response to Sun 45 Degrees to Orbital Plane



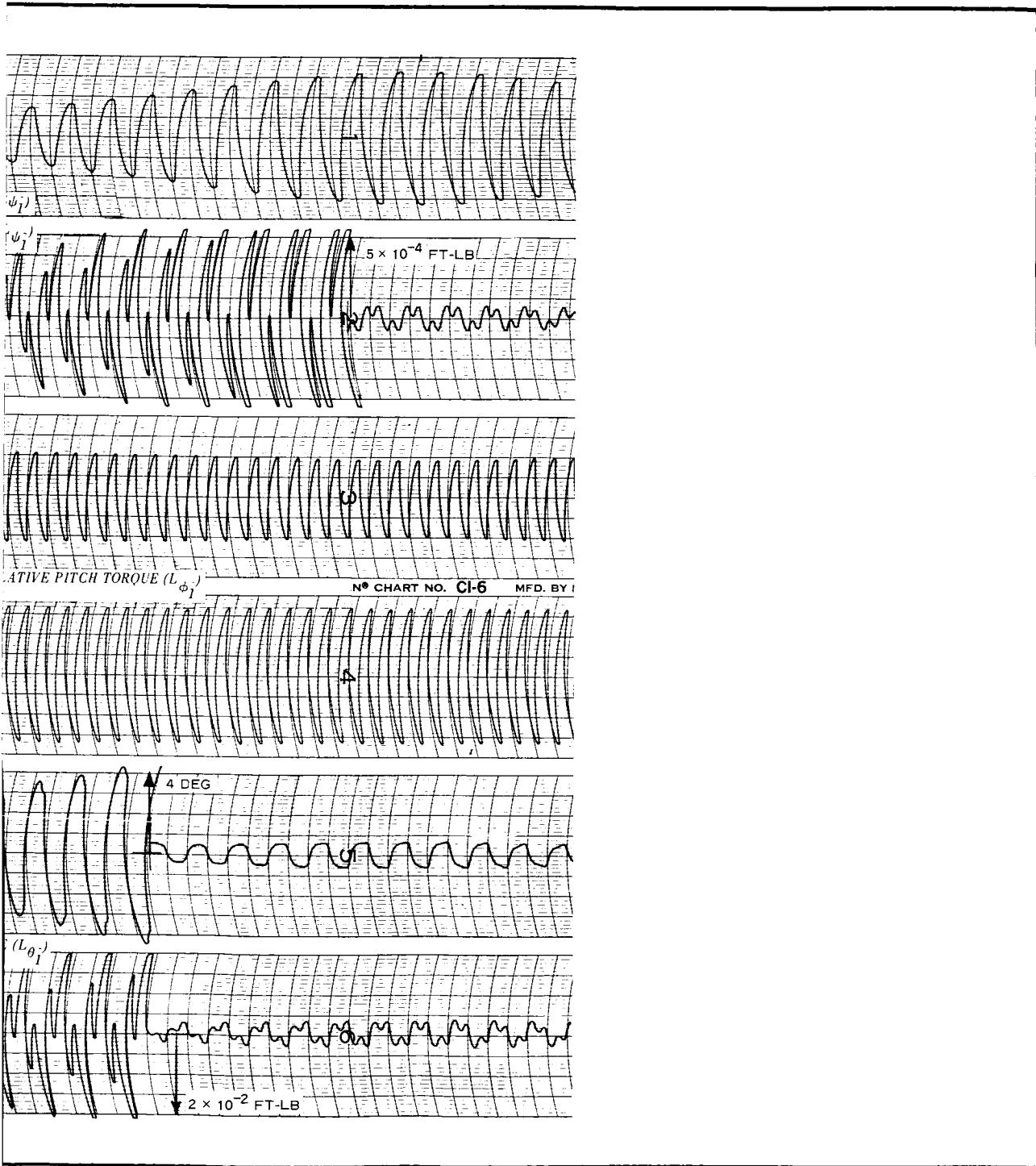
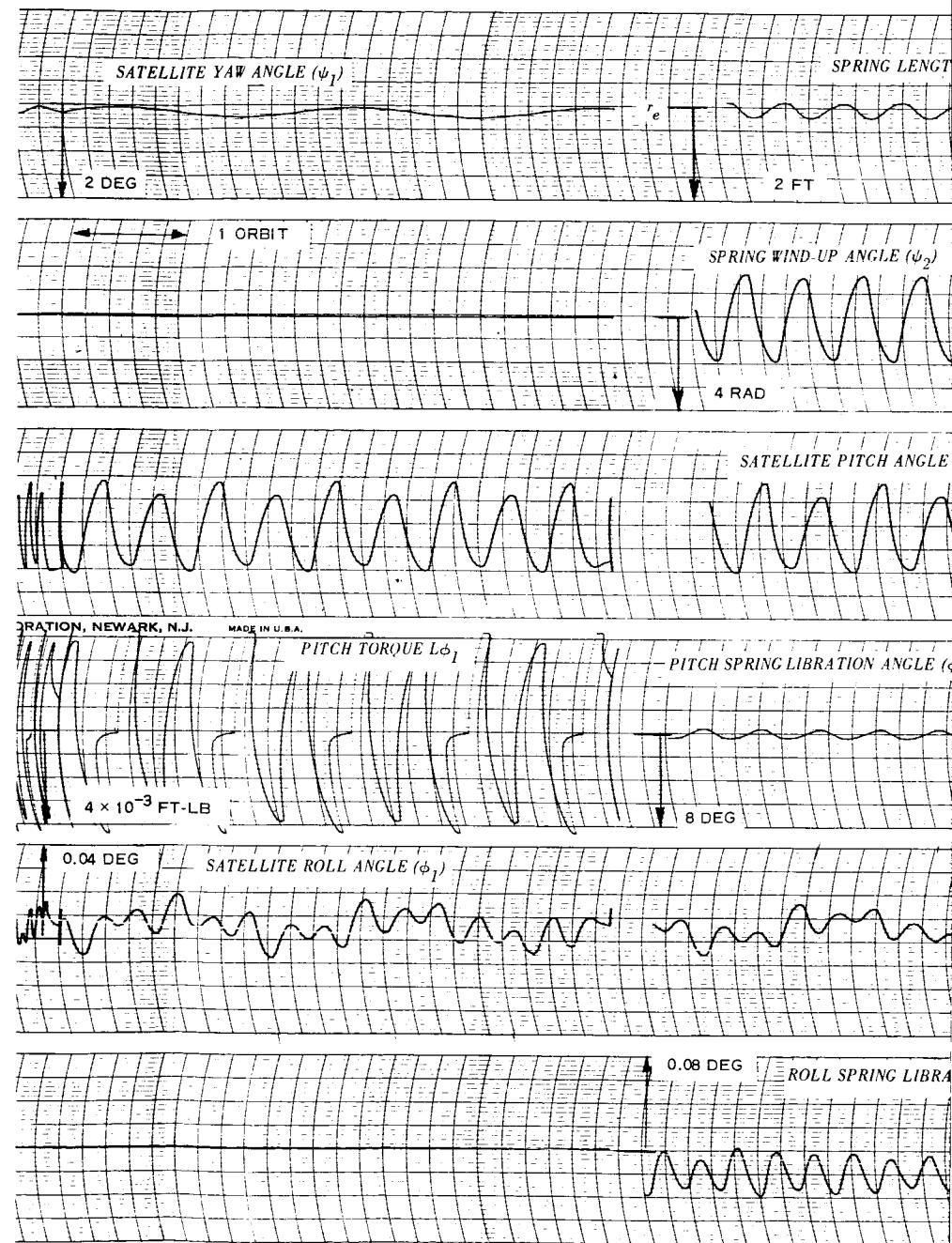


Figure D-33 - Preferred Unphotolyzed Configuration, Steady-State Response to 0.01 Eccentricity



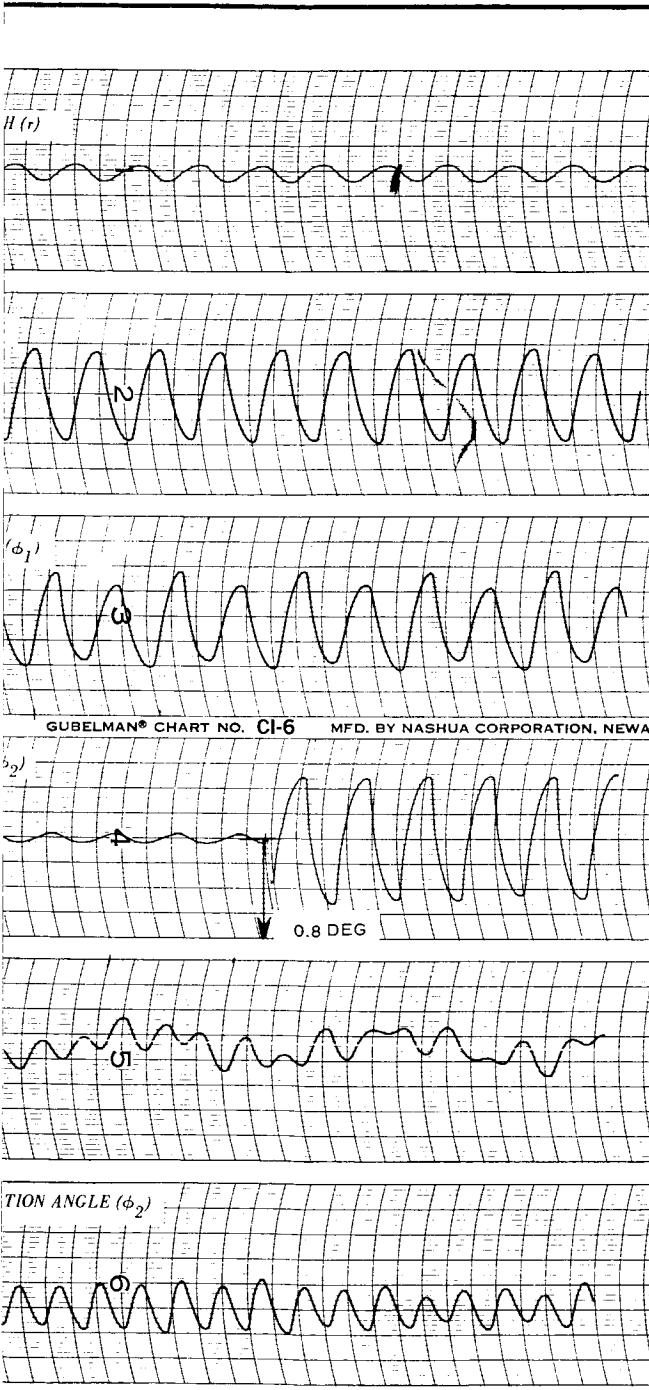


Figure D-34 - Preferred Unphotolyzed Configuration, Steady-State Response to Sun in Orbital Plane

2

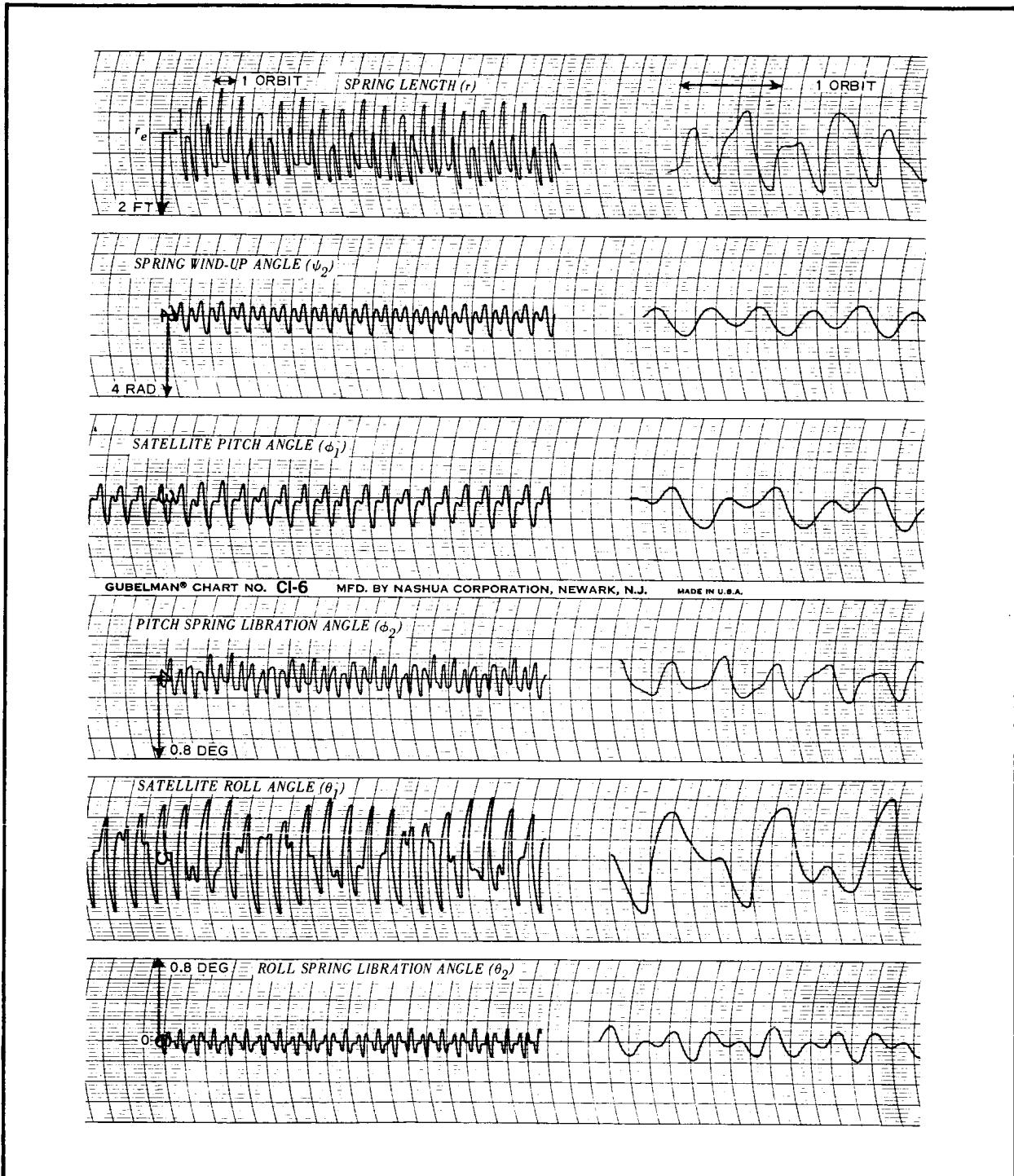
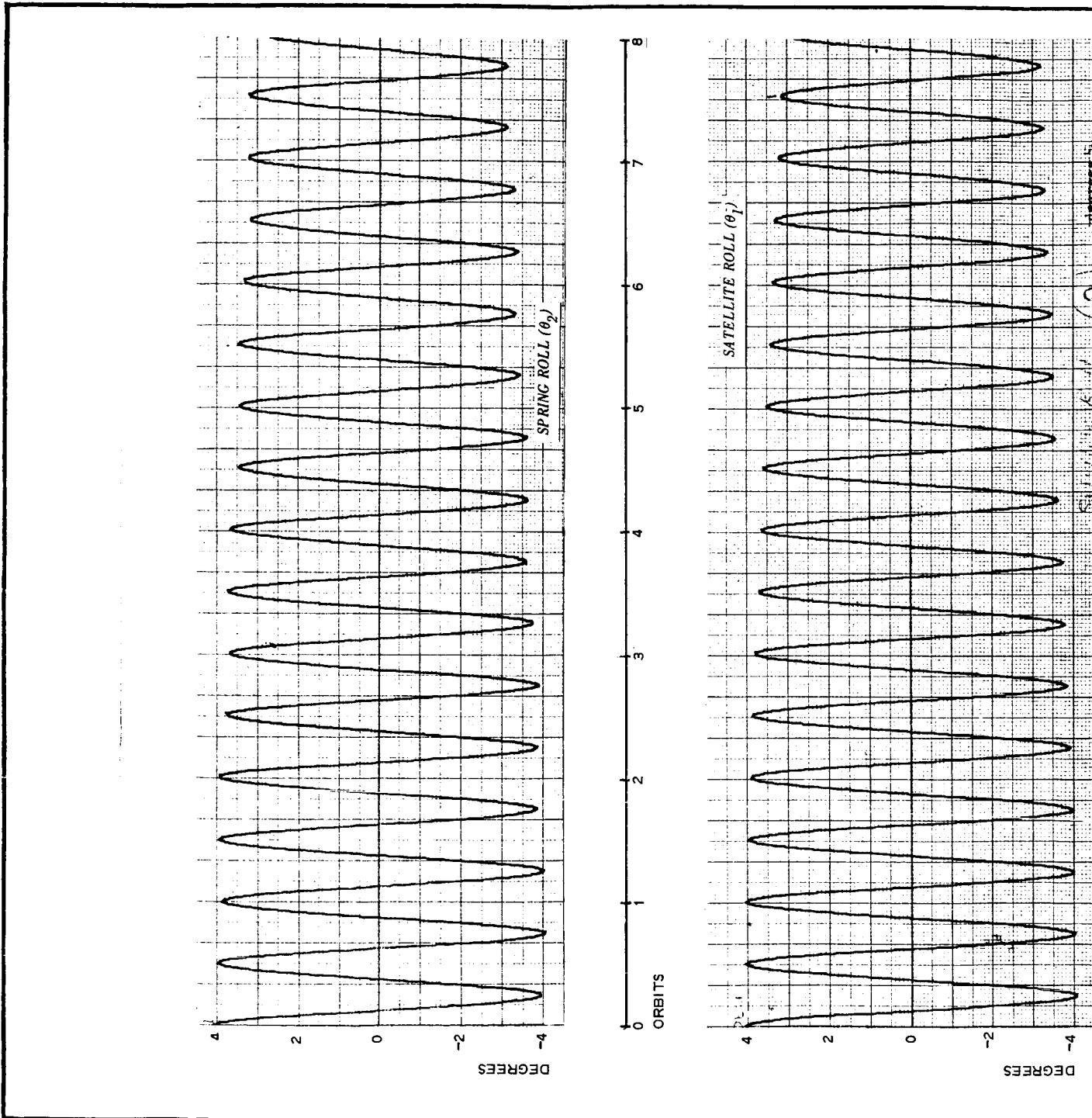
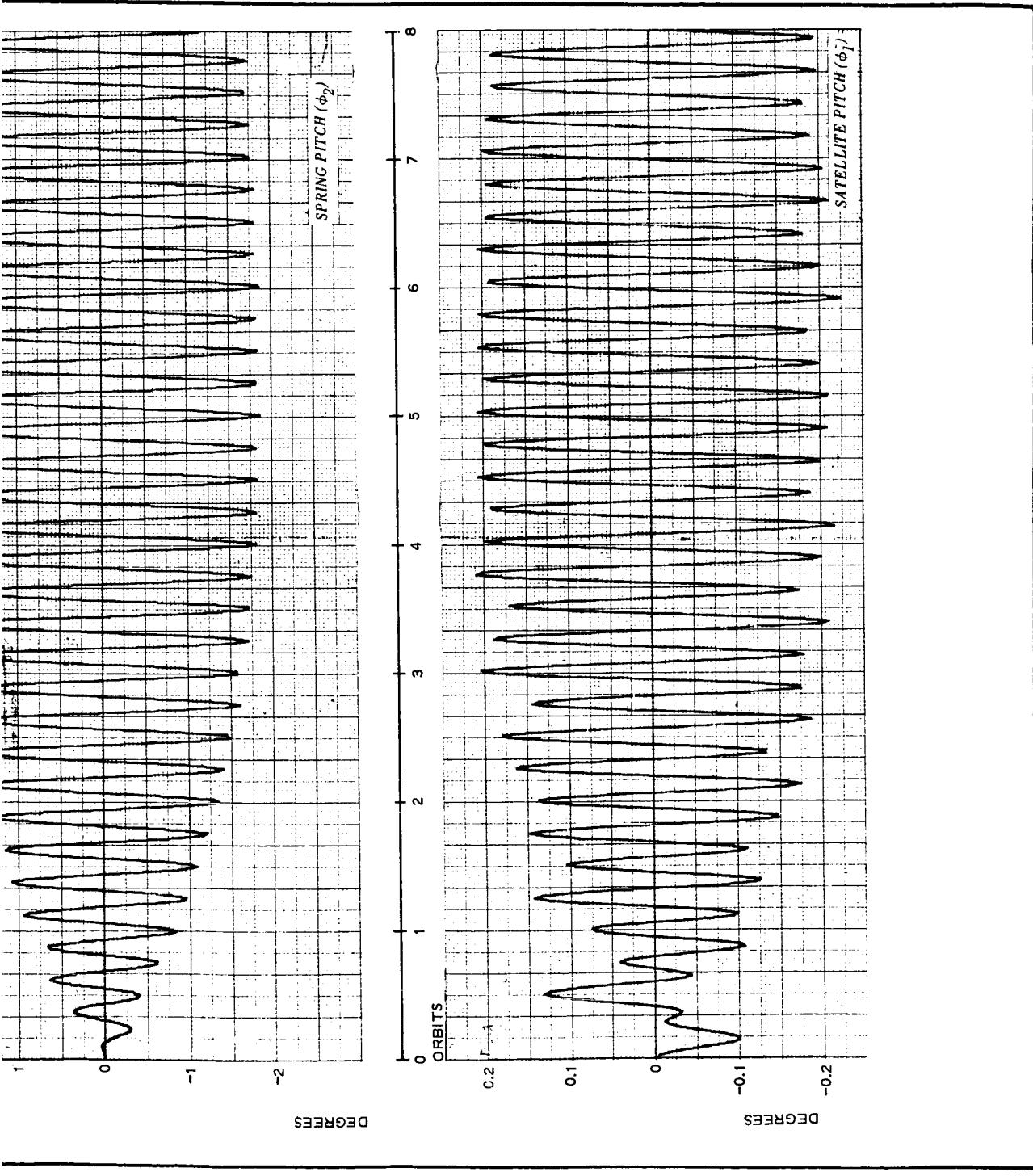


Figure D-35 - Preferred Unphotolyzed Configuration, Steady-State Response to Sun 45 Degrees to Orbital Plane

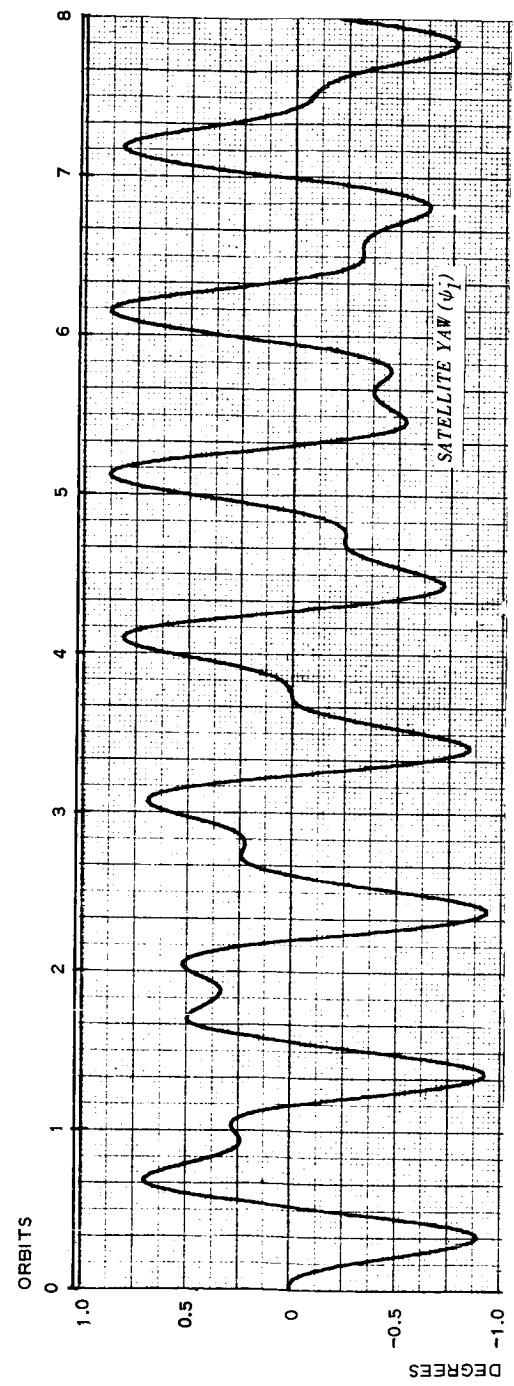
APPENDIX E - TRANSIENT-RESPONSE AND STEADY-STATE-RESPONSE
HISTORIES FROM DIGITAL-COMPUTER STUDY



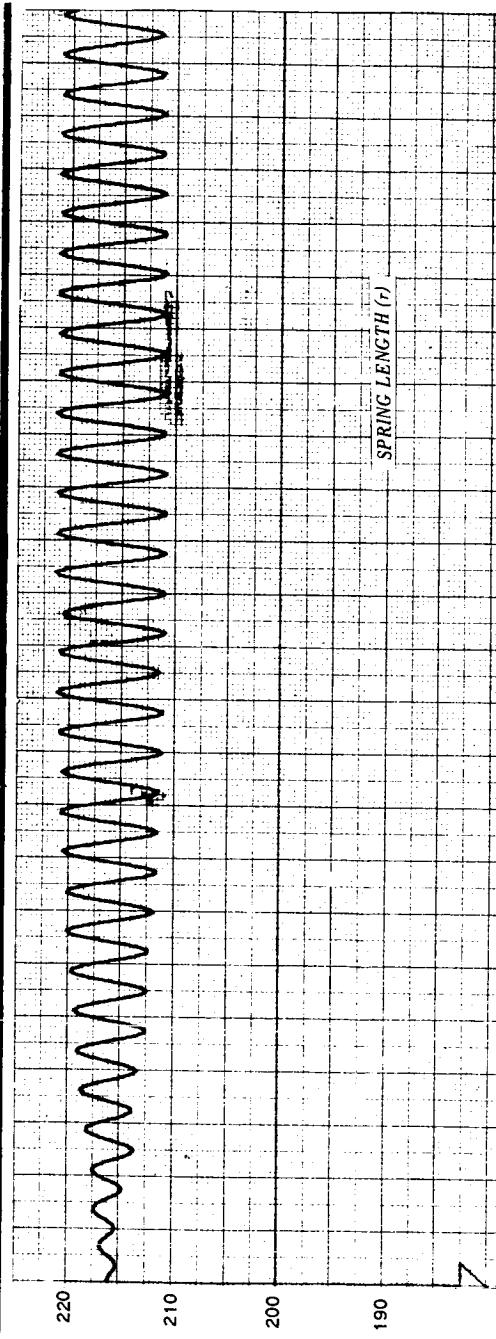


Run 127, Sheet 1 - Trial Roll-Transient-Response Run,
 $K_1 = 1.0840 \times 10^{-5}$ Lb per Foot

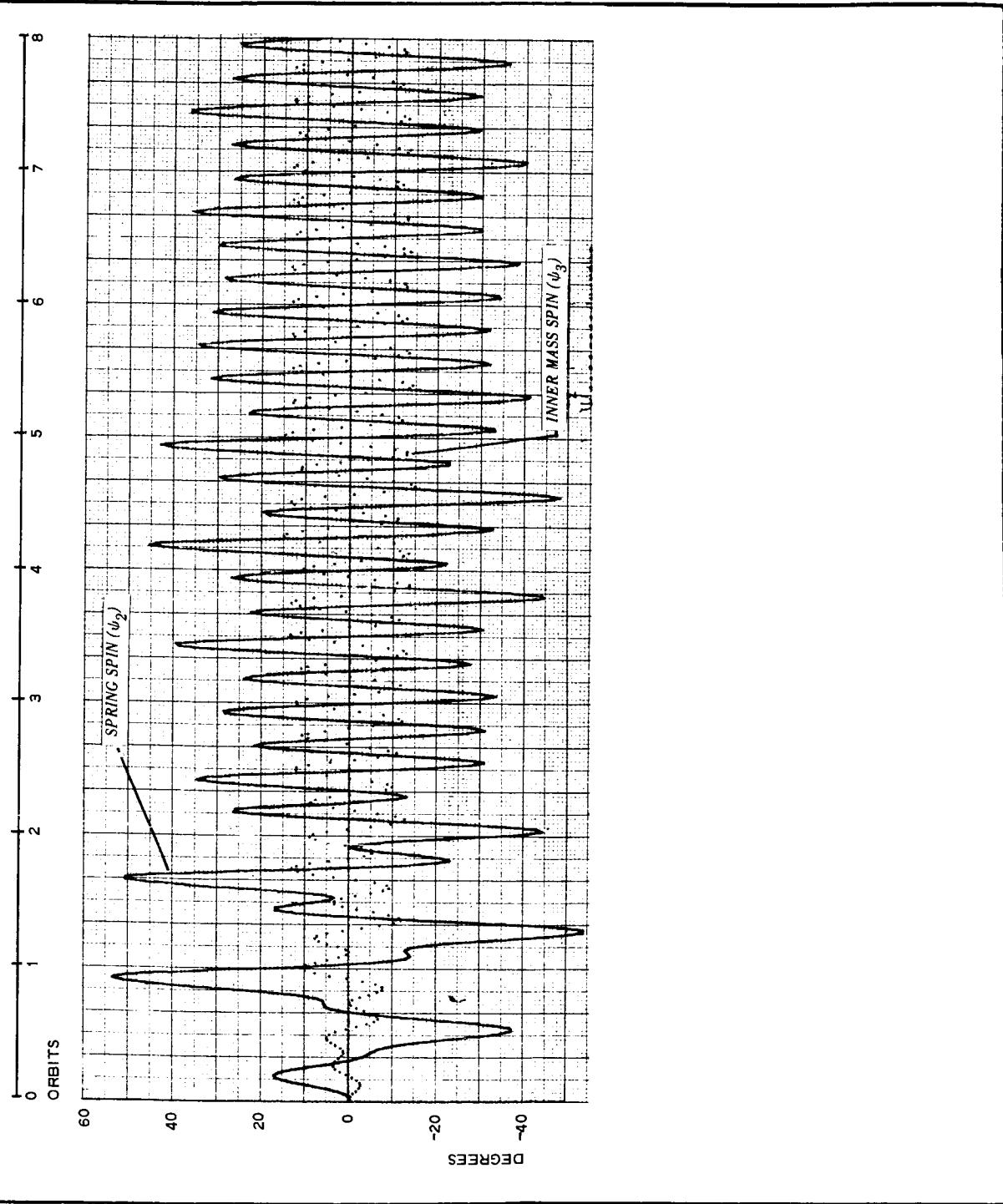
2



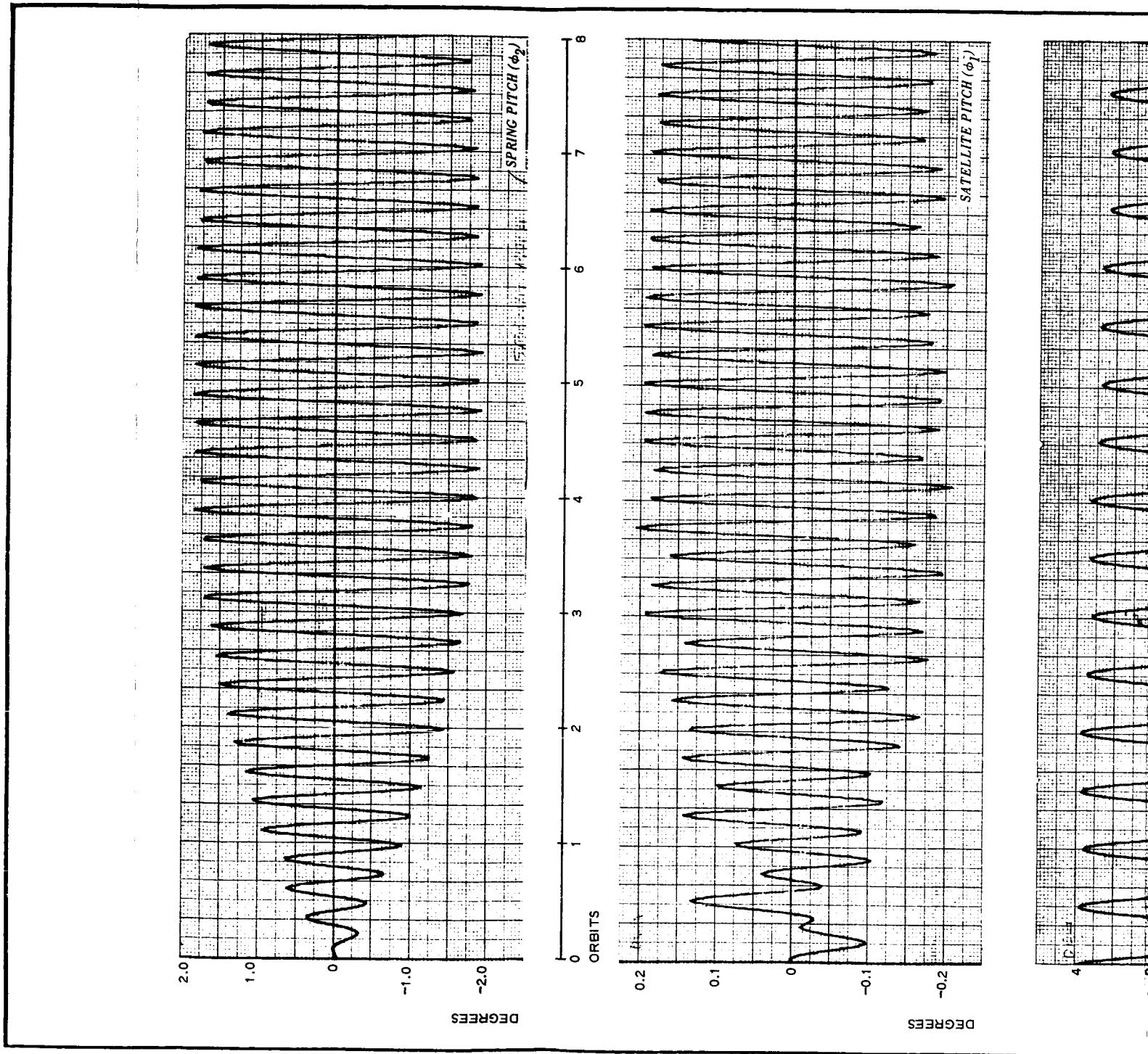
SATELLITE YAW (ϕ)

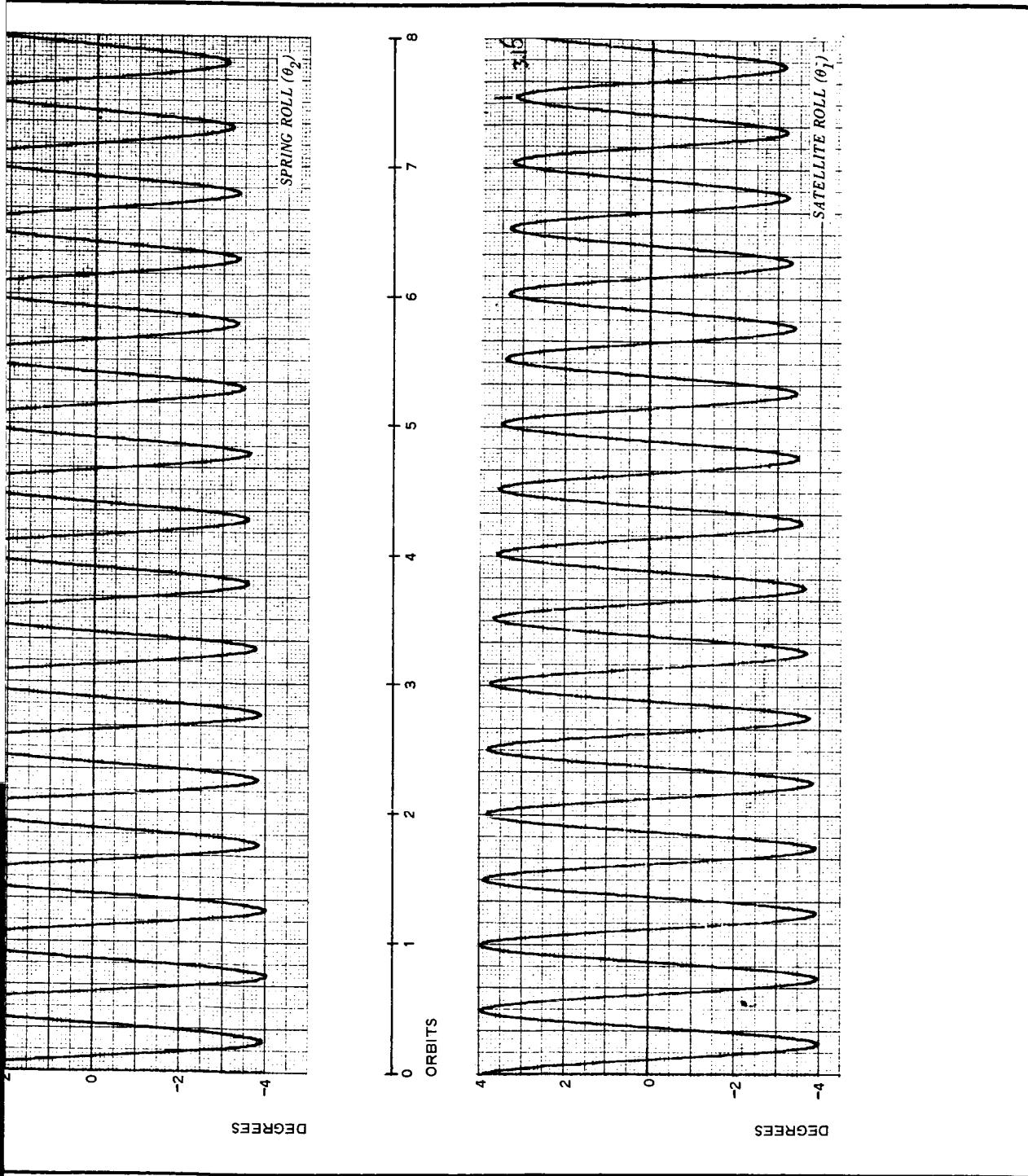


SPRING LENGTH (r)



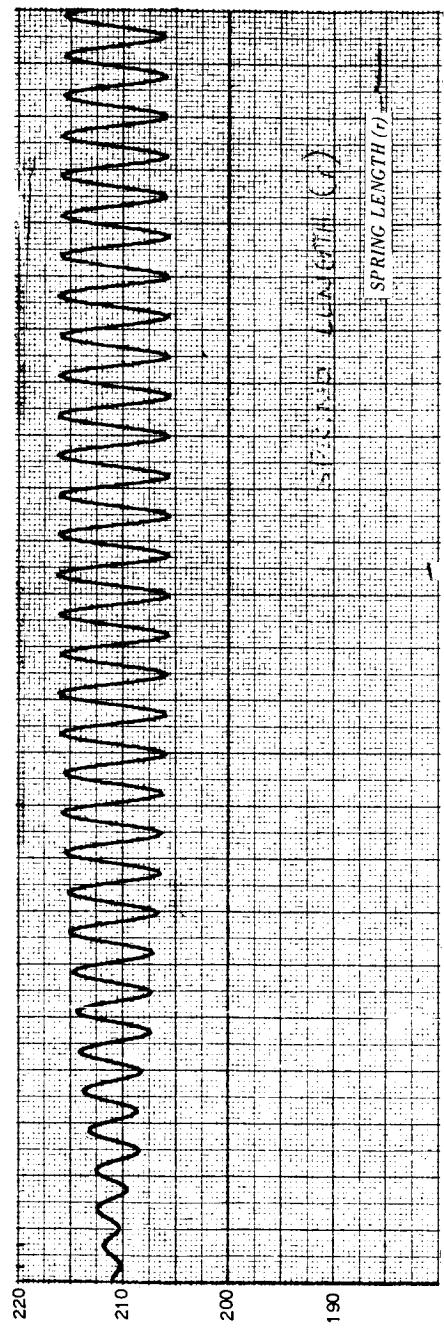
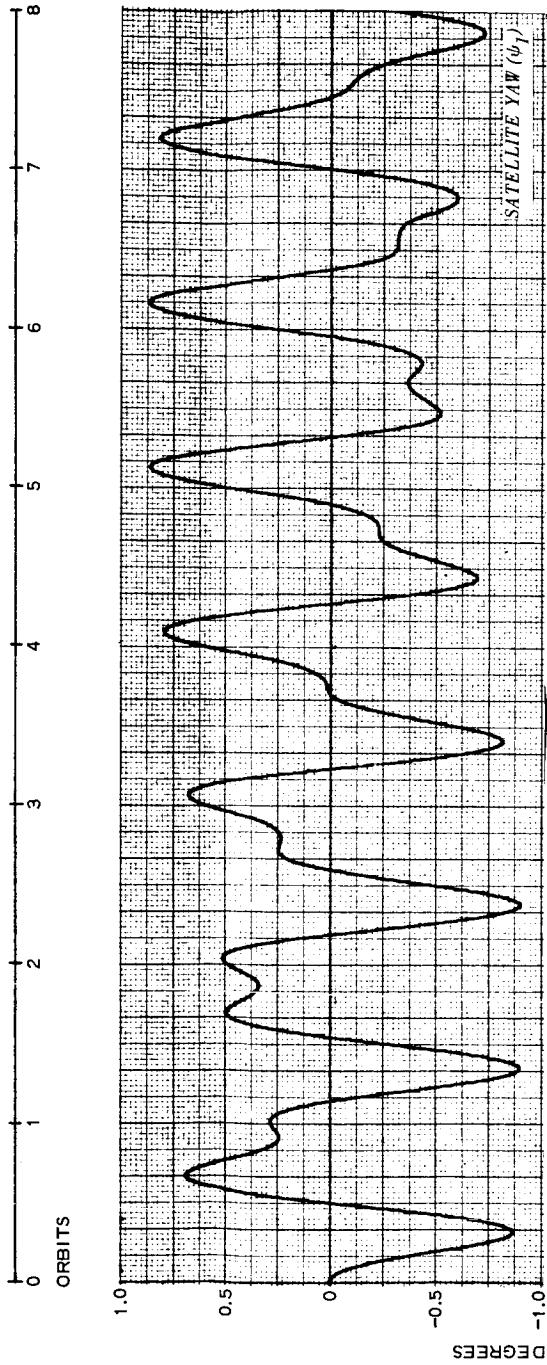
Run 127, Sheet 2 - Trial Roll-Transient-Response Run,
 $K_1 = 1.0840 \times 10^{-5}$ Lb per Foot

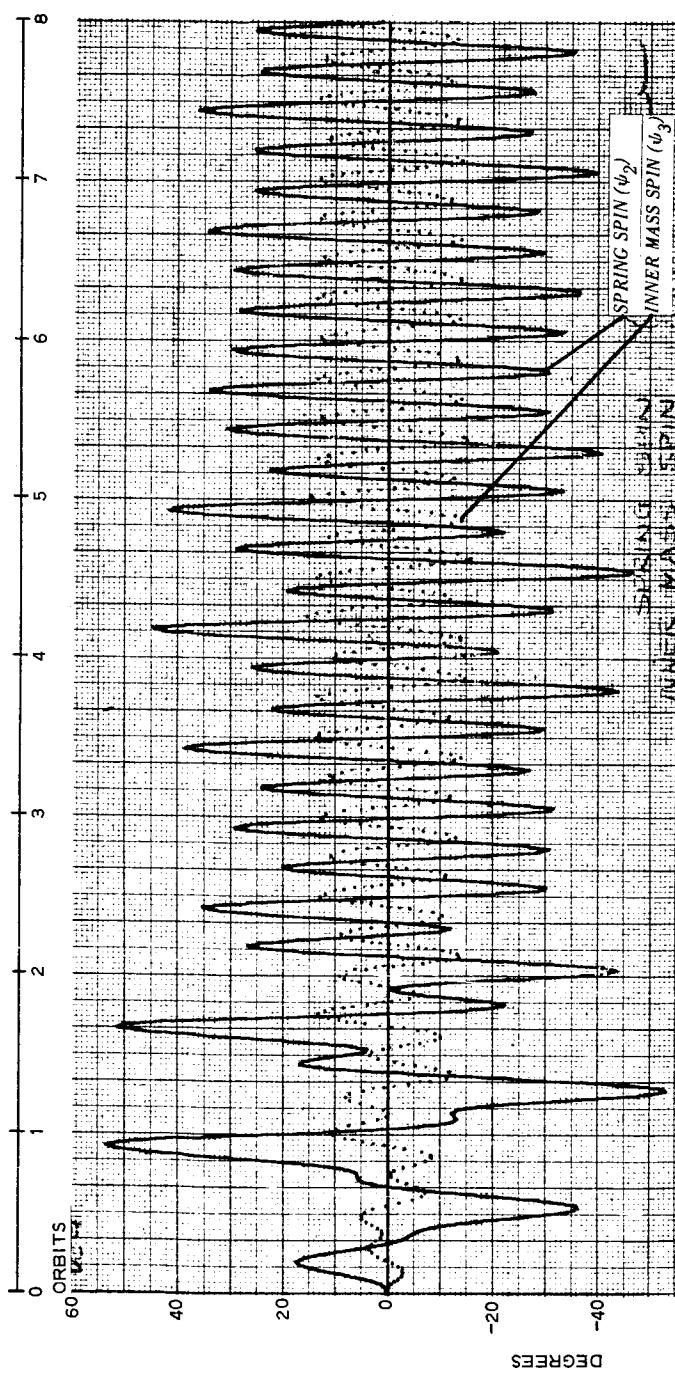




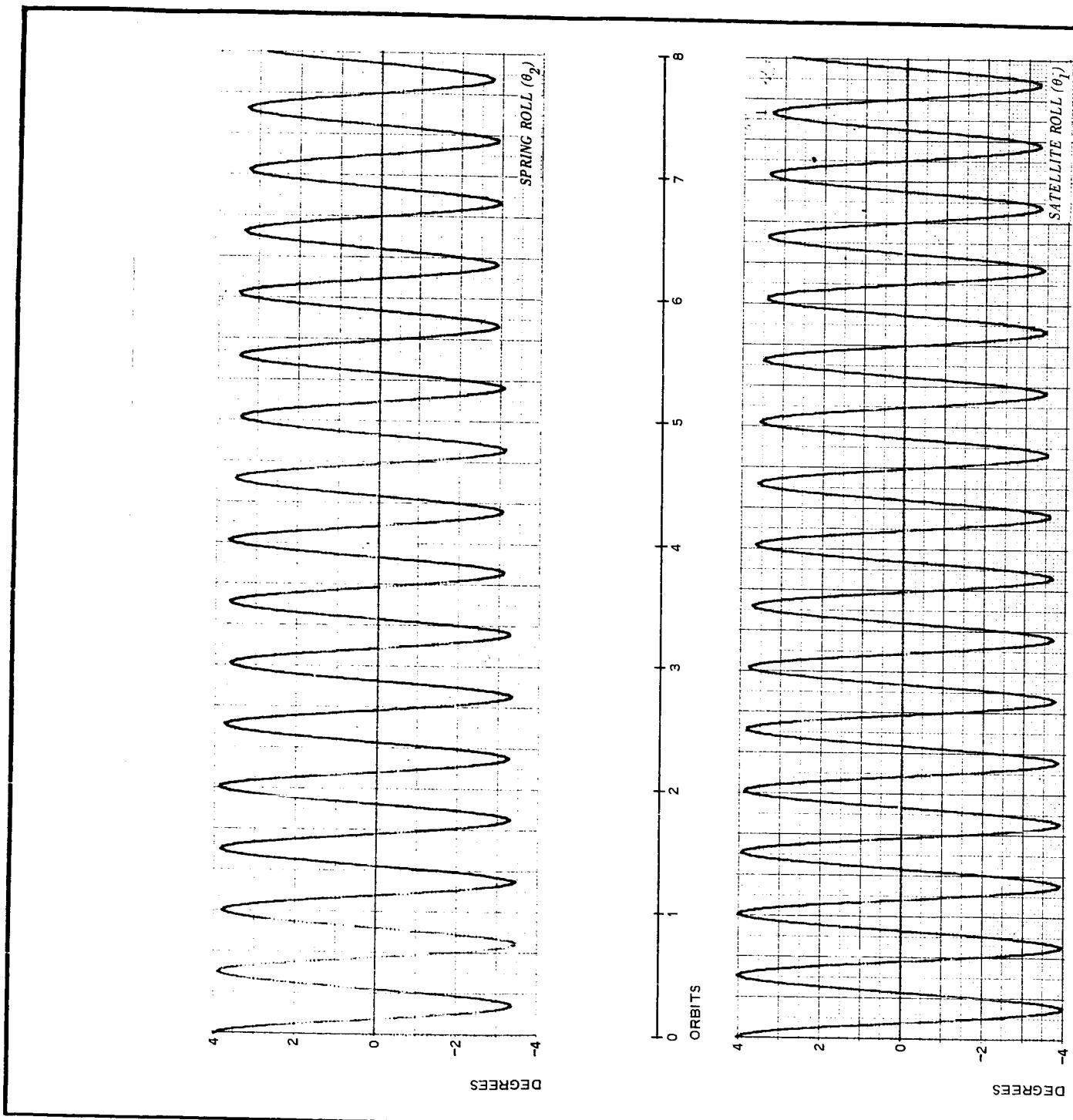
Run 128, Sheet 1 - Trial Roll-Transient-Response Run,
 $K_1 = 1.0992 \times 10^{-5}$ Lb per Foot

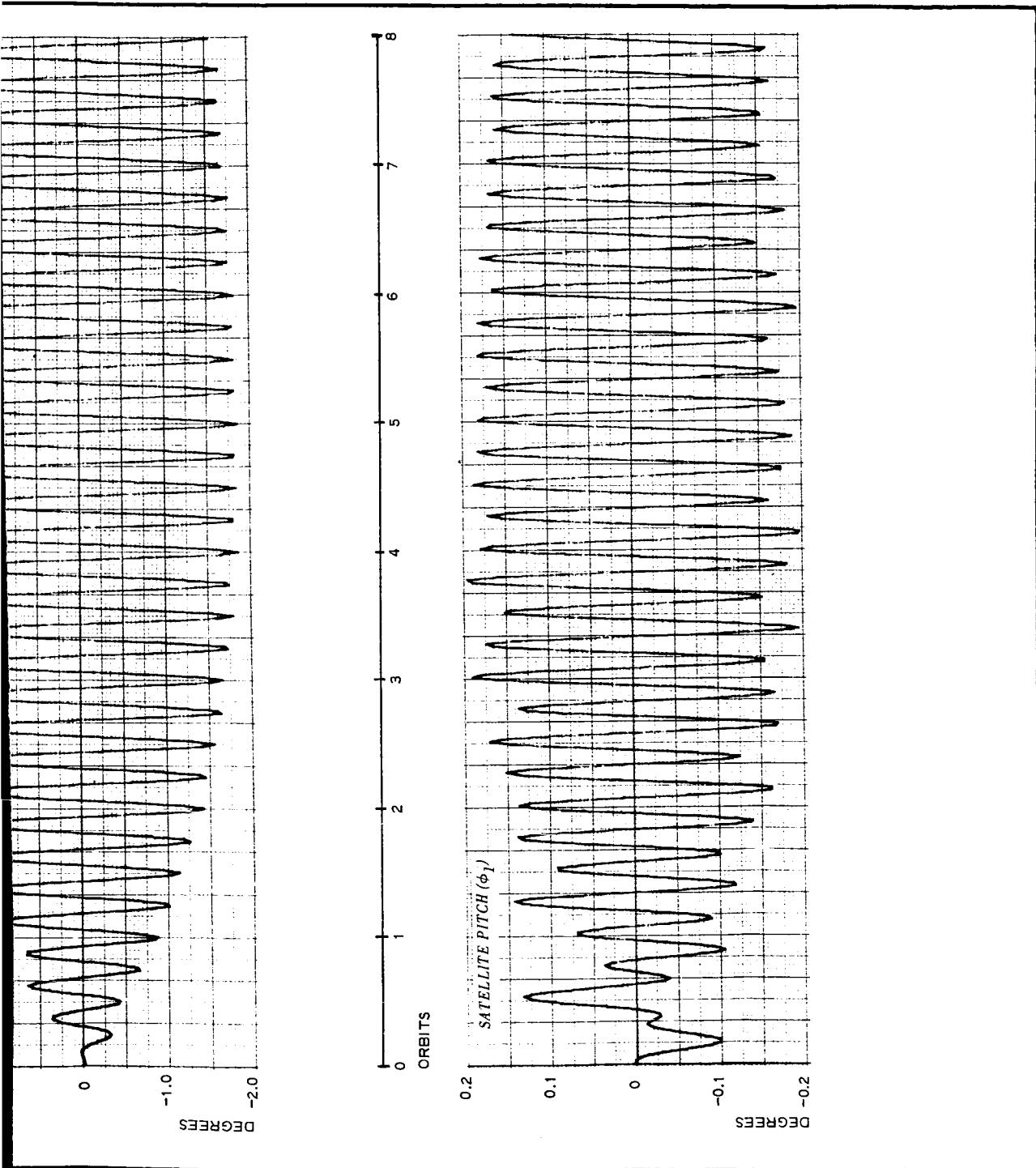
2



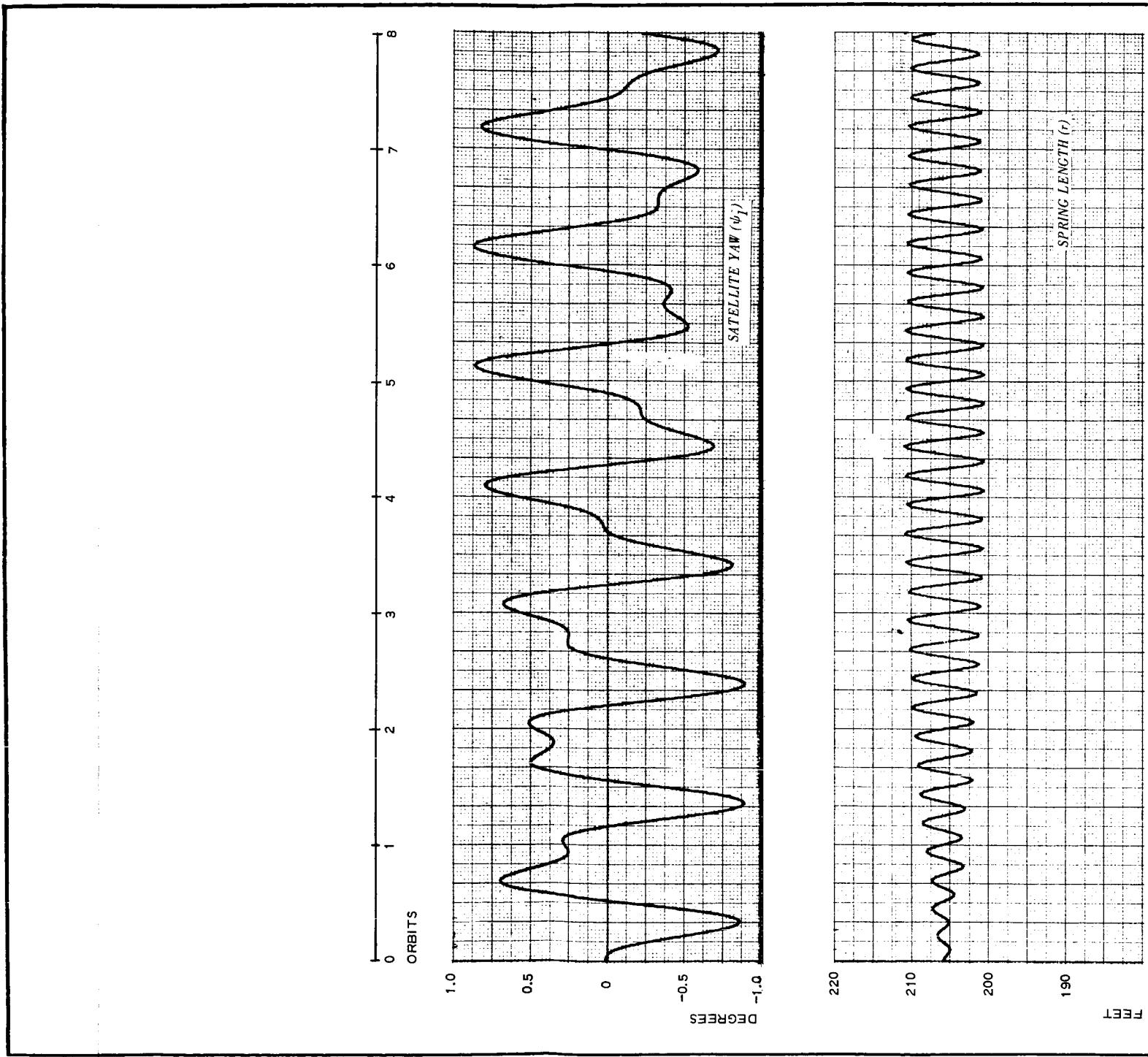


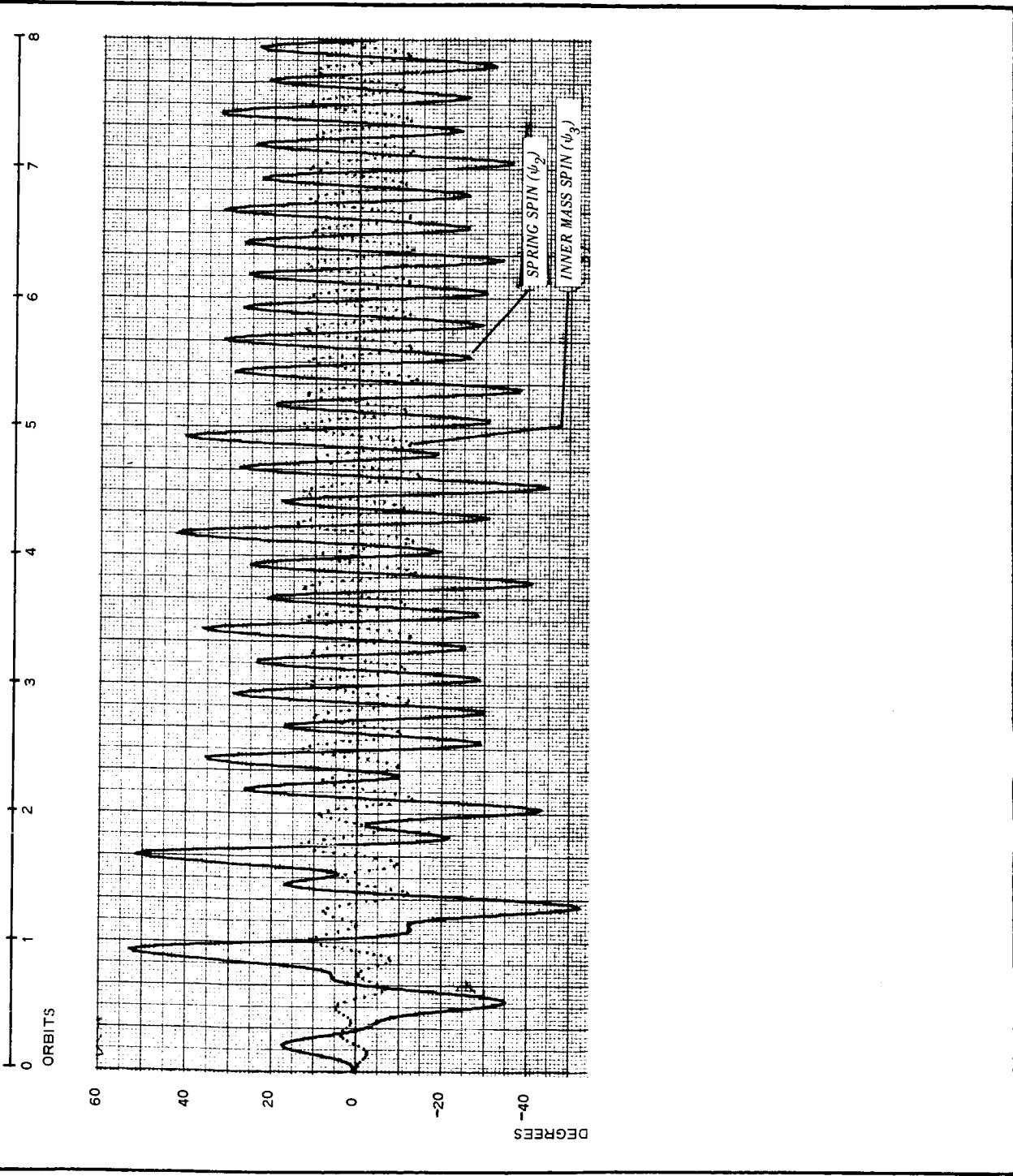
Run 128, Sheet 2 - Trial Roll-Transient-Response Run,
 $K_1 = 1.0992 \times 10^{-5}$ Lb per Foot





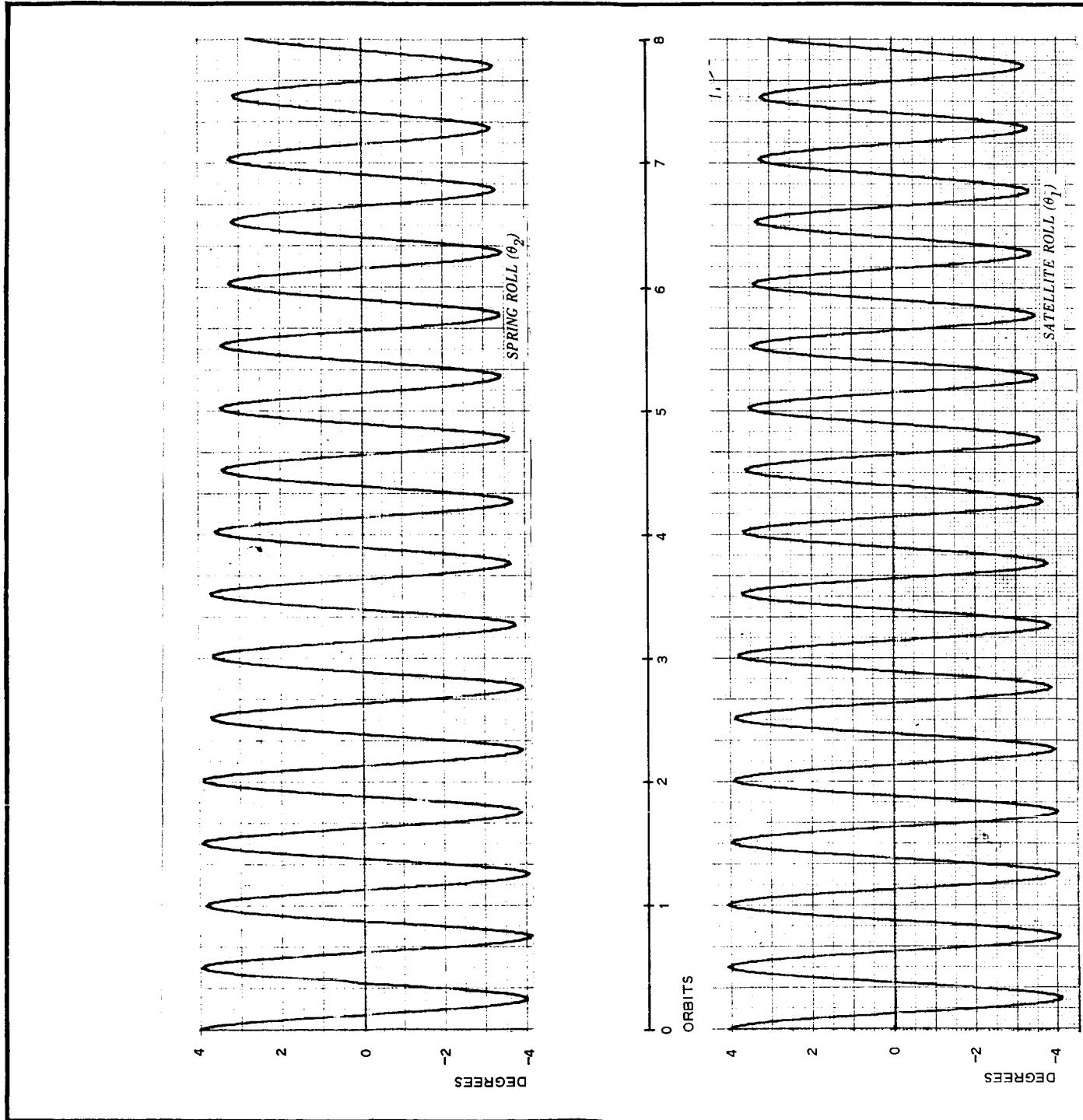
Run 129, Sheet 1 - Trial Roll-Transient-Response Run,
 $K_1 = 1.1145 \times 10^{-5}$ Lb per Foot

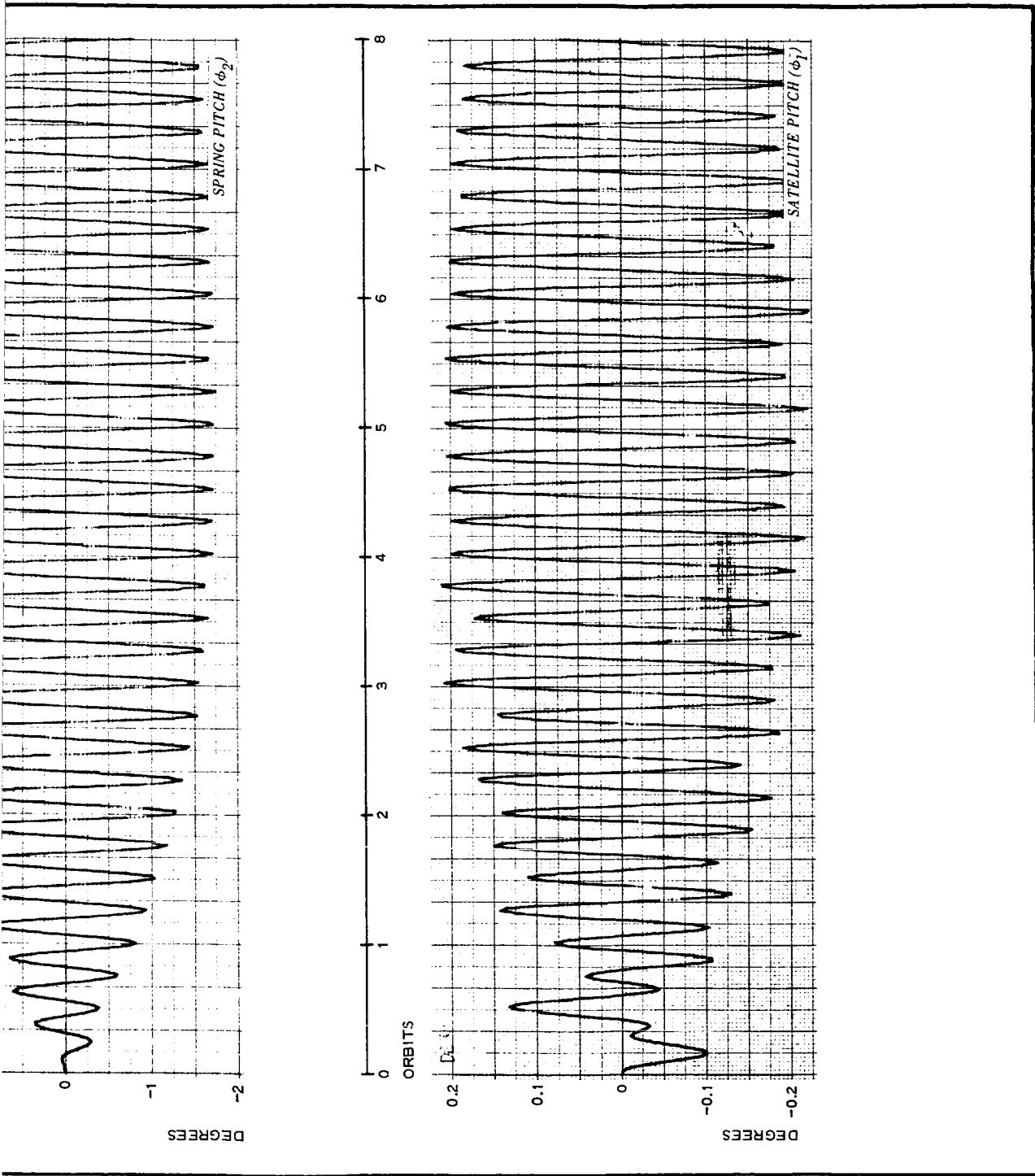




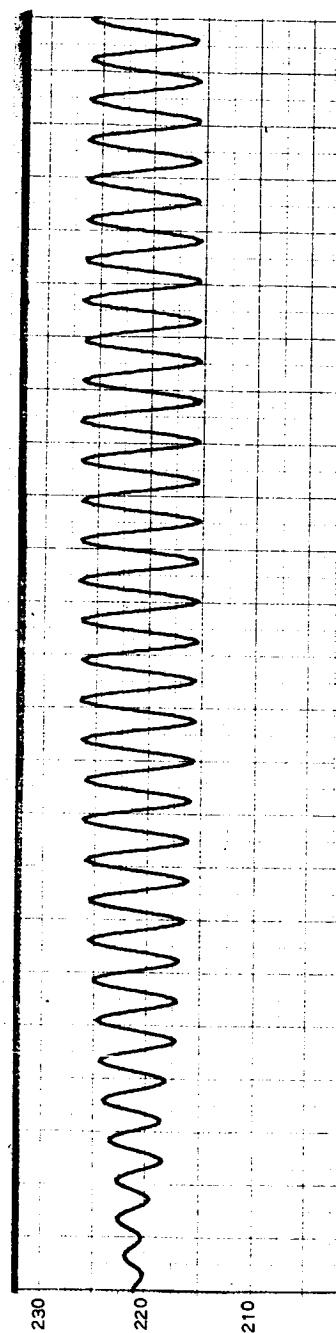
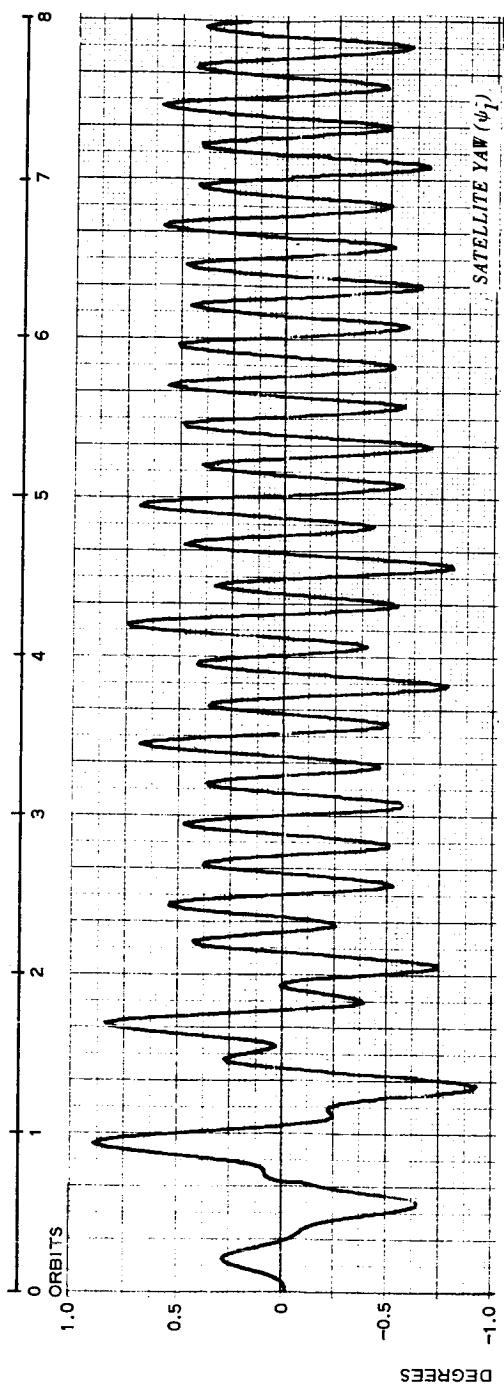
Run 129, Sheet 2 - Trial Roll-Transient-Response Run,
 $K_1 = 1.1145 \times 10^{-5}$ Lb per Foot

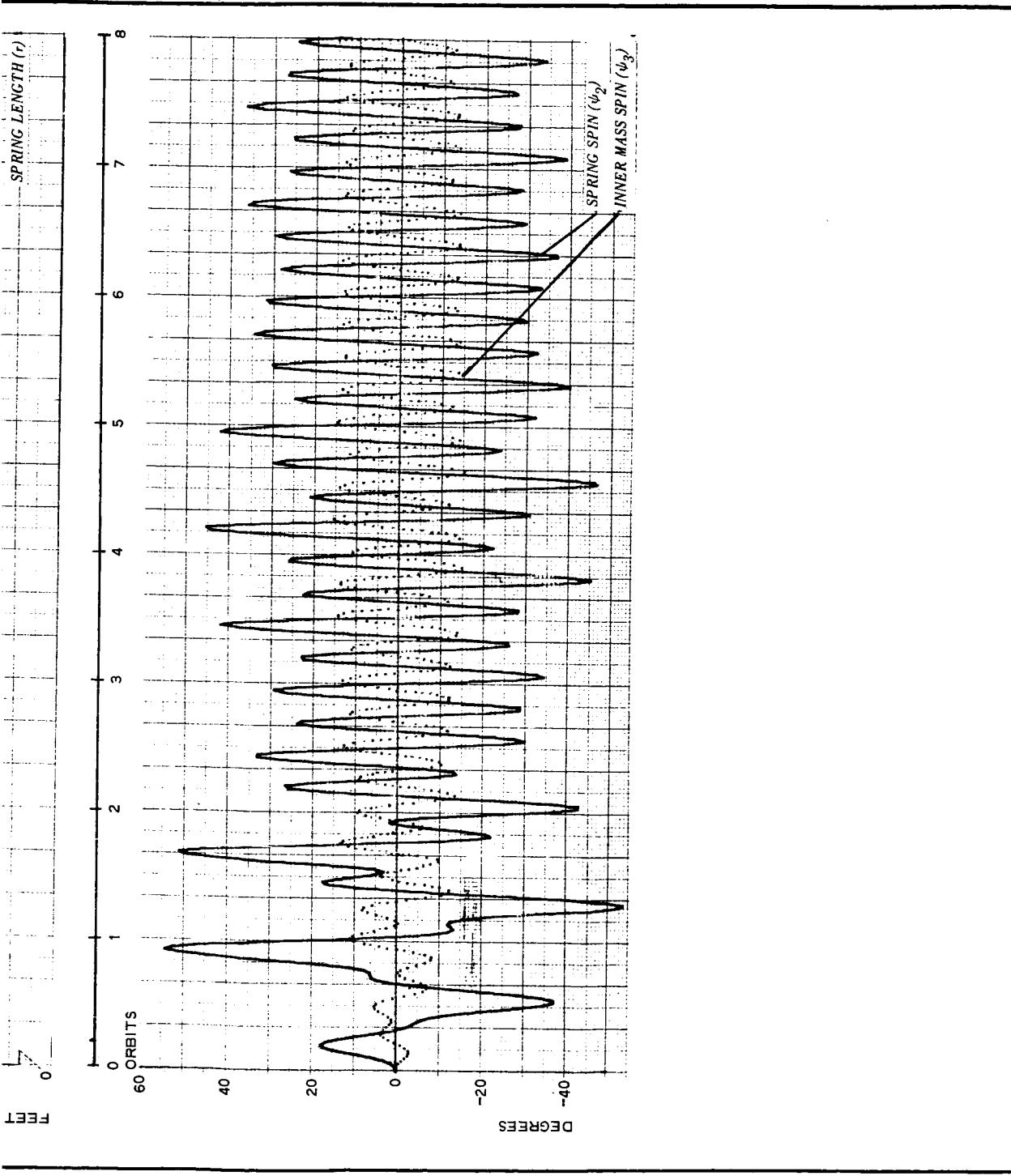
2



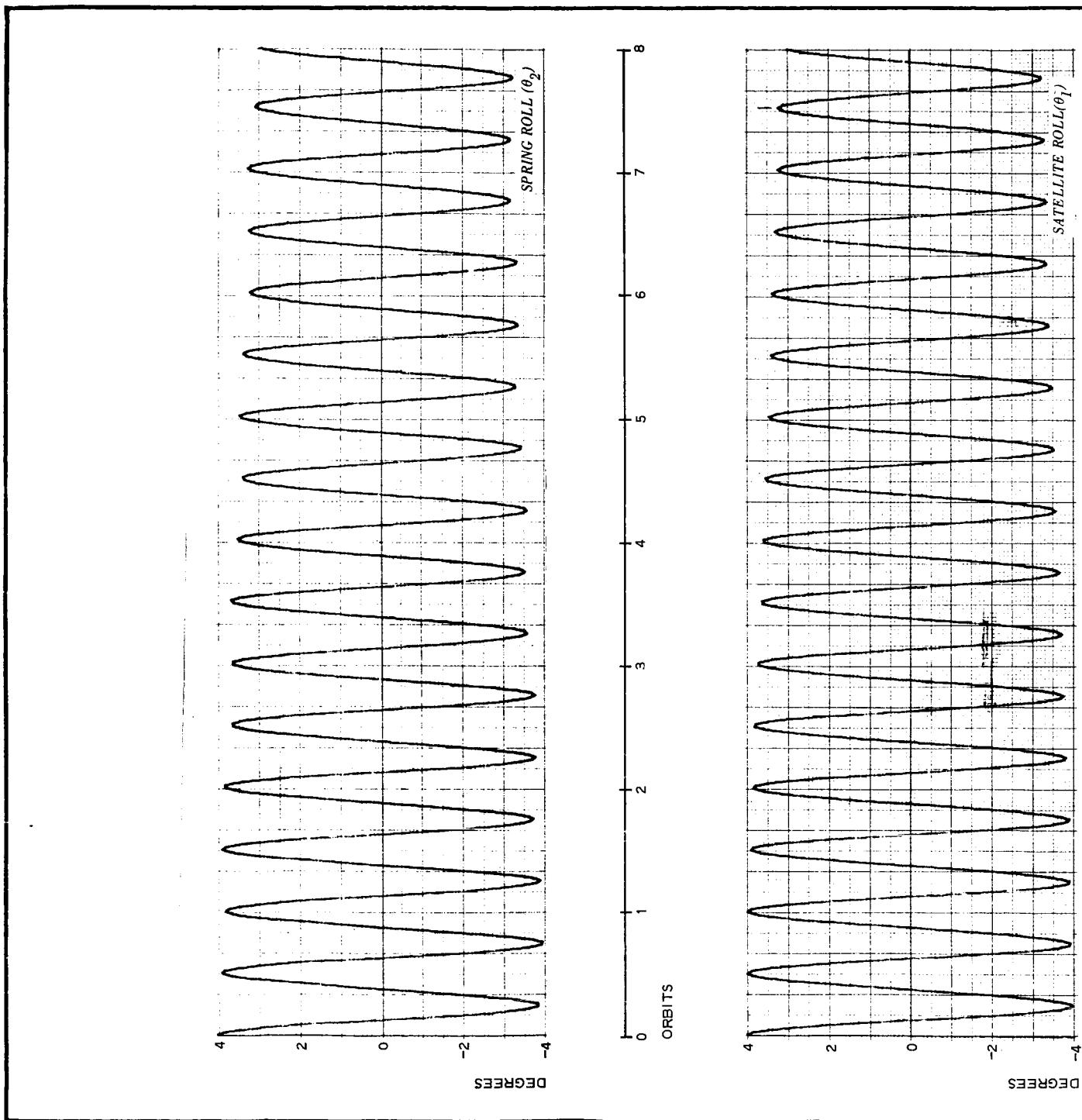


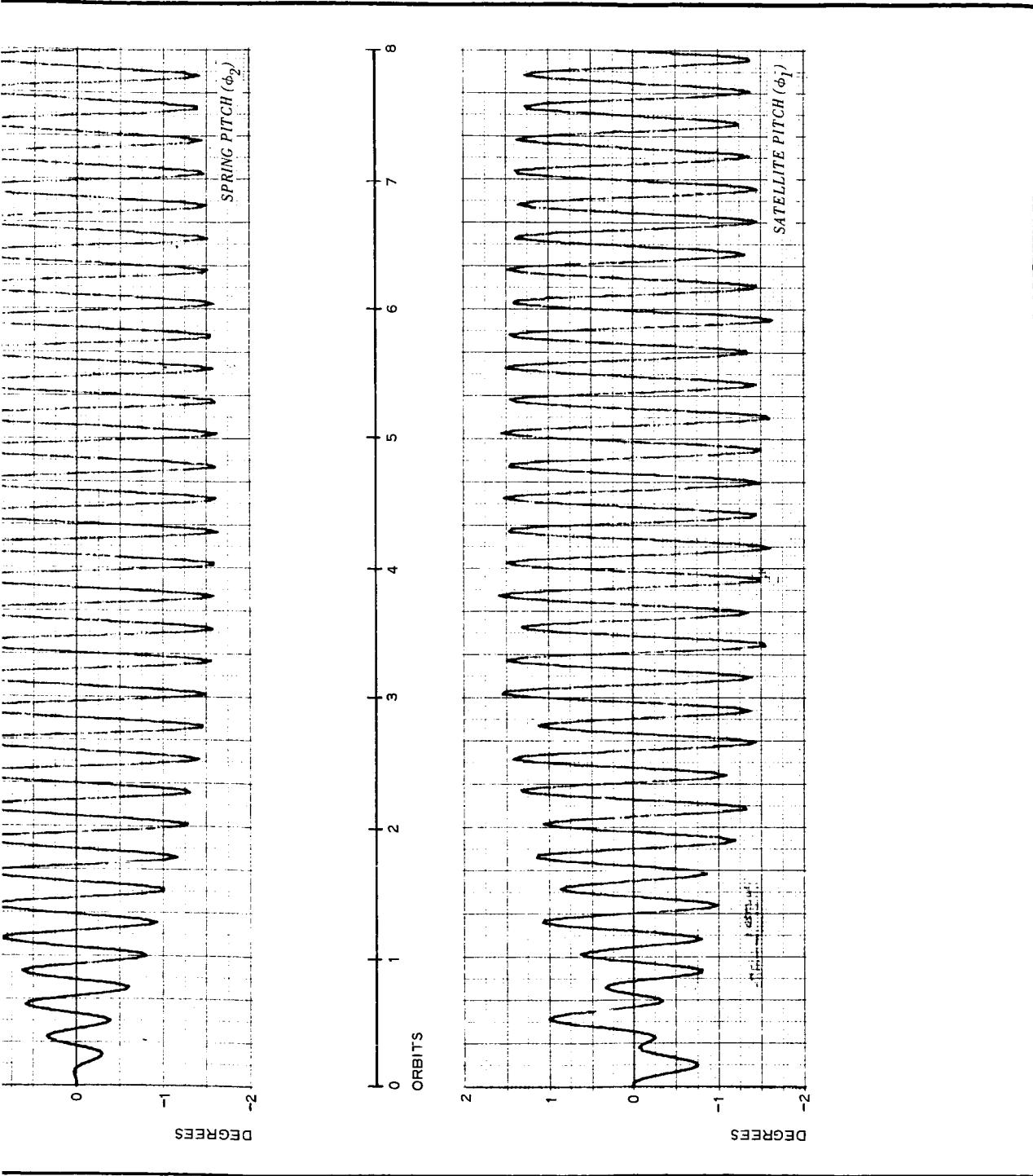
Run 135, Sheet 1 - Trial Roll-Transient-Response Run,
 $K_1 = 1.068 \times 10^{-5}$ Lb per Foot



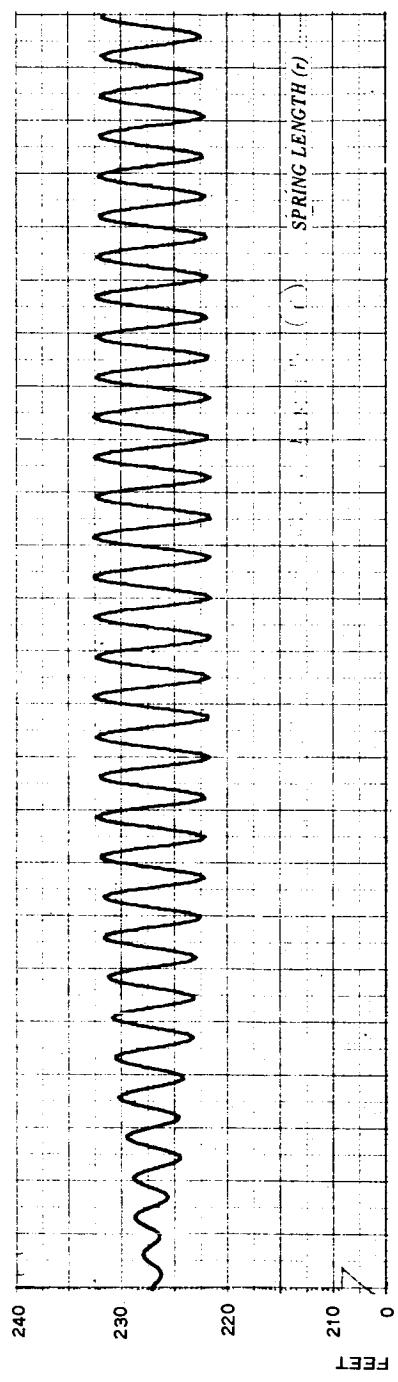
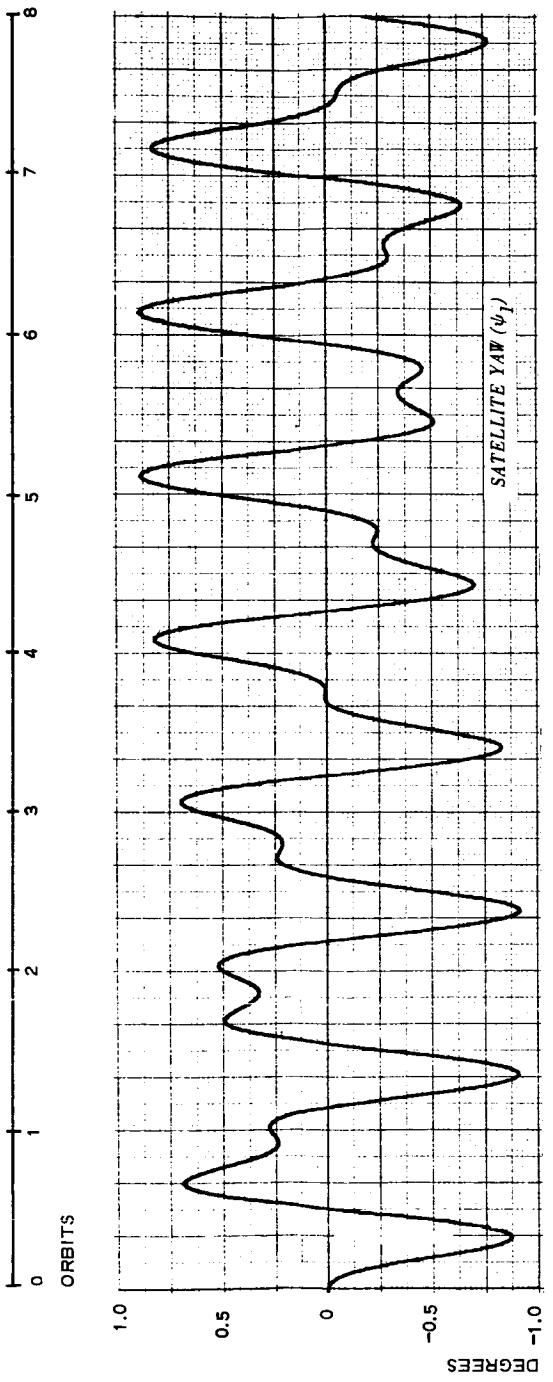


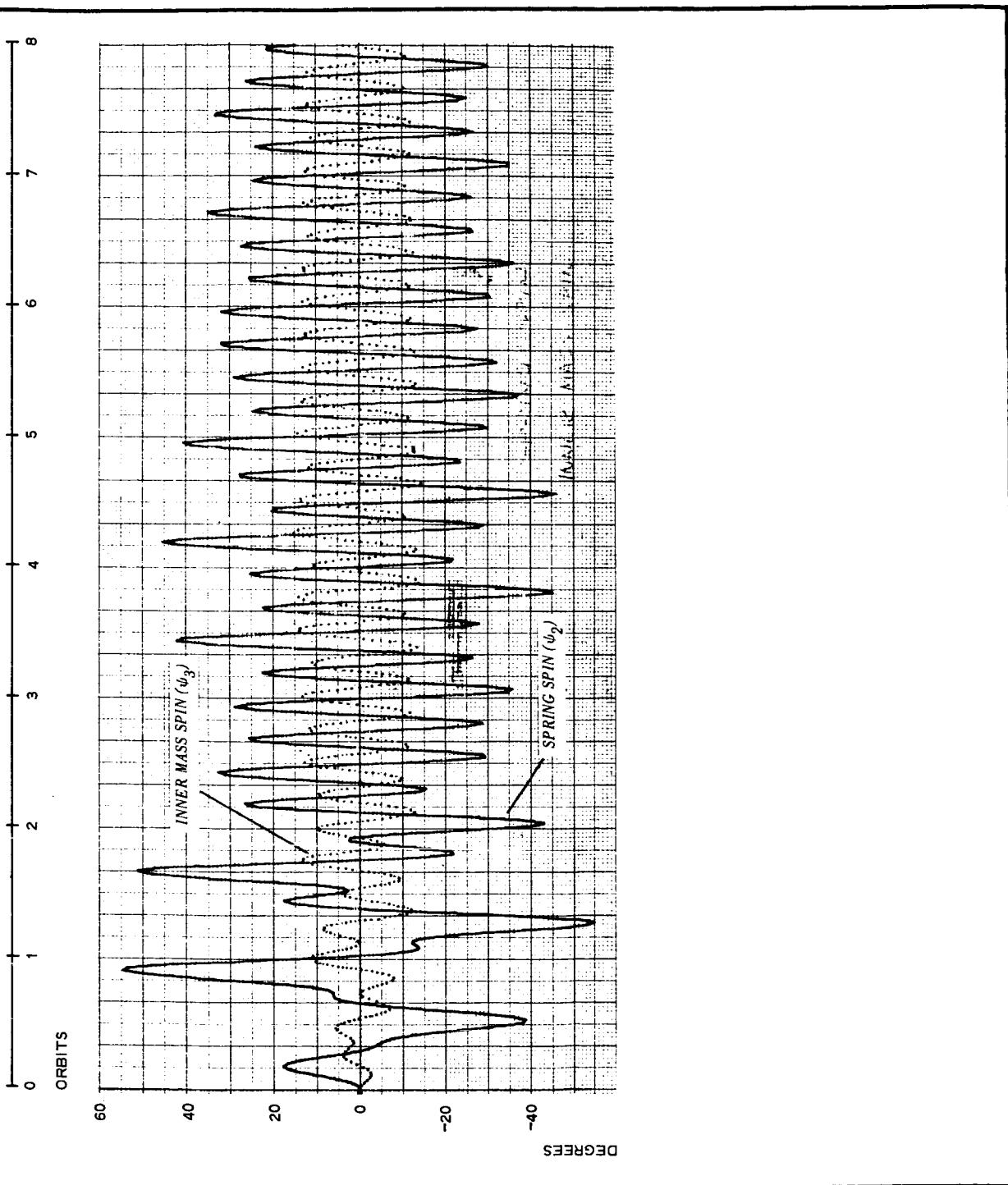
Run 135, Sheet 2 - Trial Roll-Transient-Response Run,
 $K_1 = 1.068 \times 10^{-5}$ Lb per Foot



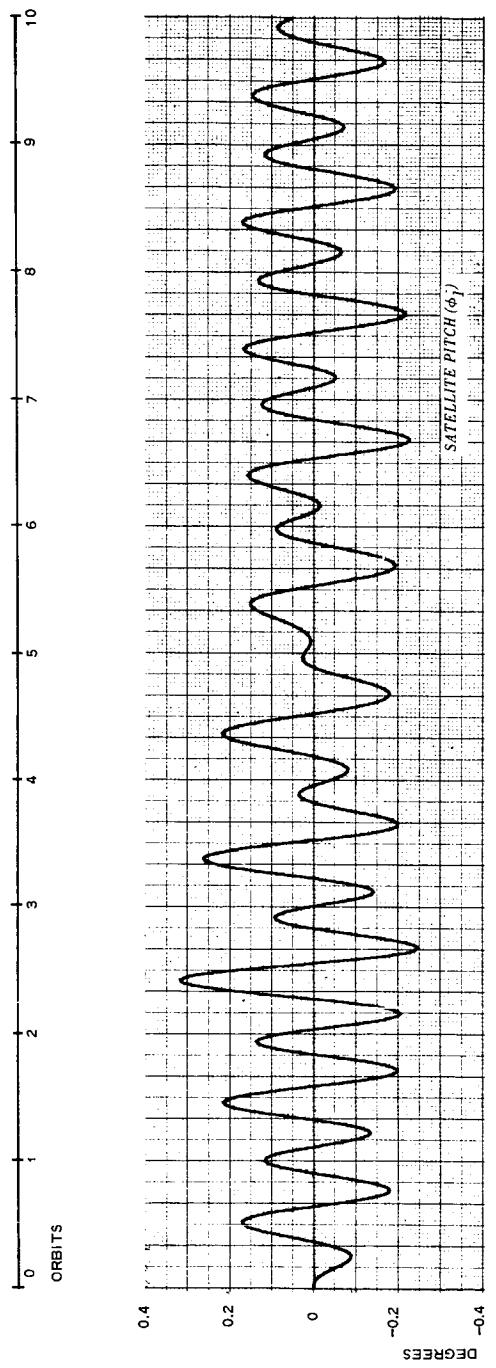
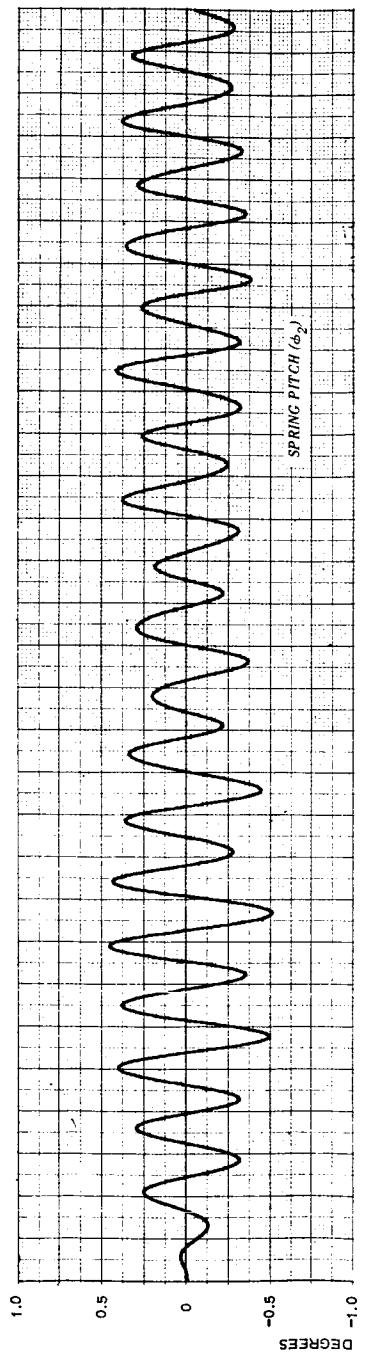


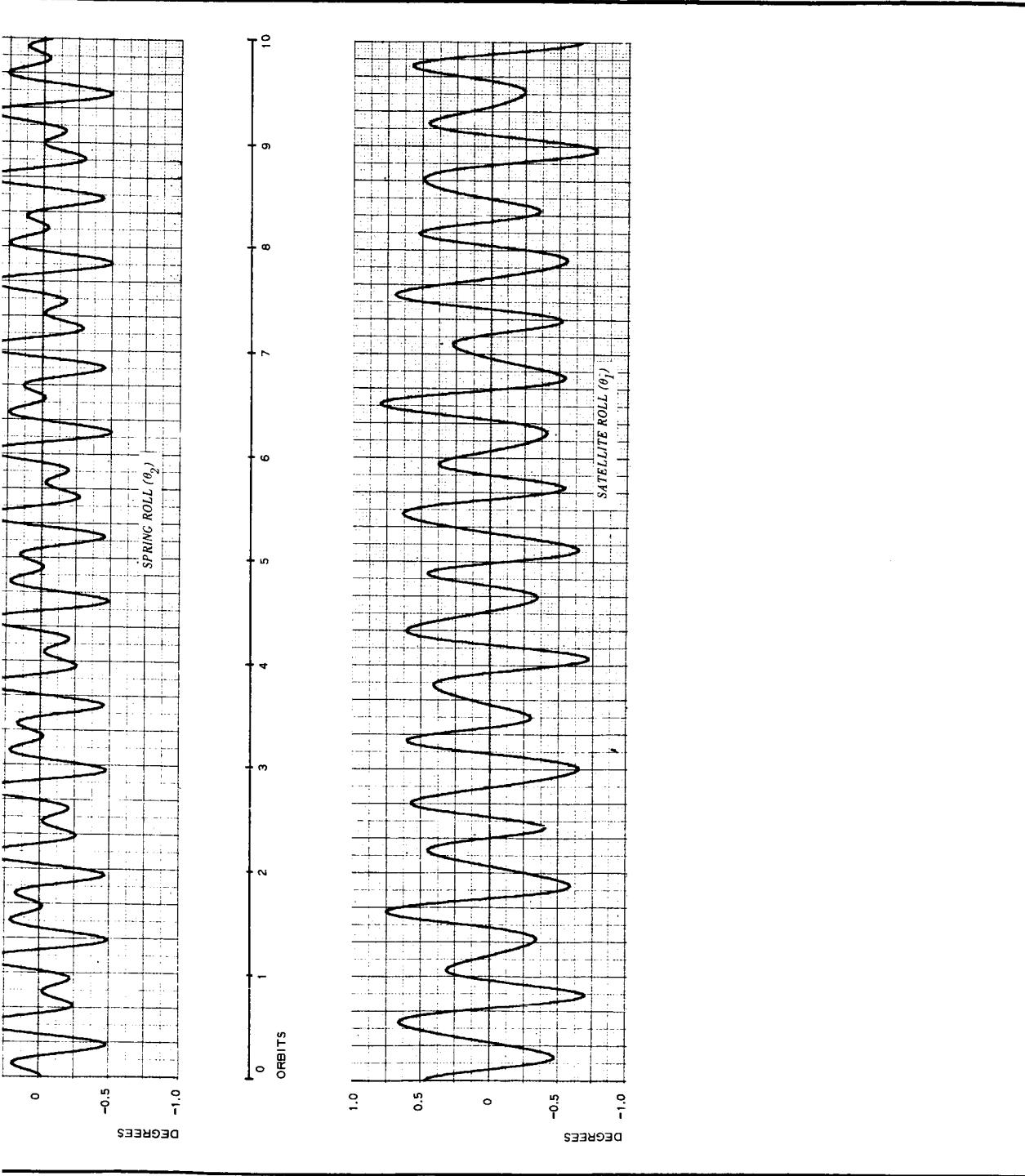
Run 136, Sheet 1 - Trial Roll-Transient-Response Run,
 $K_1 = 1.0535 \times 10^{-5}$ Lb per Foot





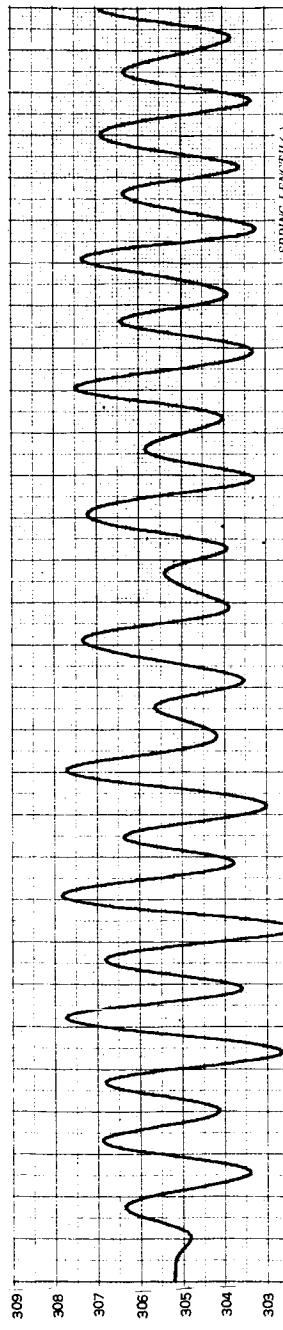
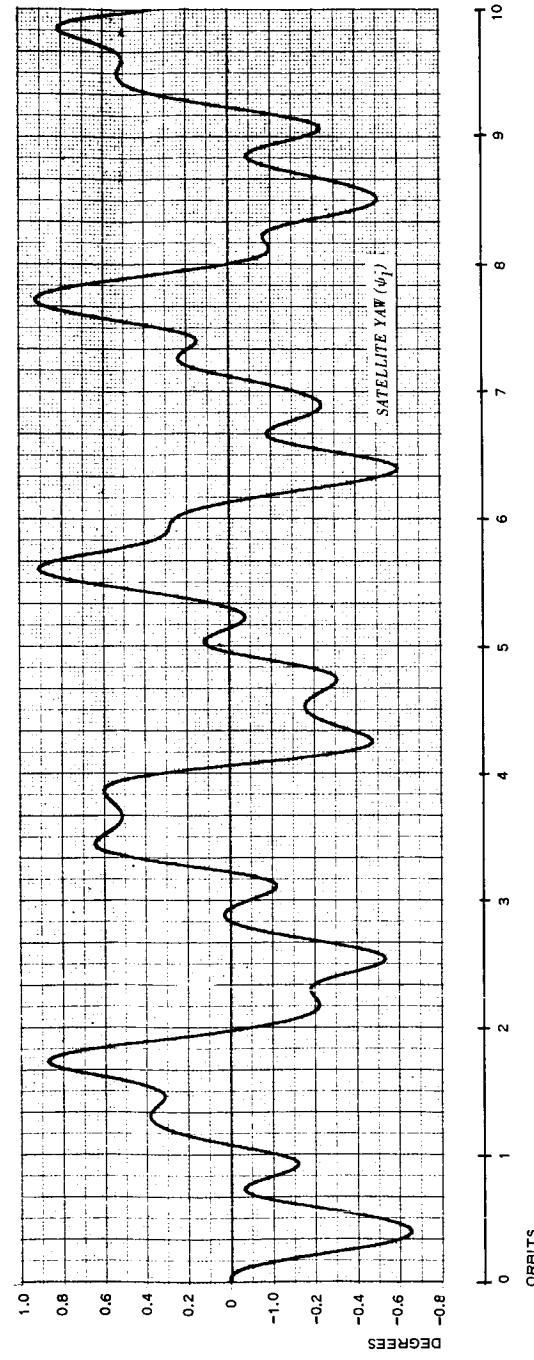
Run 136, Sheet 2 - Trial Roll-Transient-Response Run,
 $K_1 = 1.0535 \times 10^{-5}$ Lb per Foot

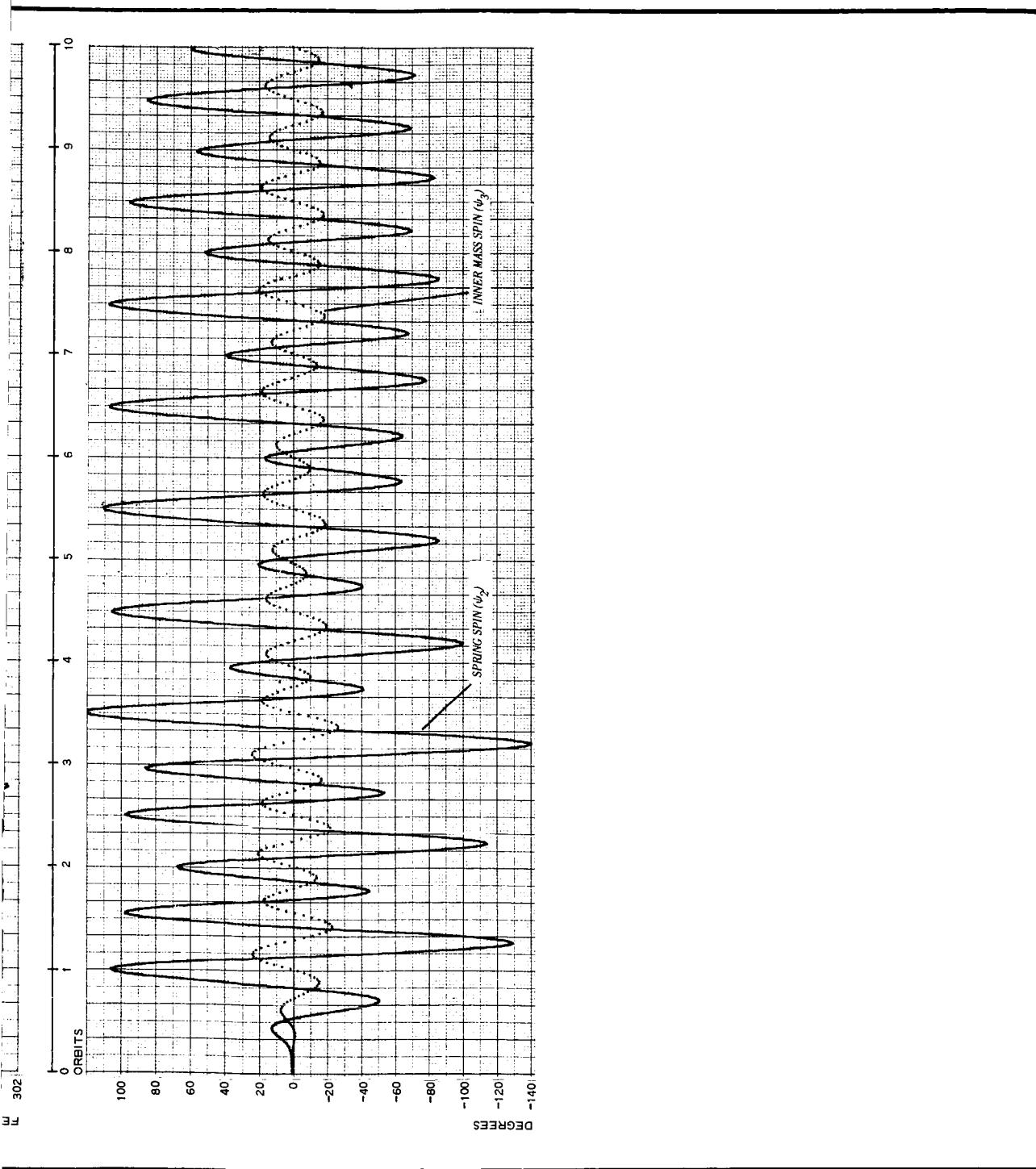




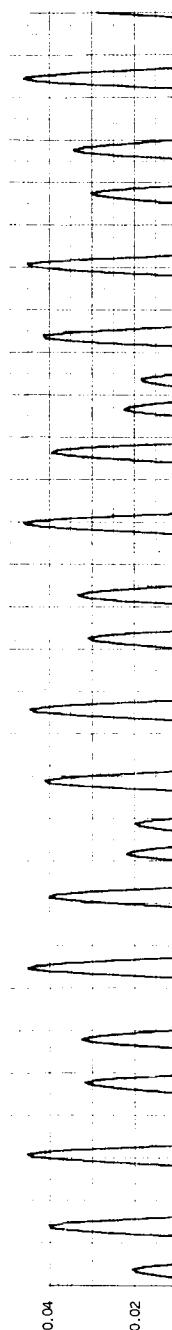
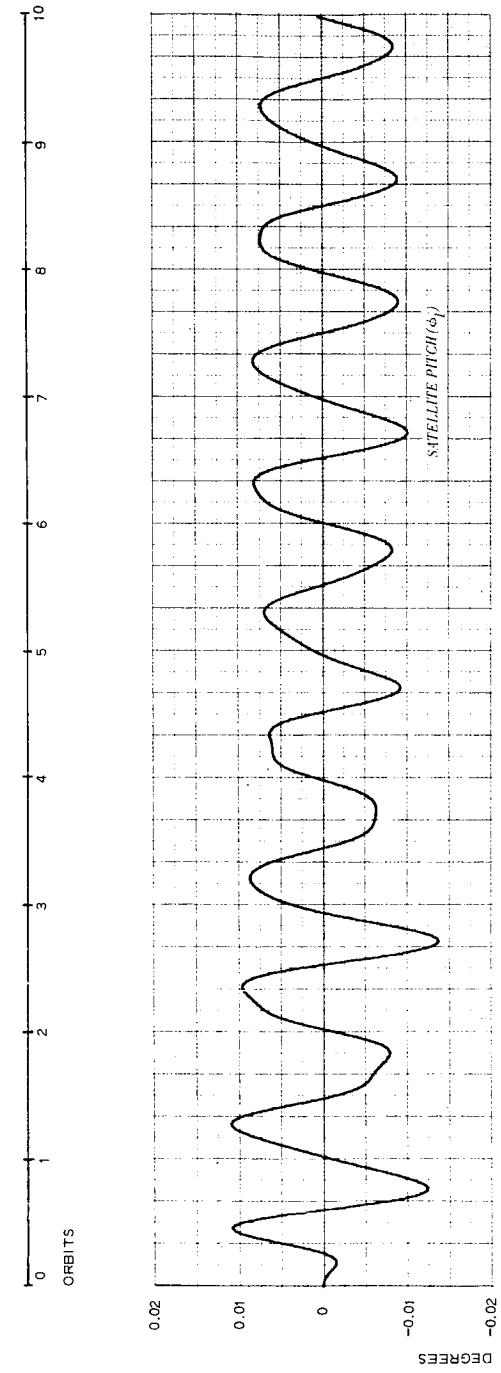
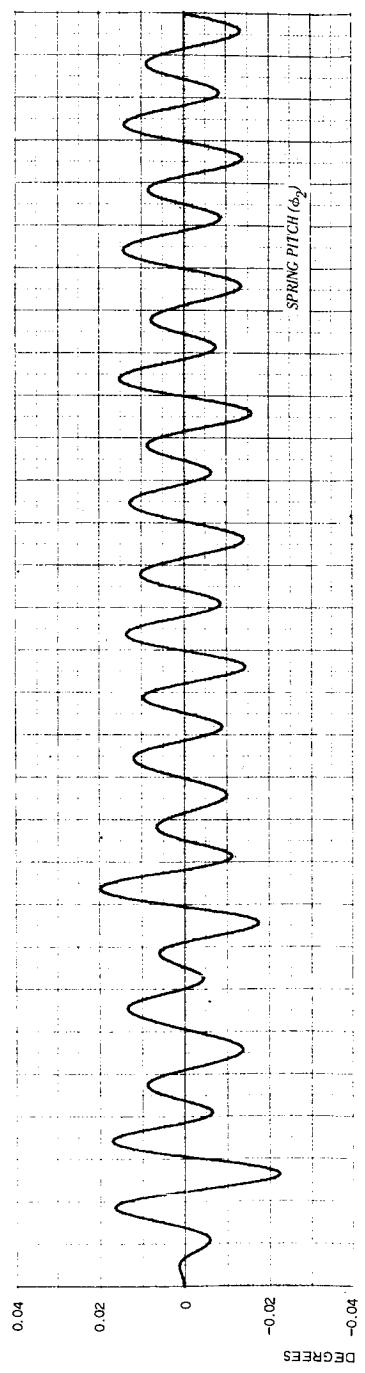
Run 131, Sheet 1 - Preferred Configuration, Steady-State Response to Sun 45 Deg to Orbital Plane (Unphotolyzed Satellite)

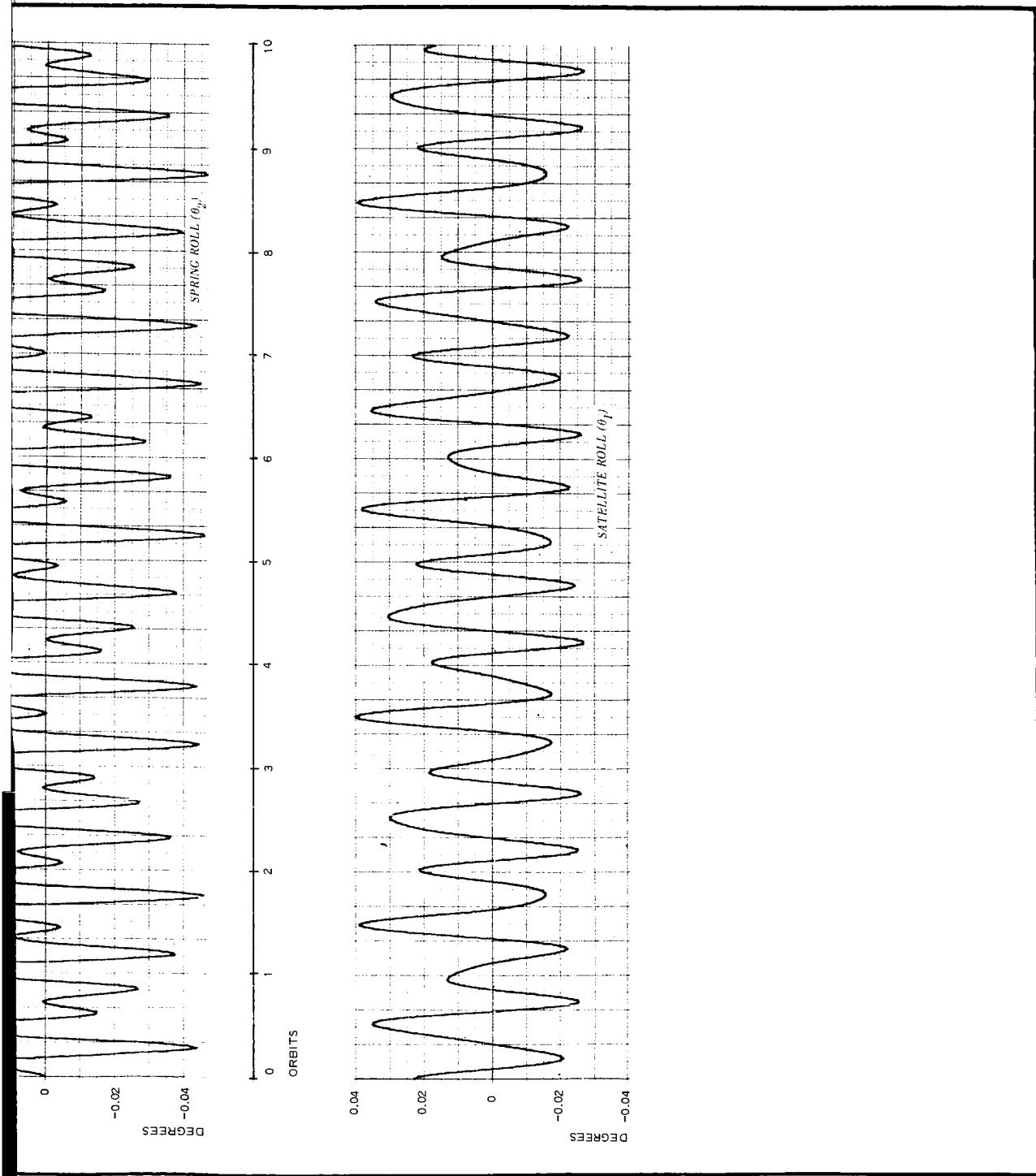
2





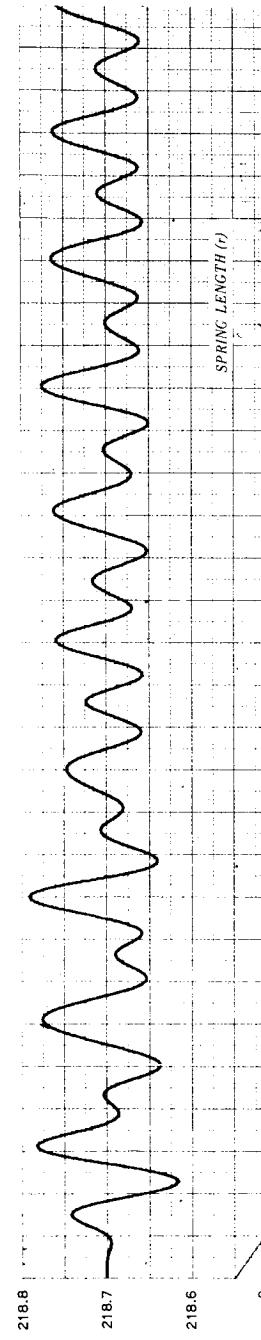
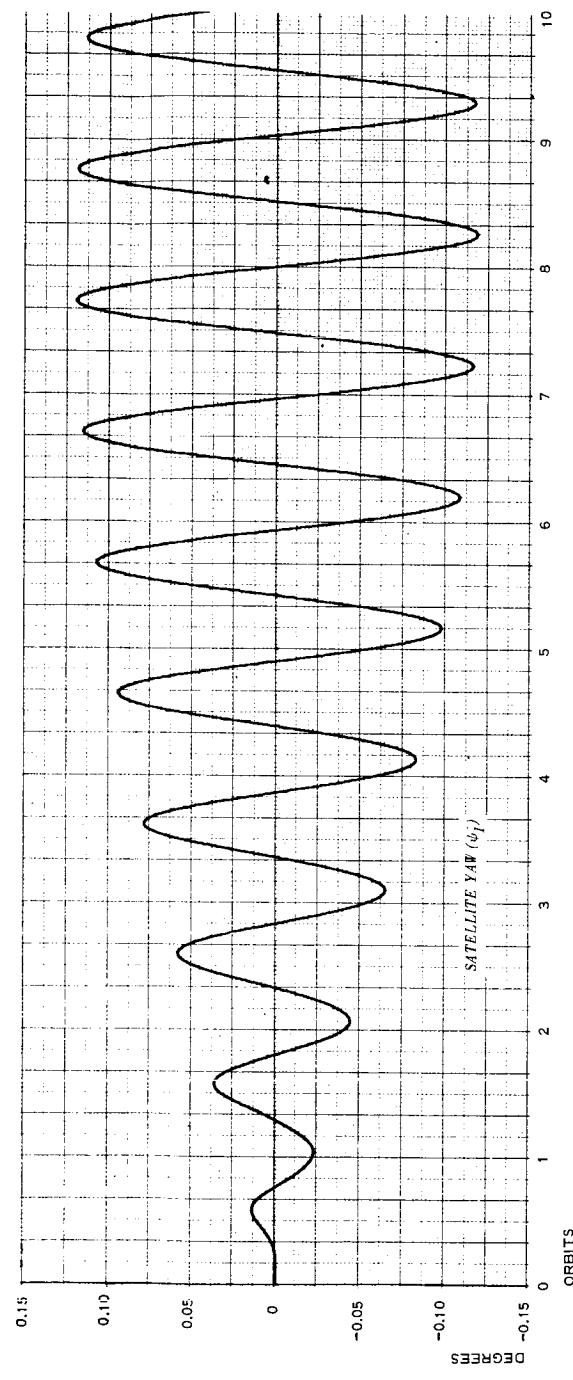
Run 131, Sheet 2 - Preferred Configuration, Steady-State Response to Sun 45 Deg to Orbital Plane (Unphotolyzed Satellite)

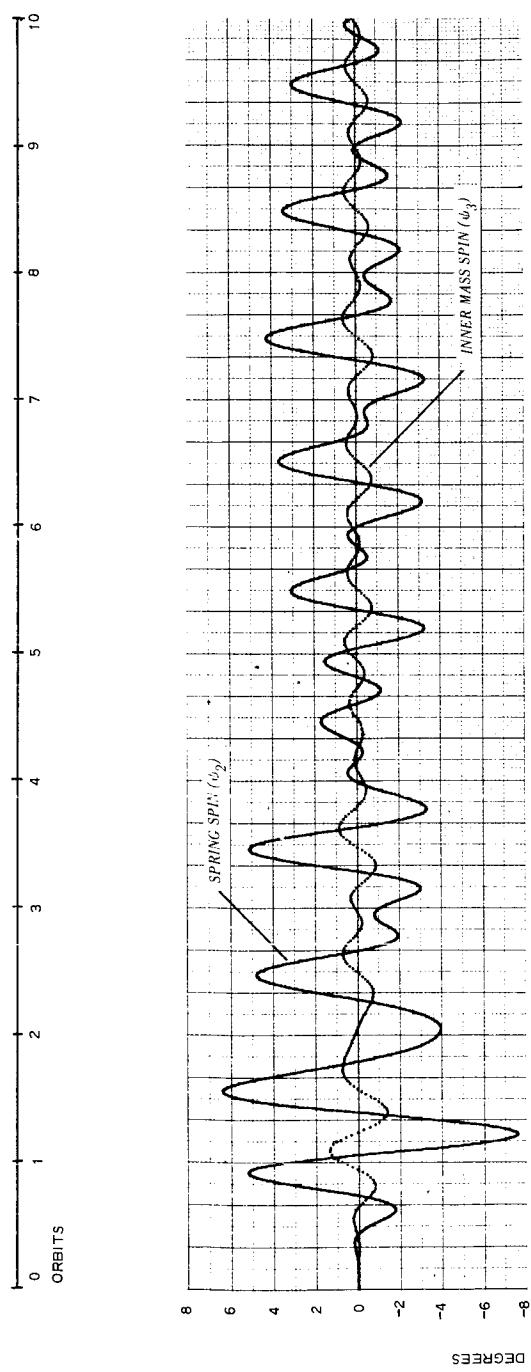




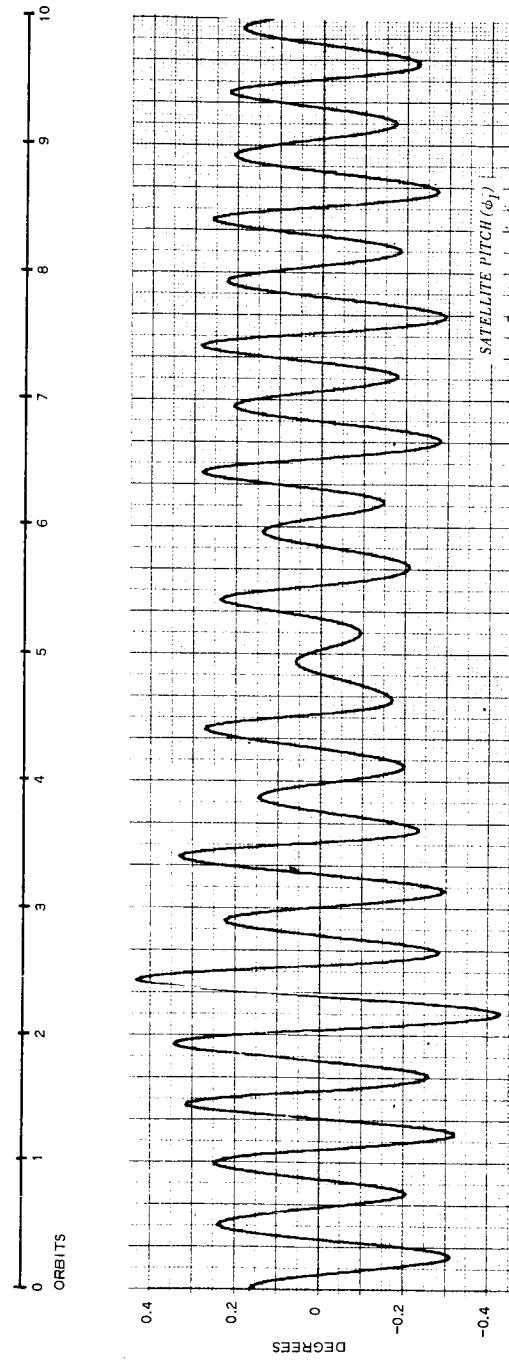
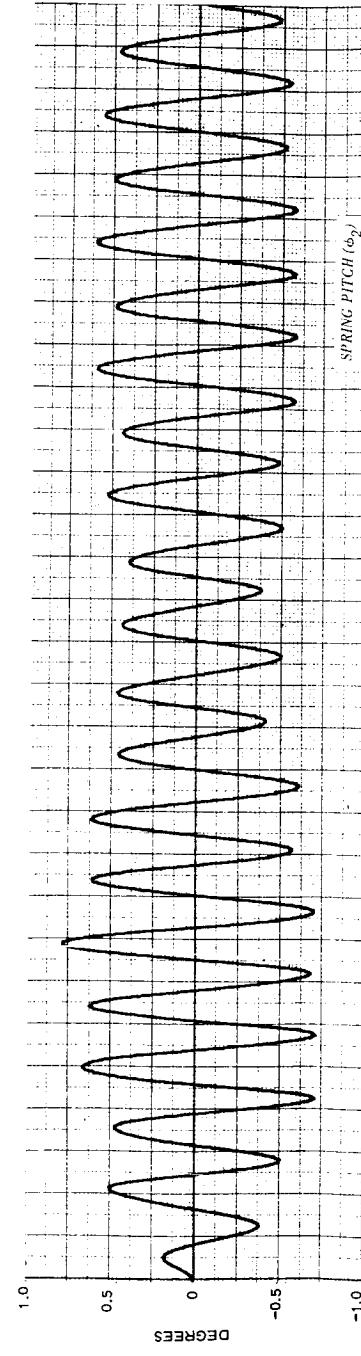
Run 132, Sheet 1 - Optimum Configuration Steady-State Response to Sun 45 Deg to Orbital Plane

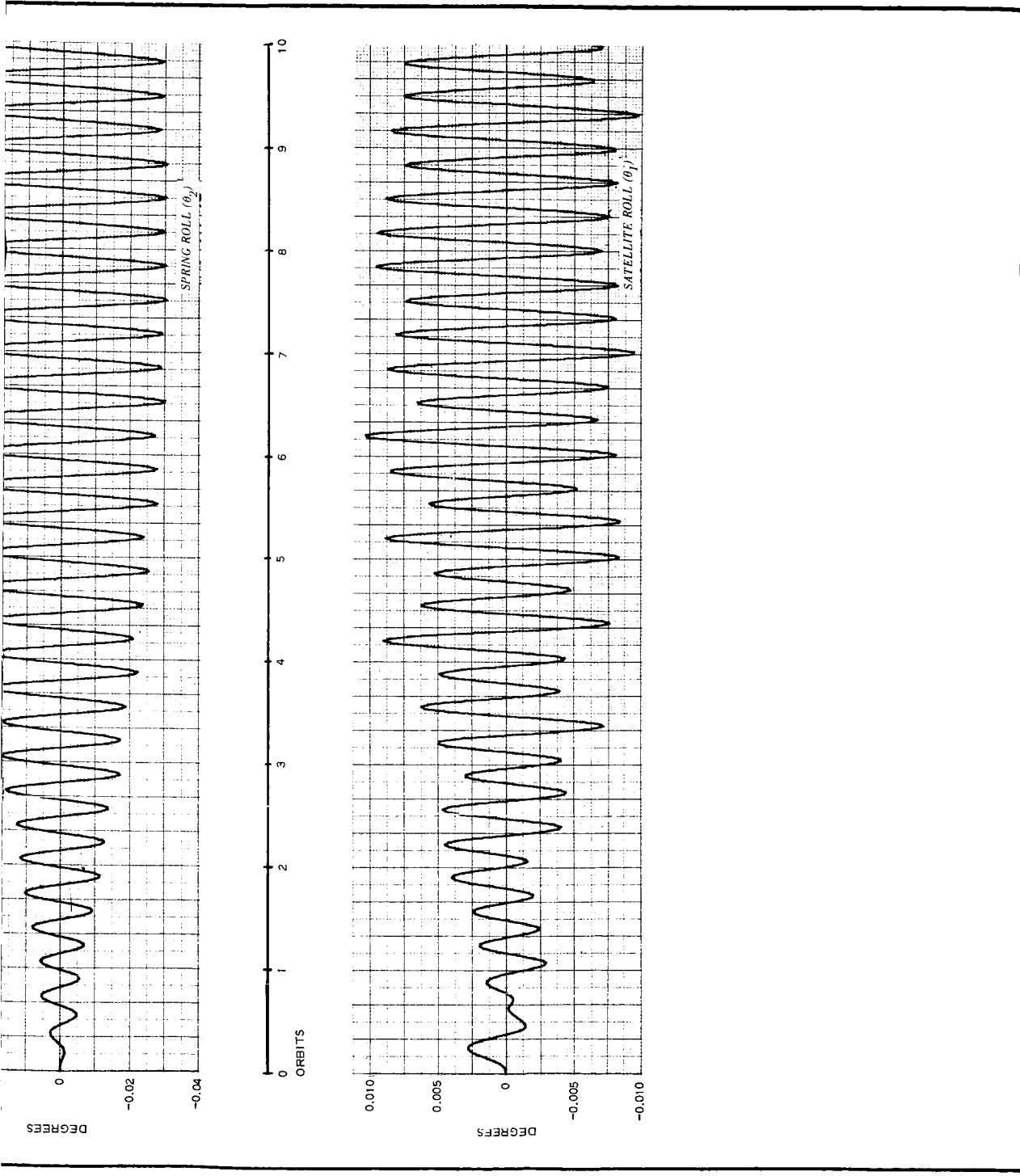
2





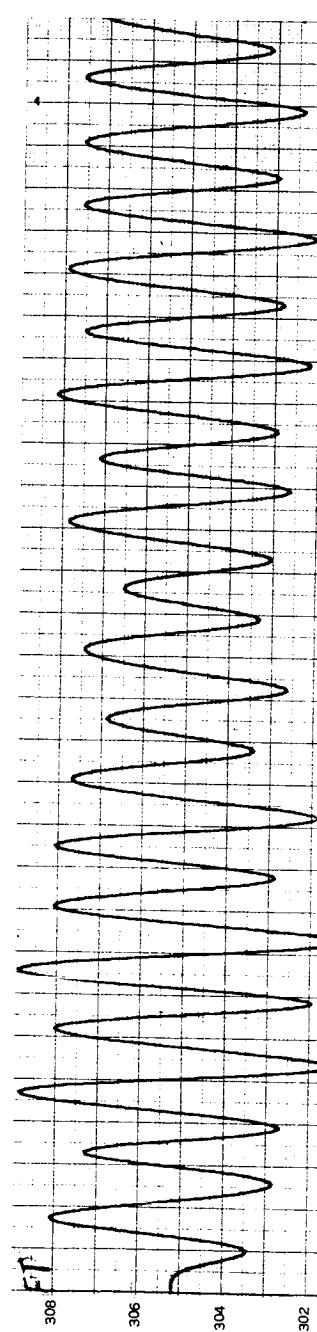
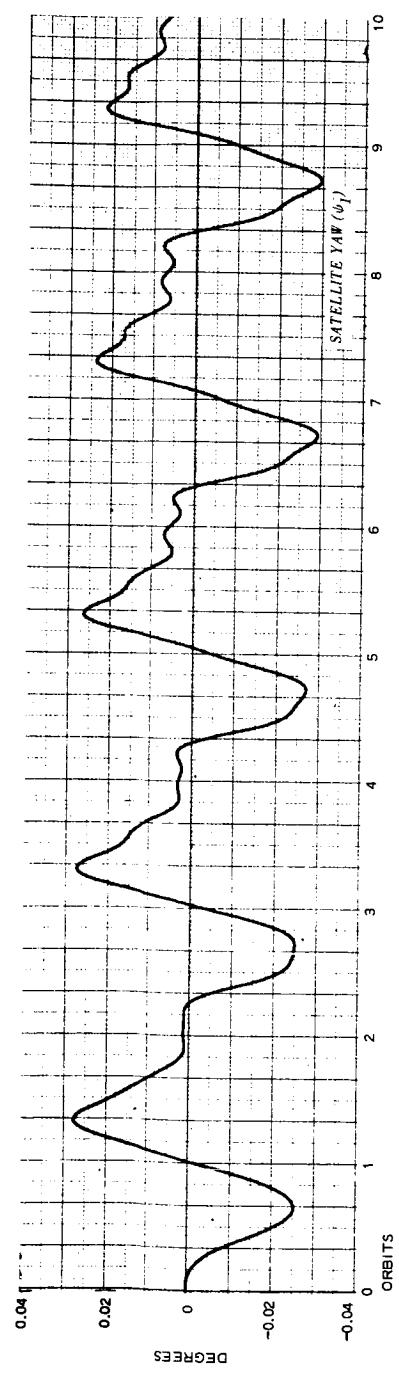
Run 132, Sheet 2 - Optimum Configuration Steady-State Response to Sun 45 Deg to Orbital Plane

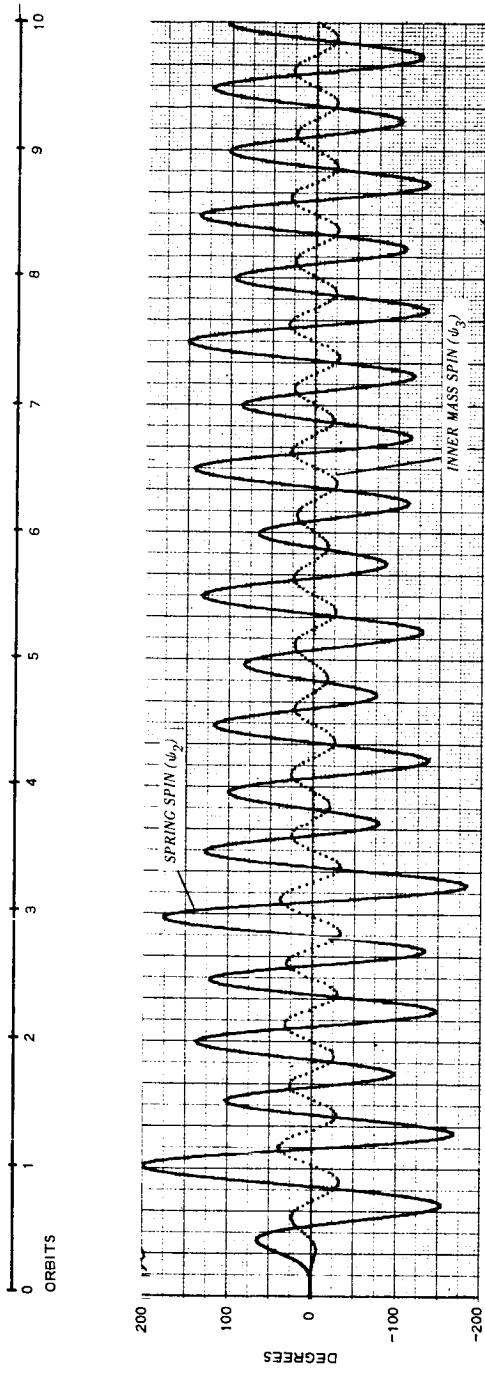




Run 133, Sheet 1 - Preferred Configuration, Steady-State Response to Sun in Orbital Plane (Unphotolyzed Satellite)

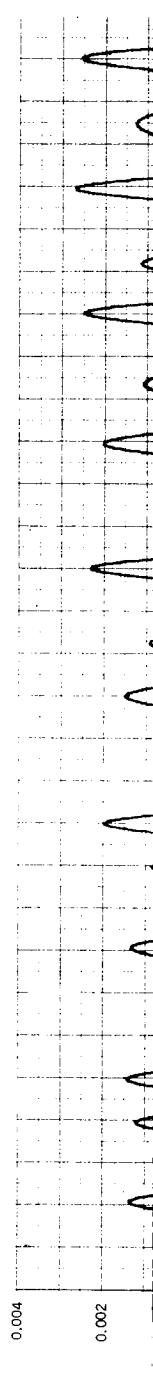
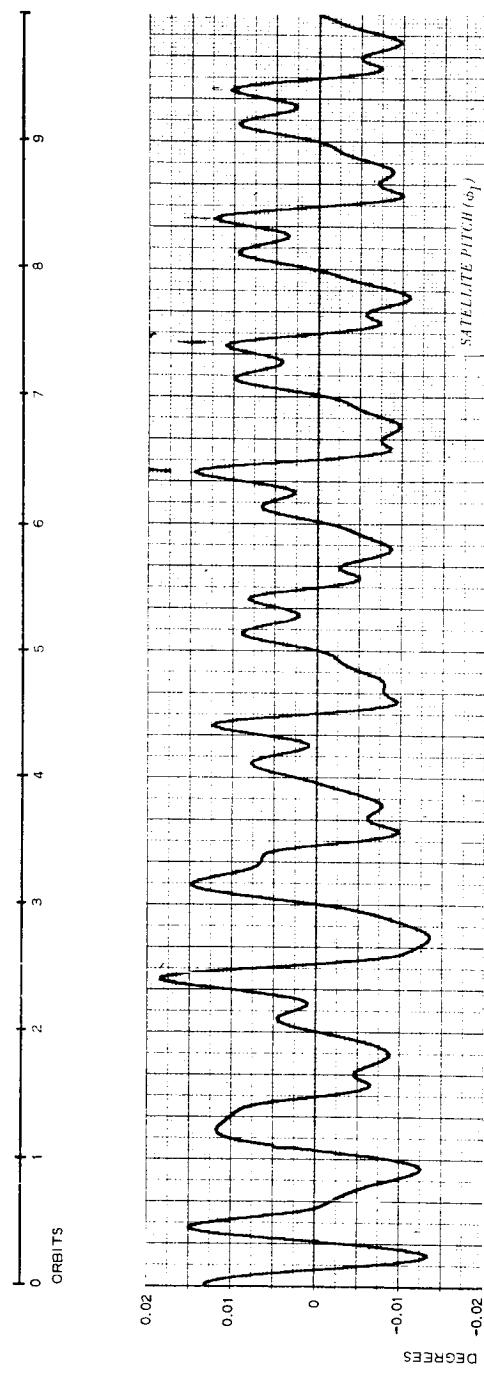
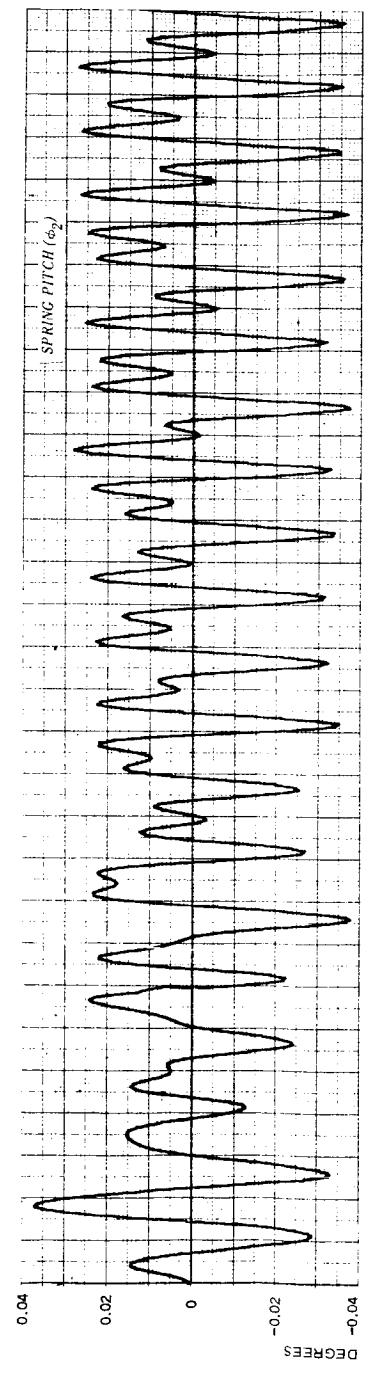
2

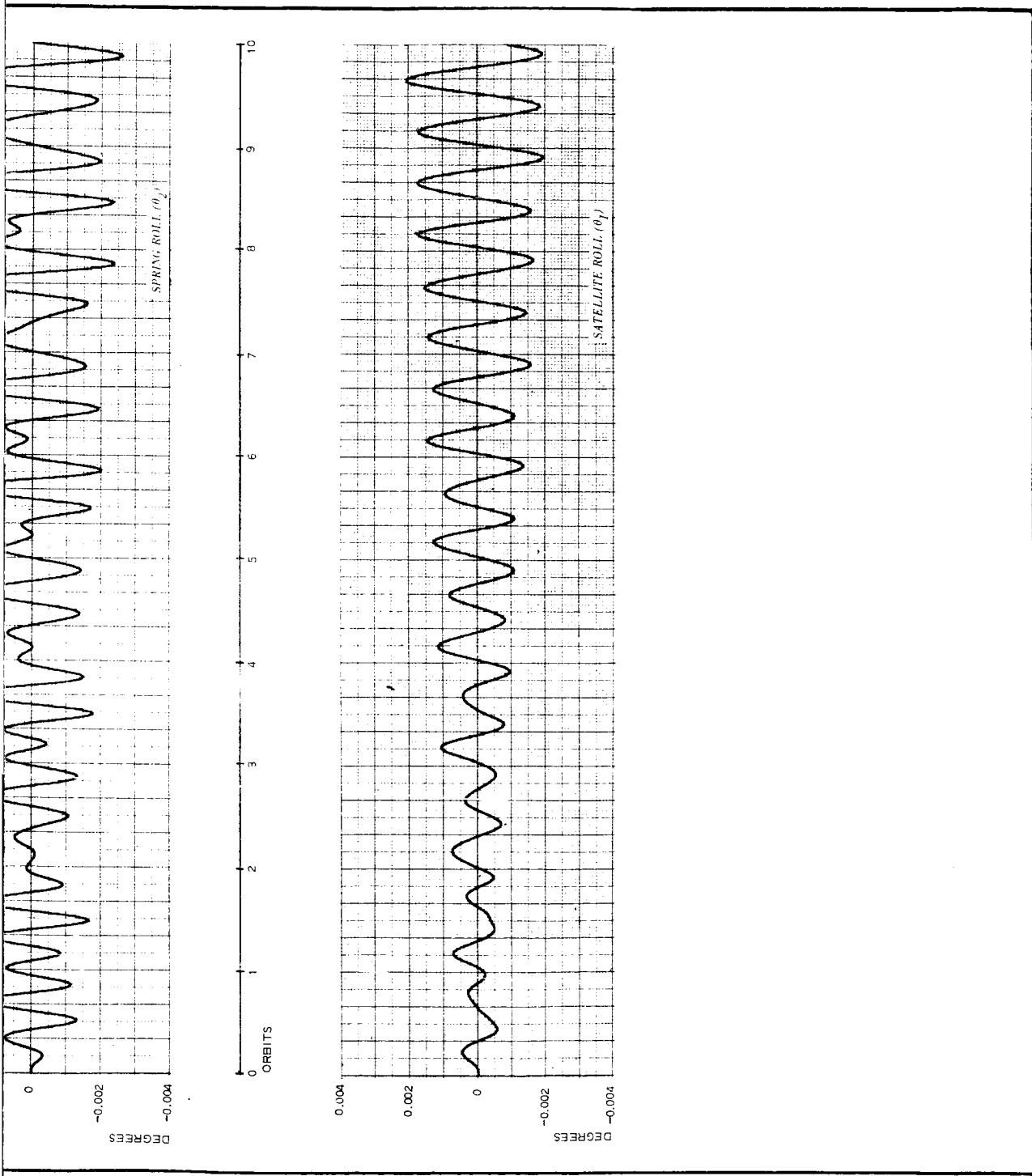




Run 133, Sheet 2 - Preferred Configuration, Steady-State Response to Sun in Orbital Plane (Unphotolyzed Satellite)

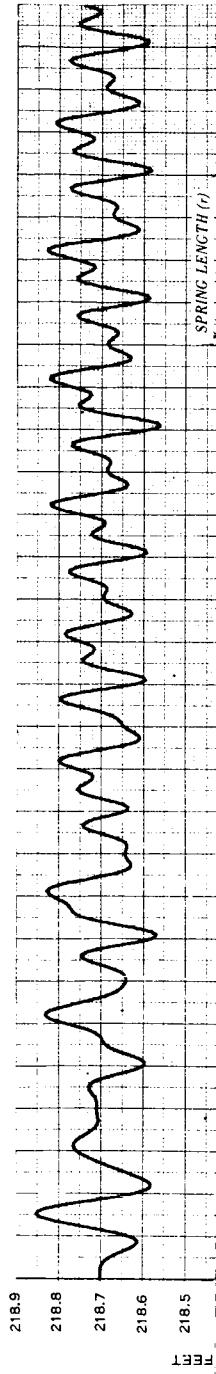
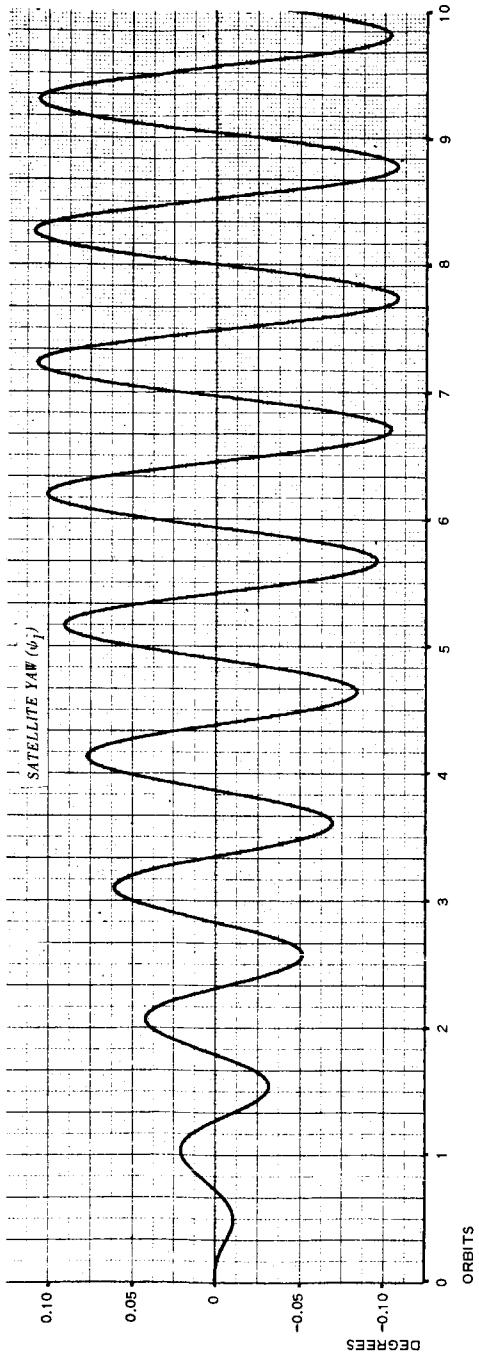
2

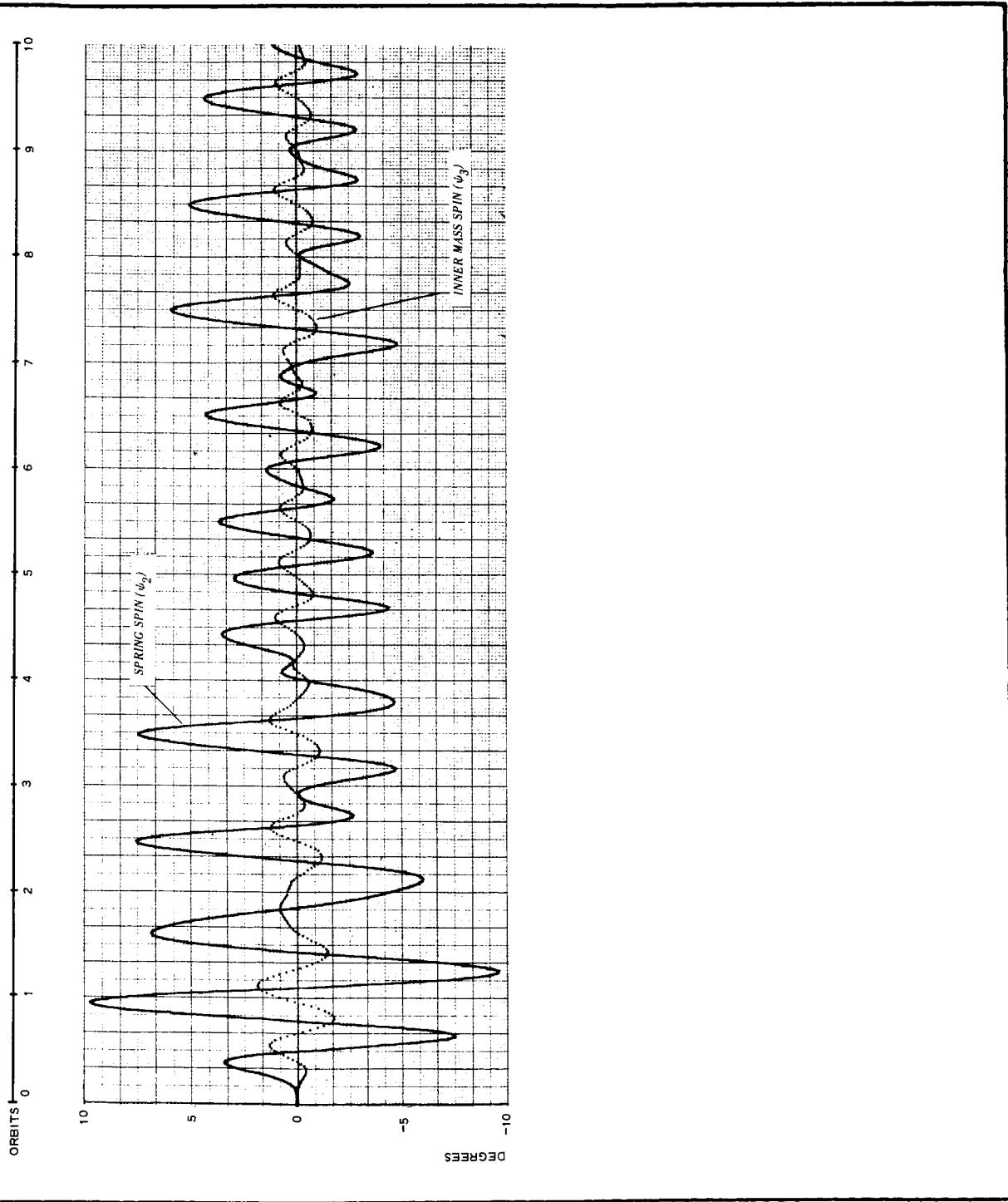




Run 134, Sheet 1 - Optimum Configuration, Steady-State Response to Sun in Orbital Plane

2





Run 134, Sheet 2 - Optimum Configuration, Steady-State Response to Sun in Orbital Plane

ABSTRACT

GER 11790

This study extends the results of a preliminary analysis of a proposed gravity-gradient stabilization and damping system previously reported in a "Feasibility Study and Preliminary Design of a Gravity-Gradient Stabilized Lenticular Test Satellite." The dynamic characteristics of the stabilization system were studied by simulation of the equations of motion on analog and digital computers. Results show that the settling-time constant of transient libration in the pitch axis is about three orbital periods, and for the roll axis, about six orbital periods. Steady-state forced librations caused by solar-pressure torques and orbital eccentricity are less than two degrees in amplitude.